Shear Banding in Time-Dependent Flows of Complex Fluids

ROBYN LUCY COOKE

Shear Banding in Time-Dependent Flows of Complex Fluids

Robyn Lucy Cooke

A Thesis presented for the degree of
Doctor of Philosophy

Supervised by Dr. Suzanne Fielding
Department of Physics
Durham University
UK

March 2013

Declaration

The work in this thesis is based on research carried out under the supervision of Dr. Suzanne Fielding, in the Department of Physics, Durham University, UK. No part of this thesis has been submitted elsewhere for any other degree or qualification and it is all my own work unless referenced to the contrary in the text.

Acknowledgements

First and foremost, I would like to thank my supervisor Suzanne Fielding. I am deeply grateful for her support, wisdom, and endless patience, and have thoroughly enjoyed working with her throughout my PhD. I have learned a great deal from Suzanne, not least about the subject of my PhD, but also about research methodology, and as such I am indebted to her for raising the quality of my research and the standard of my technical writing.

I would also like to thank those whom I have had the pleasure of working with during my PhD. I am thankful to Mike Cates for his collaboration during research on the fluidity and glassy polymer models. I am very grateful to Peter Olmsted and Stephen Agimelen for interesting and helpful discussions regarding step strains in polymeric materials. Likewise, I am indebted to Richard Graham for such discussions, and also for his help regarding analytics of the rolie-poly model under a step strain. I am also thankful to Peter Sollich for helpful feedback and data regarding the SGR model, and to Ron Larson for collaboration on the glassy polymer model. Finally, I would like to thank Nigel Clarke and Beth Bromley for their support as my second supervisors, Thibaut Divoux for providing questions for research on soft glassy materials, and to Alexei Likhtman for insightful and interesting discussions.

I am very grateful to all my friends and colleagues at Durham who have supported me during my PhD. In particular, I would like to thank my office mates Dawn Geatches, Paul Tulip, Lara Small, Kate Howarth, and Ricard Matas-Navarro for their encouragement and for always lending a kind ear. I am thankful to Dave Hoyle for many helpful discussions about polymers, and from whom I have learned

a great deal. Sincere thanks are also owed to Ewan Hemingway for his scrutinous and determined eye for detail, and many extremely helpful and interesting discussions on stability theory and complex fluids. I am also grateful to Mike Johnson for always helping fix my computer, and would like to thank Alt-J and Madeleine Peyroux, whose music has kept me going.

Finally, I would like to thank my family and personal friends for their endless love and support. I am particularly grateful to Dave, who has always believed in me, and my parents and Poppy for always being there for me. Thanks also to Catherine Hill and Luke O'Driscoll for always listening to my over-excited complex fluids-based rants. Finally, I would like to thank George, who has supported me at every step and for whom I am truly grateful.

Abstract

We explore theoretically the time-dependent rheological response of complex fluids to step stress, shear startup and strain ramp deformations. We study soft glassy materials and entangled polymeric materials above and below the glass transition using the scalar fluidity, soft glassy rheology (SGR), rolie-poly (RP), Giesekus and glassy polymer (GP) models. For each deformation we investigate fluid-universal, deformation specific criteria for the onset of linear instability to shear banding.

In step stress, the shear rate response of the RP and Giesekus models is qualitatively similar to experiment, but only in the RP model does significant transient shear banding arise. Motivated by experiments, we explore 'creep' and 'fluidisation' in the glass phase of the SGR model. Finally, we show the GP model has similar behaviour in step shear stress as it does in extensional loading; we also explain why strain hardening reduces the magnitude of transient shear banding.

In shear startup, we explore 'elastic' and 'viscous' contributions to linear instability to shear banding. We use this to explain: the range of shear rates for which time-dependent shear banding arises in the RP model; why no significant time-dependent shear banding arises associated with the stress overshoot in the Giesekus model; the occurrence of age-dependent transient shear banding in the scalar fluidity model; and also why strain hardening again decreases the magnitude of transient shear banding in the GP model.

Finally, we investigate stress relaxation in the RP model after strain ramps with rates that probe the chain stretch relaxation rate τ_R^{-1}. We show that after 'slow' ramps (relative to this rate) linear instability to heterogeneity arises for strain amplitudes $\gamma \gtrsim 1.7$, and that 'fast' ramps of the same amplitude result in a delayed onset of linear instability, provided convective constraint release is sufficiently inactive.

Contents

List of Figures

List of Tables

1

Introduction

The term ‘complex fluid’ covers a vast range of materials, many of which are ubiquitous in every day life and whose deformation and flow properties, that is, their *rheology*, is essential to their use, e.g., non-drip paint, drilling muds, toothpaste, foodstuffs, cosmetics and plastics. These materials usually have a mesoscopic substructure that dominates their response to deformation. Such substructures may be: concentrated colloidal particles in a disordered, metastable configuration; entangled polymeric molecules — that is, many objects that form entanglements with each other, resulting in topological constraints on their motion; bubbles in a foam that deform elastically under deformation but rearrange plastically after a certain strain or stress is met; or liquid crystalline materials containing long rod-like molecules that undergo flow induced transitions between an isotropic or nematically aligned state.

The subject of this thesis concerns a shear-induced phenomenon commonly seen

in complex fluids called *'shear banding'*, whereby an initially homogeneous material separates into macroscopic 'shear bands' of differing viscosity that coexist at a common shear stress under an applied shear flow [55, 98, 119, 125]. Shear banding has been shown to occur in a vast range of materials, such as entangled polymer solutions and melts [18, 19, 138, 162], triblock copolymer solutions [12, 99], wormlike micellar solutions [16, 70, 71, 76, 89, 95–97, 110, 144], lyotropic lamellar phases [145], emulsions [37, 126], carbopol microgels [45], colloidal glasses [141], and foams [140]. Most of these rheological studies investigated the *steady state*, i.e., the long time behaviour in which the dynamics of the stress (or bands) no longer change as a function of time. In this long time limit, shear banding is usually studied alongside the steady state 'flow curve', the relation between the steady state shear stress and the spatially averaged shear rate, of the material. It is thought the cause of steady state shear banding is a negative slope in the underlying constitutive relation between shear stress and shear rate: this relation is that which would arise if the flow were constrained to be homogeneous. This criterion for steady state shear banding of a negative slope in the underlying constitutive relation is well known [160, 172].

More recently though, there has been much research on the time-dependent rheological response of complex fluids during the initial startup of deformation, before a steadily flowing state is established. It has been shown that *time-dependent shear banding* can arise during this response, in a manner apparently independent of the steady state criterion described above. In addition, such time-dependent shear banding has been shown to arise in materials with different underlying structure provided certain common rheological signatures are seen in the time-dependent flows of step stress [16, 19, 42, 64, 74–77, 161], shear startup [19, 43, 45, 77, 138] and strain ramp [9, 16, 17, 52, 91, 135, 168] deformations. This is indicative of a generic underlying cause for the onset of time-dependent shear banding. Clearly, criteria for the onset of shear banding during these time-dependent flows that are independent of the material in question are needed. Dr. Suzanne Fielding has recently derived such criteria, separately for three time-dependent deformation protocols: step stress, shear startup and strain ramp [117], which depend only on the experimentally measured rheological response functions, and are independent of the material type. In

this thesis, we will examine the use of these criteria during an investigation of the time-dependent rheological responses of models for three classes of material: soft glassy materials, and entangled polymeric materials above and below the glass transition, in each deformation protocol. Our calculations pertain to the formation of shear bands that arise during the time-dependent response of startup of shear flow before a steadily flowing state is established. They therefore not only describe how steady state shear bands are established from such a flow in systems that show steady state banding, but also describe the formation of transient shear bands, and the subsequent return to homogeneous shear, in systems that do not band at steady state.

Our aim is to unify the understanding of time-dependent shear banding in these different classes of material, whilst also providing new understanding of their time-dependent stress or shear rate responses to these three deformation protocols.

In the material classes described above, the description: 'entangled polymeric materials above the glass transition' includes polymer fluids such as entangled polymer solutions and melts. However, it also includes entangled wormlike micelles whose long, chain-like substructures undergo the same stress relaxation mechanisms as polymers, with the additional mechanisms of chain breaking and reforming [27].

1.1 Layout of thesis

This thesis is organised as follows. In Chapter 2 we outline the three deformation protocols: step stress, shear startup and strain ramp that we will investigate in Chapters 4, 5 and 6, respectively. We then introduce the concept of shear banding, and subsequently provide a literature review for each deformation protocol and class of material, in order to provide a context for the rest of the thesis.

In Chapter 3 we outline the theoretical rheology required to model such materials, and describe the models used in this thesis: the rolie-poly (RP) and Giesekus models for entangled (non-glassy) polymeric materials; the 'scalar fluidity' and soft glassy rheology (SGR) models for soft glassy materials; and the glassy polymer (GP) model. We outline a 'general framework' within which the criteria described above will be

derived, after which we describe the time-dependent linear stability analysis used in these derivations and throughout this thesis. In the appendix of Chapter 3 we also include details of our numerical methods.

In Chapters 4, 5 and 6 we investigate the rheological response of complex fluids to the step stress, shear startup and strain ramp deformations, respectively. In each of these chapters we will first derive the protocol-specific criteria described above, which predict the onset of linear instability to shear banding independently of model or material type; credit for these criteria is given to Dr. Suzanne Fielding. We will then explore the use of these general criteria in the models noted above during an investigation of their time-dependent responses to deformation.

In Chapter 4, we begin by exploring the rheological response of the rolie-poly and Giesekus models to a step stress. We show the shear rate response of both models is qualitatively similar to that found in experiments of entangled polymeric materials, but only the RP model gives rise to significant transient shear banding. In the SGR model we explore 'creep': the progressive decrease of the shear rate in time, and subsequent 'fluidisation': the sudden increase of the shear rate over several orders of magnitude in a short time, in response to an imposed shear stress exceeding the yield stress. This research is motivated by recent experiments in soft glasses [42, 64] that show transient shear banding to arise during the fluidisation process, the onset of which is reported to decrease with the imposed stress [11, 28, 42, 64, 66, 118, 150]. Recent simulations of the SGR model [117] also show shear banding to arise during fluidisation. Here, we expand on that study with details of the creep and fluidisation behaviour. We show that during creep the shear rate follows a power law in time with an exponent dependent on the 'noise temperature' of the model. We also show that the time at which 'fluidisation' occurs depends on the imposed shear stress via a power law for stresses close to the yield stress, and exponentially for larger stresses. Finally, in the GP model we show that qualitatively similar results are found in the shear geometry in response to a step stress as those in the extensional load protocol as studied previously in Ref. [58]. Using the criterion, we also explain how strain hardening reduces the magnitude of transient shear banding.

In Chapter 5, we explore the 'elastic' and 'viscous' contributions to linear insta-

bility to shear heterogeneity in the shear startup protocol. We use this to explain the onset of age-dependent transient shear banding in the scalar fluidity model, and the range of shear rates for which time-dependent shear banding arises in the RP model. We also explain how 'viscous' and 'cross' terms in the general criterion introduced above stabilise the Giesekus model against time-dependent shear banding, so that shear bands are seen to arise only as the system nears steady state; these results are contrary to experimental findings. As we found in step stress, we also find in shear startup that strain hardening reduces the magnitude of transient shear banding in the GP model.

In Chapter 6, we investigate the stress relaxation functions of the RP model following strain ramps with rates that probe the chain stretch relaxation rate τ_R^{-1}. We use the general criterion introduced above to show that 'slow' ramps (relative to this rate) result in linear instability to shear rate heterogeneity if the strain amplitude exceeds $\gamma \sim 1.7$. We also show that 'fast' ramps result in a delayed onset of linear instability if convective constraint release is sufficiently inactive. We compare qualitative features of our results with those of experiments in order to defend the capability of the RP model to describe entangled polymeric materials.

Finally, we conclude our findings in Chapter 7.

2

Theoretical & Experimental Motivation

2.1 Rheology

Rheology is the study of the deformation and flow of materials. In this thesis we will consider three experimental protocols that investigate the rheology of complex fluids, which all involve a planar shear device consisting of a sample sandwiched between (theoretically, infinitely long) parallel plates, as depicted in Figure 2.1.1. This geometry is a theoretical idealisation of the experimentally used geometries of a Couette cell with a narrow gap, or a cone-and-plate cell with a small cone angle.

We define the $\underline{\hat{x}}, \underline{\hat{y}}$ and $\underline{\hat{z}}$ directions as the flow direction, the flow-gradient direction, and the vorticity direction, respectively; throughout we assume translational invariance in the $\underline{x}, \underline{z}$ directions. The bottom (stationary) and top (moving in the $\underline{x}$ direction) plates are located at $y = 0, L$, respectively; these define the 'shearing cell'. The sample can then be subjected to various types of deformation, for example, a

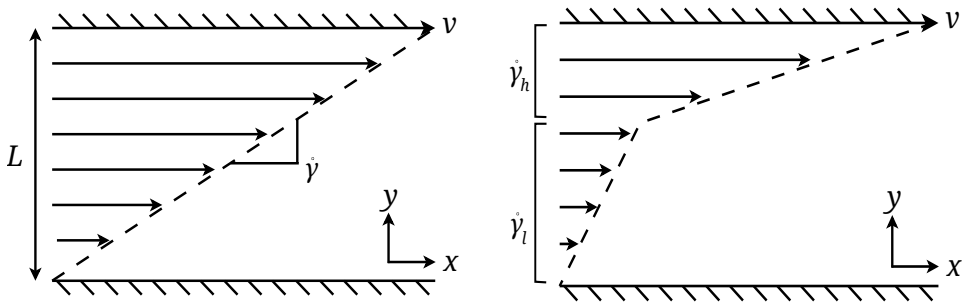

(a) Homogeneous velocity profile (b) 'Shear banded' profile

Figure 2.1.1: Velocity profile examples for (a) a homogeneous velocity field and (b) a shear banded state. The cell is comprised of two parallel plates at $y = 0, L$; the top plate is moved in the $\underline{x}$ direction with $\underline{v} = v\underline{\hat{x}}$, spatial invariance in the $\underline{x}, \underline{z}$ directions is assumed. The local shear rate is the spatial gradient of the velocity: $\dot{\gamma}(y) = \partial_y v(y)$, the spatial average of which is the 'global' shear rate: $\overline{\dot{\gamma}} = \frac{1}{L}\int_0^L \dot{\gamma}(y)dy$.

constant force could be applied to the top plate in the $\underline{x}$ direction (and a counter force to the bottom plate), or the top plate could be moved with a constant velocity $\underline{v} = v\underline{\hat{x}}$.

From such protocols one can measure, for example, the shear component of the total stress tensor: $\Sigma_{xy} \equiv \Sigma$; the 'global' shear rate $\overline{\dot{\gamma}}$, i.e., the spatial average of the local shear rate $\dot{\gamma}(y)$ defined as the spatial gradient of the velocity field within the shearing cell $\dot{\gamma}(y) = \partial_y v(y)$ [see Figure 2.1.1 (a)]; or the (global) shear strain: $\gamma = \int_0^t \overline{\dot{\gamma}}\, dt$. If the fluid velocity varies linearly across the cell, i.e., the flow is *homogeneous*, the local shear rate will be constant across the cell, as shown in Figure 2.1.1 (a). Later, we will introduce the concept of 'shear banding' whereby this homogeneous velocity field becomes unstable to heterogeneous perturbations and (usually[1]) splits into high and low shear rate bands with $\dot{\gamma}_h$ and $\dot{\gamma}_l$, respectively, as shown in Figure 2.1.1 (b).

In this chapter, we will first define the three rheological protocols used in Chapters 4, 5 and 6. In Section 2.1.2 we will define the 'constitutive' and 'flow' curves, followed by an introduction to the concept of shear banding in Section 2.1.3. Finally, for each protocol we will provide a review of the literature of both experiment and theory concerning the rheological responses of soft glassy materials and entan-

[1]More complex, (often time-dependent) heterogeneous profiles can sometimes be seen [89] involving, for example, multiple bands of different shear rate coexisting in the cell.

gled polymeric materials above and below the glass point, with a particular focus on shear banding behaviour. These reviews form the motivation for the research presented in Chapters 4, 5 and 6 of the thesis.

2.1.1 Rheological protocols

The deformation protocols considered in this thesis are the step stress, shear startup and strain ramp protocols, which we now outline individually. For simplicity in this section we will (for now) assume a homogeneous velocity profile so that $\overline{\dot{\gamma}} = \dot{\gamma}(y)$. However, the general descriptions of the shear rate $\dot{\gamma}$, etc., below also remain valid for the spatially averaged variables (e.g., of shear rate $\overline{\dot{\gamma}}$) of heterogeneous flows. The protocols below assume the sample to be well rested before deformation is imposed.

Step stress

In the step stress protocol a constant shear stress Σ is applied to the material for times $t > 0$, as shown in Figure 2.1.2 (a). In a Newtonian liquid where the shear stress is proportional to the shear rate with a proportionality constant known as the viscosity $\Sigma = \eta\dot{\gamma}$, the material would respond by flowing at a constant rate $\dot{\gamma} = \Sigma/\eta$. In the non-Newtonian materials studied in this thesis, the intrinsic relaxation mechanisms have much longer timescales so that the shear rate is not instantaneously prescribed by the stress, and the experimentally measurable deformation rate is time dependent. A typical example of such a time dependence $\dot{\gamma}(t)$ is sketched in Figure 2.1.2 (b).

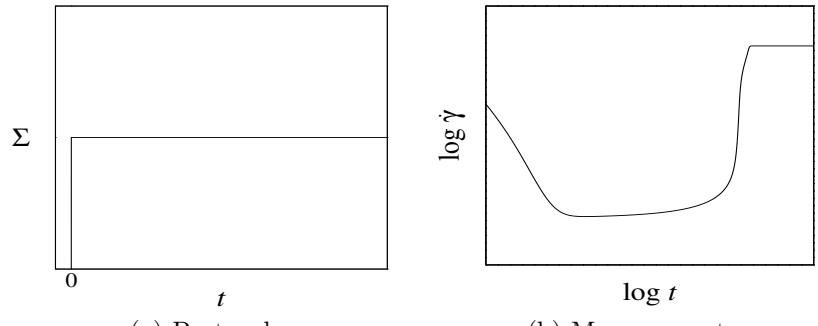

(a) Protocol (b) Measurement

Figure 2.1.2: Step stress protocol: (a) impose a constant shear stress Σ at $t = 0$, and (b) measure the shear rate, $\dot{\gamma}(t)$, as a function of time.

Complex fluids typically reach a *steady state* under such a deformation whereby $\partial_t \dot{\gamma} = 0$, as shown in the $t \to \infty$ limit of Figure 2.1.2 (b). Note that we will also refer to this protocol as the 'imposed stress' protocol.

Shear startup

In the shear startup protocol a constant shear rate $\dot{\gamma}$ is applied for times $t > 0$ to the material, and the resulting shear stress is measured as a function of time $\Sigma(t)$. Note that in this protocol the strain simply increases linearly in time: $\gamma(t) = \dot{\gamma}t$. As a result, all figures of the shear stress *vs.* time may be re-scaled by $\dot{\gamma}$ to obtain the shear stress *vs.* strain $\Sigma(\gamma)$ relationship. Note that we will also refer to this protocol as the 'imposed shear rate' protocol.

For a Newtonian liquid the shear stress is instantaneously prescribed by the shear rate such that $\Sigma = \dot{\gamma}\eta$, whereas the response of the shear stress for complex fluids such as those considered in this thesis is again time dependent $\Sigma(t)$. The viscoelasticity inherent in these materials means that they initially respond in an elastic-like manner with a linear increase of the shear stress with strain $\Sigma \sim G\gamma$ (where G is an elastic modulus), before flowing like a viscous liquid with a stress that is constant in time $\partial_t \Sigma = 0$. In fact, the elastic-like response can be so dramatic that the stress undergoes an *overshoot* leading to a region in which the stress decreases in strain $\partial_\gamma \Sigma < 0$ before finally reaching its steady state value, as demonstrated in Figure 2.1.3 (b).

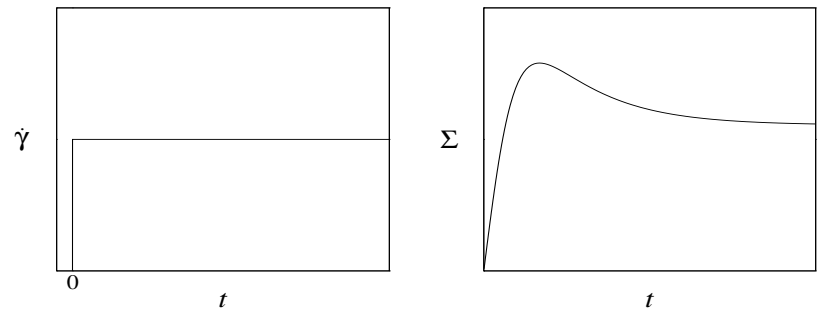

(a) Protocol (b) Measurement

Figure 2.1.3: Shear startup protocol: (a) impose a constant shear rate $\dot{\gamma}$ at $t = 0$, and (b) measure the shear stress, $\Sigma(t)$, as a function of time. Scaling of the x axis by $\dot{\gamma}$ provides the shear stress as a function of strain: $\Sigma(\gamma = \dot{\gamma}t)$.

Strain ramp

In this protocol a constant shear rate $\dot{\gamma}_0$ is applied to the sample for a time t_0 until the desired strain amplitude $\gamma_0 = \dot{\gamma}_0 t_0$ is met. The shear rate is subsequently switched off $\dot{\gamma} \to 0$ so that the strain $\gamma(t) = \gamma_0$ remains fixed, and the resulting shear stress relaxation function $\Sigma(t')$ is measured, where $t' \equiv t - t_0$ is the time elapsed since the end of the step, see Figure 2.1.4. (We will often refer to $t = t_0$ as the time of shear cessation.) The limit $t_0 \to 0$ and $\dot{\gamma}_0 \to \infty$ at fixed γ_0 then provides a theoretically 'ideal' step strain in which the strain is stepped up from $\gamma = 0$ to $\gamma = \gamma_0$ infinitely quickly. However, in experiment this limit is unachievable. We will also show in Chapter 6 that the stress relaxation function following ramps of different rates $\dot{\gamma}_0$ reveals important physics about the material in question. In that chapter, we will consider a 'fast ramp' in which the rate is finite, but much faster than the rate of the slowest relaxation mechanism in the system: $\dot{\gamma}_0 \gg \tau_d^{-1}$. Note that in experiment a strain ramp is usually termed a step strain despite the finite rate with which it is applied.

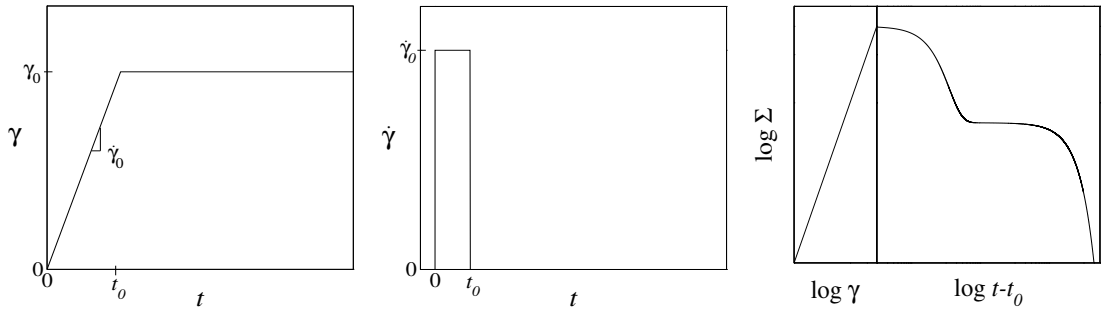

(a) Protocol: strain (b) Protocol: shear rate (c) Measurement

Figure 2.1.4: Strain ramp protocol: (a, b) impose a constant shear rate $\dot{\gamma}_0$ for a time t_0 until the desired strain $\gamma_0 = \dot{\gamma}_0 t_0$ is achieved; an 'ideal' step strain is met in the limits $\dot{\gamma}_0 \to \infty$, $t_0 \to 0$ with fixed strain amplitude γ_0. (c) measure the total shear stress Σ during (*vs.* strain γ) and after the ramp (*vs.* time $t' = t - t_0$).

2.1.2 Steady state constitutive and flow curves

In the shear startup protocol described above, the steady state value of the shear stress is obtained in the limit $\partial_t \Sigma(\dot{\gamma}) \to 0$. One can then plot the relation between the steady state shear stress and the imposed shear rate: $\Sigma(\dot{\gamma})$. We now consider

a thought experiment in which the system is artificially constrained to remain homogeneous: we define the resulting steady state relation $\Sigma(\dot{\gamma})$ as the *'constitutive curve'*. (This theoretical curve can be obtained in numerics where it is possible to artificially constrain the system to homogeneity, as we shall see in Chapter 3.) On the other hand, if heterogeneity is allowed in the flow gradient direction ($\underline{y}$) so that shear bands could in principle arise, the resulting steady state relation of shear stress *vs.* (global) shear rate $\Sigma(\overline{\dot{\gamma}})$ may in fact be different to that of the homogeneously constrained system. We therefore define this relation $\Sigma(\overline{\dot{\gamma}})$ with heterogeneity allowed in the flow gradient direction as the *'flow curve'*. (Clearly, this is the only curve obtainable in experiment, where it is not possible to constrain the flow to be homogeneous.)

Note that the constitutive and flow curves can also be obtained by imposing a constant stress, i.e., via the steady state obtained from the step stress protocol $\partial_t \dot{\gamma} \to 0$. However, to avoid confusion we will use the definitions above as a default (i.e., the constitutive and flow curves are those obtained under an imposed shear rate), and explicitly state when we are referring to the curves obtained under imposed stress conditions.

Sweep tests

Note that the above constitutive and flow curves are found by imposing a constant shear rate on a material initially at rest until the steady state is met, where this protocol is repeated for many values of the shear rate. However, in experiment the curves are often obtained by *'sweeping'* up and down the flow curve. To do this, the shear rate is increased in steps up to some maximum value (and then decreased in steps for the downward sweep), pausing at each step for a 'residence' time to allow the system to reach a steady state[2] before taking the value of the stress at that shear rate. These 'sweeps' often return different functions of $\Sigma(\overline{\dot{\gamma}})$ than those obtained using the protocol for the flow curve described above, and often depend on the residence time of each step. In glassy systems such a dependence on the

[2]Note that this condition of a sufficiently long residence time to allow a steady state to be met is not always enforced in experiment.

residence time is unavoidable in practice, however careful the experimentalist is.

2.1.3 Shear banding

Steady state shear banding

In Newtonian fluids, the velocity profile found using the planar shear geometry is expected and indeed found to be homogeneous, so that the local fluid velocity at any point y across the cell changes linearly across the gap, as depicted in Figure 2.1.1 (a). However, many complex fluids exhibit a shear induced phenomenon called 'shear banding' in which this homogeneous velocity gradient profile becomes unstable to heterogeneous perturbations and splits into high and low shear rate bands that coexist in the cell, so that the local shear rate varies spatially $\dot{\gamma} = \dot{\gamma}(y)$, as shown in Figure 2.1.1 (b). Such a shear banded profile has been found in many types of complex fluid, such as entangled polymer solutions and melts [18, 19, 138, 162], triblock copolymer solutions [12,99], wormlike micellar solutions [16,70,71,76,89,95–97,110,144], lyotropic lamellar phases [145], soft glassy materials [35,37,45,126,141], and foams [140]. For several excellent reviews of shear banding see Refs. [55,98,119, 125]. At steady state, shear banding usually arises for imposed shear rates within a characteristic *stress plateau* found in the flow curve, where the stress is constant over a range of imposed shear rates. Note that a curved geometry causes a gradient of stress across the shearing cell that leads to a slight positive slope of the stress plateau region in the flow curve [120]. Concentration coupling (for example, between micelle concentration and the flow rate) can also lead to a positive slope of the plateau region in the flow curve [60]. An example of the stress plateau and associated shear banded flow profiles from experiments on wormlike micelles [71] is shown in Figure 2.1.5.

The origin of the shear banding phenomenon at steady state is thought to be due to an underlying negative slope in the constitutive curve (defined above): $\partial_{\dot{\gamma}}\Sigma < 0$ that renders homogeneous flow unstable to shear heterogeneity for shear rates in the region of negative slope [160,172]. An example of such a constitutive curve with a negative slope is shown in Figure 2.1.5 (a) in a dashed line, where results were obtained by Helgeson *et al.* [71] using the Giesekus model [65]. The corresponding

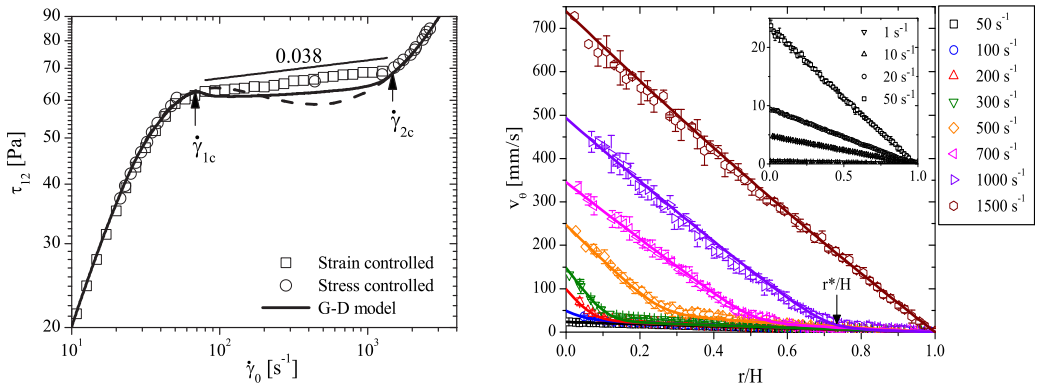

Figure 2.1.5: (a) Flow curves obtained from experiments on wormlike micelles, squares: from the steady state shear of the shear startup protocol, circles: from the steady state of the step stress protocol, and a solid line shows results from numerics of the Giesekus model. The constitutive curve for the Giesekus model is shown in a dashed line. (b) Velocity profiles obtained from the steady state of the shear startup protocol, at rates with corresponding symbols in the key (symbols: experiment, line: predictions from Giesekus model). Reprinted with permission from Ref. [71], copyright The Society of Rheology.

flow curve is found by removing the constraint of homogeneity from the flow gradient direction[3], and does indeed show the expected stress plateau (along with the associated shear banding) in agreement with the experimental results; see the solid lines in Figure 2.1.5 (a) and (b).

The results presented above are not specific to the Giesekus model, indeed any model with a nonmonotonic constitutive curve is capable of showing the steady state shear banding and associated stress plateau when the constraint of homogeneity is removed from the flow gradient direction[3]. For example, such features have been shown in the rolie-poly model for entangled polymeric materials [2, 33, 92]; a two species elastic network model for wormlike micelles [174]; the Johnson Segalman model formulated by considering the non-affine deformation of polymer chains [82, 120]; a modified version of the soft glassy rheology model that includes coupling between the effective noise temperature and the flow dynamics [57]; a kinetic elasto-plastic model for soft glassy materials [103]; and a phenomenological fluidity model for yield stress fluids [128].

[3]With the appropriate modification of the model by the inclusion of diffusive terms — see Chapter 3.

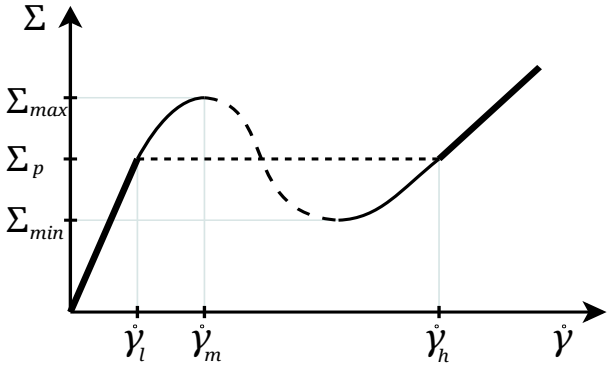

Figure 2.1.6: Schematic of a nonmonotonic constitutive curve (s shaped curve), the unstable (negatively sloping) region is shown dashed. The resulting flow curve is shown in a thick solid and a thin dotted line, which has a stress plateau at Σ_p.

Unique selection of the stress plateau Σ_p

In the above we explained that a homogeneous shear flow in the regime of negative slope of a nonmonotonic constitutive curve is unstable — this is in the dashed region of the nonmonotonic constitutive curve shown in Figure 2.1.6. In experiment, the flow curve (shown by the thick solid and dotted lines of the figure) has a stress plateau (or weak increase of shear stress with shear rate due to concentration coupling or device curvature, as discussed above) at a strain-history independent and reproducible value of the shear stress Σ_p.

The thick, solid lines of Figure 2.1.6 are often referred to as the 'stable' branches of the constitutive curve. Note that the thin, solid lines are in fact meta-stable [132]: given a sufficiently large heterogeneous perturbation, steady state flow for (most[4]) shear rates in this region will show shear banding with a shear stress value of the plateau Σ_p.

[4]In fact, for models with diffusive nonlocal terms, this will occur for shear rates $\dot{\gamma}_a < \dot{\gamma} < \dot{\gamma}_b$ where this range is contained within the plateau range: $\dot{\gamma}_l < \dot{\gamma}_a$ and $\dot{\gamma}_b < \dot{\gamma}_h$, and depends on the diffusion constant D; see Ref. [132].

Time-dependent shear banding

So far, we have discussed shear banding in the steady state limit of the shear startup protocol. However, recent results have shown that shear banding can actually arise during the time-dependent response of shear startup, and is usually most pronounced just after an overshoot in the shear stress [see Figure 2.1.3 (b) for an example of a stress overshoot] during a decline of the shear stress in strain: $\partial_\gamma \Sigma < 0$. In fact, this *time-dependent* shear banding associated with the stress overshoot in the shear startup protocol has also been shown to occur in materials that do not show banding at steady state. For example, it has been found during shear startup in yield stress fluids such as carbopol gels [43, 45] and entangled polymeric materials [19, 77, 138] that are less well entangled than those that shear band at steady state. That these materials show transient shear banding but do not band at steady state implies that their constitutive curve is in fact monotonic. It also implies that the steady state condition for shear banding does not govern the *time-dependent* shear banding properties. However, the fact that time-dependent shear banding arises during the same generic feature of negatively sloping shear stress in strain of completely different materials suggests a generic, material independent cause of the instability.

Similar comments apply to the response to the step stress protocol: here, time-dependent shear banding has been shown to arise during a sudden, rapid increase of the shear rate $\dot{\gamma}(t)$ [similar to that shown in Figure 2.1.2 (b)] in both soft glassy [42, 64] and entangled polymeric [16, 19, 74–77, 161] materials. Again, the fact that time-dependent shear banding should arise during the same generic feature of the shear rate response function $\dot{\gamma}(t)$ in different materials indicates a generic underlying cause that is independent of the particular fluid in question.

Finally, it has also been shown that, during relaxation after a ramp strain, entangled polymer solutions or melts [9, 17, 52, 91, 135, 168] and wormlike micelles [16] can split into two (or more) macroscopic bands that shear in opposite directions (so that the spatially averaged shear rate remains zero). This was unexpected: such flows are considered to be in the very low Reynolds number regime and are thus effectively inertialess: after shear cessation the material should remain stationary at all locations in the cell. The effect is usually seen for strain ramp amplitudes ex-

ceeding $\gamma_0 \sim 1.5$ regardless of the polymeric material in question, again, suggestive of a generic underlying cause.

The above results indicate generic underlying causes of instability to time dependent shear banding that do not depend on the properties of the material in question, and form the motivation for the results presented in this thesis. In each of Chapters 4, 5 and 6 we will consider the linear stability to shear heterogeneity of three classes of complex fluids undergoing the step stress, shear startup and strain ramp protocols, respectively. In each chapter, we will first derive protocol-specific criteria for the onset of linear instability to shear heterogeneity that are independent of model or fluid type, and depend only on the rheological response functions; credit for these criteria is given to Dr. Suzanne Fielding. We will then demonstrate the use of these criteria in models for soft glassy materials and entangled polymeric materials above and below the glass transition during an investigation of the rheological responses of each model to deformation. To provide a more detailed context for this research, we will first briefly describe the three classes of material outlined above, after which we review the experimental and theoretical literature in each class of material concerning time-dependent shear banding, separately for each deformation protocol: step stress, shear startup and strain ramp.

Classes of material

Soft glassy materials: the term 'soft glassy material' (SGM) covers a wide range of materials from granular materials and foams to emulsions and physical gels [29]. These materials are characterised by disordered, meta-stable configurations of their mesoscopic substructures (emulsion droplets, for example) and usually possess a 'yield stress' Σ_y: the material behaves like a solid and will not 'flow' until the imposed stress exceeds this value. As a result they are often known as 'yield stress fluids' (YSF). Their steady state flow curves often follow that of the Herschel-Bulkley model [42, 72]:

$$\Sigma = \Sigma_y + \eta\dot{\gamma}^n, \tag{2.1.1}$$

where $n \sim 0.2 - 1$. These materials also show varying degrees of ageing and thixotropic behaviour, whereby rheological responses to deformation show dependence on the 'waiting time' t_w (i.e., the 'age' of the material) elapsed since sample preparation, and also on the strain history [38]. Their rheological response is usually a result of competition between *ageing* and deformation induced *rejuvenation*. That is, at rest, the local dynamics slow down and the material's response becomes progressively more elastic in time (ageing). Under deformation this can be reversed (rejuvenation) and the material can be 'fluidised'.

Polymeric fluids: here, we consider any material whose substructure is characterised by entanglements between long, chain-like objects. This includes, for example: concentrated solutions or melts of high molecular weight polymers; concentrated solutions of wormlike micelles, whose self-assembled structure results in long chains that can reversibly break and reform, but also form entanglements; concentrated solutions of DNA, for which the response to deformation is determined by its topology rather than its chemistry. In these materials, entanglements between chains form topological constraints on the chain's motion. These constraints dominate the material's response to deformation.

Glassy polymeric materials: in the above we described polymeric fluids whose entangled nature dominates their response to flow. Quenching these materials to just below their glass transition temperature T_g leads to additional glassy dynamics, such as ageing and deformation induced rejuvenation, described above. The response to deformation is then characterised by a combination of polymer and soft glassy dynamics.

2.2 Step stress

We first consider the step stress protocol (also known as the 'creep' protocol in experiment) that involves imposing a constant total shear stress Σ and measuring the shear rate $\dot{\gamma}(t)$ required to maintain this stress, see Figure 2.1.2.

2.2.1 Polymeric fluids

As explained above, entangled polymeric materials often show a 'stress plateau' (or region over which the shear stress weakly increases with shear rate) in their flow curve. Step stress experiments on these materials have shown that, for values of the imposed stress nearest that of the plateau (or on the weakly increasing portion of the flow curve) $\Sigma \sim \Sigma_p$, the shear rate response shows a sudden and dramatic increase by several orders of magnitude (from a small initial value) over a short time before reaching its steady state value [16, 18, 75, 76, 136, 161]. It has also been shown that during this rapid increase of the shear rate, time-dependent shear banding arises [16, 18, 19, 74–77, 161] and in some cases a return to homogeneous shear is seen as the steady state is neared [19]. Difficulty in obtaining this latter result in experiment arises due to the occurrence of edge fracture that severely limits the determination of the steady state shear rate and velocity profile [79, 136] under the step stress protocol. It remains a formidable task to determine whether steady state shear banding exists in these polymeric materials under the imposed stress protocol.

Relatively little research has been done concerning the time-dependent response to the step stress protocol within models for entangled polymeric materials, though steady state sweep tests under the step stress protocol were briefly investigated in the Johnson Segalman model by Radulescu *et al.* in Ref. [132]. In Chapter 4 we will explore the time-dependent shear rate response to a step stress and any resulting shear banding in the rolie-poly (RP) [92] and Giesekus [65] models. We will show that while both models show qualitatively similar behaviour to that found in experiment with respect to the shear rate response, only the RP model shows qualitatively similar time-dependent shear banding behaviour.

2.2.2 Soft glassy materials

Experiment: yield stress and steady state flow curves

As explained previously, these materials usually have a 'yield stress' Σ_y. For imposed stresses below this, the material does not flow: rather, it deforms slowly with a rate that progressively decreases with time. It has recently been suggested that these

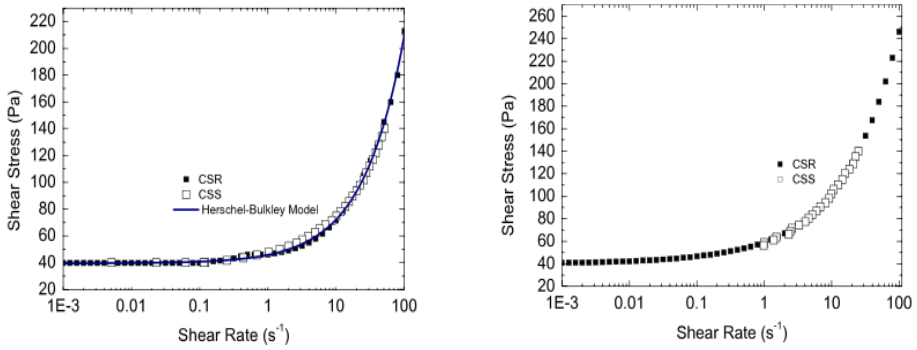

(a) 'Simple' YSF (b) 'Thixotropic' YSF

Figure 2.2.1: (a) and (b): steady state flow curves obtained under imposed stress (open squares) and imposed shear rate (filled circles) for a 'simple' YSF in (a) and a 'thixotropic' YSF in (b). Note that there is a critical shear rate that can be obtained under imposed stress for the thixotropic YSF ($\dot{\gamma}_C \sim 1$). Figures reproduced with permission from Ref. [126].

materials should be categorised into two types [113]: that of 'simple' or 'thixotropic' yield stress fluids (YSF), depending on their steady state rheological behaviour.

'Simple' YSF are typically repulsive glasses (hard sphere glasses with little or no inter-particle attractions), foams and emulsions; an archetypal material is a carbopol gel [45]. Such materials are generally considered to be non-ageing and non-thixotropic; however, rheological responses to deformation of such materials have been shown to exhibit age dependence [43]. Simple YSF are usually characterised by having little or no hysteresis in up/down sweeps on the flow curve[5] [44, 45, 51, 113, 126], and show a continuous transition from solid-like to liquid-like behaviour on increasing the imposed stress above Σ_y. Note that due to the continuous transition between solid/liquid-like behaviour, the steady state shear rate obtained under imposed stress continuously decreases to zero as $\Sigma \to \Sigma_y$ — see Figure 2.2.1 (a).

On the other hand, 'thixotropic' YSF are typically attractive emulsions and colloidal suspensions. They are usually characterised by significant hysteresis in the up/down sweeps on the flow curve [51,126], and also show a discontinuous transition from solid-like to liquid-like behaviour on increasing the imposed stress above Σ_y, see Figure 2.2.1 (b). This discontinuity is known as the 'viscosity bifurcation' [34,

[5]As previously explained, this involves consecutively stepping the shear rate up (or down on a downward sweep) and waiting a 'residence' time at each step.

35, 133]: below a critical imposed stress Σ_C (where $\Sigma_C > \Sigma_y$) the material stops flowing abruptly, while above it the material flows like a liquid. This critical stress corresponds to a critical shear rate $\dot{\gamma}_C$ below which no steady state flow can be found under imposed stress, see Figure 2.2.1 (b). This region of the flow curve that is inaccessible under imposed stress may be accessed on imposing a shear rate $\dot{\gamma} < \dot{\gamma}_C$; in this range steady state shear banding has been reported [37, 126]. It has been shown that an emulsion behaving as a simple YSF can be continuously 'tuned' towards thixotropic YSF behaviour by the addition of clay particles that induce attractions between particles [51, 126].

We remark that this classification system does not actually depend on whether the material shows age dependence or thixotropy, but only on the steady state behaviour; the names 'simple' and 'thixotropic' are perhaps misleading as age dependence has been found in *both* classes of material.

Theory and modelling

Microscopic modelling of SGMs has been achieved through Mode Coupling Theory [21, 22, 63] where the specific interactions (e.g., repulsive or attractive) between particles can be specified, though this approach is currently largely limited to homogeneous flows of monodisperse colloidal glasses. Phenomenological models that involve a governing equation for the relaxation time [41,116,128] or a structural parameter [34, 35] have been successfully used to describe both 'simple' and 'thixotropic' YSF behaviour, though their ability to accurately represent the underlying physics is limited.

Progress has been made in between these two scales through models [14, 50, 154] that describe disordered, soft materials at the mesoscale. One such model is the 'soft glassy rheology' (SGR) model [153, 154] that we will fully describe in Chapter 3 and use in Chapter 6. The model is based on that of Bouchaud's 'trap model' [80] that likens the disordered, meta-stable configurations of these systems to the description of particles that slowly hop between cages (effecting energy minima) formed by neighbouring particles; such a description broadly captures the experimental phenomenology [102, 171]. The SGR model builds on this by allowing such particles to

gain strain energy due to external deformation and undergo activated 'hopping' over their local energy barrier (termed 'yielding' events). Here, the 'activation' describes (in a mean field way) interactions with yielding events elsewhere in the system and is governed by a (constant) effective 'noise temperature' x. The model has a glass transition at $x = x_g$ resulting in ageing for $x < x_g$ [54, 62], whereby (with no external deformation applied) particles evolve sequentially into deeper and deeper energy minima and no equilibrium state is found. With deformation imposed this ageing behaviour can be reversed via strain induced 'rejuvenation'. The resulting steady state rheological behaviour is that of 'simple' YSF according to the description above: a continuous transition from solid- to liquid-like behaviour on the increase of imposed stress above Σ_y, though the response is significantly dependent on the sample's age[6] [54,62]. The constitutive curve is monotonic [153] and thus no steady state shear banding is expected[7]. Variants of the model that allow for non-constant x have also been considered [57,69]; specific forms of which can result in 'thixotropic' YSF behaviour and a decreasing branch of the constitutive curve that extends to $\dot{\gamma} \to 0$, leading to steady state shear banding for small imposed shear rates.

In Chapter 4 we will explore the response of the shear rate $\dot{\gamma}(t)$ to an imposed stress slightly larger than the yield stress in the SGR model (with x constant).

Creep, fluidisation and shear banding

As mentioned, simple YSF continuously transform between solid- and liquid-like behaviour on increasing the imposed stress above the yield stress. Following the imposition of a stress close to (but larger than) the yield stress these materials often display *creep*, i.e., slowly deform at a rate that continuously decreases in time, usually with a power law[8] $\dot{\gamma}(t) \sim t^{-a}$, for a significant amount of time before suddenly 'fluidising' (characterised by a sudden increase of the shear rate) and flowing with a shear rate on the flow curve, see Figure 2.2.2 for an example of such behaviour.

Creep: The power law creep described above is often referred to as 'Andrade

[6]The 'age' is the time elapsed between sample preparation and the onset of deformation.

[7]Recall that the criterion for steady state shear banding is (usually) a negative slope of the shear stress in shear rate in the constitutive curve.

[8]The value of a is material dependent, though generally $0 < a \leq 1$.

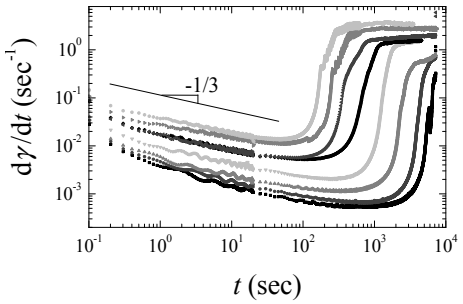

Figure 2.2.2: 'Creep' and 'fluidisation' behaviour of the shear rate in time $\dot{\gamma}(t)$ for a polycrystalline hexagonal columnar phase with imposed stresses: $\Sigma = 12, 13, 15, 19, 21, 22, 50, 35$ Pa (bottom to top). Figure reproduced with permission from Ref. [11], copyright 2006 American Physical Society.

creep' after E. Andrade who discovered it in metals drawn extensionally at a constant stress [39]. It has subsequently been found in heterogeneous solids such as fibre composite materials [118] and paper [143] under the extensional protocol, but has also widely been reported in soft glassy materials under a step stress in the shear geometry [11, 28, 42, 150].

Fluidisation: For imposed stresses exceeding the yield stress, creep is usually followed by a dramatic and sudden increase of the shear rate in time; this is often called 'fluidisation'. The time at which this occurs (the 'fluidisation time') is reported to decrease with increasing values of the imposed stress, becoming negligibly small at very *large* stresses so that the creep regime is barely discernible (see Figure 2.2.2). (At the other extreme, the fluidisation time diverges $\tau_{\rm f} \to \infty$ as the imposed stress is decreased towards the yield stress $\Sigma \to \Sigma_y$.) Various relations between the fluidisation time and the imposed stress have been attributed to this behaviour [11, 28, 42, 64, 66, 118, 150], but no consensus as to the origin and correct formula for it has yet been agreed.

Shear banding: It has also recently been reported that transient shear banding arises during the rapid increase of the shear rate up until the inflection point of the shear rate in time $\dot{\gamma}(t)$ [42,64]. In fact, it was shown that the time at which the system returned to homogeneous shear following transient shear banding corresponded directly to the inflection point in $\dot{\gamma}(t)$ [42], a result which has also been shown to occur in simulations of the SGR model [117]. We will show in Chapter 4 that these results are in direct agreement with the times up to which the system is predicted

to be linearly unstable to shear banding by the criterion for the step stress protocol.

Motivated by the observation of shear banding in relation to the fluidisation behaviour, we will investigate the power law creep and the relation between the imposed stress and fluidisation time in the SGR model in Section 4.5. The author thanks Dr. Thibaut Divoux for motivating this research.

2.2.3 Glassy polymeric materials

Linear polymers quenched to just below their glass transition temperature T_g show many of the features of the above soft glassy systems, but have additional complexity arising from polymeric contributions to the stress [158]. Various models have been proposed that aim to combine the underlying polymer dynamics with the glassy features of ageing and deformation induced rejuvenation [30–32, 73, 84, 164].

A recent model [that we will for convenience throughout this thesis refer to as the 'glassy polymer' (GP) model] [58, 59] begins its description of glassy polymers by distinguishing between the 'fast' and 'slow' degrees of freedom in short and large sections of a polymer chain, respectively. The short-scale, faster degrees of freedom control the rate of rearrangement of local segments of the polymer chain. To include the glassy dynamics of the polymer chains, the model considers the relaxation time of the short-scale degrees of freedom, i.e., the segmental relaxation time $\tau(t)$, to have its own time- and strain rate- dependent dynamics that describe ageing and rejuvenation. The model has been shown to accurately describe the dynamics of the segmental relaxation time $\tau(t)$ found in experiments using an extensional deformation protocol [88]. These experiments show that the segmental relaxation time initially decreases dramatically during the early stages of extensional deformation under a constant load, after which it reaches a minimum concurrent with the onset of strain hardening, and thereafter rises indefinitely [88]. Fielding *et al.* [58] demonstrated that the GP model semi-quantitatively reproduces these results; see Figure 2.2.3.

The initial response to a constant extensional load of glassy polymers is similar to that of simple soft glassy fluids under shear stress described above: the extension rate (equivalently the shear rate in SGMs) first decreases during creep, followed by

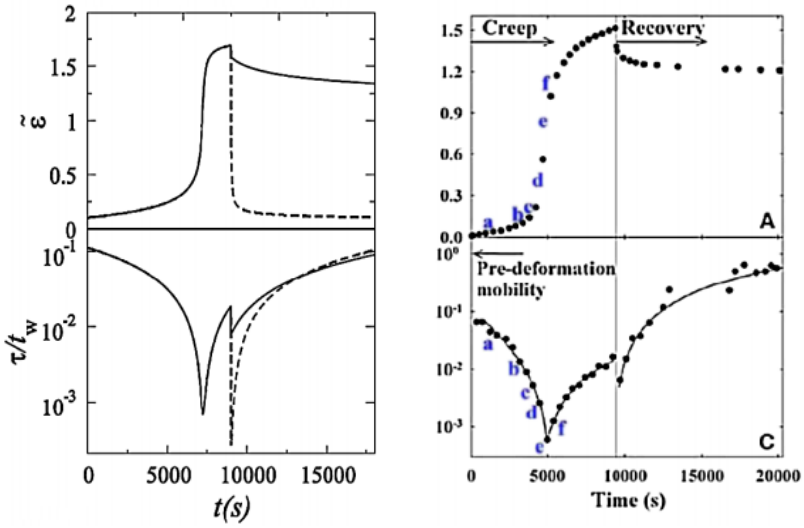

(a) (b)

Figure 2.2.3: Glassy polymers under a constant extensional force in the GP model from Ref. [58] in (a) and in experiments of PMMA in the glass phase ($T < T_g$) from Ref. [88] in (b). Note that the load is removed at $t \sim 9000s$. Top: local strain in time (solid/dashed line in (a) with 'crinkle' factor $\theta = 0.1, 1$, respectively, see Ref. [58]). Bottom: segmental relaxation time. Sub-figure (a) reproduced with permission from Ref. [58] copyright 2012 American Physical Society, and (b) Ref. [88] reprinted with permission from AAAS.

a sudden 'fluidisation' caused by shear induced rejuvenation whereby deformation induces a decrease in the viscosity (in polymer glasses this is due to a shear induced increase in the segmental mobility) and thus a faster extension rate resulting in a feedback mechanism. However, during this fluidisation process 'strain hardening' occurs, curbing the growth of the extension rate and causing the system to 're-vitrify' whereby the segmental mobility decreases [58, 59, 88].

The GP model is based on a similar formulation to that of the Eindhoven Glassy Polymer (EGP) model [84, 164]. However, unlike the GP model, the EGP model includes factorable effects of ageing and strain induced rejuvenation, resulting in a rate of increase of the relaxation time $\dot{\tau}$ (i.e., rate of ageing) during rest that is permanently affected by any strain induced rejuvenation; e.g., $\dot{\tau}$ is different before and after a step strain [58]. This is contrary to results of phenomenological and mesoscopic models for non-polymeric glassy systems, and was argued [58] to render the EGP model incapable of reproducing the dramatic 'dip' of τ concurrent with the onset of strain hardening seen in experiment in the extensional geometry, see

Figure 2.2.3.

In Chapter 6 we will investigate analogous creep tests to those in Ref. [58] in the shear geometry, where we will also investigate the possibility of transient shear banding.

2.3 Shear startup

2.3.1 Polymeric fluids

Steady state and time-dependent shear banding in entangled polymer melts and solutions have been intensively studied in the last seven years since banding was first discovered to arise by Wang and co-workers in Ref. [168]. Actually, shear banding has been thought possible in entangled polymer melts for over two decades [155], following the prediction of a nonmonotonic constitutive curve for these materials in a model by Doi and Edwards [47]. This model considers a test chain to be constrained within a 'tube' of confinements provided by a mean field of entanglements with other polymers; an idea which formed the basis for many subsequent 'tube' based models [67, 78, 92, 105, 108, 109, 127].

In contrast, steady state shear banding in wormlike micellar solutions has been confirmed and studied experimentally for nearly two decades [16, 70, 71, 76, 89, 95–97, 110, 144], owing to a significantly smaller problem of edge fracture in these materials compared to entangled polymer melts (apparently due to their much smaller elastic moduli) [18, 151]. These results followed predictions of a nonmonotonic constitutive curve in a model by Cates [27, 155] that combined entangled polymer relaxation mechanisms from Doi and Edwards' theory with the additional mechanism of 'tube breaking' specific to wormlike micelles, which can reversibly break and reform.

The most recent research on entangled polymer solutions or melts [17–20, 77, 136, 138, 161] and wormlike micelles [16, 76] shows that shear banding in startup is not limited to steady state flow, but also arises during the time-dependent response after the stress overshoot, i.e., during the negative slope of stress in strain $\partial_\gamma \Sigma < 0$. (This stress overshoot commonly arises in these materials for imposed shear rates that are faster than the rate at which stress is relaxed in the material.) Time-

dependent shear banding of this form was not only found to arise in samples that *do* shear band at steady state, where the magnitude of time-dependent shear banding is generally much greater than that found at steady state [18, 19, 136, 138, 162], but also found to occur in less well entangled polymer solutions that *do not* shear band at steady state [19, 77, 138]. It has also been shown that time-dependent shear banding can be so pronounced that elastic-like recoil with negative local velocities can arise [18, 19, 138].

Similar results of time-dependent shear banding associated with the stress overshoot have been found in a two species elastic network model [174]; in molecular dynamics simulations of polymer melts [26]; and in the rolie-poly (RP) model [2–4] that can have either monotonic or nonmonotonic constitutive curves, depending on the value of its parameter β. The last of these is a model for entangled polymer melts based on the 'tube' theory of Doi and Edwards; we will fully describe the RP model in Chapter 3 for use throughout this thesis. A detailed investigation of time-dependent shear banding during shear startup in the rolie-poly model was performed by Adams *et al.* in Refs. [2–4]. The authors showed that time-dependent shear banding (including negative-velocity recoil) arose during the negative slope of shear stress in strain for shear startup at a rate in the region of the least slope of the constitutive curve, regardless of whether the curve was monotonic or not. They showed that this shear banding persisted to steady state for values of the parameters that gave nonmonotonic constitutive curves, and the magnitude of shear banding at steady state was weaker than it had been during the negative slope of shear stress in strain. The authors also showed that decreasing the entanglement number[9] Z resulted in a smaller range of shear rates for which a nonmonotonic constitutive curve had a negative slope, so that for sufficiently small values of Z (at fixed β) the constitutive curve could be rendered monotonic. All of these results are (qualitatively) consistent with the experimental results described above.

In Chapter 5 we will derive a criterion for the onset of linear instability to shear heterogeneity for shear startup that is independent of material type, and which shows

[9] In experiment this corresponds to decreasing the level of entanglement of the polymer sample; above we described how less well entangled samples did not show steady state shear banding.

that the negative slope of shear stress in strain does indeed contribute towards linear instability (credit for this criterion is given to Dr. Suzanne Fielding). We will explore the use of this criterion in the RP and Giesekus models in order to explain their shear banding properties during shear startup. We will also show that the Giesekus model does not show the time-dependent shear banding properties described above for the RP model.

2.3.2 Soft glassy materials

In the Section 2.2.2 we outlined the generic rheological behaviour of soft glassy materials (SGMs), focussing on the response to a step stress deformation. We now build on that description of these materials with details of the response to the shear startup protocol.

We briefly noted above that thixotropic YSF display steady state shear banding for imposed shear rates below a critical value $\dot{\gamma} < \dot{\gamma}_c$ [37,51,107,114,126,141], which is thought to be due to an underlying negatively sloping branch of the constitutive curve that extends to the zero shear rate limit $\dot{\gamma} \to 0$ [34–36, 57, 103, 106, 112, 128, 141]. However, it has also been shown that thixotropic YSF show *time-dependent* shear banding during the negative slope of shear stress in strain $\partial_\gamma \Sigma < 0$ after the overshoot, which returns to a state of homogeneity at steady state for imposed shear rates greater than this critical value $\dot{\gamma} > \dot{\gamma}_c$ [107].

Transient shear banding that again arises during the negative slope of the shear stress in strain $\partial_\gamma \Sigma < 0$ has also been found in simple YSF that do not show steady state banding [43,45]. Similar results are found in numerics of a shear transformation zone model [100] and also in the SGR model [116], where both have monotonic constitutive curves. In the latter, the peak value of the shear stress at the overshoot (and also the strain at which it occurs) was shown to increase with the *age* of the sample[10]. This is consistent with experimental work on carbopol microgels that found the peak shear stress and strain to both increase logarithmically with the age of the sample and the imposed shear rate [43]. Similar results for the peak stress

[10]The age of the sample is the time elapsed between sample preparation and the onset of deformation.

dependence on the waiting time and shear rate have also been found in molecular dynamics simulations of a Lennard-Jones glass [165].

In Chapter 5 we will investigate the response of a scalar fluidity model (that has a monotonic constitutive curve) to shear startup, and show that similar age-dependent transient shear bands to those found in experiments and simulations of the SGR model arise.

2.3.3 Glassy polymeric materials

Under *extensional* deformation at a constant strain rate $\dot{\epsilon}$, polymer glasses show an overshoot of the tensile stress as a function of strain similar to that of the shear stress in strain of non-polymeric glasses in the shear geometry (described in Section 2.3.2). It has also been shown that the peak stress at the overshoot rises with the age of the sample and the imposed strain rate [84, 164], as found in the shear equivalent in non-polymeric glasses described in Section 2.3.2. However, in polymer glasses this tensile stress overshoot is followed by an indefinite rise of the stress due to strain hardening. The glassy polymer model shows qualitatively similar behaviour during extension at a constant strain rate $\dot{\epsilon}$ [58]. Startup in the *shear* geometry is expected to give similar results of an overshoot and subsequent indefinite rise of the shear stress. We will show this to be true in the GP model during shear startup in Chapter 5, where we will also investigate the possibility of shear bands arising during the negative slope of shear stress in strain.

2.4 Strain ramp

So far, we have described the experimental and theoretical literature regarding the response of soft glassy materials and entangled polymeric materials above and below the glass transition to both the step stress and shear startup protocols. We will now describe the relevant experimental and theoretical literature regarding the response of (non-glassy) entangled polymeric materials to a strain ramp deformation. Note that in experiment the rate of a strain ramp is usually set by the inertial limitations

of the rheometer, and the stress relaxation response to different ramp rates is not commonly investigated. The protocol is usually referred to as a step strain protocol, which we will also refer to it as in what follows.

We do not know of any reports of shear rate heterogeneity during stress relaxation after a strain ramp in soft glassy materials. This lack of experimental evidence is consistent with our predictions in Chapter 6: there, we will use the general criterion for the onset of linear instability to the growth of shear rate perturbations specific to the strain ramp protocol to explain why we do not expect any shear rate heterogeneity during stress relaxation in such materials.

2.4.1 Polymeric fluids

Stress relaxation function in experiment

The shear stress relaxation behaviour of polymeric materials after a step strain has been studied for over four decades [47, 49, 85, 121–124, 142, 146, 166]. The general form of the shear stress relaxation function[11] $\Sigma(t', \gamma_0)$ resulting from different step strains of amplitude γ_0 is shown in Figure 2.4.1 (a). Here, the shear stress has been scaled by the strain amplitude, such that $\Sigma(t', \gamma_0) = \gamma_0 G(t', \gamma_0)$, which defines the nonlinear elastic modulus $G(t', \gamma_0)$. For small strain amplitudes $\gamma_0 \ll 1$ the response is linear: the stress relaxation function depends linearly on γ_0 and follows a single exponential decay on a timescale τ_d; see e.g., the top curve of Figure 2.4.1 (a). One can then define the 'linear relaxation modulus': $G(t') = \lim_{\gamma_0 \to 0} G(t', \gamma_0)$ that is independent of the strain amplitude.

For larger strain amplitudes $\gamma_0 > 1$ the stress relaxation function becomes nonlinear in strain and develops a double exponential decay as a function of time. The faster exponential decay has timescale τ_k and is nonlinearly dependent on time and strain, while the slower has the same timescale as the linear modulus: τ_d, but is *time-strain separable*. This is shown in Figure 2.4.1 (b), where the nonlinear relaxation modulus $G(t', \gamma_0)$ is scaled by a shift factor to fit the linear relaxation modulus $G(t')$ at a time $t' = \tau_d$, for several strain amplitudes. Figure 2.4.1 (c) shows this

[11] Recall from Section 2.1.1 that $t' = t - t_0$ is the time elapsed since the end of the step strain, and γ_0 is the strain amplitude.

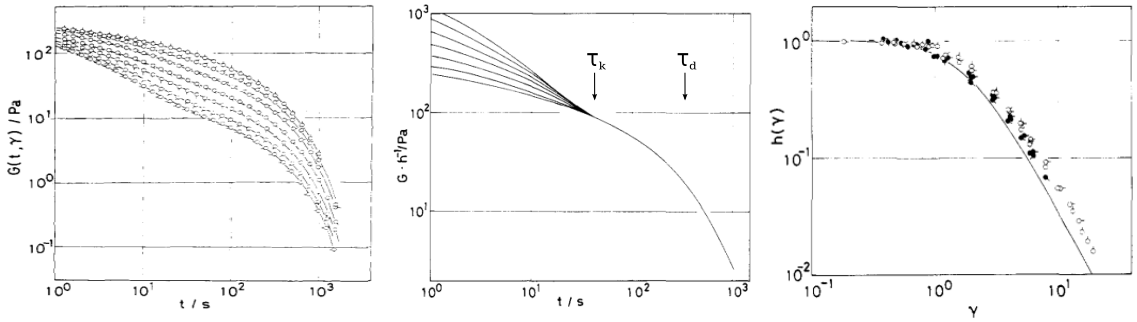

(a) (b) (c)

Figure 2.4.1: (a) Relaxation modulus $G(t', \gamma_0) = \Sigma(t', \gamma_0)/\gamma_0$ as a function of time following step strains of amplitude: $\gamma_0 < 0.57$ (i.e., the linear response), $1.25, 3.04, 4.0, 5.3, 6.1$ (top to bottom). (b) Data of (a) shifted vertically to superpose at time $t' = \tau_d$ by a factor $-\log h(\gamma_0)$. (c) The shift factor $h(\gamma_0)$ as a function of strain amplitude; solid line: the Doi-Edwards damping function. Figure shows data for Polystyrene solutions reprinted with permission from Ref. [123], copyright 1982 American Chemical Society.

shift factor, known as the *damping function*:

$$h(\gamma_0) = \frac{G(t', \gamma_0)}{G(t')}, \qquad \text{for } t' \gg \tau_k \tag{2.4.1}$$

as a function of the strain amplitude. The damping function has been shown to be independent of the polymer molecular weight or concentration over a wide range [47, 122, 123], though discrepancies occur at higher molecular weight or concentration [8, 121, 122]; we will discuss these later.

For later use, we now also introduce the *Lodge-Meissner relation* [93]:

$$N_1(t', \gamma_0) = \gamma_0 \, \Sigma(t', \gamma_0), \tag{2.4.2}$$

where $N_1 = \Sigma_{xx} - \Sigma_{yy}$ is the first normal stress difference. This relation was first derived for viscoelastic liquids by assuming that during a step strain the material behaves as an elastic solid. In a homogeneous, elastic solid the principle axes of the stress tensor remain parallel to those of the strain tensor during deformation [85]. From this, it can be shown that the ratio of the first normal stress difference N_1 to the shear stress Σ is a constant equal to the strain amplitude γ_0. This continues

to be true even as both N_1 and Σ relax as a function of time after a step strain; this result is the Lodge-Meissner relation. It is expected to hold in viscoelastic materials, e.g., entangled polymeric materials, that have an elastic response during the step. Indeed, the relation has been shown to hold for polymer solutions and melts generally [85], except for very well entangled materials [87] in cases that we will discuss later.

The Doi-Edwards damping function

The primary theory used to explain this double exponential stress relaxation behaviour and obtain a comparable damping function[12] is the Doi-Edwards (DE) theory [47], which considers polymers to be effectively trapped within a 'tube' of confinements, as explained in Section 2.3.1. Within the theory, stress relaxation following a step strain is predicted to occur in two stages: first, chain retraction within the tube of entanglements that is strain and time dependent occurs on a timescale τ_R, called the 'Rouse' relaxation time. This is followed by 'reptation' that is time-strain separable occurring on a (relatively much slower) timescale τ_d, whereby the polymer undergoes one dimensional diffusion along its own length out of the tube of constraints, see Figure 2.4.2 for a schematic of these mechanisms.

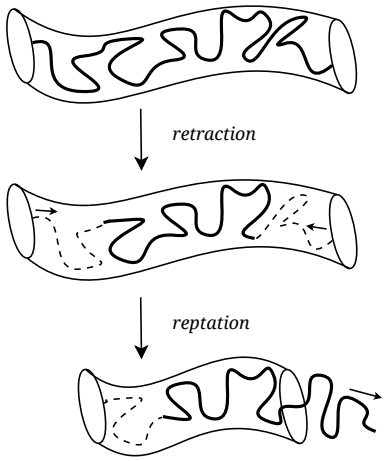

Figure 2.4.2: Schematic of chain retraction and reptation relaxation mechanisms following a large step deformation.

[12]For a good review of other analytical damping functions used to describe experiment see Ref. [142].

The predictions of the model agreed well with experiment: it was shown in experiment that the time at which time-strain separability occurs $t' \sim \tau_k$ is proportional to the entanglement Rouse relaxation time of the material: $\tau_k \propto \tau_R$ [123, 159], in agreement with the DE prediction of time-strain separability for $t' \gtrsim \tau_R$. In addition, the resulting 'Doi-Edwards damping function'[13] $h_{DE}(\gamma_0)$, which has no adjustable parameters, has been shown to agree well with experiments on polymeric materials [46, 122, 123, 142, 146]; see Figure 2.4.1 (c). Note that the DE damping function effectively describes the fraction of the total stress relaxation that occurs through reptation only.

The damping function has been used extensively in both experiment and theory, in particular, as we shall describe below, it has been used to categorise materials depending on how closely their damping functions resemble that of Doi-Edwards'. However, since the damping function uses only information about the shear stress once time-strain separability occurs, no information about the stress relaxation function at times $t' < \tau_k$ is retained. We will show in Chapter 6 that both the stress response during the step, and the form of the stress relaxation function resulting from step strains performed at different rates $\dot{\gamma}_0$ (particularly at times $t' < \tau_R$), reveals important physics of the underlying relaxation mechanisms in the RP model. Therefore, we will not use the damping function in Chapter 6, but will comment on its form where appropriate.

The effect of convective constraint release

The DE theory was later refined by the inclusion of *chain stretch* arising in flows faster than the retraction rate $\dot{\gamma} \gg \tau_R^{-1}$, in models such as the GLAMM model [67], for which the rolie-poly (RP) model [92] is a single mode approximation used extensively in this thesis. The GLAMM and RP models also incorporated additional relaxation mechanisms, notably that of convective constraint release (CCR), the mechanism and effect of which on the stress relaxation function we will describe below.

In the RP model and in the absence of the CCR mechanism, stress relaxation

[13] Defined as in Eqn 2.4.1.

after a step strain applied sufficiently quickly to cause appreciable stretch to arise during the step, $\dot{\gamma}_0 \gg \tau_R^{-1}$, follows a similar double exponential decay as in the DE model described above. First, chain stretch relaxes via chain retraction on the Rouse timescale τ_R, followed by reptation on the timescale τ_d. For step strains performed at rates much slower than the stretch relaxation rate $\dot{\gamma}_0 \ll \tau_R^{-1}$ appreciable stretch does not arise, and stress relaxation occurs only via reptation, i.e., with a single exponential decay that is time-strain separable.

Convective constraint release (CCR) is a mechanism through which entanglements forming the tube of constraints on a 'test' chain can be lost. This occurs when a polymer that forms an entanglement point (or constraint) on the test chain itself reptates or relaxes its stretch sufficiently so that one of its ends passes through the entanglement point, thus releasing the constraint on the test chain. The consequence of CCR for a system relaxing after a fast step strain ('fast' with respect to stretch relaxation: $\dot{\gamma}_0 \gg \tau_R^{-1}$) is that stress relaxation is accelerated during the stretch relaxation process, i.e., at times $t' < \tau_R$. As a result, the system begins its time-strain separable (reptation) relaxation from a lower stress, leading to a weaker prediction of the damping function $h(\gamma_0)$; this was noted by the authors of the RP model [92]. We will demonstrate and quantify this effect in the RP model in Chapter 6, where we will also investigate its effect on the linear stability to shear heterogeneity during stress relaxation.

Categorisation into types A, B and C

As noted above, at high molecular weight or concentration the experimentally determined damping function differed from that of Doi and Edwards' [8, 87, 121, 122]. In fact, three types of behaviour relative to the Doi-Edwards' damping function were found, which lead to the categorisation of the responses into types A, B or C [121, 166], as shown in Figure 2.4.3. Type A was deemed 'normal' behaviour: the same as that predicted by the DE damping function, and occurred most frequently for moderately entangled polymeric materials. Type B classified those data with a damping function that sat above the DE predicted function, and occurred most often for very weakly entangled systems. Type C represented those data that lay

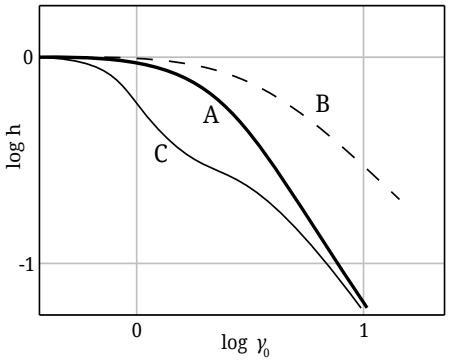

Figure 2.4.3: Schematic of deviations from the DE damping function. Type A data (thick line) agrees with the DE damping function, type B (dashed) data lies above the DE damping function and type C (solid, thin) lies below it, often displaying a 'kink' as shown.

significantly below the DE damping function, often having a pronounced 'kink' as shown in Figure 2.4.3. Type C behaviour occurred most often in very well entangled fluids with entanglement numbers $Z \gtrsim 50$ [122], where the entanglement number $Z = \tau_d/3\tau_R$ [47] is known as the number of entanglements per molecule. Results reported as type C behaviour often showed failure of the Lodge-Meissner relation (Eqn 2.4.2) [87, 134]. For excellent reviews classifying the experimental literature into types A to C see Osaki [121], or a more recent review by Venerus [166]. The latter found the occurrence of type B data to be much less than A or C, while the remaining literature appeared equally shared between A and C. That is, the DE damping function correctly described roughly half of the experimental literature for entangled polymers at that time. Both reviews concluded that the most likely cause of type C data is strain localisation (possibly in the form of wall slip) [87,166], which we now turn our discussion towards.

Strain localisation

In experiment, strain localisation in the form of 'macroscopic motions', i.e. non-zero, heterogeneous local velocities: $v(y, t > t_0) \neq 0$, has recently been shown to occur after a step strain for sufficiently large strain amplitudes $\gamma_0 \gtrsim 1.5$ in both entangled polymer melts and solutions [9, 17, 52, 91, 135, 168] and wormlike micelles [16]. An example is shown for an entangled polymer melt in Figure 2.4.4. As

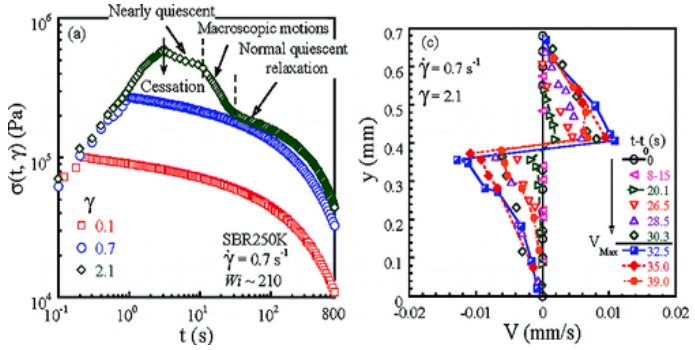

Figure 2.4.4: (left) Stress relaxation function following a step strain in experiment [20]. (right) resulting 'macroscopic motions' showing a failure plane at $y \sim 0.4$mm: the figure shows the displacement of particles at different times after shear cessation, relative to their position at shear cessation (no displacement occurs until $t - t_0 \sim$ 15s after shear cessation). The figure shows data for an entangled polymer melt, reprinted with permission from Ref. [20], copyright 2009 American Chemical Society.

noted in Section 2.1.3, this result was originally surprising since these materials are generally considered to be inertialess: a 'pepper line' drawn across a sample as the step ends should remain in place indefinitely. Strain localisation is no longer such a surprising result since it is now understood that such materials readily exhibit shear heterogeneity, for example, in the form of shear banding during startup.

An instability that could lead to such strain localisation was shown to exist in the DE model by Marrucci and Grizzuti [104]. The DE theory predicts a maximum in the shear stress as a function of the strain amplitude $\Sigma(t', \gamma_0)$ at $\gamma_0 \sim 2$ when this function is plotted at a time instant $t' \sim \tau_k$. This results in a negative slope for some strain amplitudes: $\partial_{\gamma_0}\Sigma(t' \sim \tau_k, \gamma_0) < 0$; a result that also occurs in experiment, but is not obvious when plotting the damping function $h(\gamma_0)$ alone. Marrucci and Grizzuti used a free energy calculation to show that step strains with amplitudes in the negative slope are unstable (to heterogeneity or some form of phase separation) once chain retraction has occurred. In Chapter 6, we will confirm that such step strain amplitudes result in linear instability to shear heterogeneity in the RP model once chain stretch has relaxed after shear cessation, leading to a 'delayed' onset of 'macroscopic motions' similar to those observed in experiment [20]. However, we will show that this delayed instability can be avoided if convective constraint release is sufficiently active. We will also derive a material-independent criterion for the onset of linear instability to shear heterogeneity, which predicts instability for step

strains (performed at a rate much faster than any intrinsic relaxation rate) that end as the shear stress is a decreasing function of strain[14].

In order to clarify any relation between strain localisation and type C behaviour, Wang and co-workers [135] used different solvents to affect the degree to which wall slip may occur in an entangled polymer solution during relaxation after a fast step strain, whilst preserving the entanglement number, Z. Their results showed that the same polymer can undergo all three types of behaviour depending on the ability of the material to undergo wall slip, but in all cases 'macroscopic motions' (as described above) occurred: either at the sample interior leading to type A or B behaviour, or at the sample/wall interface leading to type C behaviour where the stress also underwent an accelerated stress relaxation, resulting in a damping function below that of Doi-Edwards', i.e., type C behaviour. They therefore concluded that the categorisation into types A, B or C bears no real meaning with regard to whether a sample undergoes strain localisation or not. However, it appears a greater magnitude of heterogeneity occurs in samples that readily undergo wall slip, apparently leading to an accelerated stress relaxation that results in a weakened damping function and type C categorisation.

The Wang group also showed that there may be a significant 'induction time' (during which the material relaxes homogeneously) between the end of the step and the onset of the 'macroscopic motions' that arise concurrently with the onset of an accelerated stress relaxation [17, 20]. An example is shown in Figure 2.4.4. This 'induction time' was reported to be significantly larger than τ_R, leading the group to claim the phenomenon was not related to stretch relaxation and thus could not be described by the DE theory (or refinements of) [20]. This is in spite of the fact their work showed the 'induction time' to scale with τ_R [20], and also contrasts with earlier work that indicated a good agreement of the induction time with τ_R [9]. The group set forward their own theories [169, 170] to describe the macroscopic motions (and also shear banding that arises during shear startup) that rely on the idea of the entanglement network 'yielding'. While the DE theory considers the tube of constraints formed by a mean field of entanglements to be indefinitely present if no

[14]Credit for this criterion is given to Dr. Suzanne Fielding.

relaxation mechanisms occur, the Wang theory [169] considers an entanglement point as a particle in a finite potential well, which may escape the well depending on the imposed deformation. In such a picture, the 'entanglement network' is considered to 'yield' under strong deformations, and may do so inhomogeneously.

Despite the claims of the Wang group that the DE theory and models refined from it are unable to describe the inhomogeneous deformations observed experimentally after a step strain [169], such results have been shown to occur in a two species elastic network model [174], and in the rolie-poly model by Olmsted and co-workers [3, 4, 6, 7] (both are founded in the DE theory). Indeed, the latter also performed a detailed investigation on the dependence of the macroscopic motions on the initial state of the material [6, 7]. They reported that in extreme cases a very large shear rate can develop across a stationary point in the cell (a so-called 'fracture' plane), so that the local velocity is very difficult to resolve. These results are qualitatively similar to experimental findings of a 'failure' plane over which the shear rate is extremely high and the local velocity difficult to resolve [20, 52], see Figure 2.4.4.

In Chapter 6, we will investigate the stress relaxation and linear stability properties of the RP model following strain ramps performed at different rates, including an exploration of the effect of the convective constraint release mechanism. We will also briefly explore the heterogeneous dynamics of the local velocity during relaxation after the same strain ramps in the model. (However, we will avoid overlapping with the work of Agimelen *et al.* [7] who focussed on the heterogeneous dynamics following step strains performed at a fixed rate and strain amplitude, and without the inclusion of the convective constraint release mechanism.) We will show that the model exhibits 'macroscopic motions' during stress relaxation after a fast strain ramp that results in both type A and C behaviours, where the latter occurs only when very large shear rate heterogeneities arise. We will also show that a transition from type A to type C behaviour is possible in the model when the entanglement number Z is increased, and that type C behaviour results in failure of the LM relation. Our results are consistent with the experimental literature.

3

Theory & Methods

3.1 Introduction

This thesis aims to explore the linear stability to shear heterogeneity in time dependent shear deformation protocols of three classes of material: soft glassy materials, and entangled polymeric materials above and below the glass transition temperature. We aim to do so in a manner that explores the many shared shear banding features shown by these materials that appear to relate more to generic signatures in the experimentally measured rheological response functions than the specific type of material. To do this, in each chapter that follows, we will first derive a criterion for the onset of linear instability to shear heterogeneity that is independent of fluid or model type, and is specific to the deformation protocol studied in that chapter. Credit for these criteria is given to Dr. Suzanne Fielding. We will then demonstrate the use of these criteria during an investigation of the rheological response to defor-

mation of models for each class of material: the rolie-poly (RP) and Giesekus models for polymeric fluids; the soft glassy rheology (SGR) model and scalar fluidity model for soft glassy materials; and the glassy polymer (GP) model. We therefore begin this chapter with a brief overview of each of these models and provide an outline of their associated constitutive equations.

In order for the criteria that we shall derive for the onset of banding to be fully general (without the need for specifying a model or fluid type), we will outline in Section 3.3 a 'general framework' into which all the above models fit, for a planar shear flow. The subsequent investigation in each chapter of the stress or shear rate response during deformation in each model will use this 'general framework' throughout to aid a clear presentation of the results, thereby avoiding the redefinition of any variables. Within this general framework, we then outline in Section 3.4 the basic concept of a time-dependent linear stability analysis that will be used extensively in Chapters 4, 5 and 6. We also explain the different 'noise' conditions that seed the growth of heterogeneity in Section 3.5.

Finally, an explanation of the numerical methods required for solving such constitutive equations with or without heterogeneity allowed in the flow gradient direction are detailed in Appendix I, where we also detail the numerical methods for the SGR model.

3.2 Models

We now outline the models used in this thesis: the rolie-poly and Giesekus models for (non-glassy) polymeric fluids, the scalar fluidity and soft glassy rheology models for SGMs, and the glassy polymer model. We have specifically chosen not to study the Johnson-Segalman model [82] that has been widely used to model entangled polymeric materials as it has recently been shown to exhibit unphysically large shear stress oscillations at high shear rates [174].

We begin with an outline of the theoretical rheology required to employ the models described in this section.

Force balance, incompressibility and flow geometry

As described in Chapter 1, complex fluids contain mesoscopic substructures that dominate their rheological response to deformation [86]. In this chapter we will outline the basic features of a theoretical framework that can be used to address the rheology of complex fluids. We begin by decomposing the total stress in any fluid element into 'viscoelastic' and Newtonian solvent parts (plus an isotropic pressure):

$$\underline{\underline{\Sigma}} = G(\underline{\underline{\sigma}} - \underline{\underline{I}}) + 2\eta\underline{\underline{D}} - p\underline{\underline{I}}. \tag{3.2.1}$$

Here p is the pressure, determined by the incompressible flow condition $\underline{\nabla}\cdot\underline{v} = 0$, $\underline{\underline{\sigma}}$ is the viscoelastic conformation tensor, η the Newtonian solvent viscosity, G an elastic modulus for the viscoelastic substructure, and $\underline{\underline{D}} = \frac{1}{2}(\underline{\underline{K}} + \underline{\underline{K}}^T)$ where $K_{\alpha\beta} = \partial_\beta v_\alpha$ is the velocity gradient tensor. The 'viscoelastic' stress $G(\underline{\underline{\sigma}} - \underline{\underline{I}})$ is the contribution to the total stress from the aforementioned substructure, e.g., from the polymeric or soft glassy degrees of freedom, and will thus be specified by the constitutive equations of the appropriate model, e.g., the rolie-poly model[1]. The 'Newtonian solvent' contribution may actually be due to the presence of a solvent, or may simply represent the viscous stresses arising from the extremely fast degrees of freedom of the material not described by the model for the viscoelastic stress.

For most experimental regimes of the highly viscoelastic materials of interest in this thesis, the viscous forces are usually much greater than the inertial ones, resulting in a very small Reynolds number $Re \ll 1$. In this thesis we will use the creeping flow limit $Re \to 0$ throughout, leading to the force balance equation:

$$\underline{\nabla} \cdot \underline{\underline{\Sigma}} = \underline{\nabla} \cdot \left[G(\underline{\underline{\sigma}} - \underline{\underline{I}}) + 2\eta\underline{\underline{D}} - p\underline{\underline{I}}\right] = 0. \tag{3.2.2}$$

As introduced in Section 2.1 above, we shall consider the shear flow of a sample confined within two infinitely long parallel (to the $\underline{x}, \underline{z}$ directions) plates situated at

[1]Note that we have defined the viscoelastic conformation tensor as that which relaxes to the identity tensor at rest so that the 'extra stress' from the viscoelastic substructure $G(\underline{\underline{\sigma}} - \underline{\underline{I}}) \to 0$. We could equally define it as that which relaxes to the zero tensor at rest by substituting $\underline{\underline{\hat{\sigma}}} = \underline{\underline{\sigma}} - \underline{\underline{I}}$ in the above and all that follows, including the constitutive equations in each model below.

$y = \{0, L\}$. The top plate is moved in the $\underline{x}$ direction, and translational invariance in the $\underline{x}, \underline{z}$ directions is assumed so that the flow inside the cell: $\underline{v} = v(y,t)\underline{\hat{x}}$. We define the local shear rate $\dot{\gamma}(y,t) = \partial_y v(y,t)$ and also the spatially averaged (or 'global') shear rate: $\overline{\dot{\gamma}}(t) \equiv \frac{1}{L}\int_0^L \dot{\gamma}(y,t)dy$. Eqn 3.2.2 then results in the condition of uniform total shear stress across the cell $\partial_y \Sigma_{xy} = 0$, rendering the decomposition of the total stress into viscoelastic and Newtonian solvent parts $\Sigma_{xy} = G\sigma_{xy}(y) + \eta\dot{\gamma}(y)$ essential for the description of shear banded flows in which the shear rate and viscoelastic shear stress vary across the cell.

For clarity of presentation, and since we will usually be considering the dynamics of the shear stress, where $\underline{\underline{\Sigma}}, \underline{\underline{\sigma}}$ appear unembellished in this thesis we are referring to the total shear stress $\Sigma_{xy} \equiv \Sigma$ (or simply, 'the stress') and the viscoelastic shear stress $G\sigma_{xy} \equiv G\sigma$. Unless otherwise specified, we shall use units in which the cell width $L = 1$ and the elastic modulus $G = 1$ throughout (except within the derivation of the criteria where we leave G variable for generality). Due to this choice of units for G we may think of σ as the viscoelastic shear stress, even though it is (strictly speaking) the viscoelastic shear conformational variable.

Choice of shearing protocol

In Section 2.1.1 we outlined three shearing protocols that we will use in Chapters 4, 5 and 6 respectively, these are: step stress, shear startup and strain ramp.

Step stress: in this protocol a constant shear stress Σ is imposed, and the dynamics of the shear rate vary in time via: $\dot{\gamma}(y,t) = \frac{1}{\eta}\left[\Sigma - G\sigma(y,t)\right]$ (see Eqn 3.2.1, note that by force balance Σ is *spatially* constant). Here, $\sigma(y,t)$ is obtained from the relevant constitutive equation in which $\dot{\gamma}(t)$ is now time-dependent. Recall that the spatially averaged (or 'global') shear rate can be found by: $\overline{\dot{\gamma}}(t) = \frac{1}{L}\int_0^L \dot{\gamma}(y,t)\,dy$.

Shear startup: in this protocol a constant shear rate $\overline{\dot{\gamma}}$ is imposed and the dynamics of the total shear stress vary in time via: $\Sigma(t) = G\bar{\sigma}(t) + \eta\overline{\dot{\gamma}}$ (here bars denote spatially averaged values). Again, note that $\Sigma(t)$ is spatially constant by force balance. Both σ and $\dot{\gamma}$ vary spatially: $\sigma(y,t)$ is found from the relevant constitutive equation and the local shear rate found by force balance: $\dot{\gamma}(y,t) = \frac{G}{\eta}\left[\bar{\sigma}(t) - \sigma(y,t)\right] + \overline{\dot{\gamma}}$.

Strain ramp: a strain ramp is simply a fast shear startup where the imposed

shear rate $\overline{\dot{\gamma}}$ is set to zero after some strain $\gamma_0 = \overline{\dot{\gamma}} t_0$ has been met, and therefore the above applies directly to this protocol with $\overline{\dot{\gamma}} = 0$ for $t > t_0$.

Models with age-dependence

So far, we have assumed the material's response to deformation to be time translational invariant so that the choice of t at which deformation is applied is arbitrary. However, soft glassy materials often show rheological responses that have dependence on the 'waiting time' or 'age' of the sample, i.e., on the elapsed time between sample preparation and the onset of deformation. The scalar fluidity, SGR and glassy polymer models all have age-dependence, and as such we define the time elapsed since the onset of deformation as $\Delta t = t - t_w$, where t_w is the 'waiting time' and t the total time elapsed since sample preparation. The rheological protocol for age-dependent materials is shown in Figure 3.2.1.

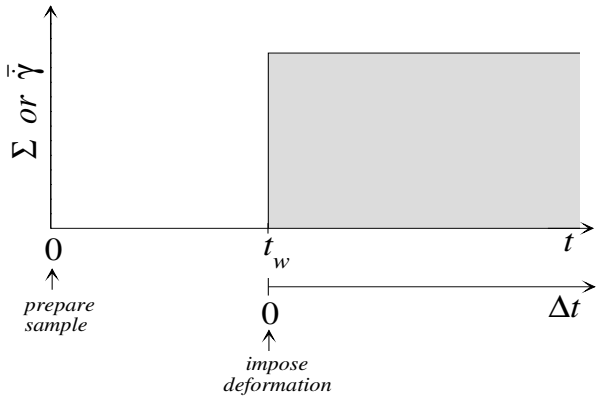

Figure 3.2.1: A schematic for the rheological protocol for materials with age dependence. A sample is prepared at $t = 0$ and left at rest until a time $t = t_w$ when deformation is imposed (this schematic assumes the deformation to be either a step stress or shear startup protocol). We define the time elapsed since the onset of deformation as $\Delta t = t - t_w$.

3.2.1 Rolie-poly model

Entangled polymer melts are usually modelled by considering a test chain that is constrained laterally to its local primitive path [solid line in Figure 3.2.2 (b)]

by a mean field provided by entanglements[2] with other polymers. Edwards [48] proposed that this effectively creates a 'tube' of confinement around the chain, as shown in Figure 3.2.2. It was further suggested by de Gennes [40] that the polymer chain would undergo one dimensional diffusion along its own length and eventually escape the tube of constraints; unoccupied tube segments are then forgotten as the chain progressively recovers an isotropic distribution of entanglements. This process was termed 'reptation' by its analogy with snake-like motion. The most popular 'tube model' to result from these initial steps was that of Doi and Edwards [47] (which we term the 'DE' theory from here on) whose basic treatment of polymers we briefly outlined in Chapter 2. The theory was an important step in modelling entangled polymers. In particular, it gave good agreement with the experimentally determined 'damping function' (as shown in Chapter 2). The theory also predicted the timescale for reptation to be proportional to the cube of the molecular weight of the chains: $\tau_d \propto M^3$, which is very close to the experimental result $\tau_d \propto M^{3.4}$ [47]. However, the theory did not incorporate the relaxation mechanism of convective constraint release (CCR), which describes how constraints forming the tube can be lost when the polymer forming the entanglement itself reptates or retracts through that point; nor the mechanism by which contour length fluctuations (CLF) allow constraints at the ends of the tube to be lost. The theory also did not allow for chain stretch during strongly nonlinear flows with deformation rates approaching the inverse Rouse time, e.g., during shear flow at rates $\dot{\gamma} > \tau_R^{-1}$. Many models based on the original DE theory were developed in an attempt to include such mechanisms [78, 105, 108, 109, 127] including the GLAMM model [67], that provides a stochastic microscopic equation of motion for the chain and the surrounding tube. However, the GLAMM model is computationally intensive; two of its authors therefore derived a single mode approximation to the model for the description of the stress or flow rate response to deformation, by removing the contour dependence from the full GLAMM theory. This single mode approximation is the rolie-poly (ROuse LInear Entangled POLYmers or 'RP') model [92], whose constitutive equation for the viscoelastic

[2]Such entanglements are considered to be dynamic (rather than static) entities.

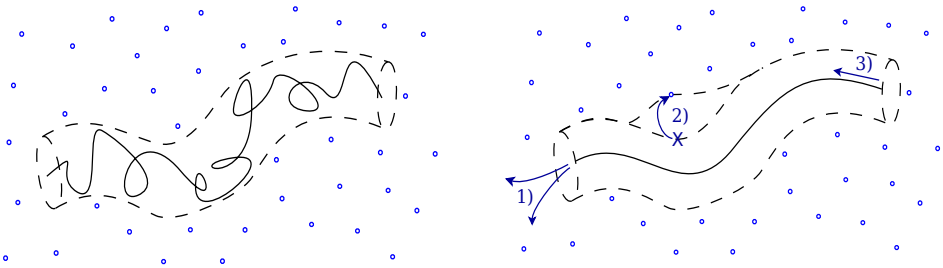

(a) (b)

Figure 3.2.2: (a) Representation of the tube model: points represent the intersection of surrounding polymers with the view plane — the entanglement points surrounding the test chain effect a 'tube' of constraints. (b) Schematic of stress relaxation mechanisms in the RP model: 1) reptation, 2) constraint release, 3) stretch relaxation.

conformation tensor is given by:

$$\partial_t \underline{\underline{\sigma}} = \underline{\underline{K}} \cdot \underline{\underline{\sigma}} + \underline{\underline{\sigma}} \cdot \underline{\underline{K}}^T - \frac{1}{\tau_d}\left(\underline{\underline{\sigma}} - \underline{\underline{I}}\right) - \frac{2(1-A)}{\tau_R}\left[\underline{\underline{\sigma}} + \beta A^{-2\delta}\left(\underline{\underline{\sigma}} - \underline{\underline{I}}\right)\right], \qquad (3.2.3)$$

where $A \equiv \sqrt{3/T}$, $T \equiv \mathrm{tr}\,\underline{\underline{\sigma}}$ denotes the magnitude of chain stretch in the system, and $\underline{\underline{K}}$ is the deformation tensor as defined previously. The timescale τ_d is the 'reptation' time: the timescale on which a test chain escapes its tube of constraints by undergoing 1D diffusion along its own length. τ_R is the Rouse relaxation time: the timescale on which chain stretch relaxes; these two relaxation times are related by the number of entanglements on a chain: $Z = \frac{\tau_d}{3\tau_R}$ [47]. β is the convective constraint release (CCR) parameter that describes the efficacy of constraint release events[3], and has range $0 \leq \beta \leq 1$, see Figure 3.2.2 for a schematic of these three mechanisms. δ is a parameter also related to convective constraint release that, following Ref. [92], we set to $\delta = -\frac{1}{2}$ throughout this thesis. Unfortunately, the CCR parameter is difficult to directly relate to experiment and there is no consensus on its correct value, though a small value $\beta \sim 0$ was used by the authors to best fit the experimental data [92]. In addition, a recent study using a diffusive form of the model found 'fracture-like' velocity profiles after a step strain for similarly small values of β, that are qualitatively similar to experiments on entangled polymeric

[3]More specifically, it is related to the number of constraint release events required to result in a portion of the tube 'hopping' a distance of the tube diameter.

materials [7]. In Chapter 6 we will investigate the effect of varying β on the stress relaxation via the stretch and orientation relaxation mechanisms following a fast ramp-strain, and its resulting effect on linear instability to shear banding. We will also allow β to vary in Chapter 5 where its effect on the overall shear banding properties will be investigated.

Componentwise, in a homogeneous shear flow at rate $\dot{\gamma}$ the constitutive equations reduce to[4]:

$$\begin{aligned}
\partial_t T &= 2\dot{\gamma}\sigma \quad -\tfrac{1}{\tau_d}(T-3) \quad -\tfrac{2(1-A)}{\tau_R}\left[T+\beta A\,(T-3)\right], \\
\partial_t \sigma &= \dot{\gamma}\sigma_{yy} \quad -\tfrac{1}{\tau_d}\sigma \quad -\tfrac{2(1-A)}{\tau_R}\left(1+\beta A\right)\sigma, \\
\partial_t \sigma_{yy} &= \quad -\tfrac{1}{\tau_d}(\sigma_{yy}-1) \quad -\tfrac{2(1-A)}{\tau_R}\left[\sigma_{yy}+\beta A\,(\sigma_{yy}-1)\right],
\end{aligned} \tag{3.2.4}$$

resulting in a system with three dynamical variables.

In the limit of fast stretch relaxation $\tau_R \to 0$ Eqn 3.2.3 reduces to: [92]:

$$\partial_t \underline{\underline{\sigma}} = \underline{\underline{K}}\cdot\underline{\underline{\sigma}} - \frac{1}{\tau_d}\left(\underline{\underline{\sigma}}-\underline{\underline{I}}\right) - \frac{2}{3}\,\mathrm{tr}\left(\underline{\underline{K}}\cdot\underline{\underline{\sigma}}\right)\left[\underline{\underline{\sigma}}+\beta(\underline{\underline{\sigma}}-\underline{\underline{I}})\right], \tag{3.2.5}$$

with constant chain stretch $T \to 3$. We denote this the 'non-stretching' RP (nRP) model and the former (Eqn 3.2.3) the 'stretching' RP (sRP) model in what follows. We also chose units in which $\tau_d = 1$ and consider small solvent viscosities $\eta \ll G\tau_d$. Componentwise, the non-stretching RP model is given by:

$$\begin{aligned}
\partial_t \sigma &= \dot{\gamma}\left[\sigma_{yy} - \tfrac{2}{3}\left(1+\beta\right)\sigma^2\right] \quad -\tfrac{1}{\tau_d}\sigma, \\
\partial_t \sigma_{yy} &= \tfrac{2}{3}\dot{\gamma}\left[\beta\sigma - \left(1+\beta\right)\sigma_{yy}\sigma\right] \quad -\tfrac{1}{\tau_d}\left(\sigma_{yy}-1\right),
\end{aligned} \tag{3.2.6}$$

i.e., having only two dynamical variables.

Steady state behaviour

The original DE model results in a negative slope of shear stress in strain $\partial_{\dot{\gamma}}\Sigma < 0$ in the constitutive curve caused by the 'over-alignment' of the chains during flow at rates $\dot{\gamma} > \tau_d^{-1}$. Originally this was considered a major failing of the DE model as no evidence of steady state shear banding that would arise from such a constitutive

[4]Recall that we define $\sigma \equiv \sigma_{xy}$ and $T \equiv \mathrm{tr}\underline{\underline{\sigma}}$.

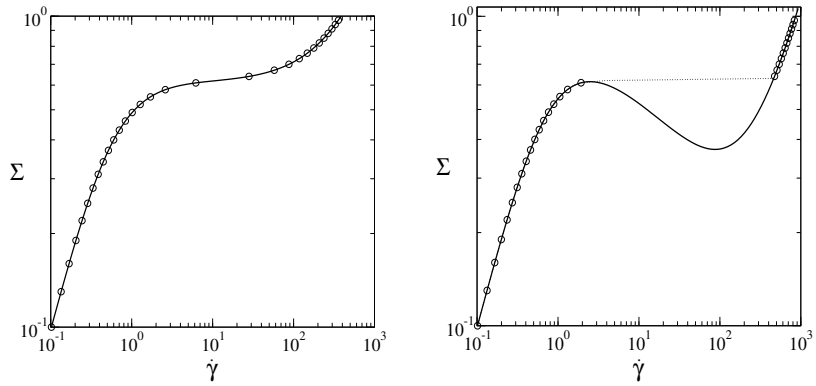

(a) $\beta = 1$ (b) $\beta = 0$

Figure 3.2.3: Steady state constitutive curves in the non-stretching RP model for two values of $\beta = 1, 0$ in (a), (b), respectively. These are obtained by imposing either a constant shear rate $\dot{\gamma}$ and measuring the steady state total shear stress response $\Sigma(\dot{\gamma}, t \to \infty)$ (solid line), or a constant total shear stress Σ and measuring the steady state shear rate response $\Sigma[\dot{\gamma}(t \to \infty)]$ (circle symbols). Convergence of the constitutive curves from these two protocols is obtained only for monotonic constitutive curves. Solvent viscosity: $\eta = 10^{-3}$, and homogeneity is enforced in the flow gradient direction.

instability existed for entangled polymeric materials at that time. The RP model was then considered a successful step forwards from the DE model, since the action of CCR can increase the total shear stress and remove the negative slope entirely. This is possible because constraint release events cause the tube to make stochastic 'hops', so that the tube itself obeys Rouse dynamics. This small deviation from an 'over-aligned' state that caused the original constitutive instability can result in a sufficient increase of the total shear stress to result in a monotonic constitutive curve (for sufficiently large values of β; for small values of β a nonmonotonic curve persists — see Figure 3.2.3). As described in Chapter 2, entangled polymeric materials have recently been shown to undergo steady state shear banding for imposed shear rates on the weakest slope of the flow curve, indicating that an underlying nonmonotonic constitutive curve may actually be correct for these materials.

Figure 3.2.3 shows our numerical results for the steady state constitutive curve for the non-stretching RP model obtained by imposing a constant shear rate $\dot{\gamma}$ and measuring the total shear stress response $\Sigma(\dot{\gamma}, t \to \infty)$. Note that homogeneity is enforced — this is the definition of the 'constitutive curve' that we defined earlier. We also plot the constitutive curve obtained by imposing a constant total shear

stress[5] and measuring the steady state shear rate response $\dot{\gamma}(t \to \infty)$. The constitutive curves obtained through each protocol differ only when the chosen parameters result in a nonmonotonicity in the constant shear rate protocol. The response under the step stress protocol then results in 'top-jumping' of the shear rate response when the imposed stress exceeds that of the underlying maximum Σ_{max}; we investigate this later in Chapter 4.

In the full (sRP) model (Eqn 3.2.4) there are three regimes of the constitutive curve depending on the imposed shear rate: *i)* $\dot{\gamma} < \tau_d^{-1}$: the linear regime where the total shear stress increases linearly with shear rate; *ii)* $\tau_d^{-1} < \dot{\gamma} < \tau_R^{-1}$: a middle regime whose slope depends on CCR (see next); and *iii)* $\dot{\gamma} > \tau_R^{-1}$: the high shear rate regime in which CCR and chain stretch are the dominant relaxation mechanisms, and the total shear stress again increases with the shear rate[6] (note that here we have assumed $\eta \ll G\tau_R$). The second (ii) region is negatively sloping if $\tau_R \ll \tau_d$ are sufficiently well separated (i.e., at sufficiently high entanglement number Z) and β and η are sufficiently small, see Figure 3 of [2].

3.2.2 Giesekus model

A constitutive equation for concentrated polymeric solutions or melts was derived by Giesekus [65], who considered that dumbbells oriented due to flow would result in anisotropic drag on the surrounding dumbbells. Giesekus began with the Upper Convected Maxwell model for dilute solutions and assumed the viscoelastic stress tensor would be proportional to an anisotropic mobility tensor, with a proportionality constant α. The resulting constitutive equations have the form:

$$\partial_t \underline{\underline{\sigma}} = \underline{\underline{K}} \cdot \underline{\underline{\sigma}} + \underline{\underline{\sigma}} \cdot \underline{\underline{K}}^T - \frac{1}{\lambda}\left(\underline{\underline{\sigma}} - \underline{\underline{I}}\right) - \frac{\alpha}{\lambda}\left(\underline{\underline{\sigma}} - \underline{\underline{I}}\right)^2, \tag{3.2.7}$$

where λ is the relaxation time which we set to $\lambda = 1$ from here on, and α is the anisotropy parameter with range $0 \leq \alpha \leq 1$. With $\alpha = 0$ anisotropy does not affect flow and the Upper Convected Maxwell (UCM) model is recovered, while the

[5] Recall from Chapter 2 that in the step stress protocol a constant Σ is imposed and the dynamics of $\dot{\gamma}(t)$ are time dependent.

[6] For $\delta \leq 0$ the gradient of this increase follows: $G\tau_d/(6Z+1)^2 + \eta$ [2].

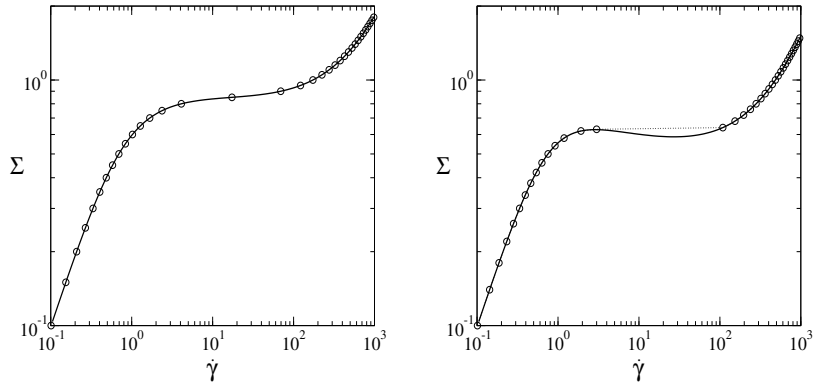

(a) $\alpha = 0.6$ (b) $\alpha = 0.8$

Figure 3.2.4: Steady state constitutive curves in the Giesekus model for two values of $\alpha = 0.6, 0.8$ in (a), (b), respectively. These are obtained by imposing either a constant shear rate $\dot{\gamma}$ and measuring the steady state total shear stress response $\Sigma(\dot{\gamma}, t \to \infty)$ (solid line), or a constant total shear stress Σ and measuring the steady state shear rate response $\Sigma[\dot{\gamma}(t \to \infty)]$ (circle symbols). Convergence of the constitutive curves from these two protocols is obtained only for monotonic constitutive curves. Solvent viscosity: $\eta = 10^{-3}$, and homogeneity is enforced in the flow gradient direction.

maximum anisotropic drag is achieved with $\alpha = 1$. Componentwise, in shear flow at rate $\dot{\gamma}$ the constitutive equations reduce to:

$$\begin{aligned} \partial_t \sigma_{xx} &= 2\sigma\dot{\gamma} - \tfrac{1}{\lambda}(\sigma_{xx} - 1) - \tfrac{\alpha}{\lambda}\left[\sigma^2 + (\sigma_{xx} - 1)^2\right], \\ \partial_t \sigma &= \dot{\gamma}\sigma_{yy} - \tfrac{1}{\lambda}\sigma - \tfrac{\alpha}{\lambda}\sigma\left[(\sigma_{xx} - 1) + (\sigma_{yy} - 1)\right], \\ \partial_t \sigma_{yy} &= - \tfrac{1}{\lambda}(\sigma_{yy} - 1) - \tfrac{\alpha}{\lambda}\left[\sigma^2 + (\sigma_{yy} - 1)^2\right], \end{aligned} \tag{3.2.8}$$

resulting in a system with three dynamical variables.

Provided a spectrum of relaxation times λ_i is used[7], the Giesekus model shows good agreement with the experimentally measured steady shear viscosity [10, 23, 24, 131] and damping function [83] found in polymeric materials. The Giesekus model is also considered useful in modelling entangled polymeric materials as it admits both nonmonotonic and monotonic constitutive curves depending on the values of α and η (see Figure 3.2.4). Indeed, it has been successful in modelling the steady state shear banding properties of entangled wormlike micelles [70, 71].

[7]This is called a multi-mode approach. It involves evolving N modes each with its own viscoelastic conformation tensor $\underline{\underline{\sigma}}_i$ and relaxation time λ_i using Eqn 3.2.7. The total stress is then found by summing over all modes $\underline{\underline{\Sigma}} = \sum_i^N G_i \underline{\underline{\sigma}}_i$, where G_i are the elastic moduli of each mode.

The steady state constitutive curve obtained under an imposed shear rate in the Giesekus model is shown in Figure 3.2.4, where we also show the constitutive curve obtained via an imposed stress. As we also found in the RP model, these curves converge only for monotonic curves obtained through the former protocol.

3.2.3 Soft glassy rheology model

The 'soft glassy rheology' (SGR) model [154] describes disordered soft materials such as emulsions, dense colloidal suspensions, and surfactant onion textures. Under shear the system initially deforms elastically until the energy barrier for the rearrangement of particles is overcome and the particles rearrange in a plastic 'yielding' event. This situation may be represented by a 'particle' picture in which a particle in an energy well or 'trap' can gain elastic strain energy due to deformation, but given sufficient energy will 'hop' out of its trap.

To be more precise, the model captures this particle picture by defining mesoscopic 'elements' that are large enough to define a local strain variable l associated with the element, but small enough that the strain can be considered constant across it. Each element is trapped in a potential energy well (or 'trap') of depth E. Elements gain elastic strain energy $\frac{1}{2}kl^2$ on the application of external deformation, where the local strain rate follows the macroscopic (global) strain rate $\dot{l} = \dot{\gamma}$, and k is an elastic constant that we set to $k = 1$ throughout by rescaling all stress and strain variables. (Before the onset of deformation the macroscopic strain is zero: $\langle l \rangle = 0$; we follow Refs. [54, 62] and achieve this by setting all element strains $l = 0$ before deformation is applied.) If the element escapes the trap (called 'yielding') l is returned to zero and a new trap of depth E is chosen from an exponential distribution $\rho(E) = e^{-E/x_g}$ for the element (where x_g is a constant that we define below). Yielding occurs via activated 'hopping' over the energy barrier $E - \frac{1}{2}kl^2$ with a rate[8] $\Gamma_0 \exp\left[-(E - \frac{1}{2}kl^2)/x\right]$, see Figure 3.2.5 for a schematic of these processes. Here, Γ_0 is an attempt rate that we set to $\Gamma_0 = 1$ throughout[9], and x is the effective noise 'temperature'. Such 'noise' is expected to describe in a mean field way the

[8] This defines the hopping (or relaxation) time of an element: $\tau(E, l) = \tau_0\, e^{\left(E - \frac{1}{2}kl^2\right)/x}$.
[9] Equivalent to setting the microscopic relaxation time $\tau_0 = 1$.

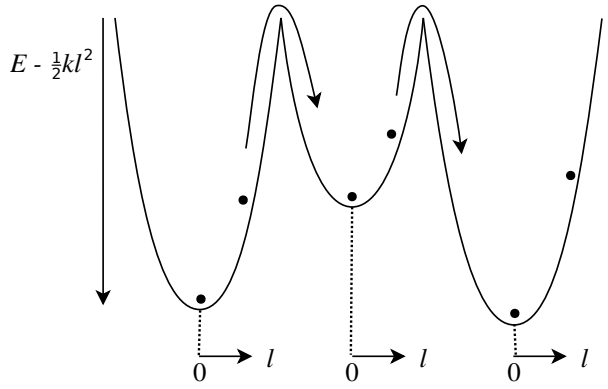

Figure 3.2.5: Schematic of particle hopping in the SGR model. Under external deformation particles gain elastic strain energy $E = \frac{1}{2}kl^2$ at a rate governed by $\dot{l} = \dot{\gamma}$. However, with a rate depending on the noise temperature x, they undergo activated 'hopping': the particle escapes the energy well, its strain is reset $l \to 0$ and it enters a new energy well of depth E' chosen from a prior distribution $\rho(E') = e^{-E'/x_g}$ uncorrelated to the previous energy depth. Figure adapted from Ref. [153].

interaction with yielding events elsewhere in the system. Note that this 'noise' is not thermal in origin — the magnitude of thermal fluctuations is considered to be too small to activate yielding events in realistic soft glassy materials: $E \gg k_B T$. Incorporating all of the above, the time-dependent probability distribution of element strains and trap energies $P(l, E, t)$ obeys the governing equation:

$$\partial_t P = -\dot{\gamma}\frac{\partial P}{\partial l} - \Gamma_0 e^{-(E-\frac{1}{2}kl^2)/x} P + \Gamma(t)\,\rho\,(E)\,\delta(l). \tag{3.2.9}$$

On the right-hand side of this equation, the first term describes the increase of strain energy of particles in between hopping events due to external deformation. The second describes activated hopping of particles out of their traps, and the third chooses a new trap of energy depth E for the particle to enter after a yielding event, and sets the particle strain to zero [$\delta(l)$ is the Dirac delta function]. In Eqn 3.2.9, Γ is the total yielding rate:

$$\Gamma = \Gamma_0 \left\langle e^{-(E-\frac{1}{2}kl^2)/x} \right\rangle_P = \Gamma_0 \int e^{-(E-\frac{1}{2}kl^2)/x}\, P(E,l,t)\, dE\, dl. \tag{3.2.10}$$

The macroscopic shear stress is the average over all local element stresses $\Sigma = kl$:

$$\Sigma(t) = k\,\langle l \rangle_P = k \int l\, P(E,l,t)\, dE\, dl. \tag{3.2.11}$$

(Note that the model is scalar in that it considers the shear stress to be uncoupled from all other stress tensor components.) In the absence of flow the model corresponds to Bouchaud's trap model [80, 81, 115] in which $x = x_g$ defines a glass transition: for $x > x_g$ the particle energy distribution $P(E, t)$ evolves towards a Boltzmann distribution. For $x < x_g$ the equilibrium distribution of energies is not normalisable and the average relaxation time $\langle \tau(E) \rangle \to \infty$; the particles evolve sequentially into deeper and deeper traps, i.e., the system *ages*. Under steady shear this process is halted as the strain of an element constantly increases via $\dot{l} = \dot{\gamma}$ so that even the deepest traps can be escaped. However, the transient stress response to imposed shear is found to be strongly age-dependent [54, 62], with a more pronounced stress overshoot for older systems before the stress relaxes onto its final age-independent value in steady state [116]. Throughout we set $x_g = 1$ so that $x = 1$ defines the glass transition. The constitutive curve follows (in the small shear rate limit that we are interested in $\dot{\gamma} \ll 1$) [153]:

$$\begin{array}{lrcll} \text{Newtonian regime} & \Sigma & \propto & \dot{\gamma} & \text{for} \quad x > 2, \\ \text{Power law regime} & \Sigma & \propto & \dot{\gamma}^{x-1} & \text{for} \quad 1 < x < 2, \\ \text{`glass phase'} & \Sigma - \Sigma_y & \propto & \dot{\gamma}^{1-x} & \text{for} \quad x < 1. \end{array} \tag{3.2.12}$$

Note that in the glass phase $x < 1$ the constitutive curve has a yield stress $\Sigma_y(x)$. The linear and nonlinear responses to shear startup, step strain and step stress protocols have been studied in detail by Fielding and co-workers [54, 62]. In the step stress protocol above the glass transition $1 < x < 2$, they determined a creep power law relation for the shear rate as a function of time[10]: $\dot{\gamma} \sim \Delta t^{x-2}$ that is valid as long as the response remains linear; the authors found this persists to times $\Delta t_f \sim \Sigma^{1/(1-x)}$, at which crossover into the steady state flowing regime occurs. In Chapter 4 we will show that this crossover time is indeed proportional to the 'fluidisation time' τ_{f} defined in Section 2.2.2.

In the 'glass phase' $x < 1$, the authors found logarithmic creep $\dot{\gamma} \sim \Delta t^{-1}$ in the linear regime at 'long' times, i.e., for $\Sigma \ll 1$ and times $\Delta t \gg t_w$, which apparently

[10]Recall that in models with age-dependence Δt defines the time elapsed since the onset of deformation, where $\Delta t = t - t_w$, and t_w is the 'waiting time'.

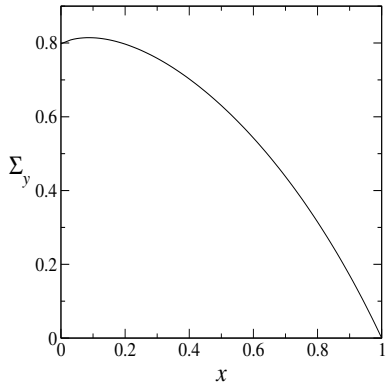

Figure 3.2.6: Yield stress $\Sigma_y(x)$ as a function of the noise temperature; data kindly provided by Prof. Peter Sollich [153].

persists for larger $\Sigma \to \Sigma_y$ (approaching from below). However, no creep law was found for 'short' times $\Delta t \ll t_w$ for stresses far below the yield stress, nor did the authors verify logarithmic creep for $\Sigma > \Sigma_y$ at either long or short times. We explore both of these creep regimes in Chapter 4, along with a relation for the fluidisation time τ_{f}. This is relevant to the aim of this thesis as it has recently been shown that transient shear banding arises in SGMs during the fluidisation process, onset at the end of the creep regime [42, 64]. Note that the power law relations determined in Chapter 4 use the yield stress $\Sigma_y(x)$, values for which were kindly provided by Prof. Peter Sollich, and are shown in Figure 3.2.6.

Finally, we note that the probability distribution $P(E, l, t)$ can be cast into infinitely many stress and fluidity-like moments, credit for which is given to Dr. Suzanne Fielding [53][11]:

$$P_{m,n} = \int_{-\infty}^{\infty} dl \int_{0}^{\infty} dE \, \frac{l^m}{\tau^n} P(E, l, t), \tag{3.2.13}$$

where:

$$\partial_t P_{m,n} = \dot{\gamma}\, m\, P_{m-1,n} + \frac{\dot{\gamma} n}{x} P_{m+1,n} - P_{m,n+1} + \frac{1}{1 + n/x} P_{0,1} \delta_{m,0}, \tag{3.2.14}$$

for $m, n = 0, 1, 2, \ldots$; in particular we note that the macroscopic shear stress $\Sigma =$

[11] see also Supp. Mat. of [117].

$P_{1,0}$. In the language of the next section, we also note the 'fluidity': $\langle \frac{1}{\tau} \rangle = P_{0,1}$, i.e., the average inverse relaxation time.

3.2.4 Scalar fluidity model

The 'scalar fluidity' model [116] is a phenomenological model that defines a constitutive equation for the structural relaxation time $\tau(t)$ coupled to a (scalar) shear conformational variable, with the aim of incorporating the fundamental features found in soft glassy materials of ageing and shear induced rejuvenation. This approach is similar to those of Refs. [34,35,41,128], where the dynamics of a structure or fluidity-like variable is also coupled to the stress, though here the resulting constitutive curve is monotonic. (In the language of the previous section, it effectively consists of closing the infinitely many coupled equations for $P_{m,n}$ at order $P_{1,0}$ and $P_{0,1}$.) In shear flow at rate $\dot{\gamma}$, the viscoelastic shear conformational variable $\sigma(t)$ and the relaxation time $\tau(t)$ are coupled via the constitutive equations:

$$\partial_t \tau = 1 - \frac{\tau}{\tau_0 + 1/|\dot{\gamma}|}, \tag{3.2.15}$$

$$\partial_t \sigma = \dot{\gamma} - \frac{\sigma}{\tau}, \tag{3.2.16}$$

where τ_0 is a microscopic relaxation time that we set to $\tau_0 = 1$ from here on. Credit for the derivation this model is given to Dr. Suzanne Fielding and Prof. Mike Cates[12]. Note that in intervals during which the sample is not being sheared the relaxation time increases linearly: $\tau = t + \tau_0$, where t is the time elapsed since sample preparation. In experiment, this 'preparation' might involve a temperature quench or an extremely large (usually oscillatory) strain deformation in order to remove all prior strain history. Throughout, we shall consider large waiting times $t_w \gg \tau_0$ and shear rates much slower than the microscopic relaxation rate $\dot{\gamma} \ll \tau_0^{-1}$. The steady shear at rate $\dot{\gamma}$ the relaxation time obeys $\tau(\Delta t \to \infty) = \tau_0 + 1/|\dot{\gamma}|$, and

[12]Note that the derivation of this model follows the lines of Refs. [34,35,41,128].

the constitutive curve is given by:

$$\Sigma = \dot{\gamma}(\eta + G\tau_0) + G, \tag{3.2.17}$$

resulting in a yield stress $\Sigma_y = G$ in the limit $\dot{\gamma} \to 0$.

3.2.5 Glassy polymer model

As explained in Section 2.2.3, recent experimental findings for glassy polymers in extensional loading show that the segmental relaxation time $\tau(t)$ initially drops until a minimum is reached concurrent with the onset of strain hardening, from which point ageing persists indefinitely. The glassy polymer (GP) model [58, 59] has been shown to semi-quantitatively reproduce these results. It considers the viscoelastic stress due to polymeric dumbbells suspended in a glassy solvent:

$$G\underline{\underline{\sigma}} = G^p \left(\underline{\underline{\sigma}}^p - \underline{\underline{I}}\right) + G^s \left(\underline{\underline{\sigma}}^s - \underline{\underline{I}}\right), \tag{3.2.18}$$

where $\underline{\underline{\sigma}}^{p,s}$ are conformation tensors for the contributions from polymeric (p) and solvent (s) degrees of freedom, and $G^{p,s}$ the respective elastic moduli. The decomposition of the viscoelastic stress into polymeric and solvent parts is taken to describe separate contributions from: the slow degrees of freedom of large-scale sections of the chain (p); and the short-scale, faster degrees of freedom that control the local segmental dynamics (s).

Each conformation tensor is taken to obey an upper convected Maxwell model:

$$\partial_t \underline{\underline{\sigma}}^p = \underline{\underline{K}} \cdot \underline{\underline{\sigma}}^p + \underline{\underline{\sigma}}^p \cdot \underline{\underline{K}}^T - \alpha \left(\underline{\underline{\sigma}}^p - \underline{\underline{I}}\right)/\tau, \tag{3.2.19}$$

$$\partial_t \underline{\underline{\sigma}}^s = \underline{\underline{K}} \cdot \underline{\underline{\sigma}}^s + \underline{\underline{\sigma}}^s \cdot \underline{\underline{K}}^T - \left(\underline{\underline{\sigma}}^s - \underline{\underline{I}}\right)/\tau, \tag{3.2.20}$$

where $\tau(t)$ is the segmental relaxation time, to which the polymeric relaxation time is proportional $\tau^p = \tau/\alpha$. The proportionality constant α is expected to be extremely small [58, 59] $\alpha \sim 0$, so that $\tau^p \gg \tau$. As a result, the actual value of α has little effect on the dynamics of $\underline{\underline{\sigma}}^p(t)$: the polymer effectively behaves elastically, with no relaxation dynamics.

The dynamics of $\tau(t)$ obeys a similar equation to that of the scalar fluidity model described in Section 3.2.4:

$$\partial_t \tau = 1 - (\tau - \tau_0)\,\mu|\dot{\gamma}|, \tag{3.2.21}$$

where μ is a dimensionless variable of order $O(1)$ that describes the efficacy of flow to reduce ageing (or to 'fluidise' the material), and τ_0 is a microscopic relaxation time. In the limit $G^p \to 0$, $\mu \to 1$ (and for appropriately rescaled parameters) the model reproduces the scalar fluidity model. Values of the parameters in the model have been carefully fitted to those of experiment by Fielding *et al.* [58]. We will use these values of the parameters to investigate the response to the step stress and shear startup deformations in Chapters 4 and 5. This is the only model for which we deviate from choosing dimensionless units in which $G, \tau_0 = 1$, we therefore summarise the parameter values for this model in Table 3.1.

G^p	6 MPa	η	$0.05G^p\tau_0$
G^s	$8.5G^p$	μ	12.5
τ_0	6 s	α	10^{-12}
t_w	$10^4\tau_0$	Σ_y^s	G^s/μ

Table 3.1: Parameters from Ref. [58] used in Chapters 4 and 5 for the GP model, unless otherwise stated.

Remark on the models

Our descriptions of each model above are intended to provide sufficient information to perform the calculations that were used to obtain the results presented in Chapters 4, 5 and 6. (Note that in addition to the above descriptions, diffusive terms must be added to the constitutive equations for each model for a proper description of shear banded flows. We will discuss the reasoning and details of this in the following section.) As is usually the case, each of these models contains unresolved issues. For example, the value of the CCR parameter in the RP model has not been matched to experiment via a microscopic interpretation; the constitutive equation for the polymer viscoelastic stress $\underline{\underline{\Sigma}}^p$ in the GP model is based on a simple

dumbbell description, however a more detailed approach may be required; and the effective 'noise' temperature x in the SGR model is kept constant, but for a better approximation to 'noise' resulting from yielding events, its value should be coupled to the flow dynamics. We do not attempt to justify the choices made by the authors of each model in deriving them, as our aim in this thesis is to identify their rheological response to shear deformation (with the priority being upon shear banding behaviour) as they stand. We hope that our results may aid the identification of other issues that require attention, or provide indications of how they may be ameliorated. For example, we will show in Chapter 6 that the mechanism of convective constraint release in the RP model provides a stabilising role that prevents shear heterogeneity arising after a fast strain ramp. This disagrees with experimental results of entangled polymers that do show severe heterogeneity after a large step strain. Similarly, we will show that the Giesekus model is not suitable for the description of the *time-dependent* shear banding properties of entangled polymeric materials, despite having success in modelling their steady state shear banding behaviour.

3.3 Outline of general framework

So far, we have outlined the theoretical rheology required to solve the shear flow of materials at low Reynold's number, in which we decompose the total stress into viscoelastic and Newtonian solvent contributions. We also outlined the models that provide this viscoelastic stress contribution to the total stress that results from internal mesoscopic substructures such as entangled polymer chains or emulsion droplets. In Chapters 4, 5 and 6 we aim to explore the linear stability to shear heterogeneity, and the resulting shear banding behaviour of these models in the three deformation protocols outlined in Chapter 2. In particular, we will derive a criterion for the onset of linear instability to shear heterogeneity that is independent of any model or fluid type, for each of the three deformation protocols. In order to allow complete generality of these criteria, and for clarity of our presentation throughout this thesis, we will now outline the 'general framework' in which all models described

above fit. This will be used as a starting point for the linear stability analyses used to derive each protocol-specific criterion for the onset of shear banding.

We begin by combining all dynamical variables relevant to any material in question into a vector $\underline{s} = (\sigma, \sigma_{xx}, \sigma_{yy}, ...)^T$. (Recall our notation $\sigma = \sigma_{xy}$.) In general, this will include all components of the viscoelastic conformation tensor $\underline{\underline{\sigma}}$ but may also include any soft glassy degrees of freedom, e.g., the structural relaxation time $\tau(t)$ in the scalar fluidity model. Table 3.2 outlines the vector $\underline{s}$ for each model considered in this thesis. Note that the SGR model fits into this general framework by collecting all of the (infinitely many) moments $P_{m,n}$ into the vector $\underline{s}$ and considering the limit of small Newtonian viscosity $\eta \to 0$.

Model	$\underline{s}$
non-stretching rolie-poly	$(\sigma, \sigma_{yy})^T$
stretching rolie-poly	$(\sigma, T, \sigma_{yy})^T$
Gieskus	$(\sigma, \sigma_{xx}, \sigma_{yy})^T$
soft glassy rheology	$(P_{1,0}, P_{0,1}, P_{1,1}, \ldots)^T$
scalar fluidity	$(\sigma, \tau)^T$
glassy polymer	$(\sigma^p, \sigma^s, \tau)^T$

Table 3.2: A table outlining the dynamical variables for each model considered in this thesis, and the resulting form of the vector $\underline{s}$ of the general framework.

Next, we define a projection vector[13] $\underline{p} = (1, 0, 0, \ldots)$ for the viscoelastic shear stress $G\sigma(y,t)$ so that the total shear stress may be written $\Sigma(t) = G\underline{p} \cdot \underline{s}(y,t) + \eta\dot{\gamma}(y,t)$. The dynamics of $\underline{s}$ are determined by the constitutive equation:

$$\partial_t \underline{s} = \underline{Q}(\underline{s}, \dot{\gamma}), \tag{3.3.1}$$

where $\underline{Q}$ is specified by the appropriate model. Crucially, we do not require the particular form of $\underline{Q}$ to be specified to perform the linear stability analysis through which the criteria are derived. In this way, our criteria are independent of the particular constitutive model and fluid in question.

[13]Note that the projection vector chosen here $\underline{p} = (1, 0, 0, \ldots)$ is correct for all models as they are outlined in Table 3.2, except the glassy polymer model. To select the viscoelastic shear stress with $G^p\underline{p} \cdot \underline{s}$ we must have $\underline{p} = (1, G^s/G^p, 0)$ for this model. Nevertheless, this change in $\underline{p}$ does not affect the criteria derived in Chapters 4, 5 and 6 as no assumption about the form of $\underline{p}$ is made.

As explained in Section 3.2, depending on the chosen shearing protocol, either the total shear stress Σ or the shear rate $\dot{\gamma}$ vary as a function of time, and should therefore be included as a variable in $\underline{s}$. However, in the shear startup (or strain ramp) protocols we note that the time dependence of $\Sigma(t)$ is a direct result of the time dependence of $\sigma(y,t)$. This is because by force balance (Eqn 3.2.2) we have $\Sigma(t) = G\sigma(y,t) + \eta\dot{\gamma}(y,t)$, where $\dot{\gamma}(y,t) = \overline{\dot{\gamma}} + \frac{G}{\eta}[\bar{\sigma}(t) - \sigma(y,t)]$. Hence, we may explicitly rewrite $\Sigma(t)$ in terms of $\sigma(y,t)$ and therefore need not include $\Sigma(t)$ in $\underline{s}$. Similarly, in the step stress protocol the shear rate may be written $\dot{\gamma}(y,t) = \frac{1}{\eta}[\Sigma - G\sigma(y,t)]$. Then, for the same reason we need not include $\dot{\gamma}(y,t)$ in $\underline{s}$.

'Diffusive' term: $D\nabla^2\underline{s}$

As described in Chapter 2, homogeneous steady state shear flow at a shear rate in the negative slope of a nonmonotonic constitutive curve is unstable to heterogeneous perturbations in the flow gradient direction [160, 172]. With heterogeneity allowed in this direction the material usually separates into two (or more) 'bands' flowing at shear rates $\dot{\gamma}_{min}$, $\dot{\gamma}_{max}$. With any constitutive equation of the form as described above in Eqn 3.3.1, the interface between these bands is unphysically sharp leading to a discontinuity in $\dot{\gamma}(y)$. In addition, the steady state total shear stress is not uniquely selected — rather, it depends on the shear history of the material and can have a value anywhere between $\Sigma_{min} \leq \Sigma \leq \Sigma_{max}$ of Figure 2.1.6 [120].

To avoid these problems a 'diffusive' term of the form $D\nabla^2\underline{s}$ is usually included in the constitutive equation:

$$\partial_t \underline{s} = \underline{Q}(\underline{s}, \dot{\gamma}) + D\nabla^2\underline{s}, \tag{3.3.2}$$

which results in the unique selection of the total shear stress and a lengthscale $\ell = \sqrt{D\tau_0}$ for the interface between the bands [94,120,132] (where τ_0 is a microscopic timescale and D a diffusion constant). Therefore, whenever heterogeneity is allowed in the flow gradient direction in this thesis we shall also include the diffusive term

described above to the constitutive equations for $\underline{s}$. We outline in Appendix I the numerical methods required to find solutions $\underline{s}(t)$ to Eqn 3.3.1 for systems with homogeneity (artificially) imposed, and also solutions $\underline{s}(y,t)$ to Eqn 3.3.2 for systems with heterogeneity allowed in the flow gradient direction.

Throughout this thesis we shall consider no-slip conditions of the sample at the sample-wall interface, which we achieve by using zero-gradient boundary conditions (outlined in Appendix I). We discuss the validity of no-slip boundary conditions in Chapter 7.

Constitutive and flow curves

We now define the *'constitutive curve'* as the steady state relation between the total shear stress and shear rate $\Sigma(\dot{\gamma})|_{t\to\infty}$, obtained by imposing a constant shear rate $\dot{\gamma}$ with homogeneity artificially enforced. We also define the *'flow curve'* as the same relation with heterogeneity in the flow gradient direction allowed $\Sigma(\overline{\dot{\gamma}})|_{t\to\infty}$, where $\overline{\dot{\gamma}} = \frac{1}{L}\int_0^L \dot{\gamma}(y)\,dy$ is the 'global' or average shear rate that we impose[14]. Soft glassy materials often possess a 'yield stress' that we denote Σ_y; this describes the shear stress in the limit of zero shear $\Sigma_y = \lim_{\dot{\gamma}\to 0}\Sigma(\dot{\gamma})$ in the flow curve.

The 'degree of banding'

As explained above, using numerical methods (outlined in Appendix I) we may find solutions for the local shear rate $\dot{\gamma}(y,t)$. In solutions that give shear banded flows [see Figure 2.1.1 (b)] a high shear rate $\dot{\gamma}_{max}$ and low shear rate $\dot{\gamma}_{min}$ coexist in the cell, separated by an interface with width characterised by ℓ (above). In order to determine the magnitude or the 'degree' to which this banding arises at any time, we determine the difference between the maximum and minimum shear rates in the cell, which we denote the 'degree of banding':

$$\Delta_{\dot{\gamma}}(t) = (\dot{\gamma}_{max} - \dot{\gamma}_{min})\,|_t\,. \tag{3.3.3}$$

[14]Unless otherwise specified, each point on these curves is obtained from the steady state deformation of a sample that was initially at rest.

3.4 Linear stability analysis

In any shear protocol investigated in this thesis, we solve first the flow response to deformation with homogeneity artificially enforced: $\underline{\hat{s}}(t)$ — we call this the homogeneous 'background' state. Our aim is then to examine the *time-dependent* linear stability of this homogeneous background state to the growth of heterogeneous perturbations. To investigate this, we express the response to deformation as the sum of the time-dependent homogeneous background state plus any (initially) small heterogeneous perturbations decomposed into Fourier modes[15]:

$$\underline{s}(y,t) = \underline{\hat{s}}(t) + \sum_k \underline{\delta s}_k(t)\cos(k\pi y/L). \tag{3.4.1}$$

Here, the homogeneous background is represented by hats $\underline{\hat{s}}$ (that we later neglect for clarity of presentation), and $k = 1, 2, \ldots$ is the mode number. Our aim is to determine whether the magnitude of the heterogeneous perturbations $\underline{\delta s}_k(t)$ at any time t have a positive or negative growth rate (indicating instability or stability to heterogeneity, respectively). To do this, we substitute this form of $\underline{s}(y,t)$ (Eqn 3.4.1) into its constitutive equation: Eqn 3.3.2, and expand and linearise to the first order terms in $\underline{\delta s}_k$ [neglecting terms $O(\underline{\delta s}_k^2)$ and higher]. Doing so, we find the governing equation for the heterogeneous perturbations:

$$\partial_t \underline{\delta s}_k = \underline{\underline{P}}(t) \cdot \underline{\delta s}_k, \tag{3.4.2}$$

where we neglect contributions from the diffusive terms[16] of Eqn 3.3.2 as the perturbations of interest in this thesis have wavelength $\gg l$. Here, $\underline{\underline{P}}$ is the *time-dependent* 'stability matrix':

$$\underline{\underline{P}}(t) = \underline{\underline{M}}(t) - \frac{G}{\eta}\underline{q}(t)\,\underline{p}, \tag{3.4.3}$$

[15] A similar time-dependent linear stability analysis has been done for the Johnson Segalman model in Ref. [61], the rolie-poly model in Ref. [2] and a shear transformation zone model in Ref. [101]. In this thesis we use use their methods to obtain more general rules for the time-dependent linear stability to shear heterogeneity in complex fluids.

[16] Which would add a contribution to $\underline{\underline{P}}$ of $-(\ell^2 k^2 \pi^2/\tau_0 L)\underline{\underline{I}}$ in Eqn 3.4.2. This means that diffusion terms provide a stabilising contribution to the system, i.e., they only act to decrease the growth rate of heterogeneous perturbations. If this were not the case (for example, in models with more complicated non-local terms), neglecting the diffusive terms in $\underline{\underline{P}}$ might hide linear instability.

with $\underline{\underline{M}} = \partial_{\underline{s}}\,\underline{Q}|_{\hat{\underline{s}},\hat{\dot{\gamma}}}$ and $\underline{q} = \partial_{\dot{\gamma}}\underline{Q}|_{\hat{\underline{s}},\hat{\dot{\gamma}}}$ from the homogeneous background state that we recall obeys:

$$\begin{aligned} \partial_t\,\hat{\underline{s}} &= \underline{Q}, \\ \hat{\Sigma} &= G\hat{\sigma} + \eta\hat{\dot{\gamma}}. \end{aligned} \tag{3.4.4}$$

This separation of $\underline{\underline{P}}$ (Eqn 3.4.3) into two terms with partial derivatives $\partial_{\underline{s}}$ and $\partial_{\dot{\gamma}}$ of $\underline{Q}$ exists because force balance demands uniform total shear stress:

$$\delta\Sigma_k = G\,\underline{p}\cdot\underline{\delta s}_k(t) + \eta\,\delta\dot{\gamma}_k(t) = 0. \tag{3.4.5}$$

We may therefore replace all occurrences of $\delta\dot{\gamma}_k(t)$ with $\delta\dot{\gamma}_k(t) = -\frac{G}{\eta}\underline{p}\cdot\underline{\delta s}_k(t)$.

The growth of heterogeneous perturbations $\underline{\delta s}_k$ in this linearised system corresponds to the growth of heterogeneity in the full nonlinear system as long as the perturbations remain small. In this case, $\delta\dot{\gamma}_k$ of the linear analysis is approximately equal to $\delta\dot{\gamma}_k \sim \Delta_{\dot{\gamma}}$, where $\Delta_{\dot{\gamma}}$ is the 'degree of banding' (Eqn 3.3.3) measured in the nonlinear simulation. If $\Delta_{\dot{\gamma}}$ becomes large, nonlinearities neglected in this linear analysis become important and the relation $\delta\dot{\gamma}_k \sim \Delta_{\dot{\gamma}}$ no longer holds. This linear analysis is therefore capable of capturing just the *onset* of instability to shear heterogeneity (rather than the return to stability), which is our aim.

Classical stability theory

A linear stability analysis of a dynamical system is usually performed for a *time-independent* background state, so that the stability matrix $\underline{\underline{P}}$, which depends on the background state, is time-independent [157]. Solutions to Eqn 3.4.2 then have the form $\underline{\delta s}(t) = \sum_k \underline{\delta s}_k(0)\exp(\omega_k t)$, where ω_k is an eigenvalue of $\underline{\underline{P}}$. Thus a positive, real part[17] of an eigenvalue of $\underline{\underline{P}}$ leads to exponentially growing heterogeneous

[17]Note that the imaginary part of any complex eigenvalue results in oscillations in the perturbations [whose magnitude may be growing or decaying depending on $\mathrm{Re}(\omega_k)$] with frequency $\mathrm{Im}(\omega_k)$.

perturbations, and the system is linearly unstable. Conversely, if all real parts of all eigenvalues of $\underline{\underline{P}}$ are negative, the system is linearly stable as all perturbations decay exponentially[18].

Now, how do we use the above classical stability theory with a time-dependent background state, $\underline{\underline{P}}(t)$? One possibility is to ask whether the system is linearly unstable to heterogeneity according to the eigenvalue analysis above at some time *instant* t^*. To do this, we define $\omega(t)$ largest real part of any eigenvalue of $\underline{\underline{P}}(t)$ at time t^*, and ask whether $\omega(t^*) > 0$. If so, the system is linearly unstable to the growth of heterogeneous perturbations *at that instant in time*[19], according to classical stability theory.

Non-normal growth

There is one problem with the classical stability theory approach described above: the assumption that ω describes the *decay* of perturbations is only valid if the eigenvectors of $\underline{\underline{P}}$ are *orthogonal* [148]. We outline the reason for this and its implications below, for further details we refer the reader to Schmid *et al.* [147–149]. To begin, we note that the solution to the time-independent system has the form:

$$\underline{\delta s}_k(t) = \exp(t\,\underline{\underline{P}}) \cdot \underline{\delta s}_k(0), \tag{3.4.6}$$

where $\exp(t\,\underline{\underline{P}})$ is the matrix exponential. Classical stability theory uses the eigen decomposition of $\underline{\underline{P}} = \underline{\underline{H}} \cdot \underline{\underline{\Omega}} \cdot \underline{\underline{H}}^{-1}$, where $\underline{\underline{H}}$ is the matrix whose columns are the eigenvectors of $\underline{\underline{P}}$, and $\underline{\underline{\Omega}}$ the matrix whose diagonals are the corresponding eigenvalues. We consider the norm $\|\exp(t\underline{\underline{P}})\|^2$, which describes the growth of perturbation energy from linear stability analysis, whose lower bound is given by the eigenvalue

[18] A simple example of instability involves a ball at the top of a hill: a small perturbation causes it to move away from its original position. Similarly, if the ball were in a dip, after a small perturbation is applied the ball simply rolls back to its original position, i.e, a stable system.

[19] In our ball-on-a-hill example the time-dependent background state could be represented by a time-dependent landscape for the ball. This linear stability analysis then asks whether a configuration at time t^* of ball location and current landscape is stable.

analysis from classical stability theory described above [148]:

$$\exp(2\omega t) \leq \| \exp(t\underline{\underline{P}}) \|^2. \tag{3.4.7}$$

This means that if $\omega > 0$ the system is linearly unstable, regardless of the orthogonality of the eigenvectors of $\underline{\underline{P}}$. The upper bound of the norm $\| \exp(t\underline{\underline{P}}) \|^2$ is obtained by expanding $\underline{\underline{P}}$ to find:

$$\| \exp\left(t\underline{\underline{P}}\right) \|^2 = \| \exp\left(\underline{\underline{H}}.\underline{\underline{\Lambda}}.\underline{\underline{H}}^{-1}t\right) \|^2 \leq \|\underline{\underline{H}}\|^2 \, \|\underline{\underline{H}}^{-1}\|^2 \exp\left(2\omega t\right). \tag{3.4.8}$$

For orthogonal eigenvectors: $\|\underline{\underline{H}}\|^2 \, \|\underline{\underline{H}}^{-1}\|^2 = 1$ and the upper and lower bounds agree, so that the eigenvalue analysis described above returns the growth rate of perturbations in the linearised system. This is the case for perturbations of the time-independent system [147–149].

For the time-dependent system the eigenvectors may not be orthogonal, resulting in $\|\underline{\underline{H}}\|^2 \, \|\underline{\underline{H}}^{-1}\|^2 > 1$. This means that the eigenvalue analysis described above only provides a *lower bound* for stability: positive eigenvalues $\omega(t^*) > 0$ result in linear instability, but negative eigenvalues $\omega(t^*) < 0$ do not guarantee stability. I.e., a positive real part of an eigenvalue of $\underline{\underline{P}}$ is sufficient but *not necessary* for the growth of heterogeneous perturbations. This can lead to *'transient'* or *'non-normal'* growth of perturbations at times for which all real parts of the eigenvalues of $\underline{\underline{P}}$ are negative. Indeed, we have seen such non-normal growth in the models described in Section 3.2. However, in general we find that any non-normal growth of perturbations is small relative to the growth associated with an unstable eigenvalue $\omega(t^*) > 0$, and never results in 'significant' shear banding (that is, shear banding large enough to be detected in experiment).

The above shows that caution must be used whenever considering the largest real part of an eigenvalue from stability analysis alone. We therefore integrate Eqn 3.4.2 to directly determine the solutions $\underline{\delta s_k}(t)$ whenever the eigenvalue analysis is used in this thesis. This obviates the need for considering a time-dependent eigenvalue and the danger associated with it described above. We note that neither criteria for the step stress or strain ramp protocols depend on this eigenvalue — they directly

use the condition for the growth of heterogeneous perturbations $\partial_t \underline{\delta s}_k > \underline{0}$.

A remark on the eigenvalues of $\underline{\underline{M}}$

For the derivation of the shear startup criterion in Chapter 5 it will be useful to understand the properties of the eigenvalues of $\underline{\underline{M}}$. Thus we now pause briefly to consider these. We begin by considering the linear stability of the steady state homogeneous system described by $\underline{s}(t \to \infty)$ to *homogeneous* perturbations under the constant shear rate protocol. This corresponds to the $k = 0$th mode perturbation of the above analysis, with the constraint of $\delta\dot{\gamma}_{k=0} = 0$ (due to the fixed shear rate condition). That is, the full response is written as a sum of the background state plus (initially) small homogeneous perturbations $\delta\Sigma_{k=0}, \underline{\delta s}_{k=0}$:

$$\Sigma = \hat{\Sigma} + \delta\Sigma_{k=0}, \tag{3.4.9}$$

$$\underline{s} = \hat{\underline{s}} + \underline{\delta s}_{k=0}, \tag{3.4.10}$$

$$\delta\Sigma_{k=0} = G\,\delta\sigma_{k=0} \qquad \text{(due to force balance)}. \tag{3.4.11}$$

Following the protocol of the above analysis, the perturbations then obey:

$$\partial_t \underline{\delta s}_{k=0} = \underline{\underline{M}}_{k=0} \cdot \underline{\delta s}_{k=0}, \tag{3.4.12}$$

with $\underline{\underline{M}} = \partial_{\underline{s}}\, \underline{Q}|_{\hat{\underline{s}},\hat{\dot{\gamma}}}$ as before. In this thesis we shall consider models with constitutive curves that have a unique value of the total shear stress for a given shear rate $\Sigma(\dot{\gamma})$. Such systems must be linearly stable to homogeneous perturbations (in the constant shear rate protocol) if they are to be physically meaningful, as linear instability can only result in divergence of the total shear stress $\Sigma \to \pm\infty$. Therefore, for physically meaningful systems, all real parts of the eigenvalues of $\underline{\underline{M}}$ must be negative. This leads to the results: $\mathrm{tr}\underline{\underline{M}} < 0$ and[20] $(-1)^n|\underline{\underline{M}}| > 0$, which we will use in Chapter 5.

[20]Where $|\underline{\underline{M}}| \equiv \det \underline{\underline{M}}$.

3.5 Noise and initial conditions

In a system that is linearly unstable to heterogeneous perturbations, a small amplitude perturbation must be seeded in the system in order to allow the growth of heterogeneity. In experiment, this 'noise' may arise from (for example) residual stresses due to sample preparation, imperfect rheometer feedback (i.e., mechanical noise), or a curved geometry for shear flow. We will explore the first two of these by considering the growth of perturbations in a system with *i*) a small heterogeneous perturbation added initially at $t = 0$ (or $\Delta t = 0$ in models with age-dependence) to all components of $\underline{s}$, and *ii*) a small (random) heterogeneous perturbation added at every timestep to all components of $\underline{s}$.

Initial noise: to model *i*) in the linearised system above (Section 3.4) we add a small random kick to all $\underline{\delta s}_k$ before the onset of deformation: $\underline{\delta s}_k(t = 0) = q\underline{X}_k$, where q is the magnitude of initial noise added and $\underline{X}_k$ an array of random numbers chosen from a uniform distribution with mean 0 and width 1. In the nonlinear system (i.e., that with heterogeneity allowed in the flow gradient direction, see Section 3.6) a small heterogeneity is added to all dynamical variables before the onset of deformation: $\underline{s}(y, t = 0) = q\underline{X}\cos(\pi y/L)$. Note that here we seed only the lowest Fourier mode $k = 1$, because in all models considered in this thesis this is the most unstable mode.

Continuous noise: to model *ii*) in the nonlinear system, we add a small random kick to the heterogeneity in the form of a cosine profile at every timestep, i.e., $\underline{s}(y, t + dt) = \underline{s}(y, t) + q\sqrt{dt}\underline{X}\cos(\pi y/L)$. We evolve this system at rest until a statistically steady state is reached, after which the chosen protocol (e.g., step stress) is applied. In the linearised system, this equates to adding a source term $\underline{\nu}_k(t)$ for the continuous background noise to the governing equation for the heterogeneous perturbations (Eqn 3.4.2), i.e., $\partial_t \underline{\delta s}_k(t) = \underline{\underline{P}}(t) \cdot \underline{\delta s}_k(t) + \underline{\nu}_k(t)$, where $\underline{\underline{P}}(t)$ is the stability matrix defined in Section 3.4. It is possible to implicitly average over infinitely many noise histories by evolving the *variance* of the perturbations given by the (diagonals of the) structure factor: $\underline{\underline{S}}(t) = \langle \underline{\delta s}_k(t) \cdot \underline{\delta s}_k^T(t) \rangle$ [61], where:

$$\partial_t \underline{\underline{S}} = \underline{\underline{P}} \cdot \underline{\underline{S}} + \underline{\underline{S}} \cdot \underline{\underline{P}}^T + \underline{\underline{N}}, \tag{3.5.1}$$

and $\underline{\underline{N}}(t) = \langle \underline{\nu}_k(t) \cdot \underline{\nu}_k^T(t) \rangle$ is the noise matrix. The off-diagonals of $\underline{\underline{N}}$ are all zero because the background noise is uncorrelated, and the diagonals contain the variance of the continuously added noise[21]: $\underline{\underline{N}} = \frac{q^2}{12}\underline{\underline{I}}$. As in the nonlinear system, we evolve $\underline{\underline{S}}$ to a steady state in the absence of shear before imposing deformation.

3.6 Appendix I: numerical methods

3.6.1 Homogeneously constrained systems

In all models described in Section 3.2 (apart from the SGR model, for which numerical methods are provided in Section 3.6.3) the dynamical variables obey differential constitutive equations that have derivatives with respect to time only. Therefore, when considering the fluids modelled by these equations with homogeneity in the flow gradient direction enforced, we assume all points in the y direction to evolve identically from the same initial state $\underline{s}(t = 0)$. We first initialise the system at time $t = 0$ (or $\Delta t = 0$ in systems with age-dependence) by setting $\underline{\underline{\sigma}}(t \text{ or } \Delta t = 0) = \underline{\underline{I}}$, etc. We discritise time into steps $n = 0, 1, 2, \ldots$ of size dt so that $t_n = n\,dt$, and use an explicit Euler time-stepping algorithm [130] to integrate the constitutive equations in time. To do this we use the fundamental theorem of calculus to write, in the case of a single dynamical variable $\partial_t s = Q[s(t)]$:

$$\frac{s(t + dt) - s(t)}{dt} = Q(t), \tag{3.6.1}$$

then use the discritisation of time to rewrite this as:

$$s^{n+1} = dt\, Q(s^n) + s^n. \tag{3.6.2}$$

This method is called 'explicit' (or 'forwards') Euler because the value of s^{n+1} at the next time step $n + 1$ (or time $t + dt$) is written explicitly in terms of the system

[21] Where the random amplitude of fluctuations is chosen from a uniform distribution with mean 0 and width 1, and are all modulated by the noise magnitude, q.

at step n (or time t). [An alternative 'implicit' (or 'backwards') Euler algorithm implicitly determines the value of s^{n+1} using the gradient of s at that timestep, i.e., replacing $Q(t)$ in Eqn 3.6.1 with $Q(t+dt)$.] Note that the extension of this method to solving coupled ordinary differential equations $\partial_t \underline{s} = \underline{Q}(\underline{s})$ is trivial.

When using the Euler time-stepping algorithm above we must check for *time-step convergence* of the integrated function $s(t)$, i.e., check the function obtained $s(t)$ is independent of the size of the timestep dt. This is done by halving the timestep and checking the integrated function $s(t)$ obtained with dt and $dt/2$ for convergence.

3.6.2 Systems with heterogeneity allowed

As explained in Section 3.3, when heterogeneity is allowed in the flow gradient direction, we add 'diffusive' terms of the form $\partial_y^2 \underline{s}$ (with translational invariance in the $\underline{x}, \underline{z}$ directions) to the constitutive equation for $\underline{s}$:

$$\partial_t \underline{s} = \underline{Q}(\underline{s}, \dot{\gamma}) + D\partial_y^2 \underline{s}. \tag{3.6.3}$$

To solve this numerically we use a Crank Nicolson algorithm [130], which we briefly describe below for a single component of $\underline{s}$ with $\underline{Q} = 0$. We relabel this component $s_1(t, y) \equiv \phi(t, y)$ to avoid confusion over vectors below, solving $\partial_t \phi = D\partial_y^2 \phi$.

The Crank Nicolson algorithm

Firstly, we discretise space and time into steps of size dy and dt, respectively, and define the space step number $j = 1, \ldots, J$ and time step number $n = 1, \ldots$ as before, so that $y_j = j\,dy$ and $t_n = n\,dt$. We take a small spatial step either side of some point y to $y + dy$ and $y - dy$, and expand ϕ in a Taylor series about these points:

$$\phi(y+dy) = \phi(y) + \phi'(y)dy + \frac{1}{2}\phi''(y)(dy)^2 + O\left[(dy)^3\right], \tag{3.6.4}$$

$$\phi(y-dy) = \phi(y) - \phi'(y)dy + \frac{1}{2}\phi''(y)(dy)^2 + O\left[(dy)^3\right]. \tag{3.6.5}$$

Adding these and neglecting terms of $O\left[(dy)^4\right]$ or higher order, we rearrange to find:

$$\phi''(y) = \frac{1}{(dy)^2}\left[\phi(y+dy) - 2\phi(y) + \phi(y-dy)\right]. \tag{3.6.6}$$

In principle, the explicit Euler time-stepping scheme described above could be implemented to solve the equation — however, a more numerically stable scheme combines both the implicit and explicit schemes, and is called the Crank Nicolson algorithm [130]. Using this, $\partial_t \phi = D\partial_y^2 \phi$ is written:

$$\frac{\phi_j^{n+1} - \phi_j^n}{dt} = \frac{D}{(dy)^2}\frac{1}{2}\left[\left(\phi_{j+1}^{n+1} - 2\phi_j^{n+1} + \phi_{j-1}^{n+1}\right) + \left(\phi_{j+1}^{n} - 2\phi_j^{n} + \phi_{j-1}^{n}\right)\right], \tag{3.6.7}$$

so that information about the point y at time t is obtained from points y, $y \pm dy$ at times t and $t + dt$.

Recall that we consider a shearing cell comprised of parallel plates at $y = 0, L$. Therefore, we must also specify boundary conditions for points $j = 1, J$. In principle, according to Eqn 3.6.7 these require information from points on *both* sides (i.e., from neighbours at $j = 0, 2$ for $j = 1$ and neighbours at $j = J-1, J+1$ for $j = J$), but in fact only have a single neighbour each at $j = 2, J-1$. This is resolved by choosing zero gradient boundary conditions: $\partial_y \phi = 0$, so that the values of ϕ at 'phantom' points $j = 0, J+1$ just outside the cell are the same as those at points just inside the cell: $j = 2, J-1$. Eqn 3.6.7 can then be written (with the vector form of $\phi_j^n = \underline{\phi}^n$):

$$\frac{\underline{\phi}^{n+1} - \underline{\phi}^n}{dt} = \frac{D}{(dy)^2}\underline{\underline{C}} \cdot \frac{(\underline{\phi}^{n+1} + \underline{\phi}^n)}{2}, \tag{3.6.8}$$

where:

$$\underline{\underline{C}} = \begin{pmatrix} -2 & 2 & & & \cdots & 0 \\ 1 & -2 & 1 & & \cdots & 0 \\ & & \ddots & \ddots & \ddots & \\ 0 & \cdots & & 1 & -2 & 1 \\ 0 & \cdots & & & 2 & -2 \end{pmatrix}. \tag{3.6.9}$$

We rearrange Eqn 3.6.8 to find an equation for $\underline{\phi}$ at the $(n+1)$th timestep:

$$\underline{\phi}^{n+1} = \left[\underline{\underline{I}} - \frac{D\,dt}{2(dy)^2}\underline{\underline{C}}\right]^{-1}\left[\underline{\underline{I}} + \frac{D\,dt}{2(dy)^2}\underline{\underline{C}}\right]\underline{\phi}^{n}. \tag{3.6.10}$$

To invert the first bracketed function we use the Thomas algorithm for tridiagonal matrices [129]. Note that the extension of the Crank Nicolson scheme above to coupled partial differential equations $\partial_t \underline{s} = D\nabla^2\underline{s}$ is trivial.

So far, we have outlined the numerical methods for solving equations with the forms of $\partial_t \underline{s} = \underline{Q}(\underline{s})$ and $\partial_t \underline{s} = D\partial_y^2\underline{s}$. We now combine these methods to find solutions $\underline{s}(y,t)$ to general $\partial_t \underline{s} = \underline{Q}(\underline{s}) + D\partial_y^2\underline{s}$. To do this, we employ the following protocol at each timestep. First, for each spatial point j, we update all components of the vector $\underline{s}_j$ using Eqn 3.6.2 to account for the term $\partial_t \underline{s} = \underline{Q}(\underline{s})$. Second, we update all spatial points j according to the 'diffusive' term using Eqn 3.6.10 to account for the term $\partial_t \underline{s} = D\partial_y^2\underline{s}$. Third, the force balance equation $\partial_y\Sigma = 0$, where $\Sigma = G\underline{p}\cdot\underline{s} + \dot{\gamma}\eta$, is used to update the local shear rate $\dot{\gamma}(y)$ at each point in the cell. Force balance dictates that the total shear stress is uniform across y: $\bar{\Sigma} = \Sigma_j$, allowing the local shear rate to be updated at each spatial point j via:

$$\dot{\gamma}_j = \bar{\dot{\gamma}} + \frac{G}{\eta}\underline{p}\cdot\left(\bar{\underline{s}} - \underline{s}_j\right). \tag{3.6.11}$$

Note that the size of the time and space steps must obey:

$$\sqrt{2D\,dt} < dy \ll l \ll L, \tag{3.6.12}$$

where $l = \sqrt{D\tau_0}$ (τ_0 the microscopic relaxation time of the system) defines a length-scale for the width of the interface between shear bands. The first inequality is required for stability of the Crank Nicolson algorithm [130]; the second ensures the interface between the bands is resolved properly by the numerical grid; and the third ensures the interface is narrow compared with the width of the cell. Guided by Eqn 3.6.12, we must also ensure time and space step convergence of solutions $\underline{s}(y,t)$. To do this, we first converge with respect to the time step size dt at a fixed dy, using

the method described in Section 3.6.1. We then halve the space step size $dy/2$, re-converge with respect to time-step size at this new space step, and compare the solution with that of the time-step converged solution at the previous space step dy. If the solutions are not converged, we repeat this process until sufficiently small time and space step sizes are found that provide convergent solutions $\underline{s}(y,t)$. Note that all results presented in this thesis have been checked to ensure time and space step convergence.

3.6.3 Numerical methods for the SGR model

Except for the SGR model, all models studied in this thesis involve integrating a differential constitutive equation for the tensorial stress $\underline{\underline{\sigma}}$ — methods for which we provided above in Sections 3.6.1 and 3.6.2. We now outline the numerical methods used to obtain the strain rate response to an imposed stress in the SGR model that was used to produce the results presented in Chapter 4.

In the SGR model, elements 'hop' out of their traps[22] of energy depth E with a rate dependent on the trap depth and also on the local element strain. A conventional Monte Carlo method is not suited this process in the SGR model due to the extremely slow dynamics and long simulation times required: the acceptance of a trial 'hop' has a very small probability, resulting in a high number of rejections before a trial 'hop' is accepted. Rather, following Refs. [54,57], we use a waiting time Monte Carlo (WTMC) method [15]. This is a 'rejectionless' Monte Carlo method as it *a priori* assumes an element hops, but chooses which element to hop based on the distribution of element hopping rates, and the time at which this hop occurs based on the total hopping rate. That is, the WTCM is an event based algorithm.

Specifically, we model N SGR elements $i = 1, ..., N$ with trap depths E_i and strains l_i, resulting in the element hopping rate $r_i = \exp\left[-(E_i - \frac{1}{2}l_i^2)/x\right]$. The sum of all hopping rates is $R = \sum_i^N r_i$, and the macroscopic strain rate is $\dot{\gamma} = \frac{1}{N}\sum_i^N r_i l_i$ [53, 54].

After a hopping event (or initialisation at $t = 0$) the time at which the next hop

[22]Note that here, in our terminology, a 'hop' out of a trap is equivalent to the 'yielding' events described previously.

occurs $t + \delta t$ is chosen from a distribution $P(\delta t) \propto \exp(-\delta t\, R)$ dependent on the sum of all hopping rates. Having calculated the time of the next hopping event, we then need to select which of the N elements will hop. We do so by noting that the probability that any given element will be the one to hop is given by $P_i^{hop} = r_i/R$, therefore the element that hops at $t + \delta t$ is chosen by a search of all the elements weighted by this probability. To perform the 'hop', the element strain is set to zero $l_{\text{hopper}} = 0$ and a new trap energy E_{hopper} is chosen for the element from the distribution $\rho(E) = e^{-E}$. In the SGR model the total stress is given by the macroscopic strain minus the strain relaxed through hopping events (multiplied by the elastic modulus) [54, 62]. Therefore, in order to maintain a constant total stress in the step stress protocol, the macroscopic strain must be increased after each hopping event: $\gamma(t + \delta t) = \gamma(t) + l_{\text{hopper}}(t)/N$. Since $\dot{l} = \dot{\gamma}$, all local element strains l_i must also be updated by the same amount.

We note that all results presented in this thesis have been checked for convergence with respect to the number of elements N; a typical value required is $N = 10^5$ or 10^6.

4

Step stress protocol

4.1 Introduction

In this chapter we will investigate the rheological response to an imposed shear stress of three classes of material: soft glassy materials and entangled polymeric materials above and below the glass transition. In this experimental protocol a constant shear stress Σ is imposed on the sample for time $t > 0$ and the shear rate $\dot{\gamma}(t)$ varies in time, see Section 2.1.1. We will first derive a criterion for the onset of linear instability to shear rate heterogeneity that is independent of fluid or model type. This depends only on time derivatives of the homogeneous background state: we find growth of shear rate perturbations whenever[1] $\frac{\partial^2 \dot{\gamma}}{\partial t^2} / \frac{\partial \dot{\gamma}}{\partial t} > 0$ (where $\dot{\gamma}$ is the shear rate from the homogeneous background state). We will show that this criterion correctly predicts the growth of heterogeneous perturbations during an investigation of the rheological

[1]Note that from here on we describe this criterion by using the notation $\partial_t^2 \dot{\gamma} / \partial_t \dot{\gamma} > 0$.

response to an imposed stress in four models for various classes of material:

Polymeric fluids: We will show that the rolie-poly (RP) and Giesekus models show qualitatively similar responses of the shear rate $\dot{\gamma}(t)$ to a step stress: for imposed stresses with values nearest those on the weakest slope (smallest $\partial_{\dot{\gamma}}\Sigma$) of the constitutive curve the shear rate rises suddenly by several orders of magnitude over a short time period. We find that, consistent with the general criterion, transient shear banding occurs during the upwards curving, upwards sloping region of this rise: i.e., where $\partial_t^2\dot{\gamma}/\partial_t\dot{\gamma} > 0$ in the homogeneous background state.

Soft glassy materials: As explained in Chapter 2, soft glassy materials (SGMs) usually show an initial 'creep' regime in which the shear rate progressively decreases in time in response to an imposed stress. For stresses that exceed the yield stress $\Sigma > \Sigma_y$, this creep regime is usually followed by a sudden 'fluidisation' where the shear rate dramatically rises (in a similar fashion to that of the polymer systems described above) before reaching a steadily flowing state. Various features of the $\dot{\gamma}(t)$ curve have been used to define the time at which the system 'transitions' between this solid-like (creep) and liquid-like (steady flow) behaviour (often referred to as the 'fluidisation time'), such as the minimum of the shear rate in time [11,28] or the inflection point where $d\dot{\gamma}/dt$ is maximal [42,64,156]. The general criterion derived in Section 4.2 predicts linear instability to shear rate heterogeneity for times between these two points, which we later refer to as the 'dip' and 'fluidisation' times, $\tau_{\rm dip}$ and $\tau_{\rm f}$, respectively. Recent experiments [42] and simulations of the SGR model [117] have confirmed that shear banding does arise between these two times. These results have motivated us to determine the relation of the fluidisation and dip times $\tau_{\rm f}$, $\tau_{\rm dip}$ to the imposed shear stress Σ in the SGR model, along with a relation for the shear rate in time during creep. We will focus on two regimes of the effective noise temperature: $x < 1$ (below the glass point) and $1 < x < 2$ (above the glass point). The author is grateful to Dr. Thibaut Divoux for motivating this research, and to Prof. Peter Sollich for collaboration and yield stress data of the SGR model.

Glassy polymers: Finally, we will investigate the rheological response to an imposed stress in the glassy polymer (GP) model in order to compare results in the shear geometry with recent results in the extensional geometry [58]. These exten-

sional results show that the segmental relaxation time $\tau(t)$ (which governs the rate of rearrangement of local segments of the polymer chain) initially decreases as the system begins to fluidise in response to the imposed stress, before reaching a minimum and rising indefinitely. The authors found that this 'dip' in the segmental relaxation time is concurrent with the onset of strain hardening; we will show that these basic features are also found in the shear geometry. We will also explore how shear banding arises during creep, and use the general criterion described above to explain how strain hardening reduces the magnitude of transient shear banding for increasing polymer contribution to the stress. The author is grateful to Prof. Mike Cates and Prof. Ron Larson for collaboration during research on this model.

This chapter is ordered as follows. In Section 4.2 we derive a general criterion for the onset of shear banding during the time-dependent response to a step stress. The rheological response of the RP and Giesekus models are investigated in Sections 4.3 and 4.4, respectively. We explore the 'creep' and 'fluidisation' behaviour of the SGR model in Section 4.5. Finally, we show the rheological response of the GP model to an imposed shear stress in an analogy to recent extensional load experiments and numerics in Section 4.6. The results of Sections 4.2 and 4.3 are published in Ref. [117], and those of Section 4.6 published in Ref. [59].

4.2 Criterion for instability in step stress

We perform a linear stability analysis about a time-dependent homogeneous background state within a generalised framework, as outlined in Chapter 3, in order to determine a criterion for the onset of linear instability to shear rate heterogeneity for the step stress protocol. Credit for the derivation of this criterion is given to Dr. Suzanne Fielding.

Recall that within this framework the total shear stress Σ is decomposed into viscoelastic and Newtonian solvent contributions:

$$\Sigma = G\,\underline{p}\cdot\underline{s} + \eta\,\dot{\gamma}, \tag{4.2.1}$$

where

$$\underline{s} = (\sigma, \sigma_{xx}, \sigma_{yy}, ...)^T \tag{4.2.2}$$

is a vector containing all dynamical variables and $\underline{p} = (1, 0, 0, \ldots)$ is a projection vector for the viscoelastic shear conformation variable ($\sigma \equiv \sigma_{xy}$). We note that in the step stress protocol the shear rate $\dot{\gamma}(t)$ is also a dynamical variable. However, using the above relation for the total shear stress we may replace all occurrences of the shear rate in the constitutive equation with:

$$\dot{\gamma}(t) = [\Sigma - G\underline{p} \cdot \underline{s}(t)]/\eta; \tag{4.2.3}$$

the constitutive equation then has form:

$$\partial_t \underline{s} = \underline{Q}(\underline{s}, \Sigma), \tag{4.2.4}$$

and is independent of the shear rate. Adding heterogeneous perturbations to the homogeneous background state of the form[2]

$$\underline{s}(t, y) = \hat{\underline{s}}(t) + \sum_k \underline{\delta s}_k(t)\epsilon_k, \tag{4.2.5}$$

and linearising about first order the size of the $\underline{\delta s}_k$ terms leads to:

$$\partial_t \, \underline{\delta s}_k = \underline{\underline{M}} \cdot \underline{\delta s}_k, \tag{4.2.6}$$

where $\underline{\underline{M}}(t) = \partial_{\hat{\underline{s}}} \underline{Q} \mid_{\hat{\underline{s}}}$. By differentiating the constitutive equation with respect to time we obtain:

$$\partial_t^2 \hat{\underline{s}} = \underline{\underline{M}} \cdot \partial_t \hat{\underline{s}} \, . \tag{4.2.7}$$

We therefore find that the time derivative of the homogeneous background state $\partial_t \, \hat{\underline{s}}$ (Eqn 4.2.7) obeys the same dynamical equation as that of the perturbations $\underline{\delta s}_k$ (Eqn 4.2.6). Although $\underline{\delta s}_k$ and $\partial_t \, \hat{\underline{s}}$ are not guaranteed to evolve co-linearly (owing

[2]Where $\epsilon_k = \cos(k\pi y/L)$ and the homogeneous background state is represented with hats, e.g., $\hat{\underline{s}}$. After the end of this section we will drop the hats for ease of reading, and set $G = 1$ so that σ can be thought of as the viscoelastic shear stress.

to their different initial values), we find that for all models studied in this thesis they always do become co-linear after some short time[3], so that any perturbation $\underline{\delta s}_k$ grows whenever its counterpart in $\underline{\hat{s}}$ obeys $\partial_t^2 \underline{\hat{s}} / \partial_t \underline{\hat{s}} > 0$. Incorporating force balance $\delta\dot{\gamma}_k = -\frac{G}{\eta} \underline{p} \cdot \underline{\delta s}_k$ into the above result, we find a criterion for the growth of shear rate perturbations:

$$\frac{\partial_t^2 \hat{\dot{\gamma}}}{\partial_t \hat{\dot{\gamma}}} > 0. \tag{4.2.8}$$

This means that any system is linearly unstable to heterogeneous shear rate perturbations whenever the shear rate of the underlying homogeneous background state $\hat{\dot{\gamma}}(t)$ is simultaneously upwards curving and upwards sloping in time. Clearly though, this theoretical shear rate of the homogeneous background state $\hat{\dot{\gamma}}(t)$ is distinct from the global (spatially averaged) shear rate measured experimentally $\overline{\dot{\gamma}}(t)$. However, in all models considered in this thesis the discrepancy between $\hat{\dot{\gamma}}(t)$ of the background state and $\overline{\dot{\gamma}}(t)$ of the full nonlinear system is small. Therefore, the criterion can be applied to the shear rate $\overline{\dot{\gamma}}(t)$ as measured experimentally to correctly predict the onset of shear banding and the subsequent return to homogeneity. Advantageously, the necessary derivatives of the shear rate are then readily obtained from any shear creep experiment, allowing the analysis of existing experimental literature that may not have accompanying velocimetric data to determine whether the sample suffered shear banding or not.

4.3 Rolie-poly model

The response of the shear rate $\dot{\gamma}(t)$ to an imposed shear stress Σ in the (homogeneously constrained) RP model is shown in Figure 4.3.1. The shear rate initially decays on a short timescale[4] that is suggested by numerical results to scale with

[3] This short time is much smaller than the timescale $\eta/G\tau_d$.

[4] The large initial shear rate $\dot{\gamma}(t = 0^+) = \Sigma/\eta$ is due to the initial viscoelastic shear stress $\sigma(t = 0^+) = 0$ (recall that the total shear stress is decomposed into viscoelastic and solvent contributions: $\Sigma = G\sigma + \eta\dot{\gamma}$, and $G = 1$). Initially, σ increases rapidly on a short timescale (suggested by numerics to scale with $\sqrt{\eta\,\tau_d/G}$) so that it takes the bulk of the imposed total stress: at such a time $\dot{\gamma}(t)$ is at a minimum. We do not expect this initial decay of the shear rate to be resolved in experiment, since the early time measurements of experiment are usually discarded due to 'creep ringing' arising from the coupling of the inertia of the rheometer and the viscoelasticity of the sample.

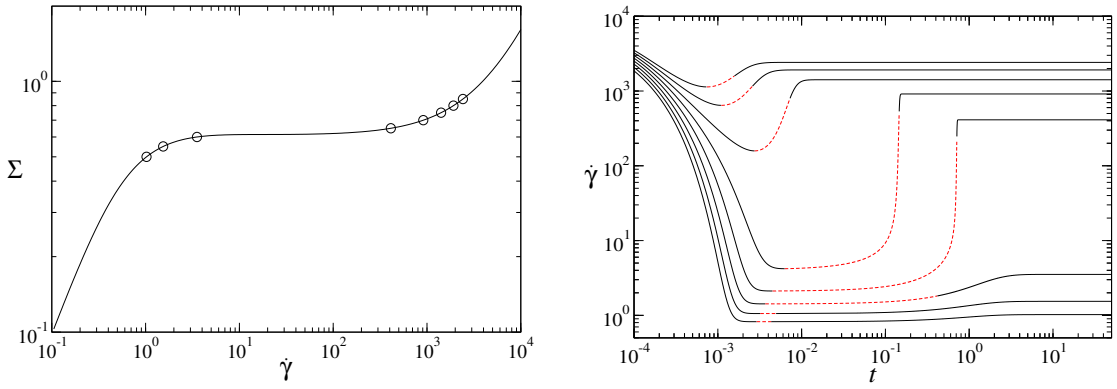

(a) (b)

Figure 4.3.1: (a) Steady state constitutive curve (these parameters result in a monotonic curve) with symbols corresponding to steady states in (b). (b) Shear rate as a function of time for imposed shear stresses $\Sigma = 0.5, 0.55, ..., 0.85$ (bottom to top) in the (homogeneously constrained) RP model; dashed where $\partial_t^2\dot\gamma/\partial_t\dot\gamma > 0$. Parameters: $\beta = 0.8$, $\eta = 10^{-4}$, $\tau_R = 0.0$.

$\sqrt{\eta\,\tau_d/G}$. Following this, the shear rate increases via an upwards curving, upwards sloping region with $\partial_t^2\dot\gamma/\partial_t\dot\gamma > 0$ (dashed in the figure), leading to linear instability to shear rate heterogeneity according to the general criterion derived in the previous section. For values of the imposed stress nearest those on the weakest slope of the constitutive curve [i.e., Σ for which $\partial_{\dot\gamma}\Sigma$ is smallest, see Figure 4.3.1 (a)] the shear rate rise is dramatic: increasing by several orders of magnitude over a short time. These results are consistent with experimental findings of polymeric materials [16, 18, 75, 76, 136, 161], and are also qualitatively similar to those found in the Giesekus model, discussed in the next section.

The results of Figure 4.3.1 are performed for a system artificially constrained to be homogeneous. Accordingly, we expect to see shear rate heterogeneity once the constraint of homogeneity is removed, onset at times for which $\partial_t^2\dot\gamma/\partial_t\dot\gamma > 0$. We allow heterogeneity in the flow-gradient direction (see Chapter 3 for details) and show (for a single value of Σ) in Figure 4.3.2 (a) the resulting global shear rate[5] $\overline{\dot\gamma}(t)$; snapshots of the velocity profile in (b) and the degree $[\Delta_{\dot\gamma}(t) = \dot\gamma_{max} - \dot\gamma_{min}]$ to which shear banding arises in (c) in response to an imposed stress ($\Sigma = 0.7$, on the

[5]In this chapter we will use $\overline{\dot\gamma}$ to denote the global (average) shear rate, and $\dot\gamma_{max,min}$ to denote the maximum/minimum local shear rate, whenever heterogeneity is allowed in the flow-gradient direction. On the other hand, where $\dot\gamma$ appears unembellished it represents the shear rate of a system with homogeneity enforced.

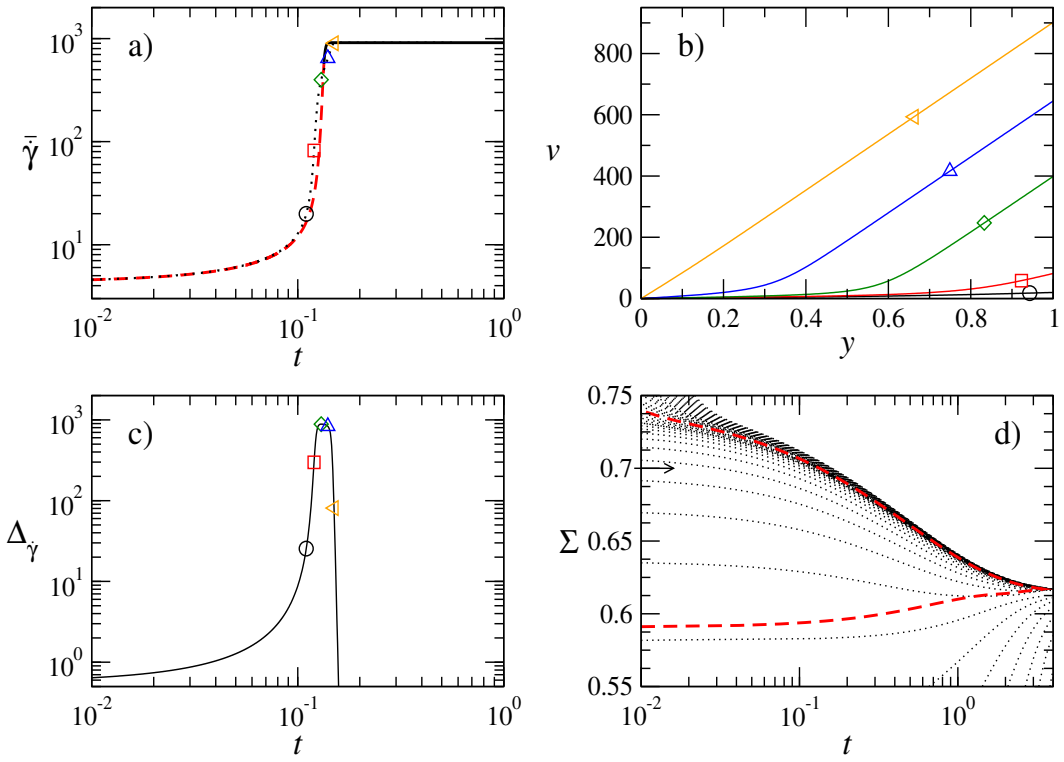

Figure 4.3.2: Step stress in the RP model: (a) global shear rate $\bar{\dot{\gamma}}$ in a homogeneously constrained system in a thick solid or dashed line, dashed where $\partial_t^2\dot{\gamma}/\partial_t\dot{\gamma} > 0$. Heterogeneity allowed: dotted line. (b) Snapshots of the velocity profile at times with corresponding symbols in (a) and (c). (c) Degree of banding: $\Delta_{\dot{\gamma}} = \dot{\gamma}_{max} - \dot{\gamma}_{min}$. d) Stability portrait (homogeneously constrained system): a horizontal slice corresponds to a single creep run with imposed stress Σ; contour of $\partial_t^2\dot{\gamma}/\partial_t\dot{\gamma} = 0$ in a thick, dashed line (inside of envelope indicates linearly unstable regime); dotted lines are contours of equal $\delta\dot{\gamma}_{k=1}(t) = \delta\dot{\gamma}_{k=1}(0)2^M$ for integer M from integrating Eqn 4.2.6 (we show only contours $M > -50$). Parameters: $\beta = 0.8$, $\eta = 10^{-4}$, $\Sigma = 0.7$, $\tau_R = 0.0$, $q = 0.1$.

weakest slope of the constitutive curve). As expected from the general criterion, and as shown in (a, b, c) of Figure 4.3.2, we find the growth of shear rate heterogeneity onset at $\partial_t^2\,\bar{\dot{\gamma}}/\partial_t\,\bar{\dot{\gamma}} > 0$. Accordingly, as long as the linearisation in the stability analysis is a good approximation, the degree of shear banding increases co-linearly with $\partial_t\dot{\gamma}$, becoming maximal at the inflection point $\partial_t^2\dot{\gamma} = 0$.

We now introduce the stability 'portrait' that we will use extensively in this thesis, which we show for the RP model in the step stress protocol in Figure 4.3.2 (d). In these portraits, a horizontal slice represents a single run with imposed stress Σ (or later, a single shear startup run at shear rate $\dot{\gamma}$), and we plot the times at which the various interesting features arise. Here, the thick, dashed line

corresponds to the 'envelope' of linear instability defined by $\partial_t^2\dot{\gamma}/\partial_t\dot{\gamma} = 0$. The arrow in (d) then indicates the single horizontal slice that represents the results presented in (a) for which $\Sigma = 0.7$. The time at which the system returns to linear stability $t \sim 0.15$ is then plotted on the portrait at $\{t, \Sigma\} = \{0.15, 0.7\}$. Inside this envelope the heterogeneous shear rate perturbations of the linearised system $\delta\dot{\gamma}_k$ (found by integrating Eqn 4.2.6) grow. The magnitude of this growth is indicated by the dotted lines: these are contour lines of equal $\delta\dot{\gamma}_k(t) = \delta\dot{\gamma}_k(0)2^M$ [integer M, and we consider the first ($k = 1$) mode only, see Chapter 3 for details]. Imposed stresses on the upper portion of the 'stability envelope' in (d) ($0.61 \lesssim \Sigma \lesssim 0.75$ for these parameters) correspond to those on the weakest slope of the constitutive curve, leading to the dramatic rise of $\dot{\gamma}(t)$ and corresponding increase of $\delta\dot{\gamma}_k(t)$. This is reflected by the high concentration of contour lines parallel to the upper portion of the stability envelope.

These results are qualitatively similar to experimental findings in entangled polymeric systems, which report transient shear banding to arise during the sharp increase of $\overline{\dot{\gamma}}(t)$ [16,18,19,74–77,161], and in some cases a return to homogeneity is seen as the steady state is neared [19]. Difficulty in obtaining this latter result in experiment is due to the occurrence of edge fracture that severely limits the determination of the steady state shear rate and velocity profile [79, 136].

Continuous noise

The above results consider a system in which a heterogeneous perturbation is added initially at $t = 0$, which might represent the sample being left in a slightly heterogeneous state as an outcome of the protocol in which it is loaded into the rheometer. In reality, noise may also arise continuously during experiment, for example, in the form of mechanical noise arising due to imperfect rheometer feedback. While we anticipate the first of these having the larger effect, we nonetheless consider the second briefly now. To do so, we investigated noise that is added continuously in time using methods described in Chapter 3. As shown in Figure 4.3.3, for the system with heterogeneity allowed in the flow gradient direction, we find qualitatively similar results to those with noise added initially only [compare with Figure 4.3.2 (c)]. We

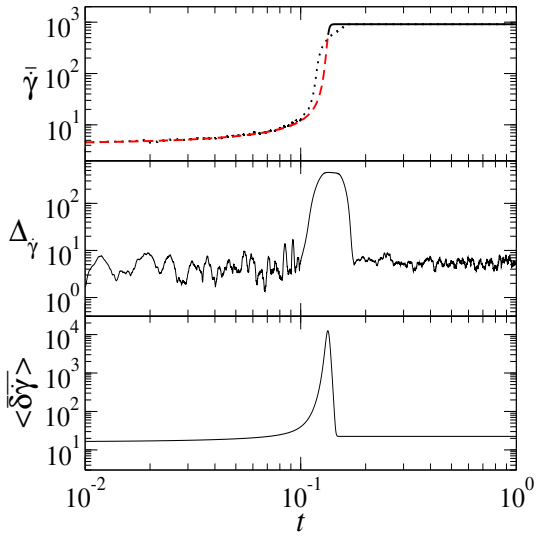

Figure 4.3.3: Step stress in the RP model with noise added continuously, parameters as in Figure 4.3.2. (a) global shear rate $\bar{\dot{\gamma}}$ (homogeneously constrained: thick solid or dashed where $\partial_t^2\dot{\gamma}/\partial_t\dot{\gamma} > 0$, heterogeneity allowed: dotted). (b) degree of shear banding: $\Delta_{\dot{\gamma}} = \dot{\gamma}_{max} - \dot{\gamma}_{min}$ from the nonlinear simulation with $q = 0.1$ (a running average over data captured at frequent points in t was used — we checked for qualitative convergence with respect to the capture frequency and running average range). (c) Heterogeneous shear rate perturbation $\langle\overline{\delta\dot{\gamma}}_k\rangle = \sqrt{\langle\delta\dot{\gamma}_k^2\rangle}$ of the linearised system found by integrating Eqn 3.5.1, see Chapter 3, $q = 10^{-5}$.

also investigated the dynamics of the heterogeneous perturbations of the linearised system: $\sqrt{\langle\delta\dot{\gamma}_k^2\rangle}(t)$ when noise is added continually (again, refer to Chapter 3 for details of these methods) and find qualitatively similar results to those with initial noise only.

Nonmonotonic constitutive curves

Note that throughout this chapter we will consider parameters of the RP (or later, Giesekus) model that lead to a monotonic constitutive curve[6]. However, we will briefly describe the response to an imposed stress for parameter values that result in a nonmonotonic constitutive curve (this description also applies to the Giesekus model).

Step stress experiments (with heterogeneity in the flow gradient allowed) that probe the underlying nonmonotonic region of the constitutive curve provide qualita-

[6]Recall that we define the 'constitutive curve' as the steady state $\Sigma(\dot{\gamma})$ curve obtained by imposing a constant $\dot{\gamma}$ (unless otherwise specified) with homogeneity enforced, and the 'flow curve' the same with heterogeneity allowed in the flow gradient direction.

tively similar results to those presented in Figure 4.3.2. For imposed stresses Σ for which the constitutive curve is multi-valued in $\dot{\gamma}$, the shear rate response follows that of the lowest branch of the constitutive curve as if there were no underlying non-monotonicity, recall Figure 3.2.3 of Chapter 3. As Σ is increased through its value at the maximum in the constitutive curve Σ_{max}, the corresponding steady state shear rate must then 'top-jump' to the high shear rate branch, leading to a discontinuity in the flow curve obtained via imposed stress[7]. This results in hysteresis in the flow curves obtained by imposing either a shear rate or stress: with imposed shear the flow curve does not follow the low shear rate branch of the constitutive curve up to $\Sigma = \Sigma_{max}$, but rather has a stress plateau at $\Sigma_p < \Sigma_{max}$. These results are in agreement with experiments on wormlike micelles that show qualitatively similar hysteresis between upward sweeps on the flow curve when performed under the imposed stress or imposed shear rate protocols [25, 90].

Note that we have never found steady state shear banding for any value of the imposed stress. This is in contrast to results of the JS model [132], where it was briefly noted that during an upward sweep on the flow curve using an *imposed stress*, the nucleation of a high shear rate band was possible for values of the shear stress within a small window $\Sigma_{\text{low}} < \Sigma < \Sigma_{\text{high}}$. (Here, the entire window is contained between Σ_p and Σ_{max}.) The upper and lower boundaries of this window are determined from the hysteresis between the up and down sweeps on the flow curve obtained under an *imposed shear rate* (see Ref. [132] for further details). Although we did not explore such sweeps on the flow curve, we do not find any such window where the flow curve (obtained from the steady state of a step stress experiment performed on a sample at rest) differs from the constitutive curve (obtained using the same protocol).

[7]Note that similar transient shear banding is seen during the upwards sloping, upwards curving portion of $\dot{\gamma}(t)$, as for the system with a monotonic constitutive curve described previously.

4.4 Giesekus model

As explained, the response of the shear rate to a step stress in the Giesekus model is qualitatively similar to that found in the RP model, as shown in Figure 4.4.1. However, in contrast to the RP model, the Giesekus model does not show 'significant' shear banding: at any instant in time the 'degree of banding' $[\Delta_{\dot\gamma}(t) = \dot\gamma_{max} - \dot\gamma_{min}]$ is never more than $\sim 5\%$ of the shear rate at the same instant in time and thus would be hard to detect in experiment[8], see (c) of Figure 4.4.1.

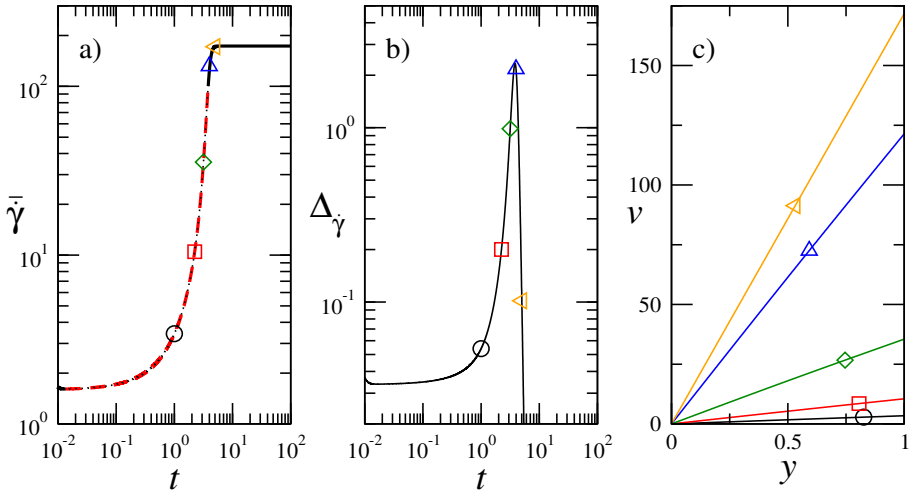

Figure 4.4.1: Step stress in the Giesekus model, (a) global shear rate $\bar{\dot\gamma}$ in a homogeneously constrained system: thick solid/dashed, dashed where $\partial_t^2\dot\gamma/\partial_t\dot\gamma > 0$. Heterogeneity allowed: dotted (indistinguishable from homogeneous). (b) Degree of banding: $\Delta_{\dot\gamma} = \dot\gamma_{max} - \dot\gamma_{min}$. (c) Snapshots of the velocity profile at times with corresponding symbols in (a) and (b). Parameters: $\alpha = 0.6$, $\eta = 10^{-3}$, $\Sigma = 1.0$, $q = 0.1$.

The reason for this is that the maximal slope of $\dot\gamma(t)$ in the Giesekus model is apparently always much smaller than that of the RP model — compare Figures 4.3.2 (a) and 4.4.1 (a). Because of this, and since $\Delta_{\dot\gamma}$ grows co-linearly with $\partial_t\dot\gamma$ (as long as the linearisation of the stability analysis holds), the resulting maximum degree of shear banding is much smaller in the Giesekus model. Clearly though, this comparison is difficult to make as the gradient of $\dot\gamma(t)$ is affected by the model parameters (and a matching of parameters is not possible). However, we attempted

[8]We note that, within the linear regime, the degree of banding $\Delta_{\dot\gamma}$ scales linearly with the magnitude of the initial noise q. Therefore, in order to make comparisons with the RP model the results presented in this (and the previous) section have $q = 0.1$. We note that q values much larger than this are unrealistic for comparison to experiment.

the comparison in Figure 4.4.1 by choosing the imposed stress to be at similar part of a comparable (also monotonic) constitutive curve. To confirm this conclusion of negligible transient shear banding in the Giesekus model, we also varied the parameters of the model and the imposed stress and never found any 'significant' shear banding; that is, a degree of banding larger than roughly 5% of the imposed shear rate.

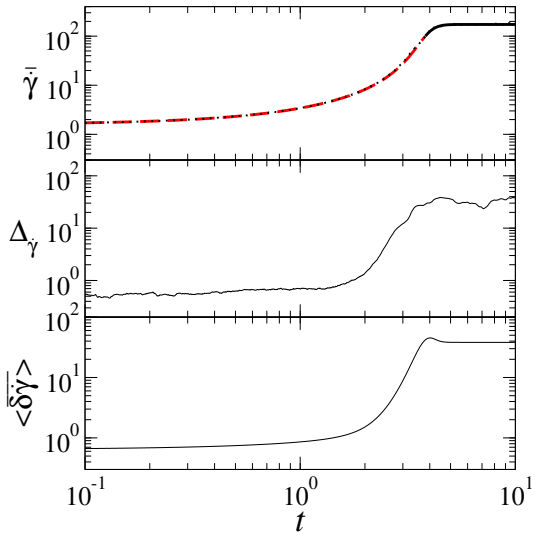

Figure 4.4.2: Step stress in the Giesekus model with parameters as in Figure 4.4.1. Top: global shear rate $\overline{\dot{\gamma}}$; homogeneously constrained: thick solid/dashed where $\partial_t^2\dot{\gamma}/\partial_t\dot{\gamma} > 0$, heterogeneity allowed: dotted (indistinguishable from homogeneous). Middle: degree of shear banding: $\Delta_{\dot{\gamma}} = \dot{\gamma}_{max} - \dot{\gamma}_{min}$ from the nonlinear simulation with $q = 0.1$ (a running average over data captured at frequent points in t was used — we checked for qualitative convergence with respect to the capture frequency and running average range). (c) Shear rate perturbation $\langle\overline{\delta\dot{\gamma}_k}\rangle = \sqrt{\langle\delta\dot{\gamma}_k^2\rangle}$ in linearised system found by integrating Eqn 3.5.1, see Chapter 3, $q = 10^{-5}$.

Continuous noise

For further comparison to the RP model, we show the analogous response with noise added continuously in the Giesekus model in Figure 4.4.2. In the RP model we showed that the degree of shear banding behaved similarly with either continuously added or initial noise. This is not so in the Giesekus model: with heterogeneous perturbations added continually the degree of shear banding does not return to some small value [e.g., does not become comparable to the magnitude of fluctuations at

(zero shear[9]) equilibrium] as the system approaches steady state, as shown in Figure 4.4.2. This difference may be due to stress relaxation being driven by the shear rate in the RP model, while in the Giesekus model stress relaxation depends on the shear rate only through the stress. In general, in the Giesekus model we find that the magnitude of fluctuations $\langle \delta\dot{\gamma}_k^2 \rangle$ in steady state shear is much larger than those at a steady state under zero shear conditions, i.e., $\langle \delta\dot{\gamma}_k^2 \rangle(\dot{\gamma}, t \to \infty) \gg \langle \delta\dot{\gamma}_k^2 \rangle(0, t \to \infty)$. In contrast, in the RP model the magnitude of fluctuations in steady state shear is comparable to those under zero shear equilibrium, see Figure 4.3.3.

[9]Recall from Chapter 3 that, when considering systems with continually added noise, we evolve the system to a statistically steady state under zero shear conditions before imposing deformation.

4.5 Soft glassy rheology model

In Section 4.2 we showed that at times for which the shear rate of the homogeneous background state obeys $\partial_t^2\dot{\gamma}/\partial_t\dot{\gamma} > 0$, the system is linearly unstable to shear rate heterogeneity. We subsequently demonstrated the resulting transient shear banding in the RP and Giesekus models. However, we will not investigate the development of transient shear bands in the SGR model (with heterogeneity allowed in the flow gradient direction), as it has already been shown that they do indeed arise during the upwards curving, upwards sloping region of the shear rate. See Figure 4.5.1, reproduced from Ref. [117] — credit is given to Dr. Suzanne Fielding for these results. [We note that these results are in direct agreement with experiments of soft glassy materials that show transient shear banding does arise during the upwards curving, upwards sloping ($\partial_t^2\dot{\gamma}/\partial_t\dot{\gamma} > 0$) region of the $\dot{\gamma}(t)$ curve [42, 64].] Rather, we will investigate in more detail than in Figure 4.5.1 the 'creep': the progressive decrease of the shear rate in time, and subsequent 'fluidisation': the sudden increase of $\dot{\gamma}(t)$ leading to steady flow in the SGR model in response to imposed stresses exceeding the yield stress. (The 'creep' and 'fluidisation' behaviours referred to here can be clearly seen for the top curve in Figure 4.5.1 for times $t < 10^3$ and at a time $t \sim 2 \times 10^3$, respectively.)

We have been motivated to perform this research as the response of materials during creep and subsequent fluidisation has recently become the focus of considerable experimental investigation [11, 28, 42, 64, 66, 150, 152, 156]; however, little is understood theoretically about these processes. Our criterion (Eqn 4.2.8) also shows that the onset of linear instability to shear banding during creep occurs at the beginning of the fluidisation process. Therefore, our aim in this section is to determine a relation for the shear rate as a function of time during creep, and a relation for the time at which fluidisation occurs as a function of the imposed stress. As a result, we will provide relations for the time during which the SGR model is linearly unstable to shear banding during creep, depending on the imposed stress and the 'noise temperature' x of the model.

Before describing our results, we shall briefly outline what is already understood about the response of the SGR model (with homogeneity enforced) with respect

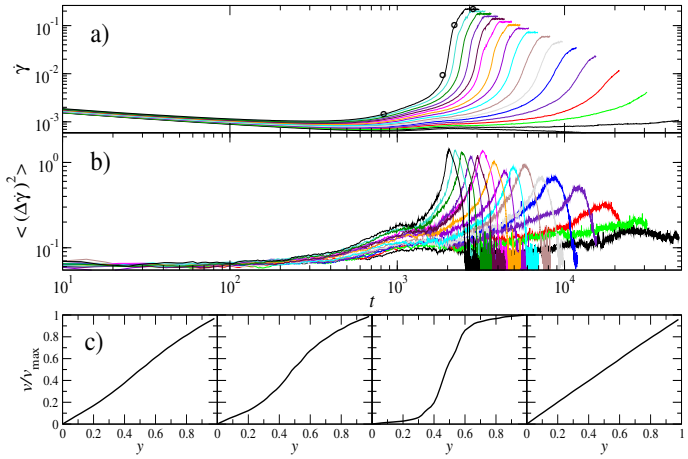

Figure 4.5.1: (a) Shear rate response in the SGR model with heterogeneity allowed in the flow gradient direction to imposed stresses $\Sigma/\Sigma_y = 1.005, 1.010, \ldots, 1.080$ (bottom to top on the right). (b) Corresponding degree of shear banding. (c) Normalised velocity profiles at times with corresponding symbols in (a). Here, $x = 0.3$, $t_w = 10^3\,[1 + q\cos(2\pi y)]$, $q = 0.1$. Figure reprinted with permission from Ref. [117], copyright 2013 American Physical Society; credit is given to Dr. Suzanne Fielding for these results. (Parameters associated with heterogeneity: $w = 0.05$, $n = 50$, $m = 10^4$, see Supp. Mat. of Ref. [117] for details.)

to the creep and fluidisation behaviour described above. Note that from here on we shall only consider the SGR model with homogeneity enforced as this allows for greater numerical efficiency, and we do not find a significant difference in the bulk rheological signatures with heterogeneity allowed/disallowed. We also remind the reader that for models that show age dependence (i.e., the scalar fluidity, SGR and GP models) we define t to be the time elapsed since sample preparation and $\Delta t = t - t_w$ the time elapsed since a constant stress Σ was imposed, where t_w is the 'waiting time' or the 'age' of the sample. Recall Chapter 3.

4.5.1 Outline of SGR model according to Ref. [62]

Fielding *et al.* [62] investigated both the linear and nonlinear responses of the homogeneously constrained SGR model to an imposed stress Σ. In this context we use 'linear' to mean that the strain response $\gamma(t)$ to a step stress remains linear in the value of the imposed stress Σ; when this is no longer valid the response is termed 'nonlinear'. (Hence, 'linear' and 'nonlinear' in this section are distinct from 'linear' and 'nonlinear' referred to elsewhere that pertain to whether heterogeneous

perturbations $\delta\dot{\gamma}_k$ are small.)

Linear response

Focussing first on the linear creep response (which in general can be obtained in the very small stress limit $\Sigma \to 0$), the authors found power law relations for the shear rate in time in both the 'short' and 'long' time regimes, i.e., for $\Delta t \ll t_w$ and $\Delta t \gg t_w$, respectively. We summarise these linear creep power laws in Table 4.1.

time range	$x < 1$	$1 < x < 2$
$\Delta t \ll t_w$	—	$\dot{\gamma}(\Delta t) = B_{\text{short}} \Delta t^{\,x-2}$
$\Delta t \gg t_w$	$\dot{\gamma}(\Delta t) = C \Delta t^{-1}$	$\dot{\gamma}(\Delta t) = B_{\text{long}} \Delta t^{\,x-2}$

Table 4.1: Summary of creep relations of the SGR model in the *linear regime* as found by Fielding *et al.* [62]. B and C are prefactors that depend weakly on x. The top-left entry is explained in the text.

(Recall that the SGR model shows Newtonian behaviour for values of the noise temperature $x > 2$. Because we are interested in the non-Newtonian behaviour we shall investigate only values of $x < 2$.) The model also shows a glass transition at $x = 1$; due to this we will always distinguish between behaviour for $x < 1$ (called the 'glass phase') and $1 < x < 2$ (above the glass point).

Note the missing entry for the glass phase ($x < 1$) in the short time regime $\Delta t \ll t_w$. In fact, the authors found that in this regime the linear creep response obeys:

$$\dot{\gamma}(\Delta t) = A t_w^{-1} \left(\frac{\Delta t}{t_w} \right)^{-x} \tag{4.5.1}$$

at early times until const $\times \left(\frac{\Delta t}{t_w}\right)^{1-x}$ becomes comparable to 1, see Ref. [62]. At $x = 1$, the authors found a cross-over into logarithmic-like behaviour.

Nonlinear response

Above the glass point ($1 < x < 2$) and for imposed stresses outside the small stress limit (above), the authors showed that the linear creep power law relations shown in the right-hand column of Table 4.1 are valid up to times $\Delta t \sim \Sigma^{1/(1-x)}$, after which

the response became nonlinear. We will show later that the 'fluidisation time' $\tau_{\rm f}$ (defined as the inflection point $\partial_t^2\dot{\gamma} = 0$ in the shear rate response) is proportional to this transition time at which nonlinear behaviour arises.

In the glass phase ($x < 1$) the response was found to be linear to arbitrarily long times, for imposed stresses much smaller than the yield stress $\Sigma \ll \Sigma_y$. [Recall that in the glass phase the system has a yield stress $\Sigma_y(x)$, see Figure 3.2.6 of Chapter 3.] However, for imposed stress values approaching the yield stress $\Sigma \lesssim \Sigma_y$ this ceases to be true. Furthermore, the authors were unable to determine a creep power law relation for the response above the yield stress $\Sigma > \Sigma_y$. This will be the subject of our investigation in Section 4.5.2.

Our research in this section concerns the nonlinear response of the SGR model in the *glass phase* ($x < 1$) for imposed stresses just above the yield stress, and has two aims. First, we aim to determine a creep power law relation for the response of the shear rate $\dot{\gamma}(\Delta t)$ to stresses *exceeding* the yield stress $\Sigma > \Sigma_y$, for which Fielding *et al.* did not determine a relation. Secondly, we aim to determine a relation for the 'fluidisation time', defined as the time at which an inflection occurs $\partial_t^2\dot{\gamma} = 0$ in the shear rate response, as a function of the imposed stress $\Sigma > \Sigma_y$. Similarly, no such prediction for the time at which the system fluidises was made by Fielding *et al.*

During this investigation we will also *confirm* the results of Fielding *et al.* [62] for the creep power law, and their prediction of the time at which the system fluidises, for the system *above the glass point* ($1 < x < 2$). This relation can be used to predict the onset of transient shear banding according to the general criterion derived in Section 4.2: $\partial_t^2\dot{\gamma}/\partial_t\dot{\gamma} > 0$.

We now define the 'fluidisation' time $\tau_{\rm f}$ referred to above, and also the 'dip' $\tau_{\rm dip}$ time, for use later on.

The 'fluidisation' time $\tau_{\rm f}$ and 'dip' time $\tau_{\rm dip}$

We show typical responses of the shear rate to an imposed stress just above the yield stress in the SGR model in Figures 4.5.2 (a) and (b). We identify the fluidisation and dip times, $\tau_{\rm f}$ and $\tau_{\rm dip}$, defined as the time of the minimum $\partial_t\dot{\gamma} = 0$ and the time

of the inflection point $\partial_t^2 \dot{\gamma} = 0$ in the shear rate $\dot{\gamma}(\Delta t)$, respectively. These times are relevant as they describe the time during which the system is linearly unstable to shear rate heterogeneity: $\tau_{\rm dip} < \Delta t < \tau_{\rm f}$, according to the general criterion (Eqn 4.2.8) derived in Section 4.2.

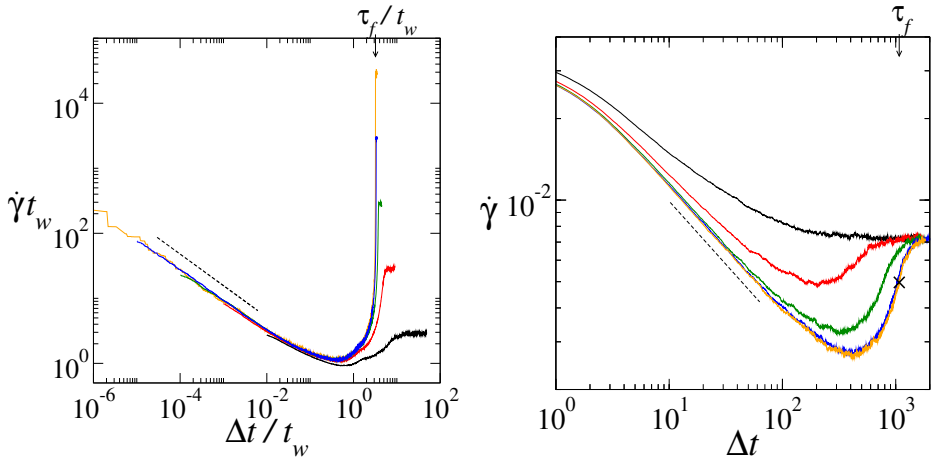

(a) $x = 0.5$ (b) $x = 1.5$

Figure 4.5.2: Shear rate responses of SGR model to a step stress. (a) in the glass phase: $x = 0.5$ and $\dot{\gamma}$, Δt scaled by t_w. Waiting times: $t_w = 10^{2,3,4,5,6}$ (bottom to top on the right) and $\Sigma - \Sigma_y = 0.05$. (b) above the glass point: $x = 1.5$, $t_w = 10^{2,3,4,5,6}$ (top to bottom), and $\Sigma = 0.1$; inflection point marked by '$\times$' on $t_w = 10^6$ curve. A dashed line shows the power law creep regime.

So far, we have outlined the SGR model as studied by Fielding *et al.* [62], pinpointed results missing from their work, which we now aim to address, and described the generic behaviour of the shear rate in the SGR model. We now present our results, focussing first on creep behaviour in Section 4.5.2, before describing fluidisation in Section 4.5.3.

4.5.2 Power law creep

In the glass phase: $x < 1$

For imposed stresses above the yield stress $\Sigma > \Sigma_y(x)$, the authors of [62] were unable to determine analytical forms for the shear rate response during the creep regime. Using numerical results of the SGR model, an example of which is shown

in Figure 4.5.2 (a), we determined a power law for this creep regime:

$$\dot{\gamma}(\Delta t) = \hat{A} t_w^{-1} \left(\frac{\Delta t}{t_w} \right)^{\mu}, \text{ for } \Delta t \ll \min\{t_w, \tau_{\text{dip}}\}, \tag{4.5.2}$$

where μ is the power law exponent that we find depends on the 'noise temperature' of the SGR model via:

$$\mu = -x, \qquad (\text{for } x < 1) \tag{4.5.3}$$

and $\hat{A}$ is a fitting parameter that depends weakly on x. We reiterate that Eqn 4.5.2 describes the shear rate behaviour during the creep regime in which the shear rate decreases in time, before the onset of fluidisation. An example of such a creep regime is shown in Figure 4.5.2 (a) — a dashed line indicates the creep power law. In Figure 4.5.3 we demonstrate the dependence of the power law exponent μ on the noise temperature x, where we plot μ as a function of x for two values of the waiting time $t_w = 10^5, 10^7$. The dashed line shows the result of Eqn 4.5.3. As shown in the figure, increasingly large waiting times t_w are needed for convergence of the exponent $\mu \to -x$ as the glass transition is approached: $x \to 1$.

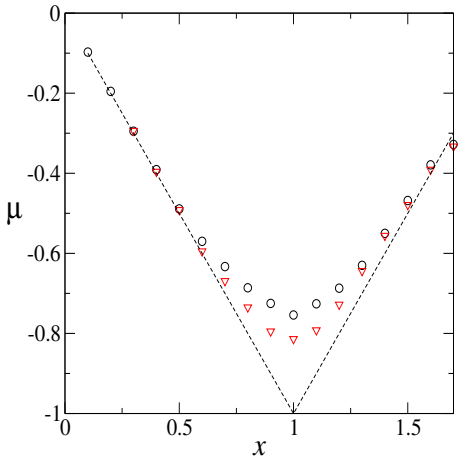

Figure 4.5.3: Creep power law exponent μ as a function of x in the SGR model, for $\Sigma - \Sigma_y = 0.05$, $t_w = 10^{5,7}$ in circles, triangles, respectively. The exponent μ is obtained by fitting $\dot{\gamma} = \hat{A} t_w^{-1} (\frac{\Delta t}{t_w})^{\mu}$ for $x \leq 1$, or $\dot{\gamma} = B \Delta t^{\mu}$ for $1 < x < 2$, over the time range $\tau_0 \ll \Delta t \ll \min\{t_w, \tau_{\text{dip}}\}$. Dashed lines show $\mu = -x$ for $x < 1$ (Eqn 4.5.3), and $\mu = x - 2$ for $1 < x < 2$ (Eqn 4.5.4).

We note that the $\Delta t \ll t_w$ condition in Eqn 4.5.2 exists because a transition to a second power law regime with an apparently different exponent was observed for

times $\Delta t \gg t_w$. This regime is difficult to access numerically, and we were unable to confirm the long time power law exponent. The $\Delta t \ll \tau_{\text{dip}}$ condition of Eqn 4.5.2 is required because the onset of fluidisation that occurs as $\Delta t \to \tau_{\text{dip}}$ signals the end of the creep regime as shown in Figure 4.5.2 (a). Note that what determines which of t_w or τ_{dip} is smallest is the magnitude of the imposed stress compared to the yield stress $\Sigma - \Sigma_y$. For larger stresses, departure (i.e., the onset of the fluidisation process) from the creep regime occurs at earlier times and we may have $\tau_{\text{dip}} < t_w$. For stresses closer to the yield stress departure from the creep regime occurs at later times and we may have $\tau_{\text{dip}} > t_w$.

Above the glass point: $1 < x < 2$

In Figure 4.5.3 we also confirm the exponent of the nonlinear creep power law *above the glass point* $(1 < x < 2)$ reported by Fielding *et al.* [62] to be:

$$\mu = x - 2, \tag{4.5.4}$$

where the creep power law obeys $\dot{\gamma} \sim B\Delta t^{\mu}$ (recall Table 4.1). Note, we again find that increasingly large waiting times t_w are required for convergence of the exponent $\mu \to x - 2$ as the glass transition is approached $x \to 1$. (This is consistent with Fielding and co-workers' finding of a cross-over to logarithmic-like behaviour at $x = 1$.)

We summarise the creep power laws for imposed stresses $\Sigma > \Sigma_y$ in Table 4.2.

	$x < 1$	$1 < x < 2$
$\Delta t \ll t_w$	$\dot{\gamma}(\Delta t) = \hat{A} t_w^{-1} \left(\frac{\Delta t}{t_w}\right)^{-x}$	$\dot{\gamma}(\Delta t) = B_{\text{short}} \Delta t^{\,x-2}$
$\Delta t \gg t_w$	—	$\dot{\gamma}(\Delta t) = B_{\text{long}} \Delta t^{\,x-2}$

Table 4.2: Creep power law relations of the SGR model for $\Sigma > \Sigma_y$ determined from numerical results for $x < 1$ or from Ref. [62] for $1 < x < 2$. $\hat{A}$ and $B_{\text{short,long}}$ are fitting parameters of $O(1)$ and are dependent on x. Note: power laws valid for $\tau_0 \ll \Delta t \ll \tau_{\text{dip}}$ (in addition to time constraints in the table, which ever is met first).

4.5.3 Fluidisation and dip times

So far we have investigated the *creep* behaviour of the SGR model. As explained, for imposed stresses above the yield stress $\Sigma > \Sigma_y$ the creep regime ends in a *fluidisation* process during which the shear rate dramatically increases before finally reaching a steady state value. Recall that $\tau_{\rm dip}$ (the 'dip' time) is the time at which the shear rate undergoes a minimum $\partial_t \dot{\gamma} = 0$, and $\tau_{\rm f}$ (the 'fluidisation' time) is the time at which it has an inflection point $\partial_t^2 \dot{\gamma} = 0$.

In the glass phase: $x < 1$

Here, we use our numerical results to determine the fluidisation time $\tau_{\rm f}$ as a function of the imposed stress $\tau_{\rm f}(\Sigma)$. We find the fluidisation time to be a decreasing function of the imposed stress with two clear regimes: one for *small stresses*[10] close to the yield stress, and another for *large stresses* further away from the yield stress. The cross-over stress between these two regimes is Σ_c. For the sake of brevity, we refer a discussion on the value and origin of the cross-over stress Σ_c to Appendix I.

In the *small stress* regime ($\Sigma < \Sigma_c$), we find the fluidisation time depends on the imposed stress via a power law:

$$\tau_{\rm f}/t_w = C(\Sigma - \Sigma_y)^{-\alpha}, \quad \text{for } \Sigma < \Sigma_c \tag{4.5.5}$$

where α is a constant of order $O(1)$ apparently independent of x. (In all that follows C, defined here, and $D \ldots F$ defined below, are fitting parameters that depend weakly on x.) We show the relation between the fluidisation time and the imposed stress determined from our numerical results in sub-figures (a, c, e) of Figure 4.5.4. Here, we plot the fluidisation time (scaled by t_w) as a function of $\Sigma - \Sigma_y$ for various values of $x = 0.1, 0.3, 0.5$, respectively. The dashed line shows the fit of Eqn 4.5.5 to the data, valid in the small $\Sigma - \Sigma_y$ region.

In the *large stress* regime ($\Sigma > \Sigma_c$), we find the fluidisation time has an expo-

[10]Note that throughout we are only considering stresses greater than the yield stress $\Sigma > \Sigma_y$.

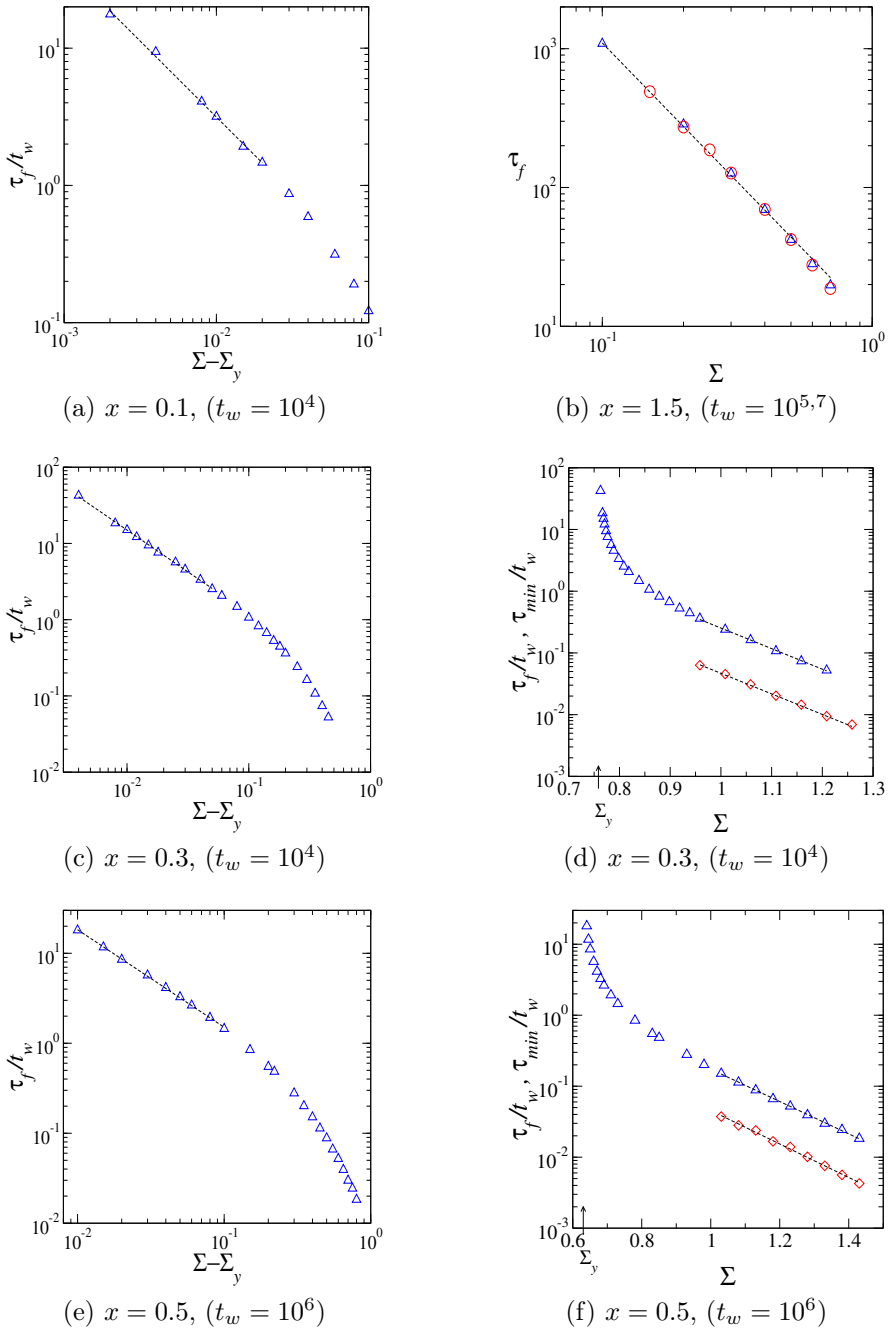

(a) $x = 0.1$, $(t_w = 10^4)$ (b) $x = 1.5$, $(t_w = 10^{5,7})$

(c) $x = 0.3$, $(t_w = 10^4)$ (d) $x = 0.3$, $(t_w = 10^4)$

(e) $x = 0.5$, $(t_w = 10^6)$ (f) $x = 0.5$, $(t_w = 10^6)$

Figure 4.5.4: Fluidisation time $\tau_{\rm f}$ (triangle symbols) as a function of $\Sigma - \Sigma_y$ (left column) or Σ (right column) for various values of x as shown in sub-captions. In (d) and (f) we also show the 'dip time' $\tau_{\rm dip}$ (diamond symbols). In (b) waiting times $t_w = 10^{5,7}$ are shown in triangles and circles, respectively. Dashed lines are fits of Eqn 4.5.5: $\tau_{\rm f}/t_w = C(\Sigma - \Sigma_y)^{-\alpha}$ in (a, c, e), and Eqn 4.5.6: $\tau_{dip,f}/t_w = E_{dip,f}\exp(-F_{dip,f}\Sigma)$ in (d, f); see Appendix I for values of fitting parameters α and $C, \ldots, F$.

nential dependence on Σ:

$$\tau_{\mathrm{f}}/t_w = E\exp(-F\Sigma), \quad \text{for } \Sigma > \Sigma_c. \tag{4.5.6}$$

See sub-figures (d, f) of Figure 4.5.4 that show the fluidisation time (scaled by t_w) as a function of the imposed stress Σ for $x = 0.3, 0.5$, respectively. The dashed line shows the fit of Eqn 4.5.6, valid for stresses far from the yield stress.

Note that for sufficiently large waiting times the exponents α and F of Eqns 4.5.5 and 4.5.6, respectively, are independent of the waiting time t_w. As the glass transition is approached $x \to 1$, increasingly large waiting times are required for convergence of the exponents with respect to the waiting time t_w. In Figure 4.5.4, the results of sub-figures (a-d) are converged with respect to waiting time t_w, whilst the exponent α and fitting parameter $F_{min,f}$ in sub-figures (e, f) still depend weakly on the waiting time, see Figure 4.8.1 of Appendix I.

Above the glass point: $1 < x < 2$

As explained in Section 4.5.1, above the glass point $1 < x < 2$ Fielding *et al.* [62] predicted departure of the shear rate from the creep regime at times $\Delta t \sim \Sigma^{\frac{1}{1-x}}$. We show that the fluidisation time τ_{f} is proportional to this departure time in Figure 4.5.4 (b), where we plot the fluidisation time τ_{f} as a function of the imposed stress. The dashed line shows the fit of:

$$\tau_{\mathrm{f}} = D\Sigma^{\frac{1}{1-x}}. \tag{4.5.7}$$

We summarise all fluidisation relations for the SGR model in Table 4.3.

$x < 1$	$1 < x < 2$
$\tau_{\mathrm{f}} = t_w C\left(\Sigma - \Sigma_y\right)^{-\alpha}$ for $\Sigma < \Sigma_c$ $\tau_{\mathrm{f}} = t_w E e^{-F\Sigma}$ for $\Sigma > \Sigma_c$	$\tau_{\mathrm{f}} = D\,\Sigma^{\frac{1}{1-x}}$

Table 4.3: Relation between the fluidisation time τ_{f} and the imposed stress Σ (or $\Sigma - \Sigma_y$) determined from numerical results for $x < 1$, or from Ref. [62] for $1 < x < 2$. $C, ..., F$ are fitting parameters that may depend on x and α is a constant $O(1)$.

The 'dip time', $\tau_{\rm dip}$

We also investigated the time at which the minimum of the shear rate occurs: $\tau_{\rm dip}$, see Figure 4.5.2. This minimum signifies the onset of the transition from solid-like behaviour (creep) to liquid-like flow (fluidisation), and is relevant as the general criterion (Eqn 4.2.8) predicts linear instability to shear rate heterogeneity for times $\tau_{\rm dip} < \Delta t < \tau_{\rm f}$.

In the *large stress* regime $\Sigma > \Sigma_c$, we find that this dip time is proportional to the fluidisation time: $\tau_{\rm dip} \propto \tau_{\rm f}$, as shown in (d, f) of Figure 4.5.4. $\tau_{\rm dip}$ then also obeys Eqn 4.5.6, albeit with a different prefactor $E_{\rm dip}$.

For reasons that we detail in Appendix I, we were unable to determine a physically meaningful $\tau_{\rm dip}$ for imposed stresses in the *small stress* regime, $\Sigma < \Sigma_c$.

4.6 Glassy polymer model

Finally, we turn to study the step shear stress protocol in the glassy polymer model. This model has been shown to describe semi-quantitatively the experimental results of Ref. [88]. In this experiment it was reported that, during extension of the sample under a constant load, the segmental relaxation time (which governs the rate of rearrangements of local segments of the polymer chain) showed a dramatic decrease as a function of time, followed by a minimum and a rise accompanied by strain hardening [58] (see Figure 2.2.3 of Chapter 2). The authors of Ref. [58] carefully fitted the parameters of the GP model to the experimental results of Ref. [88] in order to make direct comparisons with experiment. The aim of this section is to provide results comparable to those of the extensional geometry in Refs. [58, 88] for the shear geometry, and we will therefore use the same parameters used by Fielding *et al.* in Ref. [58].

Response in comparison to the results of Ref. [58]

For now, we will focus on the response to an imposed stress Σ with homogeneous flow enforced, but will later investigate the response with heterogeneity allowed in the flow-gradient direction. Recall from Chapter 3 that within the model the total

shear stress Σ is composed of solvent (s) and polymer (p) viscoelastic shear stresses and a Newtonian solvent contribution:

$$\Sigma = G^p \sigma^p + G^s \sigma^s + \eta \dot{\gamma}, \tag{4.6.1}$$

where $G^{p,s}$ are the polymer and solvent elastic moduli. The viscoelastic shear stresses obey similar governing equations (Eqns 3.2.19 and 3.2.20) that involve a polymer relaxation time $\tau^p(\Delta t) = \tau(\Delta t)/\alpha$ proportional to that of the solvent (or the 'segmental') relaxation time[11] τ, which undergoes ageing at rest but may be rejuvenated by shear. [Recall that the time elapsed since the imposition of stress is $\Delta t = t - t_w$, where t_w is the age of the sample and $\tau(t = \Delta t^-) \simeq t_w$.] As with non-polymeric glassy materials, the model has a yield stress Σ_y. Because α is extremely small ($\alpha = 10^{-12}$ was used in Ref. [58]), the polymer yield stress is very large $\Sigma_y^p = \frac{G^p}{\mu\alpha}$, leading to divergence of the overall yield stress $\Sigma_y \to \infty$ in the limit $\alpha \to 0$. Nevertheless, the solvent yield stress is finite: $\Sigma_y^s = G^s/\mu$.

The response of the shear rate, segmental relaxation time and polymer and solvent stresses to an imposed total stress (that is slightly larger than the solvent yield stress $\Sigma > \Sigma_y^s$) in the GP model are shown in Figure 4.6.1. This figure demonstrates that the basic features of experiment and numerics in the extensional geometry are also present in the shear geometry; these are: *i*) *strain:* the strain accelerates initially [$\dot{\gamma}(\Delta t)$ increases] until an inflection point is reached corresponding to a maximum in the shear rate, $\dot{\gamma}(\Delta t)$, whereupon strain hardening occurs and the shear rate progressively decreases in time. *ii*) *segmental relaxation time:* after an initial rapid decrease on loading[12], the relaxation time decreases in time with a rate that is accelerated by positive feedback through the resulting increase of $\dot{\gamma}$ (until the strain hardening regime is met); this process is analogous to the 'fluidisation' of non-polymeric SGMs. *iii*) *strain hardening:* with this increase in $\dot{\gamma}(\Delta t)$ the polymer stress also increases[13] so that the polymer bears an increasing fraction of the total

[11] Note that although τ^p is proportional to τ, α is extremely small and thus $\tau^p \to \infty$.

[12] The initial rapid decrease of $\tau(\Delta t)$ after the stress is imposed is due to the step-strain like response of the system.

[13] In fact, due to α being extremely small, $\partial_t \Sigma^p \simeq \dot{\gamma}(\Delta t)$, and thus $\Sigma^p(\Delta t) \simeq G^p \gamma(\Delta t)$.

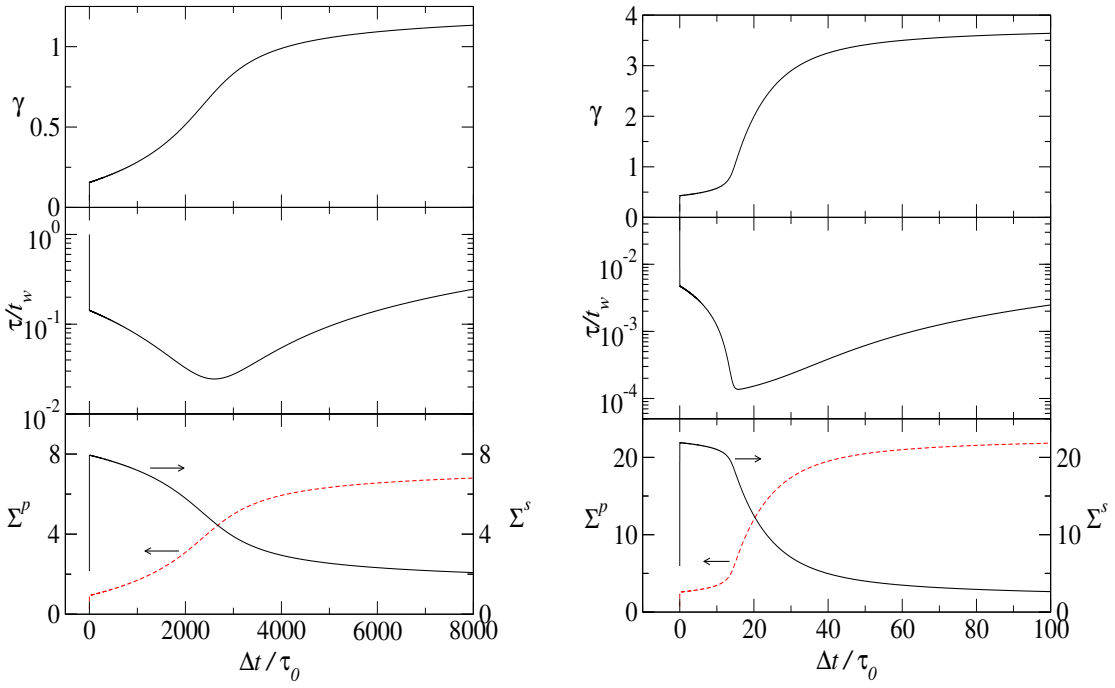

(a) $\Sigma = 8.88$ (b) $\Sigma = 24.48$

Figure 4.6.1: Top to bottom panels: response of the strain γ, reduced relaxation time τ/t_w, and solvent (s) and polymer (p) stresses: $\Sigma^{p,s} = G^{p,s}\,\sigma^{p,s}$ to a step stress. Imposed stress: (a) $\Sigma = 8.88$ so that $\Sigma/\Sigma_y^s = 2.1768$ (to match ratio of engineering stress to solvent yield stress in Ref. [58]) and (b) $\Sigma = 24.48$ so that $\Sigma/\Sigma_Y^s = 6$ and the depth of the minimum of $\tau(\Delta t)$ roughly matches that of the data in Ref. [58]. Parameters: (as in Ref. [58]) $G^p = 6$ Pa, $G^s = 8.5\,G^p$, $\tau_0 = 6$ s, $\eta = 0.05\,G^p\,\tau_0$, $\alpha = 10^{-12}$, $\mu = 12.5$, $t_w/\tau_0 = 10^4$.

imposed load. This results in both a decrease of the shear rate and a transfer of the majority of the load being held by the solvent to the polymer, signifying the onset of the strain hardening regime. The solvent stress drops below the yield stress $\Sigma^s < \Sigma_y^s$ causing the solvent to re-vitrify; the system begins to age [$\tau(\Delta t)$ increases] and the shear rate decreases towards zero.

The value of the imposed stress Σ in Figure 4.6.1 (a) was chosen so that Σ/Σ_y^s matches the ratio of the engineering stress to the solvent yield stress in Ref. [58], and shows qualitatively similar behaviour to the extensional case. However, the minimum of $\tau(\Delta t)$ occurs at a later time and with a less significant depth when compared to the results of Ref. [58]. This is likely due to the constant-force extensional protocol used that results in a decrease of the cross-section of the sample and therefore a continuous increase in the local stress (present only in the extensional protocol); this would increase the feedback mechanism that drives the fluidisation

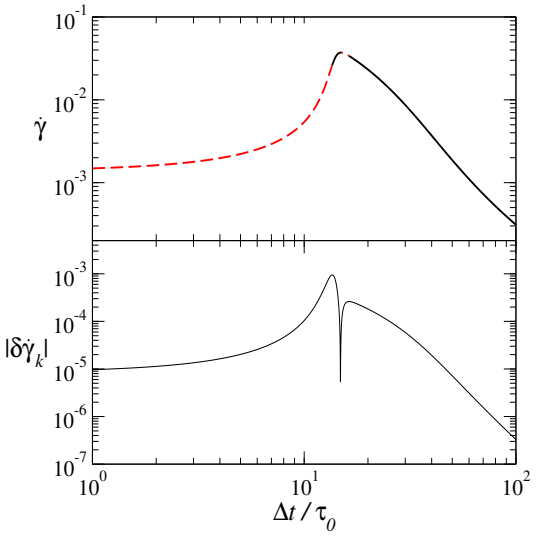

Figure 4.6.2: Top: shear rate $\dot{\gamma}$ (homogeneity enforced), dashed where $\partial_t^2\dot{\gamma}/\partial_t\dot{\gamma} > 0$, bottom: absolute value of shear rate perturbations $|\delta\dot{\gamma}_k|$ found by integrating Eqn 4.2.6. Parameters are the same as in Figure 4.6.1 (b), noise added initially of the form $\underline{\delta s}_k = q\underline{X}\epsilon_k$, where $q = 10^{-2}$, and $\underline{X}$ is an array of random numbers chosen from a flat distribution with a mean of 0 and width of 1.

process resulting in an earlier, deeper minimum of $\tau(\Delta t)$. To affirm this explanation, we show in (b) of the Figure the results for a larger imposed stress ($\Sigma/\Sigma_y^s = 6$), resulting in a more pronounced dip in $\tau(\Delta t)$ that occurs at a much earlier time.

Linear instability to shear rate heterogeneity

The general criterion derived in Section 4.2 predicts linear instability to shear rate heterogeneity at times for which the shear rate (of a system constrained homogeneously) shows simultaneous positive curvature and slope in time, i.e., when $\partial_t^2\dot{\gamma}/\partial_t\dot{\gamma} > 0$. We will now investigate this in the GP model.

We show in Figure 4.6.2 the response of the shear rate in a homogeneously constrained system to an imposed shear stress that is slightly larger than the solvent yield stress $\Sigma > \Sigma_y^s$. We also show the dynamics of the heterogeneous perturbations in the shear rate $\delta\dot{\gamma}_k(t)$ of the linearised system, found by integrating Eqn 4.2.6. Clearly, the shear rate perturbations grow in accordance with the times for which the shear rate obeys $\partial_t^2\dot{\gamma}/\partial_t\dot{\gamma} > 0$. However, we find that the magnitude of the shear rate perturbations at their peak is small. This is because strain hardening curtails the growth of the shear rate that would otherwise lead to (for example, in

the case where G^p/G^s is small, but finite) an increase in $\dot{\gamma}(\Delta t)$ by several orders of magnitude during which $\partial_t^2\dot{\gamma}/\partial_t\dot{\gamma} > 0$, and would result in significant growth of the shear rate perturbations as seen in the RP or SGR models. Due to this curtailing of the shear rate, the growth of shear rate perturbations is limited (increasingly so for increasing G^p/G^s). For example, the value of $|\delta\dot{\gamma}_k|$ at its peak (bottom panel of Figure 4.6.2) is smaller in magnitude than its value (due to the initial noise) at $\Delta t = 0$. We conclude that strain hardening plays a stabilising role that reduces the magnitude of shear banding.

4.7 Conclusions

In this chapter, we have derived a general criterion for the onset of linear instability to shear rate heterogeneity for the step stress protocol that is independent of fluid or model type, and depends only on derivatives of the shear rate in time. The criterion predicts the growth of shear rate perturbations whenever $\partial_t^2\dot{\gamma}/\partial_t\dot{\gamma} > 0$. We investigated the use of the criterion in three classes of material:

Polymeric fluids: we showed that both the RP and Giesekus models have qualitatively similar responses of the shear rate $\dot{\gamma}(t)$ to an imposed shear stress. In both cases, for values of the imposed stress nearest those on the weakest slope of the constitutive curve the shear rate rises dramatically by several orders of magnitude in a short time period. We showed that, consistent with the general criterion, transient shear banding arose during the upwards curving, upwards sloping region of this shear rate rise. However, we also showed that while the magnitude of this transient shear banding is 'significant' (i.e., $\dot{\gamma}_{max} - \dot{\gamma}_{min}$ larger than 5% of the shear rate at the same instant in time) in the RP model, it is not significant in the Giesekus model. This is because the *rate* of increase of $\dot{\gamma}(t)$ is much larger in the RP model relative to that of the Giesekus model for parameters leading to comparable constitutive curves. (In fact, we never found 'significant' transient shear banding for any parameters in the Giesekus model.) We also showed that in the RP model, the system returns to (relative) homogeneity at steady state, regardless of the form of

noise inputted into the system (i.e., initial or continuous noise). In the Giesekus model with noise added continually, a small magnitude of shear banding arises during the regime of upwards curvature and slope of $\dot{\gamma}(t)$; however, unlike that found in the RP model, this heterogeneity persists to steady state. We therefore conclude that the Giesekus model in our opinion is not appropriate for the description of the *transient* shear banding properties of entangled polymeric materials. However, the results of significant transient shear banding in the RP model are consistent with the experimental findings of entangled polymeric systems [16, 18, 19, 74–77, 161].

Soft glassy materials: The shear rate response to an imposed shear stress in the SGR model is qualitatively similar to that of the RP and Giesekus models. However, we did not explore the transient shear banding properties of the model in response to a step stress, since it has already been shown that shear bands do indeed arise during the upwards sloping, upwards curving region of the shear rate in time [117]. Rather, we investigated the *creep*: the progressive decrease of the shear rate in time), and the subsequent *fluidisation:* the sudden increase of the shear rate in time leading to steady flow in the SGR model. Our aim here was to determine relations for: the shear rate as a function of time during creep, and also for the 'dip' $\tau_{\rm dip}$ and 'fluidisation' $\tau_{\rm f}$ times (as a function of imposed stress Σ) at which the shear rate undergoes a minimum and an inflection in time, respectively. The dip and fluidisation times are relevant as they describe the time during which the system is linearly unstable to the formation of shear bands $\tau_{\rm dip} < \Delta t < \tau_{\rm f}$, according to the general criterion above.

We first focussed on the behaviour of the creep regime that can exist for a long time before fluidisation occurs. Here, we showed that in the glassy phase of the model ($x < 1$) and for imposed stresses above the yield stress, the shear rate follows a power law in time with an exponent dependent on the noise temperature: $\dot{\gamma}(\Delta t) \sim t_w^{-1} \left(\frac{\Delta t}{t_w}\right)^{-x}$. We found this creep power law to be valid for 'short' times: $\Delta t \ll t_w$. A different creep behaviour was found to exist at 'long' times $\Delta t \gg t_w$, though we were unable to access this regime to determine the power law exponent.

Next, we investigated the fluidisation behaviour of the model: this is the transition from a solid-like response (creep — described above) to liquid-like flowing

behaviour. The solid-like creep regime ends as the shear rate undergoes a minimum at a time $\Delta t = \tau_{\rm dip}$, before suddenly increasing over several orders of magnitude, passing through an inflection point at $\Delta t = \tau_{\rm f}$ before reaching a steadily flowing state. Recall that in between these two 'minimum' and 'fluidisation' times $\tau_{\rm dip} < \Delta t < \tau_{\rm f}$, the shear rate satisfies $\partial_t^2\dot{\gamma}/\partial_t\dot{\gamma} > 0$. In the *glass phase* ($x < 1$) we found two regimes depending on whether the imposed stress larger or smaller than a critical stress Σ_c. Below the critical stress, we showed that the fluidisation time depends on the imposed stress via a power law: $\tau_{\rm f}/t_w \sim (\Sigma - \Sigma_y)^{-\alpha}$ [where $\alpha \sim O(1)$]. Above the critical stress, the fluidisation time depends exponentially on the imposed stress: $\tau_{\rm f}/t_w \sim e^{-F\Sigma}$. We also showed that, as long as a clear 'dip' time $\tau_{\rm dip}$ could be found, it was proportional to the fluidisation time $\tau_{\rm dip} \propto \tau_{\rm f}$. *Above the glass point* ($1 < x < 2$) we showed that $\tau_{\rm f}$ was proportional to the time at which Fielding *et al.* [62] predicted departure from the linear creep regime: $\tau_{\rm f} \sim \Sigma^{1/(1-x)}$.

Glassy polymers: Finally, we investigated the rheological response in the glassy polymer model to an imposed shear stress in order to provide a comparison with recent numerics and experiments performed under a constant extensional load [58,88]. We showed that the shear rate, segmental relaxation time and polymer and solvent stresses respond qualitatively similarly in the shear geometry as in the extensional geometry. Strain hardening arises as the polymer takes an increasing fraction of the imposed stress, accompanied by a 'dip' in the segmental relaxation time indicating the re-vitrification of the solvent. We showed that this strain hardening inhibits the sudden increase of the shear rate in time and thus stabilises the system against shear banding according to the general criterion.

To summarise, we have shown that one should expect transient shear banding to arise generically during a step stress whenever the shear rate undergoes simultaneous positive slope and curvature in time. Until recently, it has not always been appreciated by the community that shear banding might arise during the time dependent response of complex fluids to a step stress.

4.8 Appendix I

Fitting parameters for Figure 4.5.4

Table 4.4 shows values of the fitting parameters (found using a nonlinear fitting function in Grace [1]) for the dashed lines in Figure 4.5.4.

x	C	α	E_{f}	E_{dip}	F_{f}	F_{dip}
0.1	0.019	1.11	—	—	—	—
0.3	0.096	1.10	541	100	7.67	7.67
0.5	0.124	1.08	33.0	10.4	5.25	5.43

Table 4.4: Fitting parameters for Figure 4.5.4. C, α are parameters for the fluidisation time fit using: $\tau_{\mathrm{f}}/t_w = C(\Sigma - \Sigma_y)^{-\alpha}$ for (a, c, e) of the figure. $E_{\mathrm{dip,f}}, F_{\mathrm{dip,f}}$ are parameters for the dip (dip) time and fluidisation (f) time fit using: $\tau_{\mathrm{dip,f}}/t_w = E_{\mathrm{dip,f}} \exp(-F_{\mathrm{dip,f}}\Sigma)$ for (d, f) of the figure.

Discussion on the origin of the critical stress Σ_c

Here, we discuss the origin and value of the critical stress Σ_c that divides the *small* and *large* stress regimes that result in different relations (Eqns 4.5.5 and 4.5.6, respectively) for the fluidisation time τ_{f} on the imposed stress Σ.

In fact, the separation of these regimes appears to originate in whether the fluidisation time occurs at *short* ($\Delta t \ll t_w$) or *long* ($\Delta t \gg t_w$) times. This can be clearly seen by comparing the smallest/largest fluidisation time τ_{f} for which the Eqns 4.5.5 and 4.5.6 (dashed lines) fit the data in Figure 4.5.4. [Refer to a schematic of the short and long time creep regimes in Figure 4.8.2 (below). In this schematic that assumes $\Sigma < \Sigma_c$, fluidisation occurs in the long time regime: $\tau_{\mathrm{f}} \gg t_w$. For larger stresses $\Sigma > \Sigma_c$ fluidisation occurs in the short time regime: $\tau_{\mathrm{f}} \ll t_w$.] The critical stress Σ_c then describes the stress at which fluidisation occurs at $\tau_{\mathrm{f}} \sim t_w$. By considering Eqn 4.5.5 in the limit $\tau_{\mathrm{f}}/t_w \to 1$ from above, we find that:

$$\Sigma_c = \Sigma_y + C^{1/\alpha}. \tag{4.8.1}$$

Here, $C(x) \sim O(10^{-1})$ is a fitting parameter that is weakly dependent on x whose

values from Figure 4.5.2 can be found in Table 4.4 above. (Recall that Σ_y is also dependent on x, see Chapter 3.)

Convergence of α in Figure 4.5.4 (e) w.r.t. t_w

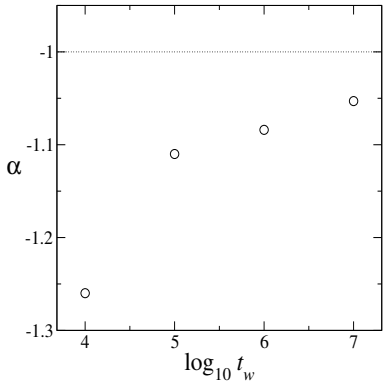

Figure 4.8.1: Convergence of the exponent α from Eqn 4.5.5 with respect to the waiting time t_w in the SGR model, for $x = 0.5$.

Discussion of τ_{dip} in the small stress regime $\Sigma < \Sigma_c$

Here, we discuss the difficulty in obtaining a meaningful τ_{dip} during the response to *small stresses* $\Sigma < \Sigma_c$.

Firstly, recall from Section 4.5.2 that there exists a *short* ($\Delta t \ll t_w$) and *long* ($\Delta t \gg t_w$) time creep regime. For imposed stresses *below* the critical stress $\Sigma < \Sigma_c$ the fluidisation time occurs during the *long time* creep regime $\tau_{\text{f}} \gg t_w$. We show this in a schematic of the response in the SGR model in Figure 4.8.2. Here, both creep regimes are seen before fluidisation occurs.

We find that the cross over between the short and long time creep regimes is accompanied by a 'pseudo-minimum' that can be seen at $\Delta t \sim t_w$, and appears to result from the number of elements that have not yet yielded (since the onset of deformation) decreasing to zero. This pseudo-minimum is shown in the schematic of Figure 4.8.2 at $\Delta t \sim t_w$; we find that the 'pseudo-minimum' apparently persists even as $\Sigma \to \Sigma_y$. Ideally, we could still extract the time of the dip τ_{dip} that actually corresponds to the transition to steady flow. However, unless a sufficient separation between τ_{dip} and t_w exists, we find that the minimum corresponding to the onset of

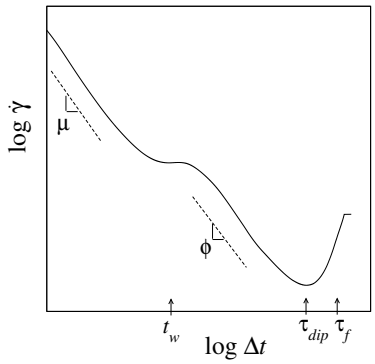

Figure 4.8.2: Schematic of generic response (valid for all $x < 2$). Two power law creep regimes exist (with exponents μ, ϕ), a transition between the two occurs at time t_w. For stresses $\Sigma > \Sigma_y$ the system will fluidise at a time $\Delta t \sim \tau_{\rm dip}$ — this time depends on the imposed stress so that, for some stresses, only the short time creep regime might be seen $\tau_{\rm dip} < t_w$.

fluidisation $\tau_{\rm dip}$ becomes lost in the 'pseudo-minimum' at $\Delta t \sim t_w$, so that extracting a meaningful $\tau_{\rm dip}$ is very difficult. We therefore do not attempt to associate $\tau_{\rm dip}$ with $\tau_{\rm f}$ of Eqn 4.5.5.

5

Shear startup protocol

5.1 Introduction

In this chapter we will investigate the rheological response of soft glassy materials and entangled polymeric materials above and below the glass transition during shear startup. In this protocol a constant shear rate $\dot{\gamma}$ is imposed on the material and the dynamics of the total shear stress $\Sigma(t)$, are measured as a function of time t, or equivalently, strain $\gamma = \dot{\gamma}t$. Recall Figure 2.1.3 of Chapter 2.

As explained in Chapter 2, there is much need of a criterion for the onset of *time-dependent* linear instability to shear heterogeneity in this time-dependent protocol with the same fluid-universal status as that of the well known steady state criterion of a negative slope in the constitutive curve[1] $\partial_{\dot{\gamma}}\Sigma|_{\gamma\to\infty} < 0$ [160]. We will derive

[1]Recall that the 'constitutive curve' is defined as the relation (with homogeneity in the flow gradient direction enforced) of the steady state total stress $\Sigma(\dot{\gamma})|_{t\to\infty}$ to the imposed shear rate. The 'flow curve' is the same curve with heterogeneity in the flow gradient direction allowed.

such a criterion in Section 5.2, for which credit is given to Dr. Suzanne Fielding. By considering large strain and large shear rate limits we will identify 'elastic' and 'viscous' terms that contribute to linear instability to shear banding. We will show that the 'elastic' term is consistent with numerous experimental findings in entangled polymeric and soft glassy materials showing time-dependent shear banding during the negative slope of shear stress as a function of strain during shear startup [18,19, 43,45,77,136,138,162].

We will show how this general criterion applies widely in models for entangled polymeric fluids using the rolie-poly and Giesekus models. (Examples of these materials include concentrated solutions or melts of high molecular weight polymers, and concentrated solutions of wormlike micelles or DNA.) We will investigate age-dependent transient shear bands in the scalar fluidity model, for which the constitutive curve is monotonic. We also show these to arise in the glassy polymer model, albeit with a reduced magnitude due to the effect of strain hardening. The author is grateful to Prof. Mike Cates and Prof. Ron Larson for collaboration during research on this model.

The results of Sections 5.2 and 5.3 are published in Ref. [117], Section 5.6 in Ref. [116], and Section 5.7 in Ref. [59].

5.2 Criterion for instability in shear startup

The well known criterion for steady state shear banding is a negative slope in the constitutive curve: $\partial_{\dot{\gamma}}\Sigma|_{t\to\infty} < 0$ [160,172]. However, as described in Chapter 2, models that do not possess this negative slope may still show *transient* shear banding. Two main causes have been suggested [2] for this ubiquitously occurring phenomenon. Firstly, a nonlinear elastic response of the material to imposed shear that leads to a negative slope of the stress in strain $\partial_{\gamma}\Sigma < 0$ might result in an 'elastic' instability to shear heterogeneity. Secondly, drawing on the well known steady state criterion for shear banding of a negative slope in the constitutive curve $\partial_{\dot{\gamma}}\Sigma|_{t\to\infty} < 0$ it has been suggested [2,68,116] that a negative slope in an 'instantaneous' or 'time-dependent' constitutive curve might lead to a 'viscous' instability to shear heterogeneity, even

if the ultimate steady state constitutive curve is monotonic. This 'instantaneous' constitutive curve can be imagined as follows: by performing several shear startup experiments at different shear rates $\dot{\gamma}$ and monitoring the stress as a function of strain for each, one can plot the constitutive curve at any instant in strain by collecting these into a single curve[2]: $\Sigma(\dot{\gamma})|_{\gamma_{inst}}$.

In this section we will derive a general criterion for the onset of linear instability to shear heterogeneity that is independent of model or material type, containing terms associated with the 'elastic' and 'viscous' instabilities above. This general criterion not only describes the onset of transient shear bands, but also describes how shear bands that persist to steady state first arise during the time-dependent response. In this derivation, we will use the 'general framework' outlined in Chapter 3 and perform a linear stability analysis about the time-dependent homogeneous background state. Credit for this derivation is given to Dr. Suzanne Fielding.

Recall from Chapter 3 that within the general framework the total shear stress Σ is decomposed into viscoelastic and Newtonian solvent contributions: $\Sigma = G\,\underline{p}\cdot\underline{s}+\dot{\gamma}\eta$, where $\underline{s} = (\sigma_{xy}, \sigma_{xx}, \sigma_{yy}, \ldots)^T$ is a vector containing all dynamical variables and $\underline{p} = (1, 0, 0, \ldots)$ is a projection vector for the viscoelastic shear conformational variable $\sigma \equiv \sigma_{xy}$. The governing equation has the form $\partial_t\,\underline{s} = \underline{Q}(\underline{s}, \dot{\gamma})$, or equivalently:

$$\partial_\gamma\,\underline{s} = \frac{\underline{Q}(\underline{s}, \dot{\gamma})}{\dot{\gamma}}. \tag{5.2.1}$$

Our aim is first to determine the gradient of the instantaneous constitutive curve formed at a fixed strain: $\partial_{\dot{\gamma}}\Sigma|_\gamma = G\,\underline{p}\cdot\partial_{\dot{\gamma}}\underline{s}|_\gamma + \eta$. We then perform a linear stability analysis about this homogeneous background state, and determine an equation for the growth of heterogeneous perturbations which we will then relate to the instantaneous constitutive curve. To achieve the first of these, we first differentiate Eqn

[2]Note that an alternative 'instantaneous constitutive curve' can be obtained that is formed at a *fixed time*: $\Sigma(\dot{\gamma})|_{t_{inst}}$. However, the criterion derived in this section includes gradients of the instantaneous constitutive curve formed at a *fixed strain*, which we will therefore use as a default throughout this chapter.

5.2.1 with respect to $\dot{\gamma}$ (at fixed strain):

$$\partial_{\dot{\gamma}}\,\partial_{\gamma}\,\underline{s}\,|_{\gamma} = \frac{1}{\dot{\gamma}}\left[\frac{\partial \underline{\underline{Q}}}{\partial \underline{s}}\cdot\frac{\partial \underline{s}}{\partial \dot{\gamma}} + \frac{\partial \underline{\underline{Q}}}{\partial \dot{\gamma}}\right] - \frac{\underline{\underline{Q}}}{\dot{\gamma}^2}. \tag{5.2.2}$$

To simplify the presentation, we define $\underline{\underline{M}} \equiv \partial_{\underline{s}}\underline{\underline{Q}}$ and $\underline{q} \equiv \partial_{\dot{\gamma}}\underline{\underline{Q}}$. Rearranging Eqn 5.2.2 we then find:

$$\partial_{\dot{\gamma}}\,\underline{s}|_{\gamma} = \underline{\underline{M}}^{-1}\left(\dot{\gamma}\partial_{\dot{\gamma}}\,\partial_{\gamma}\,\underline{s} - \underline{q} + \partial_{\gamma}\underline{s}\right). \tag{5.2.3}$$

To obtain the instantaneous constitutive curve at a fixed strain we recall that $\partial_{\dot{\gamma}}\Sigma|_{\gamma} = G\,\underline{p}\cdot\partial_{\dot{\gamma}}\underline{s}|_{\gamma} + \eta$, i.e.,

$$\partial_{\dot{\gamma}}\Sigma|_{\gamma} = G\,\underline{p}\cdot\underline{\underline{M}}^{-1}\left(\dot{\gamma}\partial_{\dot{\gamma}}\,\partial_{\gamma}\,\underline{s} - \underline{q} + \partial_{\gamma}\,\underline{s}|_{\dot{\gamma}}\right) + \eta. \tag{5.2.4}$$

For use later on we rearrange this and multiply by $\left|\underline{\underline{M}}\right|$:

$$\left|\underline{\underline{M}}\right|\left\{\partial_{\dot{\gamma}}\Sigma|_{\gamma} - G\,\underline{p}\cdot\underline{\underline{M}}^{-1}\left(\dot{\gamma}\partial_{\dot{\gamma}}\,\partial_{\gamma}\,\underline{s} + \partial_{\gamma}\,\underline{s}|_{\dot{\gamma}}\right)\right\} = \left|\underline{\underline{M}}\right|\left(-G\,\underline{p}\cdot\underline{\underline{M}}^{-1}\cdot\underline{q} + \eta\right). \tag{5.2.5}$$

Having studied these derivative properties of the homogeneous background state, we now perform a linear stability analysis as outlined in Chapter 3, by adding heterogeneous perturbations to this homogeneous background state[3]: $\underline{s}(t,y) = \underline{s}(t) + \sum_k \underline{\delta s}_k(t)\epsilon_k$ and $\dot{\gamma}(t,y) = \dot{\gamma} + \sum_k \delta\dot{\gamma}_k(t)\epsilon_k$. We substitute these into the governing equations (Eqn 5.2.1), use force balance to substitute $\delta\dot{\gamma}_k = -G\delta\sigma_k/\eta$, and linearise to first order in $\underline{\delta s}_k$ and $\delta\dot{\gamma}_k$ to find the governing equation for heterogeneous perturbations:

$$\partial_t\,\underline{\delta s}_k = \left(\underline{\underline{M}} - \frac{G}{\eta}\underline{q}\,\underline{p}\right)\cdot\underline{\delta s}_k. \tag{5.2.6}$$

The largest eigenvalue of the matrix governing the growth rate of heterogeneous perturbations crosses zero when $\left|\underline{\underline{M}} - \frac{G}{\eta}\underline{q}\,\underline{p}\right| = 0$. Using the property of determinants: $|\,\underline{\underline{M}}+\underline{\underline{A}}\cdot\underline{\underline{B}}\,| = |\,\underline{\underline{M}}\,|\,|\,\underline{\underline{I}}+\underline{\underline{B}}\cdot\underline{\underline{M}}^{-1}\cdot\underline{\underline{A}}\,|$, we have: $\left|\underline{\underline{M}} - \frac{G}{\eta}\underline{q}\,\underline{p}\right| = \left|\underline{\underline{M}}\right|\left(1 - \frac{G}{\eta}\underline{p}\cdot\underline{\underline{M}}^{-1}\cdot\underline{q}\right)$; by comparison with Eqn 5.2.5 we find the criterion for the growth of heterogeneous

[3]Where $\epsilon_k = \cos(k\pi y/L)$. After the end of this section we will set $G = 1$ so that σ can be thought of as the viscoelastic shear stress.

perturbations during shear startup:

$$\partial_{\dot{\gamma}}\Sigma|_{\gamma} - G\,\underline{p}\cdot\underline{\underline{M}}^{-1}\cdot(\partial_{\gamma}\underline{s}|_{\dot{\gamma}} + \dot{\gamma}\partial_{\dot{\gamma}}\,\partial_{\gamma}\,\underline{s}) < 0. \tag{5.2.7}$$

Limits of large strains and large shear rates

Two limits help clarify the important features of this criterion. Firstly, if a steady state is reached in the long time or large strain limit $t, \gamma \to \infty$, derivatives with respect to strain $\partial_{\gamma} \to 0$ and we recover the well known criterion for steady state instability of a negative slope in the constitutive curve $\partial_{\dot{\gamma}}\Sigma|_{\gamma\to\infty} < 0$. For this reason we label the first term in the criterion (Eqn 5.2.7) the 'viscous' term.

Secondly, we consider the large shear rate limit $\dot{\gamma} \to \infty$. If the shear startup functions $\underline{s}(\gamma)$ converge to limiting forms at high shear rates, i.e., dependence on the shear rate is lost and derivatives of $\partial_{\dot{\gamma}} \to 0$, then the sample behaves as an elastic solid and only derivatives of ∂_{γ} remain in the criterion[4]:

$$-\,\underline{p}\cdot\underline{\underline{M}}^{-1}\cdot\partial_{\gamma}\,\underline{s}\,|_{\dot{\gamma}} < 0, \tag{5.2.8}$$

which we call the 'elastic' term of the full criterion (this is the first term in the bracket of Eqn 5.2.7). In this large shear rate limit, this term (Eqn 5.2.8) results in linear instability to shear heterogeneity if a sum of the gradients (with the correct prefactors) in strain of the components of $\underline{s}$ is negative. In what follows, we will show that this is consistent with the numerous examples of transient shear banding associated with a negative slope of the shear stress in strain in both experiments and theoretical work as described in Chapter 2.

In a system with only two dynamical variables it can be shown that the 'elastic' term reduces to a function with dependence only on derivatives of the shear stress with respect to strain (note $\mathrm{tr}\underline{\underline{M}} < 0$, see Section 3.4):

$$-\mathrm{tr}\underline{\underline{M}}\,\partial_{\gamma}\Sigma|_{\dot{\gamma}} + \dot{\gamma}\partial_{\gamma}^{2}\,\Sigma|_{\dot{\gamma}} < 0. \tag{5.2.9}$$

[4]Note that here we have neglected the contribution of the Newtonian solvent viscosity that is in general small $\eta \ll \tau G$; we will discuss the validity of this assumption in Section 5.3.

The first term of Eqn 5.2.9 predicts linear instability to arise during a regime of negative slope of the shear stress in strain. The second adds a 'correction' to this from the curvature of the stress: as the stress departs from linear growth towards the overshoot it undergoes a regime of negative curvature in strain that may contribute sufficiently in Eqn 5.2.9 to cause linear instability to arise slightly *before* the overshoot. We will show this in the RP model in Section 5.3. We note that not all materials possess limiting functions of $\underline{s}(\gamma)$ during shear startup at high rates. For example, this is not usually the case in SGMs: we will show in Section 5.6 that the strain at the stress overshoot in the scalar fluidity model scales logarithmically with the shear rate.

These two limits reveal the 'viscous' and 'elastic' contributions of the first and second terms (respectively) of the general criterion (Eqn 5.2.7) to linear instability to heterogeneity. We label the remaining term the 'cross' term as it contains both derivatives with respect to shear rate and strain. Outside these limits this term can become important (as we shall see in the Giesekus and scalar fluidity models) and blur the distinction of 'elastic' and 'viscous' instabilities made above, though, as we shall see in the next section, in the RP model this distinction is clearly apparent.

In what follows we will refer to the 'criterion' as that of Eqn 5.2.7, and the 'reduced criterion' as Eqn 5.2.7 with the 'cross term' neglected:

$$\partial_{\dot{\gamma}}\Sigma|_{\gamma} - G\,\underline{p}\cdot\underline{\underline{M}}\cdot\partial_{\gamma}\underline{s}|_{\dot{\gamma}} < 0, \tag{5.2.10}$$

which represents the linear stability properties predicted by a simple combination of the 'elastic' and 'viscous' terms.

5.3 Non-stretching rolie-poly model

Time-dependent linear instability to shear heterogeneity (and the resulting shear banding) has been studied in detail by Adams *et al.* [2–4] in the rolie-poly (RP) model for the shear startup protocol. Our aim here is not to reproduce their work, but rather to study the extent to which the basic phenomena observed by Adams *et al.* accords with the general framework that we develop here. The RP model has

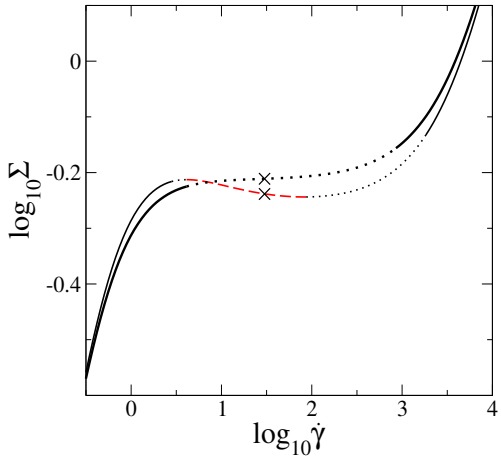

Figure 5.3.1: Constitutive curves for the nRP model for $\beta = 0.4, 1$ (bottom to top on the right) and $\eta - 10^{-4}$. Dashed: linearly unstable at steady state, dotted: *transiently* linearly unstable before the steady state is reached. Crosses at a shear rate $\dot{\gamma} = 30$, for which time-dependent behaviour is shown in Figure 5.3.2.

three dynamical variables $\underline{s} = (\sigma_{xy}, \mathrm{tr}\underline{\underline{\sigma}}, \sigma_{yy})^T$, reducing to two $\underline{s} = (\sigma_{xy}, \sigma_{yy})^T$ in the limit of fast stretch relaxation $\tau_R \to 0$. In the fast stretch relaxation limit when $\mathrm{tr}\underline{\underline{\sigma}} = 3$, the two dynamical variable criterion applies[5]:

$$|\underline{\underline{M}}|\,\partial_{\dot{\gamma}}\Sigma|_{\gamma} + G\left(-\mathrm{tr}\underline{\underline{M}}\,\partial_{\gamma}\Sigma|_{\dot{\gamma}} + \dot{\gamma}\partial^2_{\gamma}\,\Sigma|_{\dot{\gamma}}\right) - G\dot{\gamma}|\underline{\underline{M}}|\;\underline{p}\cdot\underline{\underline{M}}^{-1}\cdot\partial_{\dot{\gamma}}\,\partial_{\gamma}\,\underline{s} < 0. \qquad (5.3.1)$$

[Terms left to right are the 'viscous', 'elastic' and 'cross' terms.] The 'reduced criterion' (neglecting the 'cross' term) then depends only on derivatives of the total shear stress with respect to strain or shear rate. For this reason we will now explore the criterion within the non-stretching rolie-poly (nRP) model before later considering the extension to the 'stretching' rolie-poly model (sRP) model where $\tau_R \neq 0$.

For pedagogical purposes, we will first briefly summarise the rheological response of the model to an imposed shear rate. This was studied by Adams *et al.* [2–4], but the results shown in this chapter are the author's own numerical work. We show in Figure 5.3.1 the constitutive curves of two values of $\beta = 0.4, 1$ (and $\eta = 10^{-4}$) that result in nonmonotonic and monotonic constitutive curves, respectively. For the former, the steady state unstable region (negative slope) is shown in a dashed line, while shear rates for which the system is *transiently* linearly unstable to shear

[5]Note that $|\underline{\underline{M}}| > 0$, $\mathrm{tr}\underline{\underline{M}} < 0$, and from here on we set $G, \tau_d = 1$.

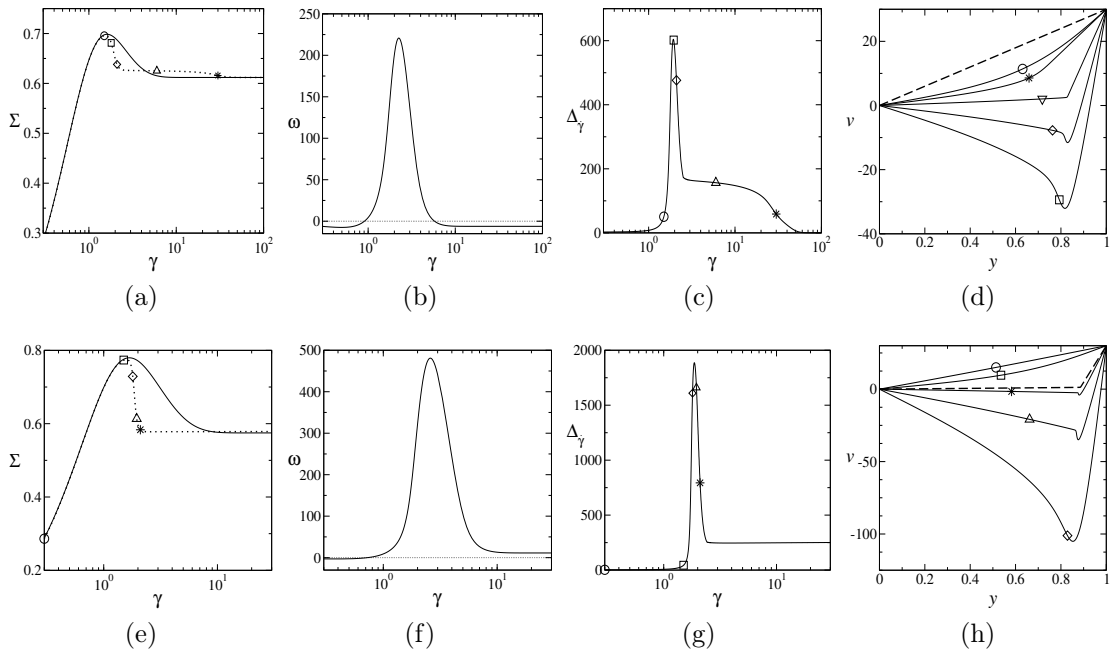

Figure 5.3.2: Responses of the nRP model to an imposed shear rate $\overline{\dot{\gamma}} = 30$ for (top row) $\beta = 1$ and (bottom row) $\beta = 0.4$ that result in monotonic/nonmonotonic constitutive curves, respectively. (a, e): total shear stress response with homogeneity enforced: solid line, heterogeneity allowed: dotted line. (b, f): largest real part of any eigenvalue from linear stability analysis ω. (c, g): 'degree of banding': $\Delta_{\dot{\gamma}} = \dot{\gamma}_{max} - \dot{\gamma}_{min}$. (d, h): snapshots of the velocity profile at strains with corresponding symbols in (a/c), (e/g); steady state velocity profile in a thick, dashed line. Parameters: $\eta = 10^{-4}$, noise added initially to the shear stress of the form $qX\cos(\pi y/L)$, $q = 0.1$, X is random number selected from a flat distribution with zero mean and unit width.

heterogeneity are shown dotted. Two crosses in the figure indicate shear rates for which we show time-dependent behaviour in Figure 5.3.2.

We show in the top row of Figure 5.3.2 the response to an imposed shear rate (with $\dot{\gamma}$ chosen from the weakest sloping region of a *monotonic* constitutive curve, see the cross in Figure 5.3.1) of the total shear stress Σ [in sub-figure (a), where both responses of the homogeneously constrained system and the system with heterogeneity allowed are shown[6]]; the largest eigenvalue[7] from linear stability analysis ω in (b); the 'degree of banding' $\Delta_{\dot{\gamma}}$ in (c); and corresponding snapshots of the velocity profile in (d), where the steady state velocity profile is shown in a thick,

[6]To do this we allow heterogeneity in the flow-gradient direction and add diffusion terms to the governing equations of $\underline{s}$ as described in Chapter 3.

[7]Found by performing a linear stability analysis about the homogeneous background state as described in Chapter 3. As before, $\omega > 0$ indicates linear instability to shear heterogeneity.

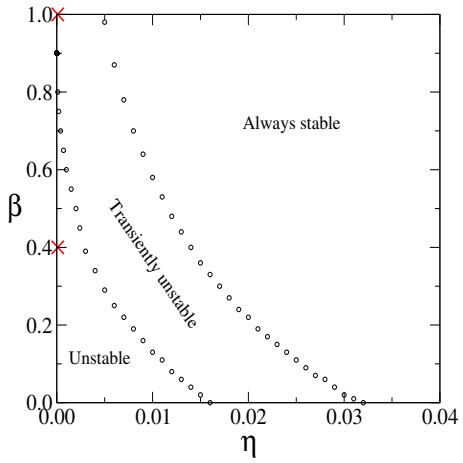

Figure 5.3.3: A parameter 'phase diagram' denoting the linear stability properties of the nRP model during shear startup at a shear rate in the smallest slope of the constitutive curve, depending on the parameters β, η. Left most region (*'Unstable'*): linearly unstable to shear heterogeneity at steady state. Middle region (*'Transiently unstable'*): system shows linear instability at some time during shear startup but is linearly stable at steady state. To the right of these regions (*'Always stable'*): the system is always linearly stable to shear heterogeneity. Crosses '$\times$' at: $\beta = 1, 0.4$ at $\eta = 10^{-4}$ in the 'transiently unstable' and 'unstable' regions, respectively.

dashed line. As shown, transient shear banding arises and is greatest in magnitude during negative slope of shear stress in strain. Note that banding can be long lived in comparison to the duration of the overshoot: see sub-figure (c) where banding is still dramatic at a strain $\gamma \sim 30$. Correspondingly, the stress appears to remain constant over this time before relaxing towards its final steady state value as the banding returns to homogeneity at these large strains. Difficulty in reaching a steady state in experiment may mean that such long lived transient banding is mistaken for steady state banding. For parameters resulting in a *nonmonotonic* constitutive curve ($\beta = 0.4$, bottom row of Figure 5.3.2) the responses are similar, except that as the homogeneously constrained system approaches steady state it remains linearly unstable to heterogeneity, and so the system with heterogeneity allowed remains in a permanently banded state [compare thick, dashed lines of sub-figures (d) and (h)].

A parameter 'phase diagram' outlining the stability properties during shear startup in the nRP model at a shear rate in the smallest slope of the constitutive curve is shown in Figure 5.3.3. The system is linearly unstable at steady state (i.e., $\partial_{\dot{\gamma}}\Sigma|_{t\to\infty} < 0$) in the bottom-left part of this plot; this region is also outlined in [2, 5]. The middle region denotes the values of β, η for which the system displays

transient linear instability to shear heterogeneity that does *not* persist to steady state (e.g., as for the top row of Figure 5.3.2). For values of β, η to the right of these regions the system is *always* linearly stable to shear heterogeneity. The top and bottom rows of Figure 5.3.2 correspond to systems with values of β, η at the two points marked ('×') on the left hand side of this phase diagram inside the 'transiently unstable' and 'unstable' regions, respectively. (Note — we chose points on the left-hand side of this figure to ensure the solvent viscosity is small $\eta \ll G\tau_d$.) We will first explore the 'elastic' instability in the former system, before exploring the additional contribution of the 'viscous' instability in the latter system.

5.3.1 'Elastic' instability

We now give numerical results for shear startup with parameters shown by the upper '×' in Figure 5.3.3, corresponding to the top row of Figure 5.3.2. We do so in the form of a portrait (similar to one outlined in Chapter 4) in $\dot{\gamma}, \gamma$ space, where horizontal slices represent a single shear startup run (with homogeneity enforced) and we plot the strains at which:

(I) the shear stress is maximal[8] $\partial_\gamma \Sigma = 0$ (dotted line);

(II) the largest eigenvalue from linear stability analysis crosses zero[9] $\omega = 0$ (large, open circles);

(III) the 'elastic' condition is met: $\dot{\gamma}\partial_\gamma^2 \Sigma \mid_{\dot{\gamma}} - \mathrm{tr}\underline{\underline{M}}\, \partial_\gamma \Sigma \mid_{\dot{\gamma}} = 0$ (solid line);

(IV) the 'viscous' condition is met: $\partial_{\dot{\gamma}} \Sigma \mid_\gamma = 0$ (dashed line, not present here);

(V) the 'reduced criterion' is met: $|\underline{\underline{M}}|\, \partial_{\dot{\gamma}} \Sigma \mid_\gamma + G\left(\dot{\gamma}\partial_\gamma^2 \Sigma \mid_{\dot{\gamma}} - \mathrm{tr}\underline{\underline{M}}\, \partial_\gamma \Sigma \mid_{\dot{\gamma}}\right) = 0$ (small, filled circles);

(VI) the system (with heterogeneity allowed) shows shear banding that crosses the 'significant' threshold: $(\dot{\gamma}_{max} - \dot{\gamma}_{min})/\bar{\dot{\gamma}} = 0.05$ (diamond symbols).

[8] The nRP model shows weak oscillations in the shear stress as it nears steady state that causes the 'elastic' condition (III) to be periodically, but weakly met. We omit these oscillations from the figures for clarity as they never become large enough for long enough to cause any growth in the perturbations (as can be seen from the contour plots of $|\delta\dot{\gamma}_k|$ in Figure 5.3.4).

[9] Note that this corresponds to the strain at which the criterion crosses zero.

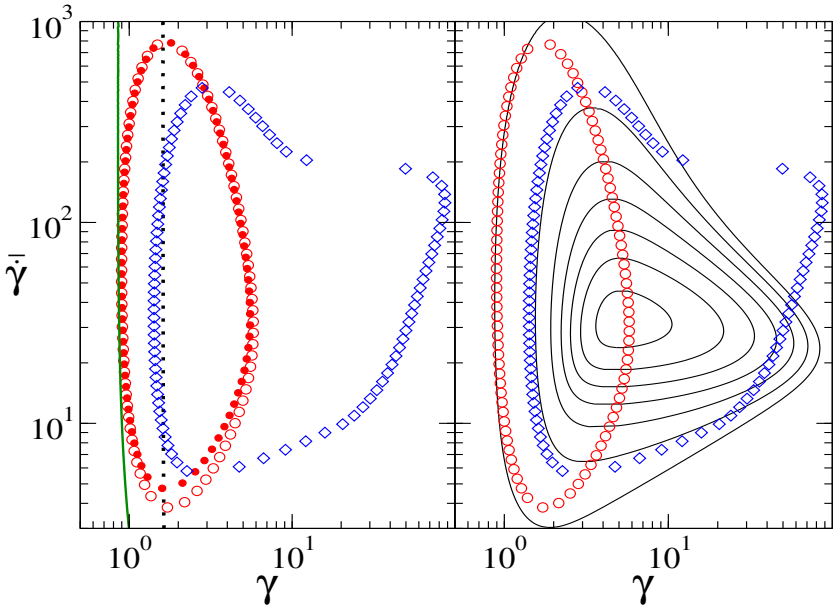

Figure 5.3.4: Shear startup in the nRP model for parameters giving a monotonic constitutive curve: $\beta = 1$, $\eta = 10^{-4}$; a horizontal slice denotes a single startup run at $\dot{\bar{\gamma}}$. Left panel: the strain at which the shear stress is maximal [(I) in text] (black dotted line); the largest eigenvalue crosses zero (II) (large open circles); the 'elastic' condition is met (III) (solid line); the 'reduced criterion' is met (V) (small, filled circles); and the threshold of 'significant' shear banding is met (VI) (open diamonds). Initial noise added to σ of the form $qX\cos(\pi y/L)$, $q = 10^{-2}$, $\underline{X}$ is an array of random numbers selected from a flat distribution with mean 0 and width 1. Right panel: contour lines of equal $|\delta\dot{\gamma}| = \dot{\bar{\gamma}}10^M$ for integer M (found by integrating Eqn 5.2.6), first contour: $M = -2$ and we show only contours $M \geq -2$. Circles and diamonds as in left panel.

(Note that the sub-figures in the top row of Figure 5.3.2 form a horizontal slice through this figure at $\dot{\bar{\gamma}} = 30$, and likewise for the bottom row of Figure 5.3.2 for $\dot{\gamma} = 30$ in Figure 5.3.5.)

We note that: firstly, the 'elastic' condition is met shortly before the shear stress overshoot due to contributions from the negative curvature of the shear stress in strain as departure from linear growth $\Sigma \sim \gamma$ occurs before the maximum is reached, recall Eqn 5.2.9.

Secondly, the strain at which the 'reduced criterion' is met agrees with that of the 'elastic' condition for a large range of shear rates. The discrepancy at low and high shear rates is due to the following:

1. at *low shear rates* $\dot{\gamma} \sim \tau_d^{-1}$ the 'viscous' term cancels out the contribution to instability of the 'elastic' term, so that the 'reduced criterion' (Eqn 5.2.10)

remains positive. This is because at these low shear rates the stress overshoot is extremely weak (with a monotonic increase of stress in strain for $\dot{\gamma} < \tau_d^{-1}$), i.e., the derivatives of stress in strain (and thus magnitude of the 'elastic' term) are small and can be cancelled out by the 'viscous' term, which is small but positive at these small shear rates.

2. At *high shear rates* prefactors of the elastic term (Eqn 5.2.8) go to zero, so that the viscous term (though small: $\partial_{\dot{\gamma}}\Sigma|_{\dot{\gamma}\to\infty} \to \eta$) forms a dominant, stabilising contribution to the criterion (Eqn 5.3.1). See Appendix I for details. As a result, linear stability to banding is restored at high shear rates, and the shear rate for which this occurs scales linearly with $G\eta^{-1}$. We therefore find that the 'elastic' condition determines the onset of linear instability to heterogeneity in the nRP model during shear startup at rates $\tau_d^{-1} \ll \dot{\gamma} \ll G\eta^{-1}$.

Thirdly, the 'cross' term provides a weak, stabilising contribution to linear instability that is negligible at high shear rates where the shear stress startup curve reaches a limiting function (i.e., independent of $\dot{\gamma}$, as described previously). Thus the region predicted to be linearly unstable to shear heterogeneity by the 'reduced criterion' (small, filled circles in the figure) corresponds closely to that of the largest eigenvalue from linear stability analysis (large, open circles).

Recall from Chapter 3 that investigating only the largest real part of the eigenvalues from a time-dependent linear stability analysis can lead to missed growth of the heterogeneous perturbations $\underline{\delta s}_k(t)$. Therefore, we also investigated the growth of these heterogeneous perturbations by integrating Eqn 5.2.6 during the time-evolution of the homogeneous background state, and used force balance $\delta\dot{\gamma}_k = -\delta\sigma_k/\eta$ to obtain the absolute value of shear rate perturbations $|\delta\dot{\gamma}_k|(t)$. We show contours of $|\delta\dot{\gamma}_k|(t)$ (scaled by the imposed shear rate $\overline{\dot{\gamma}}$) in the right hand panel of Figure 5.3.4, where each contour is a factor of 10 larger/smaller than its neighbour, and find the major growth of heterogeneous perturbations agrees with the linearly unstable region.

Using methods outlined in Chapter 3, we also evolve the perturbations in the nonlinear system. Here, we monitor the 'degree of banding' $\Delta_{\dot{\gamma}}(t)$: the difference between the maximum and minimum local shear rate as a function of time. We

find that the degree of banding is proportional to the shear rate perturbations in the linearised system $\Delta_{\dot{\gamma}}(t) \propto |\delta\dot{\gamma}_k|(t)$ during the early time region of the nonlinear response, and is thus well described by the linearised system during the onset of banding. This remains true until the magnitude of banding becomes large — here, nonlinearities neglected in the linearised system are also large and the linear analysis no longer holds. At this point deviation from $\Delta_{\dot{\gamma}}(t) \propto |\delta\dot{\gamma}_k|(t)$ occurs. We define 'significant' shear banding to be when the 'degree of banding' is more than 5% of the imposed shear rate $[(\dot{\gamma}_{max} - \dot{\gamma}_{min})/\dot{\gamma} > 0.05]$. We plot the region (delimited by diamond symbols) for which shear banding is 'significant' in the nonlinear system in the $\dot{\gamma}, \gamma$ plane of Figure 5.3.4. We note that the 'significantly' banded region in the nonlinear system (diamonds in the figure) differs significantly from the contours predicted by the linearised system (see the top-right of the figure). This departure depends on the initial noise magnitude and the parameters of the model and is (as explained above) due to the breakdown of the assumption of small perturbations made in the linear stability analysis.

5.3.2 'Viscous' instability

So far, we have considered transient shear banding in the RP model with parameters for which the constitutive curve is monotonic. We have shown that transient shear banding arises during the negative slope of shear stress *vs.* strain during startup at a range of shear rates for which the 'elastic' term dominates the criterion. We note that in the results presented above (see Figure 5.3.4), the 'instantaneous' constitutive curve formed at a fixed strain is *always* monotonic, i.e., the 'viscous' condition is never met.

We now investigate the 'elastic' and 'viscous' terms of the criterion, and the resulting time-dependent and steady state shear banding in the RP model with parameters for which the constitutive curve is nonmonotonic. We show the analogous $\dot{\gamma}$ *vs.* γ 'portrait' for these parameters in Figure 5.3.5. Shear rates for which the constitutive curve is negatively sloping at steady state, i.e., those for which the 'viscous' condition is met at steady state, can be seen in the right hand side of the left panel

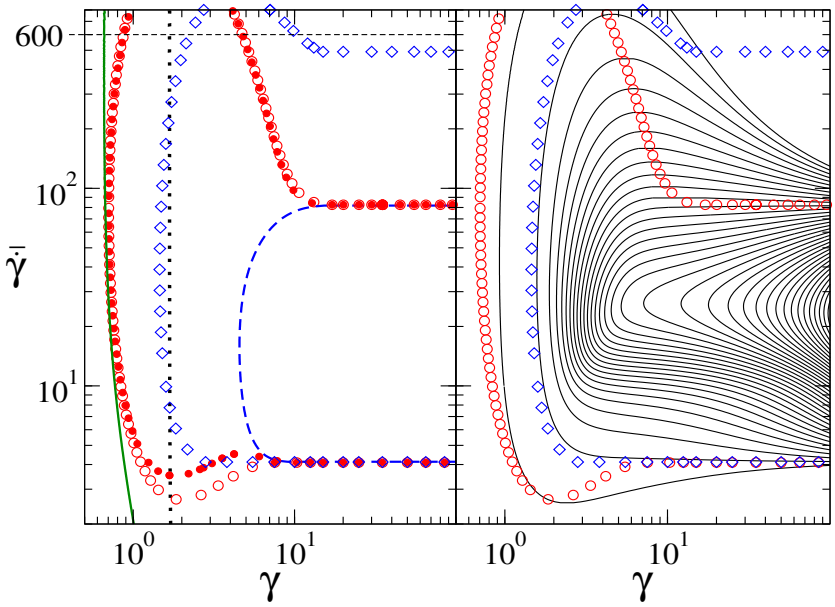

Figure 5.3.5: As Figure 5.3.4 with $\beta = 0.4$, and the additional dashed line in the left panel indicates the strain at which the 'viscous' condition is met (IV).

of the figure between the two horizontal (dashed) lines. With regard to the 'viscous' condition as a function of time before the steady state is reached, it can be seen in Figure 5.3.5 that the 'viscous' condition is only ever met for shear rates in the negative slope of the constitutive curve. In fact, we have never found the 'viscous' condition to be met transiently for any shear rate outside those in the negative slope of the constitutive curve for any parameters of the RP model (including $\tau_R \neq 0$). The overall stability portrait (Figure 5.3.5) for the RP model with a nonmonotonic constitutive curve therefore appears as such in the $\dot{\gamma}, \gamma$ plane: a vertical patch of instability around $\gamma \sim 1.7$ caused by the onset of the 'elastic' condition is seen, which joins a horizontal patch of instability that persists to steady state caused by the 'viscous' condition.

As before, we also investigated the growth of heterogeneous shear rate perturbations in the linearised system $|\delta\dot{\gamma}_k|(t)$, whose contours we plot in the right-hand side of Figure 5.3.5. Again, perturbations in the nonlinear system grow co-linearly with those of the linearised system until they become large and nonlinearities become important. There exists a range of shear rates outside those in the negative slope of the constitutive curve for which the system remains 'significantly' banded even at steady state. These correspond to shear rates for which the system is 'metastable';

the corresponding steady state stress is that of the stress plateau Σ_p (see Chapter 2). Transient shear banding that returns to homogeneity at steady state is seen for imposed shear rates that are slightly larger than those on the stress plateau, see e.g., a slice at $\overline{\dot{\gamma}} = 600$; this is consistent with experimental findings [19, 138] and molecular dynamics simulations [26] of entangled polymeric systems.

Instantaneous constitutive curve at a fixed time or strain

In the above we showed that the 'viscous' condition is never met at any strain for shear rates outside of the negative slope of the steady state constitutive curve. This indicates that transient shear banding in the RP model is *not* caused by a transient nonmonotonicity in the instantaneous constitutive curve formed at a *fixed strain*: $\partial_{\dot{\gamma}}\Sigma|_\gamma < 0$. This contrasts with recent suggestions for the cause of transient shear banding in complex fluids [2, 68, 107] that a negative slope in the instantaneous constitutive curve formed at a *fixed time*: $\partial_{\dot{\gamma}}\Sigma|_t < 0$ might be the cause of transient shear banding. In particular, it was shown by Adams *et al.* [2] in the RP model that the region of negative slope in the instantaneous constitutive curve formed at a fixed time closely corresponded with the linearly unstable region.

In fact, the reason for this is that the negative slope of the instantaneous constitutive curve formed at a fixed time approximately corresponds to the negative slope of shear stress in strain[10], as shown in Figure 5.3.6. Thus, if the system is linearly unstable during the latter (as we showed it was in the previous subsection), then so too will it be during the former. In fact, it is possible to show this result analytically, credit for which is given to Dr. Suzanne Fielding. To do so, we begin by considering the total shear stress as a function of strain and strain rate $\Sigma = f(\gamma, \tau\dot{\gamma}) = f(t\dot{\gamma}, \tau_d\dot{\gamma})$. We then note that the slope of shear stress in strain is given by:

$$\frac{\partial\Sigma}{\partial\gamma}|_{\dot{\gamma}} = f_1, \tag{5.3.2}$$

(where f_n denotes partial differentiation of f with respect to its nth argument), and the slopes of the instantaneous constitutive curves formed at fixed strain and time

[10] for a range of shear rates $\tau_d^{-1} \ll \dot{\gamma} \ll G\eta^{-1}$.

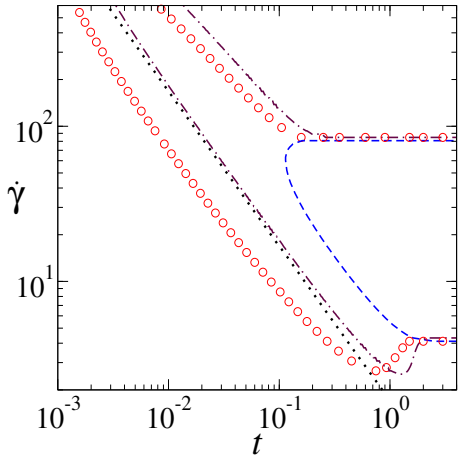

Figure 5.3.6: As Figure 5.3.5, except with features plotted at the equivalent time rather than strain. We also show (dot-dashed line) the region inside which the gradient of the instantaneous constitutive curve formed at a fixed *time* is negative: $\partial_{\dot{\gamma}}\Sigma|_t < 0$; compare to that formed at a fixed *strain* (dashed): $\partial_{\dot{\gamma}}\Sigma|_\gamma < 0$.

are:

$$\frac{\partial\Sigma}{\partial\dot{\gamma}}|_\gamma = \tau_d f_2, \tag{5.3.3}$$

$$\frac{\partial\Sigma}{\partial\dot{\gamma}}|_t = t f_1 + \tau_d f_2. \tag{5.3.4}$$

In Section 5.3.1 we showed that before the steady state is reached, the 'viscous' term (note that this is Eqn 5.3.3) is negligible for shear rates $\tau_d^{-1} \ll \dot{\gamma} \ll G\eta^{-1}$ in comparison to the slope of the shear stress in strain, Eqn 5.3.2. That is, $f_2 \ll f_1$ and so, from Eqn 5.3.4, the slope of the instantaneous constitutive curve formed at a fixed time is approximately proportional to the slope of the shear stress in strain: $\partial_\gamma\Sigma|_{\dot{\gamma}} \propto \partial_{\dot{\gamma}}\Sigma|_t$. This is valid for the range of shear rates shown above and before the steady state is reached (when $\partial_\gamma\Sigma \to 0$). We will show in Section 5.6 that a similar result exists for the scalar fluidity model.

It is not clear what the physical interpretation of the terms f_1 and f_2 should be. However, we consider that materials behaving as nonlinear elastic solids, i.e., materials whose stress response varies dramatically with strain but not with strain rate, will have $f_2 \ll f_1$ and so $\partial_\gamma\Sigma|_{\dot{\gamma}} \propto \partial_{\dot{\gamma}}\Sigma|_t$.

5.4 Stretching rolie-poly model

In the previous section we considered the time-dependent linear stability to heterogeneity during shear startup in the non-stretching RP (nRP) model in which stretch is imagined to relax infinitely quickly. During shear startup at rates $\tau_d^{-1} \ll \dot{\gamma} \ll G\eta^{-1}$ the system behaves as a nonlinear elastic solid; departure of the shear stress from linear growth and the subsequent decrease after the maximum cause the 'elastic' condition of the criterion to be met, leading to linear instability to shear heterogeneity. These results apply directly within the stretching rolie-poly (sRP) model for shear rates $\dot{\gamma} \ll \tau_R^{-1}$ for which appreciable stretch does not arise[11].

For use in this section we recall that the criterion for linear instability to shear heterogeneity during shear startup is:

$$\partial_{\dot{\gamma}}\Sigma|_\gamma - G\,\underline{p}\cdot\underline{\underline{M}}^{-1}\cdot(\partial_\gamma \underline{s}|_{\dot{\gamma}} + \dot{\gamma}\partial_{\dot{\gamma}}\,\partial_\gamma\,\underline{s}) < 0, \tag{5.4.1}$$

where we refer to the terms as the 'viscous', 'elastic' and 'cross' terms, from left to right. We also refer to the 'reduced criterion' as Eqn 5.4.1 with the 'cross' term neglected.

In the sRP model nonlinearities in the governing equations (Eqns 3.2.4) are located in the 'relaxation' terms, but the 'loading' terms are linear (see Chapter 3). [Recall that in the nRP model (Eqns 3.2.6) the opposite is true: nonlinearities are in the 'loading' terms and the 'relaxation' terms are linear.] For shear startup at rates in the 'stretching' regime $\dot{\gamma} \gg \tau_R^{-1}$ the system then behaves as a *linear* elastic solid until the relaxation terms cause deviation from this behaviour. We find that this results in the shear stress overshoot occurring at a fixed time: $t \sim \tau_R$, as shown in Figure 5.4.1 for shear rates $\dot{\gamma} \gg \tau_R^{-1}$, rather than at a fixed strain $\gamma \sim 1.7$ as it does in the non-stretching regime $\dot{\gamma} \ll \tau_R^{-1}$ (see Section 5.3). Therefore, the response to shear startup does not converge to a limiting function $\Sigma(\gamma)$ at high shear rates $\dot{\gamma} \gg \tau_R^{-1}$, as required for the 'elastic' terms to dominate the criterion during the decrease of shear stress in strain. In fact, we find that the 'viscous' and

[11] The magnitude of chain stretch in the system is represented by $\mathrm{tr}\underline{\underline{\sigma}}$; this is a dynamical variable in the sRP model so that $\underline{s} = (\sigma_{xy}, \mathrm{tr}\underline{\underline{\sigma}}, \sigma_{yy})^T$.

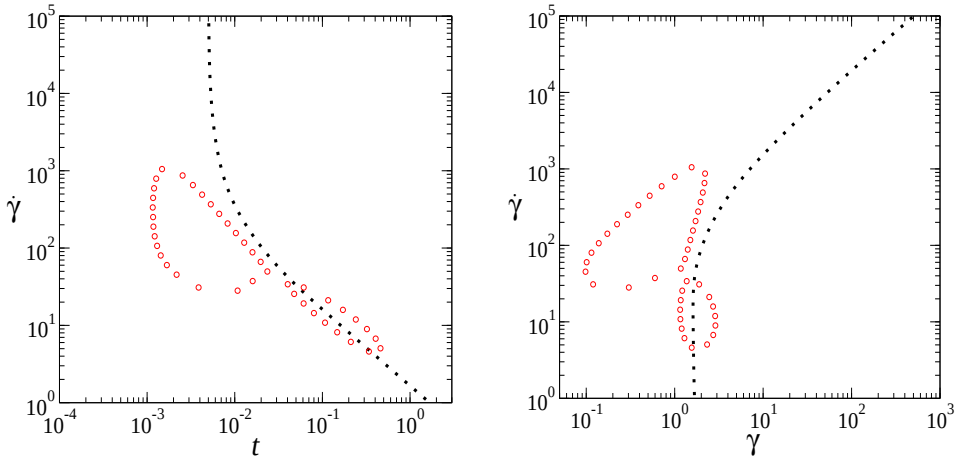

Figure 5.4.1: Shear startup in the sRP model with homogeneity enforced; a horizontal slice is a single startup run at shear rate $\dot{\gamma}$, and we plot (a) the time or (b) the strain at which the stress maximum $\partial_{t,\gamma}\Sigma = 0$ occurs (dotted line) and also the times/strains at which the system becomes linearly unstable to heterogeneity $\omega = 0$ (open circles). Parameters: $\beta = 0.9$, $\eta = 10^{-3}$, $\tau_R = 10^{-2}$.

'cross' terms are sufficiently large and positive to cancel out the negative 'elastic' term contribution towards linear instability in the region of negatively sloping shear stress in strain after the stress overshoot for shear rates $\dot{\gamma} \gg \tau_R^{-1}$, as also shown in Figure 5.4.1.

However, surprisingly, for shear rates in the stretching regime we find linear instability to heterogeneity *before* the stress maximum while the shear stress is increasing linearly in strain[12] and $\partial_\gamma \underline{s} > 0$. Note that during this linear increase in strain the 'cross' term is zero and the 'viscous' term $\partial_{\dot{\gamma}}\Sigma|_\gamma \to \eta$ is small. This instability can be seen as the upper/leftmost region delimited by open circles in Figure 5.4.1: we denote this the 'sRP-specific' instability. [Note that the lower region of linear instability in the figure is in the non-stretching regime ($\dot{\gamma} \ll 1/\tau_R$) and is due to the 'elastic' condition being met via $\partial_\gamma \underline{s} < 0$, as described in the previous section. For the parameters chosen in the figure the 'sRP-specific' instability is disconnected from this region — note that this disconnection is not general.]

To determine the cause of this 'sRP-specific' instability, we linearise the components of the 'reduced criterion' (Eqn 5.4.1 with the 'cross' term neglected) about

[12] i.e., when $\underline{s}(\gamma) = (\sigma_{xy}, \mathrm{tr}\underline{\sigma}, \sigma_{yy})^T = (\gamma, \gamma^2 + 3, 1)^T$, valid for $\gamma \ll \dot{\gamma}\tau_R$.

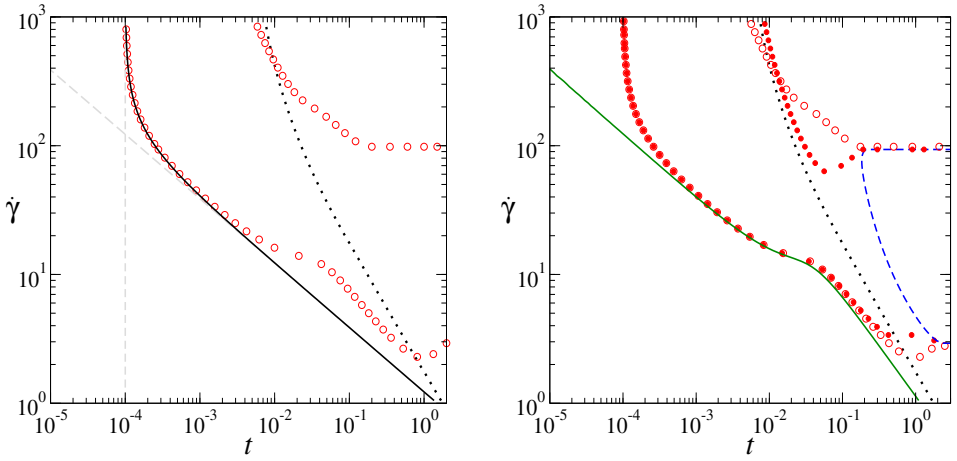

Figure 5.4.2: Portraits of shear startup in the sRP model with homogeneity enforced. A horizontal slice is a single startup run, and we plot the times at which: the shear stress undergoes an overshoot $\partial_t \Sigma = 0$ (dotted line); the times at which the largest eigenvalue from linear stability crosses zero $\omega = 0$ (large, open circles). In (a) we additionally plot lines marking: $t_s = \frac{3}{2\tau_d \dot{\gamma}^2} + \eta/G$ (solid) and individual components of this $t_s = \eta/G, \frac{3}{2\tau_d \dot{\gamma}^2}$ (dashed) due to 'viscous' and 'elastic' contributions to linear instability, respectively. In (b) we plot the onset of the 'elastic' (solid line) and 'viscous' (dashed line) conditions, and the 'reduced criterion' (filled circles). Parameters for both (a) and (b): $\beta = 0.1, \eta = 10^{-4}, \tau_R = 10^{-2}$.

small strains ($\gamma^2 \ll 1$, see Appendix II for details) and find that the onset of linear instability to heterogeneity of this 'sRP-specific' instability occurs at a time:

$$t_s = \frac{3}{2\tau_d \dot{\gamma}^2} + \eta/G, \tag{5.4.2}$$

as shown in Figure 5.4.2 (a)[13]. We find that the essential reason for the 'sRP-specific' instability is that the prefactors in the 'elastic' term $-\underline{p}.\underline{\underline{M}}$ change sign (recall Eqn 5.4.1, and see Appendix II for details). This accounts for the first term in Eqn 5.4.2. The second term restabilises the system at very short times $t < \eta/G$ and arises due to the non-zero 'viscous' term of Eqn 5.4.1 that, in this linear elastic regime, obeys $\partial_{\dot{\gamma}} \Sigma|_\gamma \to \eta$.

This result indicates that prefactors of derivatives in the criterion can result in linear instability. However, we actually find that this 'sRP-specific' instability does

[13]In Figure 5.4.2, different parameters from those in Figure 5.4.1 were chosen to show more clearly the agreement of Eqn 5.4.2 with the onset of the linearly unstable regime.

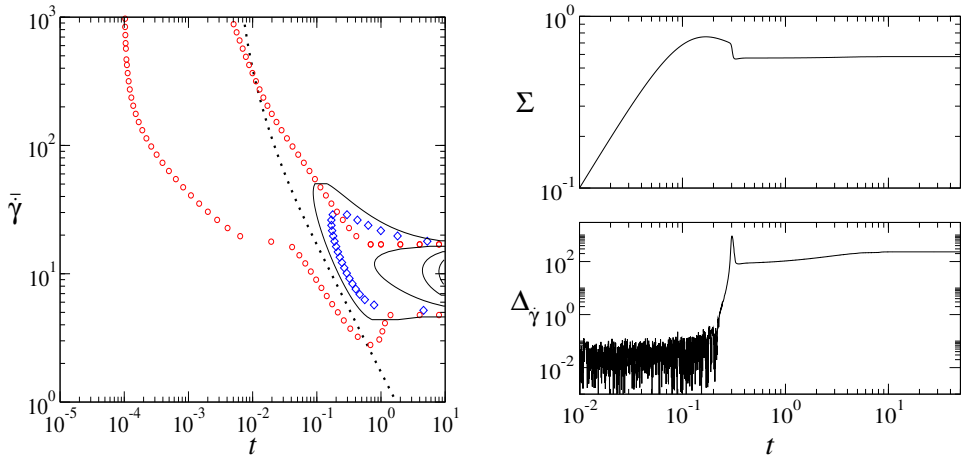

Figure 5.4.3: (a) as Figure 5.3.4 for the sRP model with $\beta = 0.4$, $\eta = 10^{-4}$, $\tau_R = 10^{-2}$, $q = 5 \times 10^{-3}$. Solid lines show contours of equal $|\delta\dot{\gamma}_n| = \dot{\gamma}10^M$ found by integrating Eqn 5.2.6, contour nearest $\partial_t \Sigma = 0$ is $M = -2$, and we show only contours $M \geq -2$. (b) Response of the total shear stress and 'degree of banding' to shear startup at rate $\dot{\bar{\gamma}} = 10$ in the sRP model with noise added continuously using methods described in Chapter 3; $\beta = 0.4$, $\eta = 10^{-4}$, $\tau_R = 10^{-4}$, $q = 10^{-3}$. Noise added at every time step to all components of $\underline{s}$ of the form: $q\underline{X}\sqrt{dt}\cos(\pi y/L)$, where $\underline{X}$ is an array of random numbers selected from a flat distribution with zero mean and unit width, and $dt = 10^{-6}$ is the timestep.

not result in significant growth of heterogeneous perturbations, as shown in Figure 5.4.3. Here, we show the contours of the absolute value of shear rate perturbations in the linearised system $|\delta\dot{\gamma}_k|$ (found by integrating Eqn 5.2.6), and also show the region of 'significant' shear banding [as before, the 'significant' threshold is defined as $(\dot{\gamma}_{max} - \dot{\gamma}_{min})/\dot{\bar{\gamma}} = 0.05$] in the nonlinear system. Neither of these measures of shear rate heterogeneity indicate significant growth of heterogeneous shear rate perturbations inside the region of the 'sRP-specific' instability. This may be due to the (relatively) small value of the largest growth rate ω, and the short time over which it is positive.

Continuous noise

We also investigate the addition of continuous noise, as described in Chapter 3. An example of shear startup in the RP model with continuously added noise is shown in (b) of Figure 5.4.3. In general, we find qualitatively similar behaviour of the 'degree of banding' in the RP model with continuous noise as with initial noise.

5.4.1 Summary of RP model response to shear startup

In summary, we have shown that the RP model shows time-dependent shear banding during shear startup for shear rates in the non-stretching regime $\tau_d^{-1} \ll \dot{\gamma} \ll \tau_R^{-1}$. This time-dependent shear banding is caused by the 'elastic' condition from the general criterion (Eqn 5.2.7) being met — this is caused by the negative slope of the shear stress *vs.* strain. This time-dependent shear banding persists to steady state for shear rates in the negative slope of the constitutive curve, which satisfy the 'viscous' condition at steady state, and also for any other shear rates in the range of the stress plateau, for which the system is meta-stable with respect to the formation of steady state shear bands. Recall Chapter 2. These results, in addition to the results of Adams *et al.* [2–4], show that the RP model has qualitatively similar behaviour to that found in experiments of entangled polymeric fluids. (Recall that such materials include concentrated solutions or melts of high molecular weight polymers, and concentrated solutions of wormlike micelles or DNA.) In particular, the RP model is capable of showing the following specific features found in experiment:

(i) shear banding that arises during the decrease of shear stress in strain and persists to steady state, where the magnitude of banding during the stress decrease in strain is far greater than that at steady state, even showing elastic recoil resulting in negative local shear rates or velocities [18, 19, 136, 138, 162]. This was shown in the RP model by Adams *et al.* [2–4] for imposed shear rates in the negative slope of a nonmonotonic constitutive curve; see also the bottom row of Figure 5.3.2.

(ii) transient shear banding that arises during the negative slope of shear stress in strain but returns to homogeneity at steady state, for imposed shear rates that are slightly larger than those that result in steady state banding (i.e., shear rates larger than those on the stress plateau) [19, 138]. This is shown in the RP model in Figure 5.3.5 by e.g., a horizontal slice at $\overline{\dot{\gamma}} = 600$ in the figure.

(iii) transient shear banding that arises during the negative slope of shear stress in strain but returns to homogeneity at steady state [19, 77, 138]. This was

shown in the RP model by Adams *et al.* [2] for values of β, η that result in a monotonic constitutive curve; see also Figure 5.3.2 (top row).

On this basis, we consider the RP model to be capable of qualitatively describing the experimental literature concerning entangled polymeric fluids.

5.5 Giesekus model

In this section we will investigate the time-dependent linear stability to heterogeneity and the resulting shear banding behaviour of the Giesekus model. This model has been successfully used to describe sweeps on the flow curve [173] and steady state shear banding in wormlike micelles [70, 71], and the stress relaxation behaviour of polymeric materials following a step strain [13, 83]. We aim to address whether the Giesekus model is capable of modelling the time-dependent shear banding properties specific to entangled polymeric fluids that are described above. Specifically, we address (i) and (iii) of the properties above. For reference, we show the (monotonic/nonmonotonic) constitutive curves for two values of the model's parameter $\alpha = 0.6, 0.8$ (respectively); this parameter denotes the extent to which anisotropy causes anisotropic drag on dumbbells, see Chapter 3.

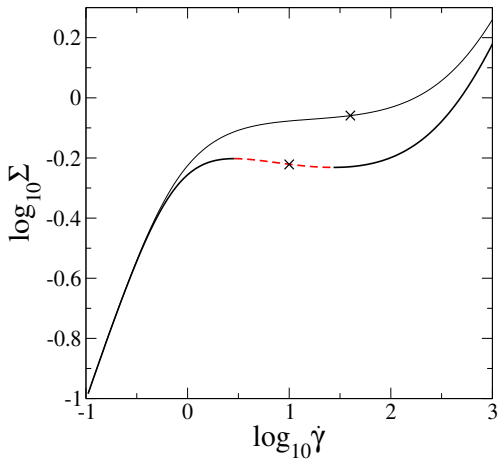

Figure 5.5.1: Constitutive curves for the Giesekus model with $\alpha = 0.6, 0.8$ (top to bottom) and $\eta = 10^{-3}$. Negative slope (linearly unstable at steady state) shown in a dashed line. Crosses at a shear rates $\dot{\gamma} = 10, 40$, for which time-dependent behaviour is shown in Figures 5.5.2 and 5.5.3, respectively.

Property (i):

Does the Giesekus model show banding that persists to steady state but is strongest during the negative slope of shear stress in strain $\partial_\gamma \Sigma < 0$?

We show in Figure 5.5.2 (a) the response during shear startup of the total shear stress (where both responses of the homogeneously constrained system and the system with heterogeneity allowed[14] are shown); the largest eigenvalue from linear stability analysis ω in (b); the 'degree of banding' $\Delta_{\dot{\gamma}}$ in (c); and corresponding snapshots of the velocity profile in (d). The parameters[15] α, η in Figure 5.5.2 are chosen to give a nonmonotonic constitutive curve with the imposed shear rate chosen from its negative slope $\partial_{\dot{\gamma}} \Sigma < 0$, as shown in Figure 5.5.1 (in order to allow comparison with the response of the RP model for a similar constitutive curve/imposed shear rate as shown in the bottom row of Figure 5.3.2). We find that while the total shear stress response in strain is qualitatively similar to that of the RP model, the linear instability and resulting shear banding behaviour is not. In the Giesekus model the largest eigenvalue does not show a large, positive peak during the negative slope of stress in strain; rather, the system is linearly stable to heterogeneity during most of this stress decrease. As a result, banding only becomes 'significant' as the steady state is neared and the steady state 'viscous' condition is met ($\partial_{\dot{\gamma}} \Sigma|_{\gamma \to \infty} < 0$). This is in contrast to the first specific feature of entangled polymeric materials described above.

Property (iii):

Does the Giesekus model show transient shear banding for a system that is stable to banding at steady state?

The response to a shear rate in the weakest slope of a monotonic constitutive curve (see Figure 5.5.1, $\dot{\gamma}$ chosen to compare with the response of RP model as shown in the top row of Figure 5.3.2) is shown in Figure 5.5.3. We find that the

[14] To do this we allow heterogeneity in the flow-gradient direction and add diffusion terms to the governing equations of $\underline{s}$, as described in Chapter 3.

[15] Where $0 \leq \alpha \leq 1$ is the anisotropy parameter in the Giesekus model; with $\alpha = 0$ the Giesekus model reduces to the Upper Convected Maxwell model representing isotropic drag on dumbbells, see Chapter 3. η is the usual Newtonian solvent viscosity and λ is the relaxation time in the model which we set to 1 throughout.

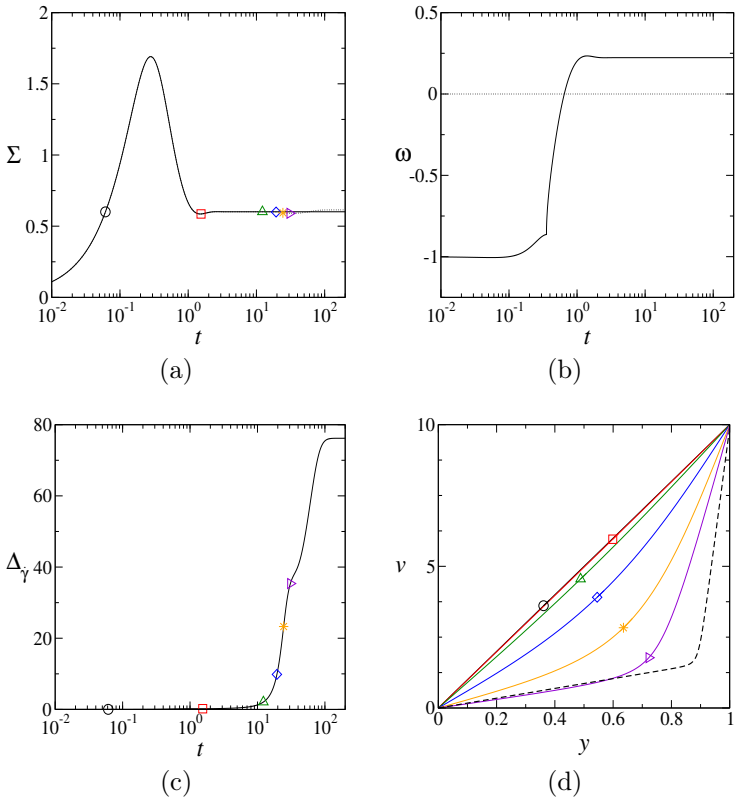

Figure 5.5.2: Response of the Giesekus model during shear startup at $\overline{\dot\gamma} = 10$ chosen from the negative slope of a nonmonotonic constitutive curve with $\alpha = 0.8, \eta = 10^{-3}$. (a) total shear stress (results with heterogeneity allowed are indistinguishable from the homogeneously constrained system). (b) largest real part of any eigenvalue from linear stability analysis ω. (c) 'degree of banding' $\Delta_{\dot\gamma} = \dot\gamma_{max} - \dot\gamma_{min}$. (d) snapshots of the velocity profile at strains with corresponding symbols in (a), (c); steady state velocity profile in a thick, dashed line. Noise added initially to all components of $\underline{s}$ of the form $q\underline{X}\cos(\pi y/L)$, where $q = 10^{-2}$ and $\underline{X}$ is an array of random numbers selected from a flat distribution with zero mean and unit width.

system is always linearly stable to shear heterogeneity and as such no 'significant' shear banding arises. For example, in Figure 5.5.3 the maximum 'degree of banding' as a fraction of the imposed shear rate is $\Delta_{\dot\gamma}/\dot\gamma = 1/40$, which would be hard to detect in experiment. In fact, in an exploration of parameter space $\{\alpha, \eta\}$ we have never found any transient linear instability to shear heterogeneity (that does not persist to steady state) related to the 'elastic' term being negative that results in significant shear banding. These results are in contrast to the second specific feature of entangled polymeric systems described above, and also to the results of the RP model.

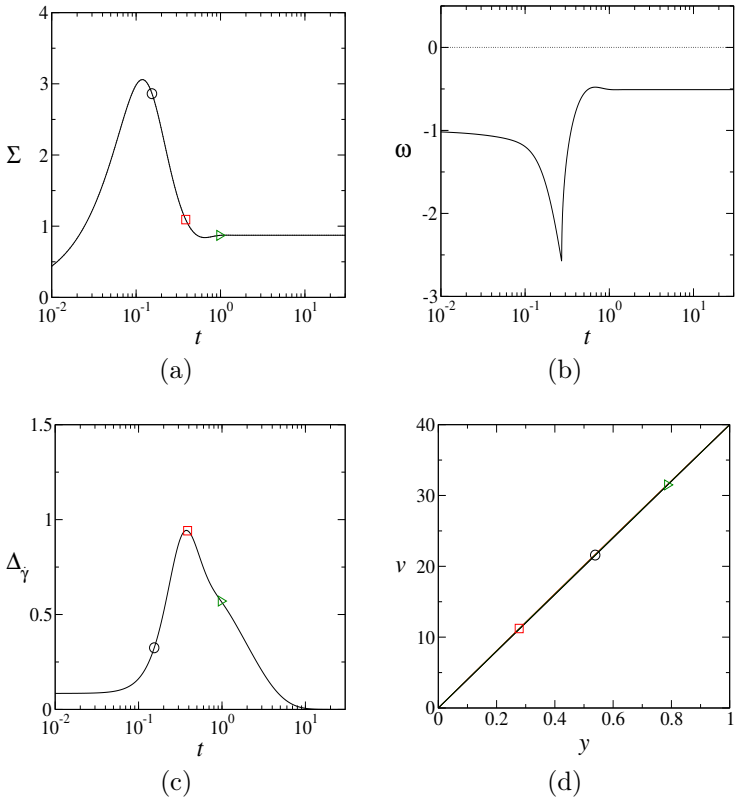

Figure 5.5.3: As Figure 5.5.2, with $\overline{\dot{\gamma}} = 40$ chosen to be at the weakest slope of a monotonic constitutive curve engineered by choosing $\alpha = 0.6$ and $\eta = 10^{-3}$.

In summary, we have shown that despite the Giesekus model being capable of describing both the stress *vs.* strain or shear rate relationships of entangled polymeric materials, it is not an appropriate model for describing the *time-dependent* linear instability and resulting shear banding behaviour of such materials. This is perhaps not surprising due to its phenomenological origin lacking any reference to the entanglements now well understood to dominate the rheological response of these materials [47]. However, that the model shows only steady state shear banding may render it useful for modelling other materials with such properties.

'Elastic' or 'viscous' instability?

As explained above, although the Giesekus model shows shear stress overshoots in strain, it is generally linearly stable to heterogeneity during the negative slope $\partial_\gamma \Sigma < 0$. We investigate why this is by examining the 'elastic', 'viscous' and 'cross'

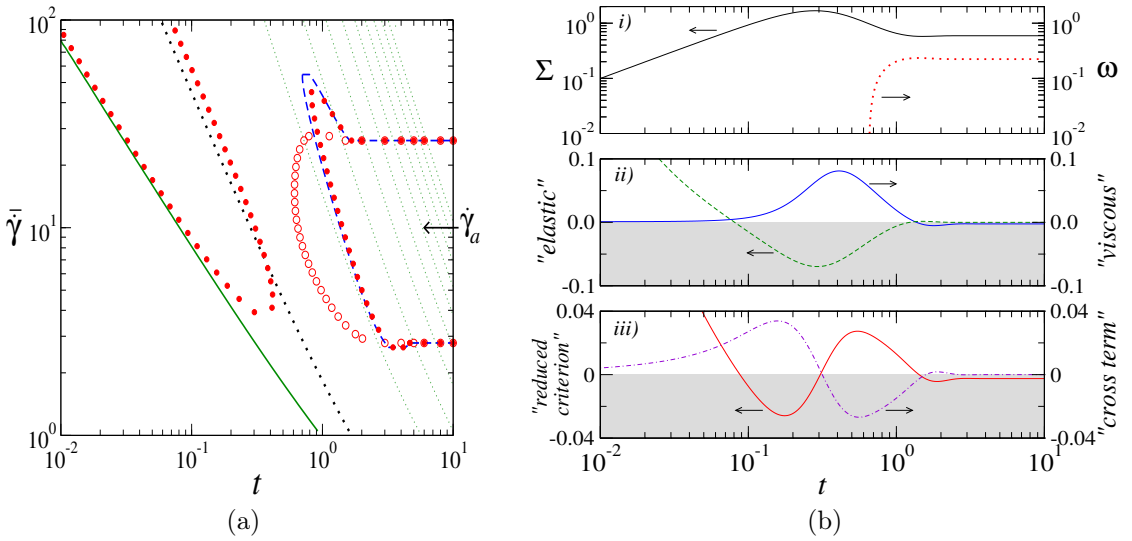

Figure 5.5.4: (a) Shear startup in the (homogeneously constrained) Giesekus model where a horizontal slice denotes a single startup run at fixed $\overline{\dot{\gamma}}$ with $\alpha = 0.8$, $\eta = 10^{-3}$. We plot the strains at which: the stress is maximal [(I) in Section 5.3] (black dotted line); the largest eigenvalue crosses zero (II) (large open circles); the 'elastic' condition is met (III) (solid line shows principle onset and thin dotted lines show subsequent weak oscillations); the 'viscous' condition is met (IV) (dashed line); and the 'reduced criterion' is met (V) (small, filled circles). (b) Response to shear startup at rate $\dot{\gamma}_a = 10$ of *i*) the total stress and largest eigenvalue; *ii*) the 'elastic' and 'viscous' terms ($-\underline{p}.\underline{\underline{M}}.\partial_\gamma \underline{s}$ and $\partial_{\dot{\gamma}}\Sigma|_\gamma$, respectively); *iii*) the 'reduced criterion' and 'cross' term (sum of 'elastic' and 'viscous' terms, and $-\dot{\gamma}\,\underline{p}.\underline{\underline{M}}.\partial_{\dot{\gamma}}\partial_\gamma \underline{s}$, respectively).

terms (left to right in the below) in the criterion[16]:

$$\partial_{\dot{\gamma}}\Sigma|_\gamma - G\,\underline{p}\cdot\underline{\underline{M}}^{-1}\cdot(\partial_\gamma \underline{s}|_{\dot{\gamma}} + \dot{\gamma}\partial_{\dot{\gamma}}\,\partial_\gamma\,\underline{s}) < 0, \tag{5.5.1}$$

and remind the reader that we refer to the 'reduced criterion' as Eqn 5.5.1 with the 'cross' term neglected.

Due to the nonlinear relaxation terms in its governing equations (Eqns 3.2.8) the Giesekus model does not reach a limiting shear startup function $\Sigma(\gamma)$ at high shear rates, and as a result the 'elastic' term does not dominate the criterion during the negative slope of shear stress in strain. In fact, we will show below that a delicate interplay between all three 'elastic', 'viscous' and 'cross' terms results in only steady state (rather than any time-dependent) shear banding.

We show the usual portrait for the Giesekus model in Figure 5.5.4 (a), in which

[16]Note that the Giesekus model is a three dynamical variable model with $\underline{s} = (\sigma_{xy}, \sigma_{xx}, \sigma_{yy})^T$.

a horizontal slice is a single shear startup run and we plot the various features (I),...,(V) described in Section 5.3. We also show the time-dependent behaviour of the terms in the criterion (Eqn 5.2.7) in (b) of the Figure[17]. The portrait shows that the region predicted to be linearly unstable by the 'reduced criterion' is in extremely poor agreement with the full criterion (compare small, filled circles with large, open circles). This indicates that the 'cross' term plays an important role in the linear stability properties of the Giesekus model, as also shown in iii) of (b): the cross term is of near equal and opposite value to the 'reduced criterion' throughout. Note that the unusual oscillation of the 'reduced criterion' is due to the combination of the 'elastic' and 'viscous' terms: the Giesekus model shows a peak in the gradient of the instantaneous constitutive curve during the negative slope of the stress in strain that cancels out the contribution of the 'elastic' term during that time. The combination of these oscillations essentially results in linear stability until gradients $\partial_\gamma \to 0$ as the steady state is neared.

5.6 Scalar fluidity model

Shear startup with homogeneity enforced

The scalar fluidity model incorporates the fundamental features found in soft glassy materials of ageing and shear induced rejuvenation. The governing equation (Eqn 3.2.16) for the viscoelastic shear conformation variable[18] $\sigma(\Delta t)$ contains a loading term dependent on the shear rate, and a term for stress relaxation on a timescale $\tau(\Delta t)$ that has its own governing equation (Eqn 3.2.15). During rest, this relaxation time increases linearly $\tau \sim t_w$ ('ageing'); however, with a non-zero shear rate the relaxation time is 'rejuvenated' by flow; at steady state[19] $\tau_{ss} \sim 1/\dot{\gamma}$.

For now we artificially enforce homogeneous flow, but will later allow heterogene-

[17]When the 'elastic', 'viscous' etc., conditions are negative they contribute towards linear instability in the criterion — thus we have shaded this region to aid the eye.

[18]Recall from Chapter 3 that the total shear stress (or simply the 'stress') Σ is composed of the viscoelastic shear stress and a Newtonian solvent contribution: $\Sigma(t) = G\sigma(t) + \dot{\gamma}\eta$; in all cases we consider small Newtonian viscosities $\eta \ll \tau_0 G$, where we set both the microscopic relaxation time (τ_0) and the elastic modulus (G) to 1 throughout. We remind the reader that the time elapsed since the onset of shear is $\Delta t = t - t_w$, where t_w is the sample age.

[19]Throughout we will consider $t_w \gg \tau_0$ and $\dot{\gamma} \ll \tau_0^{-1}$.

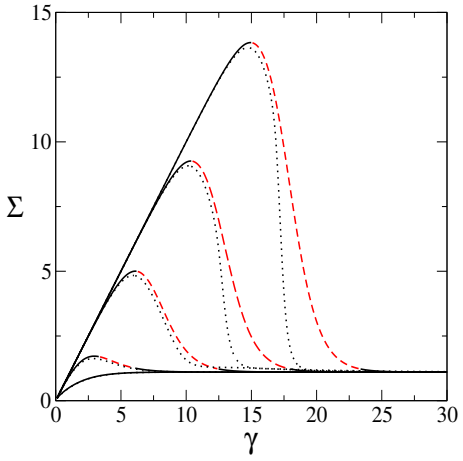

Figure 5.6.1: Total shear stress response to shear startup at $\overline{\dot{\gamma}} = 0.1$ in the scalar fluidity model for waiting times $t_w = 10^{0,2,4,6,8}$ (left to right peaks). Solid/dashed lines: homogeneity enforced (dashed where linearly unstable to shear heterogeneity); dotted lines: response with heterogeneity allowed. Parameters: $\eta = 0.05$, noise added initially in heterogeneous system to $\sigma(t = 0, y)$ of the form $q\underline{X}\cos(\pi y/L)$, where $q = 10^{-2}$ and $\underline{X}$ is an array of random numbers selected from a flat distribution with zero mean and unit width.

ity in the flow gradient direction (as described in Chapter 3). Within this constraint of homogeneous shear and for a constant imposed shear rate $\dot{\gamma}$, exact analytical solutions for the time dependent responses of $\tau(\Delta t)$ and $\sigma(\Delta t)$ in the scalar fluidity model can be derived, see Appendix III. In the shear rate limits of interest $t_w^{-1} \ll \dot{\gamma} \ll \tau_0^{-1}$ these are:

$$\tau(\Delta t) = t_w \exp\left(-\dot{\gamma}\Delta t\right) + \frac{1}{\dot{\gamma}}, \tag{5.6.1}$$

$$\sigma(\Delta t) = \frac{e^{\dot{\gamma}\Delta t} + \dot{\gamma}^2 t_w \Delta t - 1}{e^{\dot{\gamma}\Delta t} + \dot{\gamma} t_w}, \tag{5.6.2}$$

which show that for 'slow' imposed shear rates $\dot{\gamma} \ll t_w^{-1}$ the total shear stress increases monotonically in time, while for 'fast' imposed shear rates $\dot{\gamma} \gg t_w^{-1}$ age-dependent stress overshoots are seen, as shown in Figure 5.6.1. It can be shown that (to within a small correction) the value of the shear stress Σ^* and the strain $\gamma^* = \dot{\gamma}\Delta t^*$ at the stress maximum increase logarithmically with the imposed shear rate and waiting time: $\Sigma^* \sim G\gamma^* \sim G\log(\dot{\gamma} t_w)$; see Appendix IV for proof of this result, credit for which is given to Dr. Suzanne Fielding. These results are consistent with those of the SGR model [62] and molecular dynamics simulations in a Lennard-

Jones glass [165], and similar to experimental results in carbopol gels showing Σ^*, γ^* to be weak power laws of $\dot{\gamma}$ for $\dot{\gamma} \gg t_w^{-1}$ [43].

Shear startup with heterogeneity allowed

Much of the research concerning shear banding in soft glassy materials has focused on steady state shear banding observed in 'thixotropic' yield stress fluids (YSF) for imposed shear rates below some 'critical' value: $\dot{\gamma} < \dot{\gamma}_c$ [37, 51, 107, 114, 126, 141], as explained in Chapter 2. It is thought that an underlying negative slope in the constitutive curve is responsible for these results [34–36, 57, 103, 106, 112, 128, 141]. However, recent experiments have also shown *transient* shear banding (that returns to a state of homogeneous shear at steady state) associated with the shear stress overshoot in so-called 'simple' YSF[20] [43, 45] and has also been found in simulations of the SGR model [116]. Similar transient shear banding has also been reported in 'thixotropic' YSF for imposed shear rates $\dot{\gamma} > \dot{\gamma}_c$ [107].

Motivated by these results, we investigate the linear stability to shear heterogeneity in the scalar fluidity model which, owing to its monotonic constitutive curve, is linearly stable to shear heterogeneity at steady state (and is thus an appropriate model for 'simple' YSF, see Chapter 2). We perform a linear stability analysis about the time-dependent homogeneous background state (as described in Chapter 3) and find that the strains for which the system is linearly unstable to shear heterogeneity correspond closely to those for which the stress is a decreasing function of strain $\partial_\gamma \Sigma < 0$, as shown in Figure 5.6.1. The stress response with heterogeneity in the flow gradient direction allowed (using methods described in Chapter 3) is also shown in Figure 5.6.1, and shows an accelerated stress relaxation at strains for which significant shear heterogeneity is present. We show snapshots of the velocity profile at various strains during shear startup for the $t_w = 10^6$ sample in Figure 5.6.2 (b). In agreement with the region of linear instability, significant transient shear banding arises during the negative slope of the stress in strain. Indeed, elastic-like negative velocity recoil is seen whereby, although the spatially averaged shear rate is posi-

[20] Note that the term 'simple' as opposed to 'thixotropic' implies that these materials have no age-dependence; this nomenclature is misleading as 'simple' YSF have also shown age-dependent responses to deformation [43].

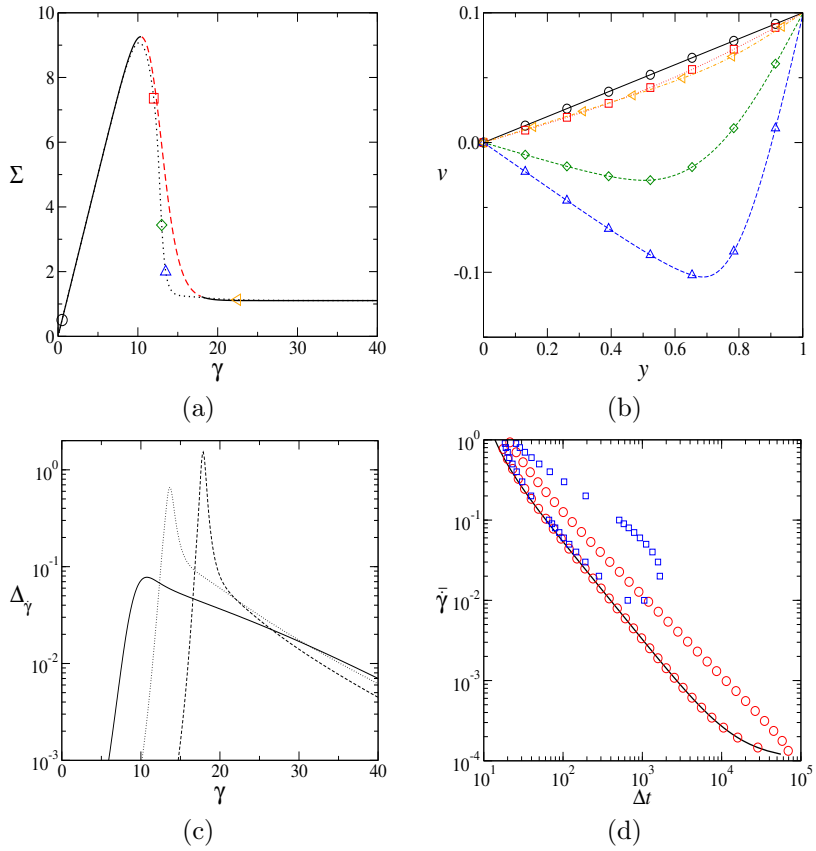

Figure 5.6.2: (a) Stress response to shear startup from Figure 5.6.1 for the run with $t_w = 10^6$. (b) Snapshots of the velocity profile at strains with corresponding symbols to those in (a). (c) Response of the 'degree of banding': $\Delta_{\dot{\gamma}} = \dot{\gamma}_{max} - \dot{\gamma}_{min}$ for $t_w = 10^{4,6,8}$ (left to right peaks). (d) Portrait in which a horizontal slice is a single startup run at rate $\bar{\dot{\gamma}}$ for waiting time $t_w = 10^4$. A solid line shows the time Δt at which $\partial_t \Sigma = 0$. Open circles delimit the region inside which the system is linearly unstable to heterogeneity; squares inside which the degree of banding is 'significant', i.e., more than 5% of $\bar{\dot{\gamma}}$. Other parameters as in Figure 5.6.1.

tive, the local velocity in some parts of the cell is negative. Similar results were also found in the RP model in Section 5.3, and have been shown to arise in experiments of entangled polymeric materials [19]. As before, we quantify the magnitude to which the system displays shear rate heterogeneity by determining the 'degree of banding' defined as the difference between the maximum and minimum local shear rate $\Delta_{\dot{\gamma}} \equiv \dot{\gamma}_{max} - \dot{\gamma}_{min}$. This is shown in Figure 5.6.2 (c) as a function of strain for three values of the waiting time; clearly the maximum attained magnitude of shear banding increases with the waiting time t_w.

We also show a similar 'portrait' to those introduced in Chapter 4 and used in Section 5.3, where horizontal slices represent a single shear startup run at rate $\dot{\gamma}$

and the times Δt (or strains γ) at which interesting features arise are plotted. In (d) of Figure 5.6.2 we show results from the homogeneously constrained system where we plot: the time at which the stress overshoot occurs as a solid line (Δt at which $\partial_t \Sigma = 0$), and the times for which the system is linearly unstable to heterogeneity (i.e., $\omega > 0$, the largest eigenvalue from linear stability is positive), here shown inside the region delimited by open circles. From the system with heterogeneity allowed (see Chapter 3 for details), we additionally plot the times for which 'significant' shear banding arises, here shown inside the region delimited by open squares. As before, we define banding to be 'significant' if the degree of banding is more than 5% of the imposed shear rate: $\Delta_{\dot{\gamma}} > 0.05\,\overline{\dot{\gamma}}$. Note that for low shear rates the system does not show 'significant' transient shear banding despite the system being linearly unstable to heterogeneity. For these low shear rates we find that the diffusive terms that are neglected in the linear stability analysis provide a weakly stabilising contribution to the growth of shear heterogeneity that becomes important at these long times. (This is the only place in this thesis that the neglect of the diffusive terms causes such a major discrepancy.)

'Fluidisation' time, τ_{f}

Manneville and co-workers [45] found that the time (called the 'fluidisation time', τ_{f}) at which carbopol gel returns to a state of homogeneous shear after transient shear banding follows $\tau_{\mathrm{f}} = \beta\dot{\gamma}^{-\alpha}$, with $\alpha \sim 2$ - 3. We briefly explore the fluidisation time in the scalar fluidity model, where we define τ_{f} as the time Δt at which the 'degree of banding' returns to a value less than 1% of the imposed shear rate[21]. We find that τ_{f} follows a relation of the same form $\tau_{\mathrm{f}} \sim \beta\dot{\gamma}^{-\alpha}$, but with $\alpha \sim O(1)$.

[21] Note that elsewhere in this thesis we have used a 5% cutoff value for the degree of banding as a percentage of the imposed shear rate in order to distinguish between 'significant' and 'non-significant' shear banding. However, we find that the value of α does not depend on the percentage cutoff value (for small cutoff values $< 5\%$), and we therefore use a smaller cutoff percentage to obtain a larger region over which to find a power law fit.

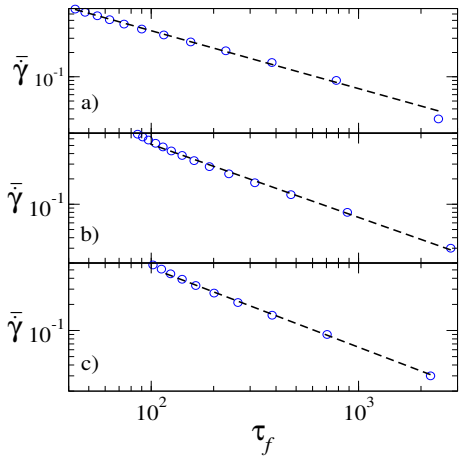

Figure 5.6.3: Portraits denoting the 'fluidisation time' $\tau_{\rm f}$, defined as the time at which the system returns to a state of relative homogeneity [defined as $(\dot{\gamma}_{max} - \dot{\gamma}_{min})/\dot{\bar{\gamma}} = 0.01$] after transient banding during startup at rate $\dot{\bar{\gamma}}$ in the scalar fluidity model with (a) $t_w = 10^4$, (b) $t_w = 10^6$, (c) $t_w = 10^8$ (other parameters as in Figure 5.6.1). Thin solid line: power law fit $\tau_{\rm f} = \beta\dot{\gamma}^{-\alpha}$ with $\alpha = 0.72, 0.87, 0.91$, $\beta = 10.1, 28.3, 35.01$ for (a, b, c) respectively.

'Viscous' or 'elastic' instability?

We now briefly examine the linear stability properties of the scalar fluidity model in the context of the 'elastic', 'viscous' and 'cross' terms (left to right terms) of the criterion:

$$\partial_{\dot{\gamma}}\Sigma|_{\gamma} - G\,\underline{p}\cdot\underline{\underline{M}}^{-1}\cdot(\partial_{\gamma}\underline{s}|_{\dot{\gamma}} + \dot{\gamma}\partial_{\dot{\gamma}}\,\partial_{\gamma}\,\underline{s}) < 0. \tag{5.6.3}$$

In Section 5.2 we discussed the high shear rate limit of the criterion. We showed that if the material obtains a limiting shear startup function $\Sigma(\gamma)$ independent of the shear rate then the 'elastic' condition (Eqn 5.2.8) for the onset of linear instability applies since all other terms with derivatives $\partial_{\dot{\gamma}} \to 0$. Recall that the elastic condition indicates that negative slopes of stress in strain contribute towards linear instability to shear banding. However, in the scalar fluidity model the stress overshoot is not a purely elastic phenomenon, but a result of competition between elastic stress growth and stress relaxation due to plastic rearrangements. As a result, the material does not obtain a limiting shear startup function $\Sigma(\gamma)$: we showed above that the shear stress at the overshoot increases with the shear rate. This means that contributions to the criterion (Eqn 5.6.3) of the 'viscous' and 'cross' terms are non-negligible during the negative slope of shear stress in strain. As we also found in the

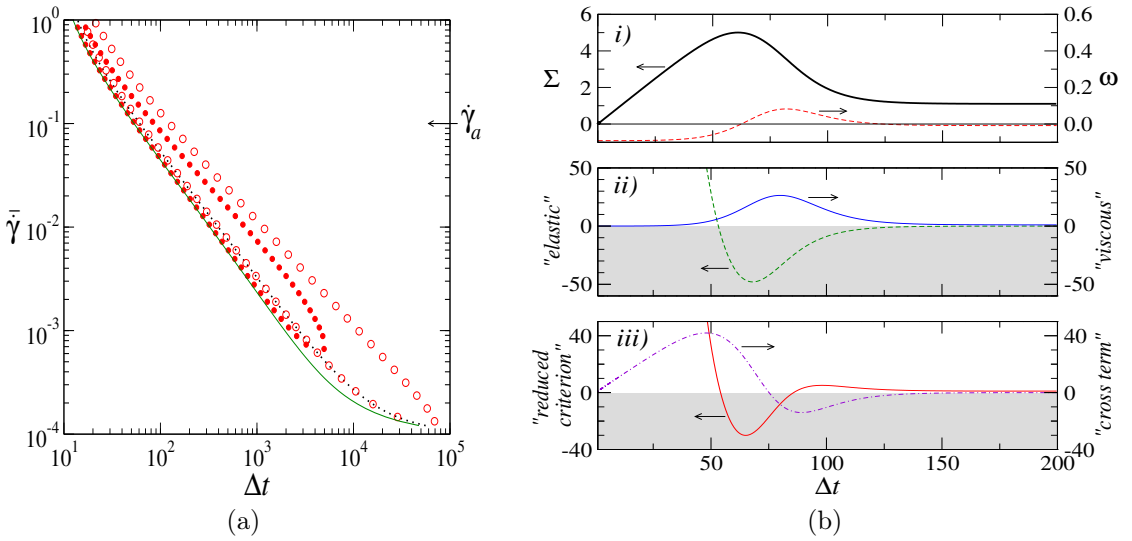

Figure 5.6.4: As Figure 5.5.4 for the scalar fluidity model with $t_w = 10^4$, $\eta = 0.05$ (recall that $\Delta t = t - t_w$). (b) Time-dependent response to a shear rate $\dot{\gamma}_a = 0.1$.

Giesekus model, this results in significant stabilising contributions of the 'cross' and 'viscous' terms to the criterion during the negative slope of stress in strain. However, we find that in the case of the scalar fluidity model the interplay of the 'elastic', 'viscous' and 'cross' terms results in linear instability to heterogeneity onset *at* the overshoot, as shown in Figure[22] 5.6.4. We find that the 'viscous' term provides only a stabilising contribution, indicating that transient shear banding is not caused by a transient nonmonotonicity in the instantaneous constitutive curve formed at a fixed strain $\Sigma(\dot{\gamma})|_\gamma$.

In Section 5.3 we discussed the instantaneous constitutive curve formed at a fixed *time* $\Sigma(\dot{\gamma})|_t$. We showed that in the nRP model the negative slope in shear stress in strain $\partial_\gamma \Sigma|_{\dot{\gamma}} < 0$ arises concurrently with the negative slope in this instantaneous constitutive curve $\partial_{\dot{\gamma}} \Sigma|_t < 0$. We find a similar results in the scalar fluidity model: it can be shown that the strain at which both overshoots occur (i.e., the strain γ at which $\partial_\gamma \Sigma|_{\dot{\gamma}} = 0$ and $\partial_{\dot{\gamma}} \Sigma|_t = 0$) is approximately the same, see Appendix V. Thus, it follows that if the negative slope of the shear stress in strain is linearly unstable to shear heterogeneity, so too will be the negative slope of the instantaneous constitutive curve formed at a fixed *time*; we demonstrate the latter

[22]When the 'elastic', 'viscous' etc., conditions are negative they contribute towards linear instability in the criterion — thus we have shaded this region to aid the eye.

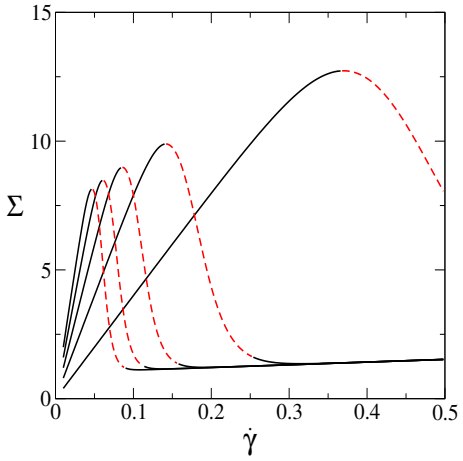

Figure 5.6.5: 'Instantaneous' constitutive curves $\Sigma(\dot{\gamma})|_{\Delta t_{inst}}$ (see text) in the scalar fluidity model (with homogeneity enforced) with $t_w = 10^6$ at time instants (right to left peaks): $\Delta t_{inst} = 40, 80, 120, 160, 200$. Dashed where linearly unstable to shear heterogeneity. $\eta = 0.05$.

in Figure 5.6.5. [In the language of the analysis of strain and strain rate derivatives of the total shear stress $\Sigma = f(\gamma, \tau\dot{\gamma}) = f(\dot{\gamma}t, \tau\dot{\gamma})$ in Section 5.3.2, this result is due to[23] $f_2 \ll f_1$ during the negative slope of shear stress in strain.] These results are consistent with experimental findings in SGMs showing transient shear banding associated with the negative slope of an 'instantaneous' constitutive curve formed at a fixed time [107]. These experimental results appear to bolster the suggestion that this transient nonmonotonicity in the constitutive curve could be the cause of instability to transient shear banding. However, in this chapter we have shown that transient shear banding is in general caused by the negative slope of shear stress in strain, which can coincide with the negative slope of the instantaneous constitutive curve formed at a fixed time.

[23]Where f_n denotes partial differentiation of f with respect to its nth argument.

5.7 Glassy polymer model

In Section 4.6 we investigated the rheological response of the glassy polymer model to an imposed stress in order to make comparisons with numerical [58] and experimental [88] results of the equivalent protocol in the extensional geometry. In this section, we explore the rheological response of the model during shear startup.

Recall from Chapter 3 that within the model the total shear stress is composed of a Newtonian solvent stress, plus solvent (s) and polymer (p) viscoelastic shear stresses:

$$\Sigma = G^p \sigma^p + G^s \sigma^s + \eta \dot{\gamma}, \tag{5.7.1}$$

where $G^{p,s}$ are the polymer and solvent elastic moduli. The solvent and polymer viscoelastic stresses each obey fluidity-like governing equations (Eqns 3.2.20, 3.2.19) with relaxation times that are proportional to one another[24] $\tau^p(\Delta t) = \tau^s(\Delta t)/\alpha$, and $\tau^s(\Delta t)$ has its own governing equation (Eqn 3.2.21) that incorporates ageing and shear induced rejuvenation. Note that since $\alpha \sim 0$ the polymer viscoelastic shear stress increases linearly in strain indefinitely $\Sigma^p \simeq G^p \gamma$. The total, polymer and solvent shear stress and first normal stress difference $N_1 = \Sigma_{xx} - \Sigma_{yy}$ responses during shear startup are shown in Figure 5.7.1. In this figure we use parameter values that were carefully fitted to experimental results by Fielding *et al.* in Ref. [58], and chose an imposed shear rate $\dot{\gamma} \ll \tau_0^{-1}$. We also allow heterogeneity in the flow gradient direction by the methods described in Chapter 3. The total shear stress response shows a maximum followed by a minimum and an indefinite rise known as strain hardening. Our results indicate that the overshoot is caused by the glassy solvent response that has the behaviour of the scalar fluidity model described in Section 5.6, while strain hardening arises from the polymer stress contribution that increases linearly in strain for the shear component (or quadratically for the first normal stress difference).

With regard to shear heterogeneity we find that, for times at which the glassy solvent stress is much larger than the polymer stress $G^s \sigma^s \gg G^p \sigma^p$, the total shear

[24] Recall that for models with waiting time (t_w) dependence we define $\Delta t = t - t_w$, where t is the time elapsed since sample preparation and t_w is the age of the sample.

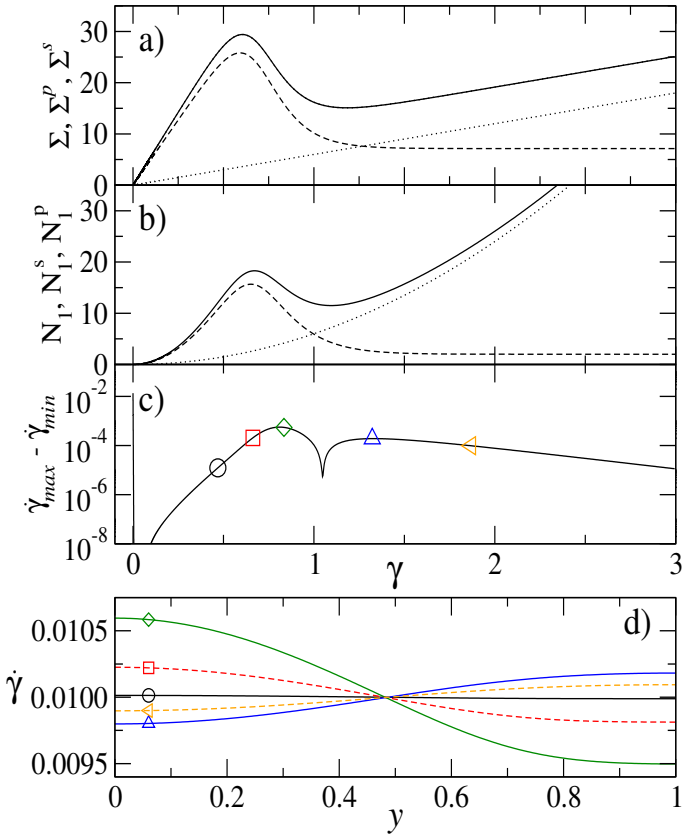

Figure 5.7.1: Shear startup in the GP model with $\overline{\dot{\gamma}} = 10^{-2}$ and heterogeneity allowed in the flow gradient direction. (a) total shear stress Σ (solid), polymer (p) and solvent (s) contributions: $\Sigma^{p,s} = G^{p,s}\sigma^{p,s}$ in dotted, dashed lines, respectively. (b) first normal stress difference N_1 (solid), polymer and solvent contributions: $N_1^{p,s} = G^{p,s}(\Sigma_{xx}^{p,s} - \Sigma_{yy}^{p,s})$ in dotted, dashed lines resp. (c) 'degree of banding' $\Delta_{\dot{\gamma}} = \dot{\gamma}_{max} - \dot{\gamma}_{min}$. (d) snapshots of the flow profile at strains with corresponding symbols in (c). Parameters as used in Ref. [58], see Table 3.1 of Chapter 3. Noise added initially of form: $qX\cos(\pi y/L)$ to all components of the conformation tensor with $q = 0.01$ and X a random number chosen from a flat distribution with width 1 and mean 0. The diffusion length $\ell = 2.5 \times 10^{-2}L$.

stress and the 'degree of banding' ($\Delta_{\dot{\gamma}} = \dot{\gamma}_{max} - \dot{\gamma}_{min}$) behave qualitatively similarly to that of the scalar fluidity model (Section 5.6). This is shown in Figure 5.7.2 where the ratio G^p/G^s is varied: at $G^p/G^s \to 0$ the behaviour of the scalar fluidity model is recovered and 'significant' shear banding arises during the negative slope of shear stress in strain. However, as we similarly found in the step stress protocol (Section 4.6), the polymer provides a stabilising contribution to linear stability by ameliorating the negative slope of total shear stress in strain. Indeed, this may be completely avoided for large enough $G^p \gg G^s$. For this reason, we find that for the parameters used by Fielding *et al.* [58] 'significant' shear banding does not arise, as

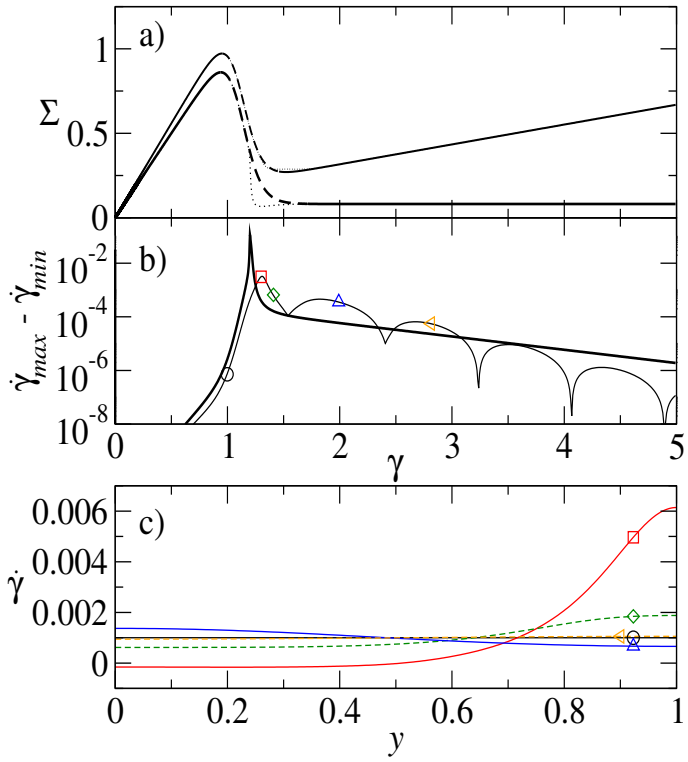

Figure 5.7.2: Startup in the GP model with $G^s, \tau_0 = 1$ and all other parameters as in Figure 5.7.1 (except $\ell = 10^{-2}$). (a) total shear stress Σ with homogeneity enforced in a solid line, dashed where linearly unstable to heterogeneity. Dotted lines: result with heterogeneity allowed. Lower curve: in fluidity model, upper curve: with polymer added, i.e., $G^p/G^s = 0, 1/8.5$, respectively. (b) 'degree of banding' $\Delta_{\dot{\gamma}} = \dot{\gamma}_{max} - \dot{\gamma}_{min}$ (thick: fluidity model, thin: with polymer) with snapshots of the flow profile for the latter at strains with corresponding symbols in (c).

shown in Figure 5.7.1. Note that the 'degree of banding' in the scalar fluidity model is age-dependent (as shown in Figure 5.6.2) and so the 'cut-off' value of G^p/G^s above which 'significant' banding is no longer seen is also age-dependent.

Finally, we note that the addition of polymer results in an oscillation of the 'degree of banding' $\Delta_{\dot{\gamma}}$ that physically represents the high shear rate band oscillating between a position on the left and right hand side of the cell with frequency $\nu = \mu\dot{\gamma}\sqrt{G^s G^p}/(G^s + G^p)$, derived in Appendix VI. The physical origin of this oscillation is not clear, but appears to result from oscillations of the same frequency of the heterogeneous perturbations in the polymer stress, segmental relaxation time and solvent stress that have phases $\pi/2, \pi, 3\pi/2$ (respectively) relative to that of $\Delta_{\dot{\gamma}}$.

5.8 Conclusions

In this chapter we have investigated the rheological response to shear startup of the rolie-poly, Giesekus, scalar fluidity, and glassy polymer models.

First, we derived a criterion for the onset of linear instability to shear heterogeneity during shear startup, the form of which is independent of model or fluid type. In this criterion, we have described the three terms containing derivatives of $\partial_{\dot{\gamma}}\Sigma$, ∂_γ and $\partial_{\dot{\gamma}}\partial_\gamma$ as 'viscous', 'elastic' and 'cross' term contributions to linear instability, respectively. At steady state only the 'viscous' term remains, recovering the well known condition for instability to heterogeneity of a negative slope in the constitutive curve $\partial_{\dot{\gamma}}\Sigma|_{\gamma\to\infty} < 0$ [160]. The 'elastic' term is consistent with numerous reports of time-dependent shear banding during the negative slope of shear stress in strain in soft glassy and entangled polymeric materials [18, 19, 43, 45, 77, 136, 138, 162].

We then investigated this criterion in the non-stretching rolie-poly (nRP) model. We showed that time-dependent shear banding associated with the shear stress overshoot is due to the 'elastic' term becoming negative. This occurs when the shear stress departs from the linear growth in strain and the derivatives $\partial_\gamma\Sigma, \partial_\gamma^2\Sigma < 0$ of shear stress in strain become negative. This is in contrast to recent suggestions that time-dependent shear banding is due to a negative slope of the instantaneous constitutive curve [2, 68, 107]. We found that this 'elastic' term dominates the criterion (resulting in time-dependent shear banding) for shear rates $\tau_d^{-1} \ll \dot{\gamma} \ll G\eta^{-1}$ until the steady state is neared. The system remains linearly unstable to heterogeneity due to the 'viscous' term for shear rates in the negatively sloping regime of the constitutive curve. These results apply in the full model for shear rates in the non-stretching regime $\tau_d^{-1} \ll \dot{\gamma} \ll \tau_R^{-1}$.

In the stretching regime of the model $\dot{\gamma} \gg \tau_R^{-1}$, we find that the 'viscous' and 'cross' terms provide a sufficiently stabilising contribution to the criterion during the regime of negative slope of shear stress in strain to ameliorate the contribution of the 'elastic' term, rendering the system linearly stable against shear heterogeneity. We also showed that prefactors of derivatives ∂_γ in the 'elastic' term can cause linear instability to heterogeneity in the stretching regime, but showed that this 'sRP-specific' instability did not result in any significant time-dependent shear banding.

In summary, the RP model shows time-dependent shear banding due to nonlinear elastic behaviour during shear startup at rates $\tau_d^{-1} \ll \dot{\gamma} \ll \tau_R^{-1}$, that may persist to steady state in any regime of 'viscous' instability for shear rates in the negative slope of the constitutive curve.

We also investigated the rheological response of the Giesekus model during shear startup, specifically with the aim of addressing the time-dependent shear banding properties of the model in comparison to experimental findings of entangled polymeric materials. We showed that the Giesekus model shows only steady state shear banding, without the time-dependent shear banding features commonly seen in entangled polymeric materials. We therefore conclude (as we also found in Chapter 4 for the step stress protocol) that, although the Giesekus model is capable of describing the bulk (spatially averaged) shear stress *vs.* strain or shear rate responses to shear startup, it is not suitable for the description of *time-dependent* shear banding in these materials. That the model shows only steady state shear banding may however render it useful for materials with such properties.

In the scalar fluidity model, age-dependent shear stress overshoots were found for imposed shear rates faster than the inverse waiting time t_w^{-1}. We showed that the resulting negative slope of the shear stress in strain is linearly unstable to heterogeneity, resulting in transient shear banding that shows elastic-like negative velocity recoil.

Finally, we investigated the rheological response of the glassy polymer model during shear startup. We showed that the glassy solvent results in age-dependent shear stress overshoots (with behaviour of the scalar fluidity model of Section 5.6), while the polymeric contribution results in strain hardening that can ameliorate the negative slope of total shear stress in strain and thus decrease the magnitude of transient shear banding observed.

5.9 Appendix I

This appendix details the proof that the viscous terms dominate the criterion in the nRP model at high shear rates $\dot{\gamma} \to \infty$, as described in Section 5.3.1.

At high shear rates prefactors of the elastic term (Eqn 5.2.8) go to zero, so that the viscous term, though small: $\partial_{\dot{\gamma}}\Sigma|_{\dot{\gamma}\to\infty} \to \eta$, cancels out the negative elastic term in the 'reduced criterion' (Eqn 5.2.10). This can be seen more clearly by dividing the 'reduced criterion' (Eqn 5.2.10) by the prefactors of the elastic term, and taking the high shear rate limit $\dot{\gamma} \to \infty$. In this limit the components of $\underline{\underline{M}}$ are expressions linear in $\dot{\gamma}$ so that the 'reduced criterion' becomes (valid at $\dot{\gamma} \to \infty$, and $a, \ldots, d$ are expressions that do not contain terms of $\dot{\gamma}$):

$$\dot{\gamma}\eta(ad - bc) + G\partial_{\gamma}^{2}\,\Sigma|_{\dot{\gamma}} - G(a + d)\partial_{\gamma}\Sigma|_{\dot{\gamma}} < 0. \tag{5.9.1}$$

Therefore, as $\dot{\gamma} \to \infty$ the 'viscous' term (left-most in the above) forms a dominant, stabilising contribution to the criterion so that linear stability to heterogeneity is restored at high shear rates, and the shear rate for which this occurs scales linearly with $G\eta^{-1}$.

5.10 Appendix II

This appendix details the derivation of Eqn 5.4.2 for the onset of linear instability to heterogeneity at small strains $\gamma^2 \ll 1$ and high shear rates $\dot{\gamma} \gg \tau_R^{-1}$ in the RP model, thus describing the onset of the 'sRP-specific' instability of Section 5.4.

At high shear rates $\dot{\gamma} \gg \tau_R^{-1}$ and small strains $\gamma \ll \dot{\gamma}\tau_R$ the stress growth in the stretching RP model follows[25]: $\underline{s} = (\sigma, T, n)^T = (\gamma, \gamma^2 + 3, 1)^T$, leading to $\partial_{\dot{\gamma}}\Sigma|_{\gamma} \to \eta$ and $\partial_{\dot{\gamma}}\partial_{\gamma}\underline{s} \to 0$. The criterion then reduces to: $\eta - G\,\underline{p}.\underline{\underline{M}}.\partial_{\gamma}\underline{s}|_{\dot{\gamma}} < 0$, where (as before) $\underline{\underline{M}} = \partial_{\underline{s}}\,\underline{Q}$ and $\underline{p} = (1, 0, 0)$ is a projection vector for the viscoelastic shear

[25]Where $T \equiv \mathrm{tr}\underline{\underline{\sigma}}$, $n \equiv \sigma_{yy}$ and $\sigma \equiv \sigma_{xy}$.

conformation variable. We find:

$$\underline{\underline{M}} \simeq \begin{pmatrix} 0 & -\frac{\gamma(1+\beta)}{3\tau_R} & \dot{\gamma} \\ 2\dot{\gamma} & -\frac{1}{\tau_R} & 0 \\ 0 & -\frac{1}{3\tau_R} & -\frac{1}{\tau_d} \end{pmatrix}, \tag{5.10.1}$$

where the approximation is found through the comparison of the order of magnitude of terms in each component of $\underline{\underline{M}}$ at small strains $\gamma^2 \ll 1$ and high shear rates $\dot{\gamma} \gg \tau_R^{-1}$. We expand the criterion (and define $\underline{Q} = \partial_\gamma \underline{s} \equiv (e, f, g)^T$):

$$\eta/G - \underline{p}.\underline{\underline{M}}.\partial_\gamma \underline{s} = \eta/G - \frac{1}{|\underline{\underline{M}}|}\left\{2\gamma(e_n g_T - e_T g_n) + (f_T g_n - f_n g_T)\right\} < 0. \tag{5.10.2}$$

By comparing the order of magnitude of terms inside the braces {} we approximate Eqn 5.10.2 to:

$$\eta/G - \frac{1}{|\underline{\underline{M}}|}\left\{-\frac{2\dot{\gamma}\gamma}{3\tau_R} + \frac{1}{\tau_R \tau_d}\right\} < 0; \tag{5.10.3}$$

expanding $1/|\underline{\underline{M}}|$ at early times $t \ll \tau_R$ we find the final condition for the onset of linear instability in the RP model at high shear rates $\dot{\gamma} \gg \tau_R^{-1}$ (valid for strains $\gamma^2 \ll 1$):

$$t_s > \frac{3}{2\tau_d \dot{\gamma}^2} + \eta/G. \tag{5.10.4}$$

5.11 Appendix III

This appendix details the derivation of the analytical functions $\tau(\Delta t)$ and $\sigma(\Delta t)$ of the scalar fluidity model during shear startup, valid within the constraint of homogeneous shear at a positive shear rate.

Analytical equation for $\tau(\Delta t)$:

The governing equation for τ is: $\partial_t = 1 - \tau/(\tau_0 + 1/\dot{\gamma})$. By the method of separation of variables we find:

$$\tau(\Delta t) = -A(\tau_0 + 1/\dot{\gamma})e^{B\Delta t} + \frac{1}{\dot{\gamma}} + \tau_0, \tag{5.11.1}$$

where $B = -\dot{\gamma}/(1+\tau_0\dot{\gamma})$. To find A we fit the initial condition: $\tau(\Delta t = 0) = t_w + \tau_0$, resulting in:

$$\tau(\Delta t) = \left(t_w - \frac{1}{\dot{\gamma}}\right) \exp\left(-\frac{\dot{\gamma}\Delta t}{1+\tau_0\dot{\gamma}}\right) + \frac{1}{\dot{\gamma}} + \tau_0. \tag{5.11.2}$$

Analytical equation for $\sigma(\Delta t)$:

Substituting the analytical form for $\tau(\Delta t)$ into the governing equation for $\sigma(\Delta t)$ we have (B as above):

$$\partial_t \sigma = \dot{\gamma} - \frac{\sigma}{(t_w - 1/\dot{\gamma})e^{B\Delta t} + 1/\dot{\gamma} + \tau_0}. \tag{5.11.3}$$

To find an analytical solution we use the integrating factor method that solves equations of form $\frac{d\sigma}{d\Delta t} + \sigma p(\Delta t) = q(\Delta t)$ via the following steps:

1. determine the integrating factor $\mu = \exp\left(\int p(\Delta t)\, d\Delta t\right)$,
2. determine $\mu\sigma = \int \mu\, q(\Delta t)\, d\Delta t$,
3. therefore find $\sigma = \frac{\int \mu q(\Delta t) d\Delta t}{\mu}$,
4. finally, fit constants of integration using the initial condition $\sigma(\Delta t = 0) = 0$.

We have: $p(\Delta t) = \tau(\Delta t)$ i.e., Eqn 5.11.2, and $q = \dot{\gamma}$. Following the above steps results in the analytical equation for $\sigma(\Delta t)$:

$$\sigma(\Delta t) = \frac{(\tau_0\dot{\gamma}+1)^2\left[\exp\left(\frac{\dot{\gamma}\Delta t}{\tau_0\dot{\gamma}+1}\right) - 1\right] + \dot{\gamma}\Delta t\ (t_w\dot{\gamma} - 1)}{\exp\left(\frac{\dot{\gamma}\Delta t}{\tau_0\dot{\gamma}+1}\right)(\tau_0\dot{\gamma}+1) + (t_w\dot{\gamma} - 1)}. \tag{5.11.4}$$

Note that for shear rates within the limits of interest: $t_w^{-1} \ll \dot{\gamma} \ll \tau_0^{-1}$, this reduces to:

$$\sigma(\Delta t) = \frac{e^{\dot{\gamma}\Delta t} + \dot{\gamma}^2 t_w \Delta t - 1}{e^{\dot{\gamma}\Delta t} + \dot{\gamma} t_w} \tag{5.11.5}$$

5.12 Appendix IV

This appendix details the derivation of the strain at the stress maximum $\gamma^* \sim \log(\dot{\gamma}t_w)$; credit for this derivation is given to Dr. Suzanne Fielding.

At the shear stress maximum during startup we have $\partial_t \sigma = \dot{\gamma} - \sigma/\tau = 0$. Prior to the maximum the viscoelastic shear stress increases linearly in strain so that at the maximum $\sigma^* \sim \gamma^*$. Substituting this into the above we find (using the analytical form for $\tau(\Delta t)$): $\log(t_w \dot{\gamma}) \simeq \log(\gamma^* - 1) + \gamma^*$, where the approximation is valid in the shear rate regime of interest $t_w^{-1} \ll \dot{\gamma} \ll \tau_0^{-1}$. Therefore, to within a logarithmic correction in γ^*, the strain at the stress maximum obeys:

$$\gamma^* \sim \log(t_w \dot{\gamma}), \tag{5.12.1}$$

and likewise, the shear stress at the maximum $\Sigma^* \sim G\gamma^* \sim G \log(t_w \dot{\gamma})$.

5.13 Appendix V

This appendix details the proof that the strain of the stress maximum in time (at a fixed shear rate) and also at the stress maximum of the instantaneous constitutive curve (formed at a fixed time) are approximately equal.

Differentiating the analytical equation for $\sigma(\Delta t)$ with respect to time at fixed $\dot{\gamma}$ within the shear rate regime of interest $t_w^{-1} \ll \dot{\gamma} \ll \tau_0^{-1}$, the *time* Δt^* at which the stress is maximal during startup obeys:

$$2 + \dot{\gamma} t_w e^{-\dot{\gamma} \Delta t^*} = \dot{\gamma} \Delta t^*. \tag{5.13.1}$$

Similarly, the *shear rate* $\dot{\gamma}^*$ at which the *instantaneous* constitutive curve (formed at a fixed time) is maximal obeys:

$$3 + \dot{\gamma}^* t_w e^{-\dot{\gamma}^* \Delta t} = \dot{\gamma}^* \Delta t. \tag{5.13.2}$$

Clearly then, the stress overshoot in *time* (for fixed shear rate) during shear startup, and *shear rate* (for fixed time in the instantaneous constitutive curve) occur at the same strain γ^* (i.e., $\dot{\gamma} \Delta t^* \simeq \dot{\gamma}^* \Delta t$), to within a small correction. That is, the strain at which $\partial_{\Delta t} \Sigma|_{\dot{\gamma}} = 0$ is roughly that at which $\partial_{\dot{\gamma}} \Sigma|_{\Delta t} = 0$.

5.14 Appendix VI

This appendix details the derivation of the frequency of oscillation of the heterogeneous shear rate perturbation $\nu = \mu\dot{\gamma}\sqrt{G^s G^p}/(G^s + G^p)$ at steady state under imposed shear in the glassy polymer model.

Using linear stability analysis (as described in Chapter 3), the stability matrix governing the growth rate of heterogeneous perturbations[26] $\partial_t \underline{\delta s}_k = \underline{\underline{P}}.\underline{\delta s}_k$ is, at steady state with $\dot{\gamma} \ll \tau_0^{-1}$ and $\alpha \to 0$:

$$\underline{\underline{P}} = \begin{pmatrix} -G^p/\eta & -G^s/\eta & 0 \\ -G^p/\eta & -\mu\dot{\gamma} - G^s/\eta & \mu\dot{\gamma}^2 \\ -G^p/\eta\dot{\gamma} & -G^s/\eta\dot{\gamma} & -\mu\dot{\gamma} \end{pmatrix}. \tag{5.14.1}$$

The determinant $|\underline{\underline{P}} - \omega\underline{\underline{I}}|$ results in a characteristic polynomial of form:

$$-\omega^3 + a\omega^2 + b\omega + c = 0, \tag{5.14.2}$$

complex conjugate solutions of which result in oscillations at frequency $\nu \sim \omega_{im}$. Since the system is stable at steady state we must also have $\omega_{re} < 0$ of the complex conjugate pair, and a purely real root $S < 0$. Eqn 5.14.2 may then be assumed to factorise as:

$$(S - \omega)\{\omega - (\omega_{re} - i\omega_{im})\}\{\omega - (\omega_{re} + i\omega_{im})\} = 0. \tag{5.14.3}$$

The determinant $|\underline{\underline{P}} - \omega\underline{\underline{I}}| = 0$ provides a, b and c of Eqn 5.14.2, which are:

$$a \simeq -\frac{1}{\eta}(G^p + G^s) \tag{5.14.4}$$

$$b \simeq -\frac{2\mu\dot{\gamma}G^p}{\eta} \tag{5.14.5}$$

$$c = -\frac{\mu^2\dot{\gamma}^2 G^p}{\eta}, \tag{5.14.6}$$

where the order of magnitude of terms in each are compared to find the approximates given. The expansion of Eqn 5.14.3 results in $a = S$, $b = -2S\omega_{re}$ and $c = S(\omega_{re}^2 +$

[26] Where $\underline{\delta s}_k = (\delta\sigma_k^p, \delta\sigma_k^s, \delta\tau_k)^T$.

ω_{im}^2). Solving these we find $S = -\frac{1}{\eta}(G^p + G^s)$, $\omega_{re} = -(\mu\dot{\gamma}G^p)/(G^s + G^p)$, and the frequency of oscillation:

$$\omega_{im} = \pm\mu\dot{\gamma}\,\frac{\sqrt{G^s G^p}}{(G^s + G^p)}. \tag{5.14.7}$$

6

Strain ramp protocol

6.1 Introduction

In this chapter we will investigate the stress relaxation behaviour, linear stability to shear heterogeneity, and resulting shear rate heterogeneities of entangled polymeric systems that are relaxing after a strain ramp. We will begin by deriving a criterion for the onset of linear instability to the growth of shear rate perturbations after a fast strain ramp within a generalised framework that is independent of fluid or model type; credit for this criterion is given to Dr. Suzanne Fielding. Following this, we will specialise our research to the rolie poly (RP) model and, through comparison with experimental results, defend its use as a model for entangled polymeric systems.

As described in Section 2.1.1, the strain ramp protocol involves shearing a material at a constant rate $\dot{\gamma}_0$ for a time t_0 until the desired strain amplitude $\gamma_0 = \dot{\gamma}_0 t_0$

is met, and the resulting stress relaxation function[1] $\Sigma(t' = t - t_0)$ is measured once the flow has been switched off $\dot{\gamma}_0 \to 0$. An ideal step strain is obtained in the limits $\dot{\gamma}_0 \to \infty$, $t_0 \to 0$ at fixed strain amplitude γ_0 in this protocol. However, reaching this limit is a formidable task in experiment where rheometers have finite response times. In this chapter we will also show that the stress relaxation function following ramps performed at different rates $\dot{\gamma}_0$ reveals important physics about the material in question. We will therefore consider a 'fast ramp' throughout this chapter, in which the rate is finite but much faster than the inverse reptation relaxation time of the material $\dot{\gamma}_0 \gg \tau_d^{-1}$.

This chapter is ordered as follows: in Section 6.2 we will derive a general criterion that is independent of fluid or model type for the onset of linear instability to the growth of heterogeneous shear rate perturbations immediately after a fast strain ramp. In Section 6.3 we specialise our research to the RP model, beginning in Subsection 6.3.1 where we explore the rheological response of the model with homogeneity enforced to ramps applied at rates that are 'fast' ($\dot{\gamma} \gg \tau_R^{-1}$) or 'slow' ($\dot{\gamma} \ll \tau_R^{-1}$) relative to the rate at which chain stretch relaxes τ_R^{-1}. This response will then form the homogeneous background state for a linear stability analysis in Subsection 6.3.2. In Subsection 6.3.3 we perform nonlinear simulations confirming that the above linear instability results in 'macroscopic motions', i.e., non-zero, heterogeneous local velocities after a strain ramp that are qualitatively similar to those found in experiments of entangled polymeric materials [16, 17, 20, 52, 91, 135, 168]. [Recall from Chapters 2 and 3 that since these materials are usually considered to be inertialess, it had previously been assumed that all local velocities should be zero after the ramp: $v(y, t') = 0$.] Using these results, we will show that the RP model is capable of qualitatively describing the features of experiments of polymer solutions and melts.

[1]Recall from Section 2.1.1 that $t' = t - t_0$ is the time elapsed since the end of the ramp.

6.2 Criterion for instability after a fast strain ramp

We now perform a linear stability analysis about a homogeneously deforming background state within a generalised framework that does not specify a model or fluid type. Doing so, we determine a general criterion for the onset of linear instability to the growth of heterogeneous shear rate perturbations immediately after a fast (relative to the internal relaxation rates of the material) strain ramp. Credit for the derivation of this criterion is given to Dr. Suzanne Fielding.

Recall that within the general framework outlined in Chapter 3, all dynamical variables are collected into one vector $\underline{s} = (\sigma, \sigma_{xx}, \sigma_{yy}, \ldots)^T$. We define the projection vector $\underline{p} = (1, 0, 0, \ldots)$ for the viscoelastic shear stress conformation variable $\sigma_{xy} \equiv \sigma$; the total shear stress is decomposed into viscoelastic and Newtonian solvent contributions: $\Sigma_{xy} = G\,\underline{p} \cdot \underline{s} + \eta\,\dot{\gamma}_0$ and the governing equations are of the form $\partial_t\,\underline{s} = \underline{Q}(\underline{s}, \dot{\gamma}_0)$. For this specific rheological protocol we shall also assume that $\underline{Q}$ may be written as separate loading and relaxation terms: $\partial_t\,\underline{s} = \dot{\gamma}_0 \underline{S}(\underline{s}) - \frac{1}{\tau}\underline{R}(\underline{s})$, a form that encompasses most widely used constitutive models, where $\underline{S}$ and $\underline{R}$ are specified by model choice. During a fast ramp[2] $\dot{\gamma}_0 \gg \tau^{-1}$ the response is dominated by loading $\partial_\gamma\,\underline{s} \simeq \underline{S}(\underline{s})$; subsequent relaxation post-ramp occurs via $\partial_t\,\underline{s} = -\frac{1}{\tau}\underline{R}(\underline{s})$.

Performing a linear stability analysis (as outlined in Chapter 3) about the system's state during relaxation post-ramp, we add perturbations[3] to the homogeneous background state[4] $\dot{\gamma}_0(y,t) = \sum_k \delta\dot{\gamma}_k(t)\epsilon_k$, $\underline{s}(y,t) = \hat{\underline{s}}(t) + \sum_k \underline{\delta s}_k(t)\epsilon_k$, and linearise to first order in the size of the $\underline{\delta s}_k$ terms. After the ramp, perturbations grow or decay according to:

$$\partial_{t'}\,\underline{\delta s}_k = \left[-\frac{G}{\eta}\,\underline{S}(\hat{\underline{s}})\,\underline{p} - \frac{1}{\tau}\partial_{\underline{s}}\,\underline{R}\,|_{\hat{\underline{s}}}\right] \cdot \underline{\delta s}_k \;\simeq\; -\frac{G}{\eta}\,\underline{S}(\hat{\underline{s}})\,\underline{p} \cdot \underline{\delta s}_k, \tag{6.2.1}$$

where the approximation is valid for small $\eta \ll G\tau$. Since $\hat{\underline{s}}$ is continuous in time

[2] In a system with multiple relaxation times having the form: $-\frac{1}{\tau}\underline{R} = -\sum_i \underline{R}_i(\underline{s})/\tau_i$, a fast ramp is defined by $\dot{\gamma}_0 \gg \tau_{min}^{-1}$, where τ_{min} is the shortest relaxation time.

[3] Where $\epsilon_k = \cos(k\pi y/L)$.

[4] For clarity in this section we represent the homogeneous background with hats, e.g., $\hat{\underline{s}}$, and recall that we associate the the subscript $_0$ with values of at the end of the ramp, e.g., $\hat{\underline{s}}_0$. Outside this subsection we will drop the hats for ease of reading, and hereafter set $G = 1$, so that σ is the viscoelastic shear stress, etc.

throughout this protocol (including at the end of the ramp), we combine the evolution of the base state immediately *before* the end of the ramp: $\partial_{\hat{\gamma}}\underline{\hat{s}} \mid_{t_0^-} = \underline{S}(\underline{\hat{s}}_0)$, with the dynamics of the perturbations immediately *after* the ramp: $\partial_{t'}\underline{\delta s}_k \mid_{t_0^+} = -\frac{G}{\eta}\underline{S}(\underline{\hat{s}}_0)\underline{p}\cdot\underline{\delta s}_k$. Doing so, and incorporating force balance: $\delta\dot{\gamma}_k = -G\delta\sigma_k/\eta$, we find that the growth of shear rate perturbations immediately after the ramp ends obeys:

$$\partial_{t'}\,\delta\dot{\gamma}_k \mid_{t_0^+} = -\frac{1}{\eta}\frac{\partial\hat{\Sigma}}{\partial\hat{\gamma}} \mid_{t_0^-} \cdot\delta\dot{\gamma}_k. \tag{6.2.2}$$

That is, the system is linearly unstable to the growth of heterogeneous shear rate perturbations immediately after the ramp if, immediately before the end of the ramp, the shear stress was a decreasing function of strain. This is consistent the prediction of instability in the Doi-Edwards (DE) model by Marrucci and Grizzuti [104].

6.3 Strain ramps in the RP model

6.3.1 Stress relaxation functions

The stress relaxation function of a material after a strain ramp reveals a great deal about the physics of the material's intrinsic relaxation mechanisms. We now investigate the rheological responses of the RP model to strain ramps of various rates $\dot{\gamma}_0$ and amplitudes γ_0. For now we artificially constrain the system homogeneously in order to reveal the effects of the relaxation mechanisms on the stress relaxation function resulting from ramps performed at different rates $\dot{\gamma}_0$. These results will later form the homogeneous background state numerically calculated for our time-dependent linear stability analysis in which (initially) small heterogeneous perturbations are added to this state.

The 'stretching' and 'nonstretching' limits

Recall from Chapter 3 that the RP model has a parameter $0 \leq \beta \leq 1$ that governs the efficacy of convective constraint release (CCR), with $\beta = 0$ describing a system without CCR, and $\beta = 1$ describing a system with the maximum efficacy of CCR.

Recall also that the model has two relaxation times: the timescale on which chain stretch relaxes τ_R, and the timescale on which reptation occurs τ_d. In well entangled polymeric materials these two timescales are well separated $\tau_R \ll \tau_d$, and their values define the 'entanglement number' $Z = \tau_d/3\tau_R$. In this chapter we will always consider strain ramps that are 'fast' with respect to reptation $\dot{\gamma}_0 \gg \tau_d^{-1}$. There are then two limits of interest with respect to the imposed shear rate during the ramp: the first is a shear rate much faster than the inverse stretch relaxation time $\dot{\gamma}_0 \gg \tau_R^{-1}$ (which we refer to as a 'fast' ramp), and the second a shear rate much slower than this $\dot{\gamma}_0 \ll \tau_R^{-1}$ (a 'slow' ramp). In these limits the RP model shows qualitatively different behaviour under the strain ramp protocol that, as will we will show, reveals the underlying physics of the stress relaxation behaviour. We now briefly describe this behaviour and define two shear rates $\dot{\gamma}_{0,s}$ and $\dot{\gamma}_{0,n}$ in these limits for use throughout the chapter:

1. *a 'fast' ramp:* at large shear rates for which appreciable stretch arises during the ramp $\dot{\gamma}_{0,s} \gg \tau_R^{-1}$, the RP model has the 'stretching' form (Eqn 3.2.4 of Chapter 3) possessing linear loading terms $\underline{S}$ and nonlinear relaxation terms $\underline{R}$ (the functions $\underline{S}$ and $\underline{R}$ are as referred to in Section 6.2). During the ramp the system behaves as a linear elastic solid with $\sigma = \gamma$, but on shear cessation exhibits a double exponential stress relaxation on the timescales τ_R (chain stretch relaxation) and τ_d (reptation). (Note that this shear rate limit effectively corresponds to the 'ideal' step $\dot{\gamma}_0 \to \infty$. In fact, to achieve this 'fast' ramp throughout this section we will analytically solve the RP constitutive equations during the ramp by assuming the limit $\dot{\gamma}_0 \to \infty$.)

2. *a 'slow' ramp:* at moderate shear rates that are fast enough to negate stress relaxation via reptation during the ramp, but are slow compared to the inverse stretch relaxation time: $\tau_d^{-1} \ll \dot{\gamma}_{0,n} \ll \tau_R^{-1}$, stretch can be imagined to relax infinitely quickly. (As such, no appreciable chain stretch arises during the ramp.) This leads to the 'nonstretching' limit of the RP model (Eqn 3.2.6 of Chapter 3) in which the loading terms $\underline{S}$ are nonlinear and the relaxation terms $\underline{R}$ are linear. In this limit the system behaves as a nonlinear elastic solid

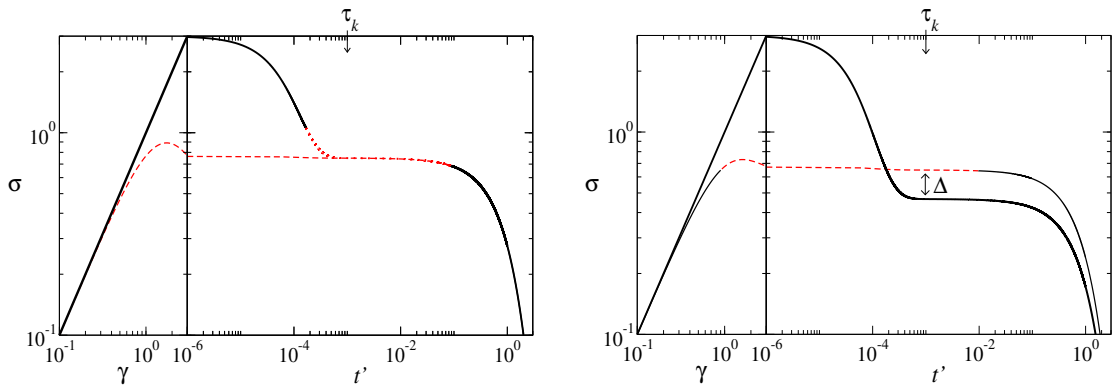

(a) $\beta = 0$ (b) $\beta = 1$

Figure 6.3.1: Shear stress during (*vs.* γ) and after (*vs.* t') a strain ramp of amplitude $\gamma_0 = 3$, with homogeneity enforced. Dotted/dashed lines denote linearly unstable regions ($\omega > 0$). *Upper curve at the end of the ramp*: strain ramp applied at rate $\dot{\gamma}_{0,s}$ (with $\dot{\gamma}_{0,s} \to \infty$), *lower curve:* strain ramp applied at $\dot{\gamma}_{0,n} = 500$. Δ is the difference between the stress values after stretch relaxation has occurred of ramps performed at shear rates $\dot{\gamma}_{0,n}, \dot{\gamma}_{0,s}$: $\Delta \equiv \sigma_0(\dot{\gamma}_{0,n}, \gamma_0) - \sigma(t' = \tau_k, \dot{\gamma}_{0,s}, \gamma_0)$. $\tau_R = 10^{-4}$, $\eta = 10^{-5}$, $\tau_k = 10\tau_R$.

during the ramp, resulting in a shear stress overshoot in strain for ramps of amplitude $\gamma_0 \gtrsim 1.7$ (as shown in Chapter 5). After shear cessation the stress follows a *single* exponential relaxation via reptation: $\sigma(t') = \sigma_0 \exp(-t'/\tau_d)$, since there is no appreciable chain stretch to relax.

This behaviour is summarised in Figure 6.3.1, where we show the behaviour of the viscoelastic shear stress[5] σ as a function of strain *during* the ramp, and as a function of time *after* a ramp applied at rates $\dot{\gamma}_{0,n}$ and $\dot{\gamma}_{0,s}$. These results are shown in (a) and (b) of the figure for systems without ($\beta = 0$) and with ($\beta = 1$) the CCR mechanism active, respectively. We also perform a time-dependent linear stability analysis as outlined in Chapter 3. The dashed/dotted lines in the figure indicate times at which the system is linearly unstable to shear heterogeneity, i.e., the largest real part of any eigenvalue $\omega(t) > 0$ (see Chapter 3) — we also checked that this corresponded to growth of the heterogeneous perturbations $\underline{\delta s}_k$ by integrating Eqn 6.2.1. From these figures it is clear that the efficacy of CCR severely affects both the stress relaxation and the linear stability of a system relaxing after a strain ramp performed at rate $\dot{\gamma}_{0,s}$. We will investigate the stability properties in Subsection

[5]Recall from Chapter 3 that we use units in which the elastic modulus is $G = 1$.

6.3.2, but for now focus on the stress relaxation functions.

(A brief remark: recall that the total shear stress $\Sigma = G\sigma + \eta\dot{\gamma}$ is composed of viscoelastic and Newtonian solvent contributions, so that after shear cessation the total shear stress is equal to the viscoelastic shear stress $\Sigma = G\sigma$. This leads to a small (since $\eta \ll G\tau_d$) instantaneous 'drop' in the total shear stress at the end of the ramp when the shear rate is turned off $\dot{\gamma}_0 \to 0$. That this drop is very small and that, in reality, shear cessation occurs over a finite time means this drop would be imperceptible in experiment. For clarity of presentation then, throughout this chapter we will present figures showing the *viscoelastic* shear stress $G\sigma$, and set $G = 1$ so that σ represents the viscoelastic shear stress. We also drop the term 'viscoelastic' from here on for the sake of being concise.)

For use in explaining the features of the stress relaxation functions we define: $\tau_k = 10\tau_R$ to denote the time after shear cessation at which stretch relaxation has completed, but at which stress relaxation via reptation is still insignificant ($\tau_k \ll \tau_d$). We use this to define the curve $\sigma(t' = \tau_k, \dot{\gamma}_{0,s}, \gamma_0)$ that corresponds to the value of the stress at $t' = \tau_k$ as a function of the strain amplitude γ_0 for a ramp performed at rate $\dot{\gamma}_{0,s}$. [We note that the same curve $\sigma(t' = \tau_k, \dot{\gamma}_{0,n}, \gamma_0)$ for a ramp performed at rate $\dot{\gamma}_{0,n}$ is simply the shear startup curve $\sigma_0(\dot{\gamma}_{0,n}, \gamma_0)$, since at this rate appreciable stretch does not arise during the ramp, and so it follows that the stress immediately after the ramp is approximately the same a time $t' = \tau_k$ later, as shown in Figure 6.3.1.] In experiment this curve is easily obtained by performing many strain ramps of different strain amplitudes γ_0 at a fixed rate $\dot{\gamma}_{0,s}$, and plotting the shear stress at time $t' = \tau_k$ *vs.* the strain amplitude γ_0. In fact, if $t' = \tau_k$ corresponds to the time at which the stress relaxation function is time-strain separable, this method corresponds to that used to obtain the damping function (Eqn 2.4.1, described in Chapter 2); that method rescales the function $\sigma(\tau_k, \dot{\gamma}_0, \gamma_0)$ by the strain amplitude to give the nonlinear relaxation modulus $G(\tau_k, \dot{\gamma}_0, \gamma_0)$. The damping function is then the shift factor required to match the nonlinear elastic modulus onto the linear elastic modulus. Note that in the results presented below, the damping function is given by $h(\dot{\gamma}_0, \gamma_0) = \sigma(\tau_k, \dot{\gamma}_0, \gamma_0)/\gamma_0$.

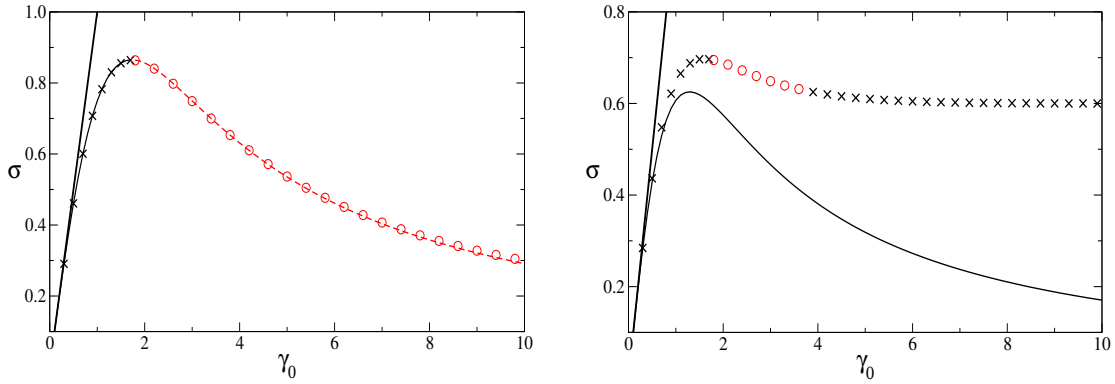

(a) $\beta = 0$ (b) $\beta = 1$

Figure 6.3.2: *Top/leftmost line:* stress immediately after a ramp applied at rate $\dot{\gamma}_{0,s} \to \infty$ of amplitude γ_0, i.e., $\sigma_0(\dot{\gamma}_{0,s}, \gamma_0)$ (this increases linearly for all γ_0). *Lower solid/dashed line:* stress at time $t' = \tau_k$ after the ramp: $\sigma(\tau_k, \dot{\gamma}_{0,s}, \gamma_0)$. *Symbols:* the stress immediately after a ramp at rate $\dot{\gamma}_{0,n} = 500$ and amplitude γ_0, i.e., $\sigma_0(\dot{\gamma}_{0,n}, \gamma_0)$. Dashed lines/circles denote linearly unstable regions ($\omega > 0$). Homogeneity enforced throughout and $\tau_R = 10^{-4}$, $\eta = 10^{-5}$.

The stress relaxation functions obtained with the CCR mechanism inactive $\beta = 0$ are shown in (a) of Figure 6.3.1, and demonstrate a key feature: for a fast ramp performed at rate $\dot{\gamma}_{0,s}$, the residual stress $\sigma(\tau_k, \dot{\gamma}_{0,s}, \gamma_0)$ remaining after stretch relaxation has completed has the same value as that of a slower ramp performed at rate $\dot{\gamma}_{0,n}$: $\sigma_0(\dot{\gamma}_{0,n}, \gamma_0)$ (provided the CCR mechanism is inactive). This is general for any strain amplitude, as shown in Figure 6.3.2 (a) where the lower solid/dashed line showing $\sigma(\tau_k, \dot{\gamma}_{0,s}, \gamma_0)$ *vs.* γ_0 agrees with the symbols that show $\sigma_0(\dot{\gamma}_{0,n}, \gamma_0)$ *vs.* γ_0. With CCR active ($\beta \neq 0$) this is not the case: the stress from the fast ramp drops significantly lower than that of the slow ramp value due to what appears to be an accelerated stress relaxation at times $t' < \tau_k$, as shown in Figure 6.3.1 (b). Again, this is general for any strain amplitude, see (b) of Figure 6.3.2 where the solid line showing $\sigma(\tau_k, \dot{\gamma}_{0,s}, \gamma_0)$ now lies significantly below the symbols that show $\sigma_0(\dot{\gamma}_{0,n}, \gamma_0)$.

These results can be explained by the following. With CCR inactive ($\beta = 0$) orientation relaxes only via reptation, i.e., the stretch and orientation relaxation mechanisms are decoupled and relax independently of each other. Thus, in such a system, the residual stress remaining after chain stretch has relaxed after a 'fast' ramp of rate $\dot{\gamma}_{0,s}$ is equal to the stress resulting from a ramp during which no chain

stretch arose, i.e., the stress after a ramp performed at rate $\dot{\gamma}_{0,n}$. However, when CCR is active ($\beta \neq 0$) stretch relaxation causes significant orientation relaxation to occur. This is because the mechanism of convective constraint release allows entanglements forming the tube of constraints on a test chain to be lost (thus relaxing orientation) when chains that form the entanglement points themselves reptate or relax their stretch sufficiently that their chain ends pass through the entanglement point. This means that orientation relaxation (that would otherwise only occur via reptation on a timescale τ_d) can be aided by stretch relaxation, resulting in an overall acceleration of stress relaxation[6] at times $t' < \tau_R$, as shown in Figure 6.3.1 (b).

These features can be shown analytically in the RP model, the details of which are provided in Appendix I for which credit and thanks are given to Dr. Richard Graham. Using these, we will now show that with CCR inactive, the stress once chain stretch has relaxed after a ramp applied at rate $\dot{\gamma}_{0,s}$ is exactly that resulting from a ramp applied at rate $\dot{\gamma}_{0,n}$, so that $\sigma(\tau_k, \dot{\gamma}_{0,s}, \gamma_0) = \sigma_0(\dot{\gamma}_{0,n}, \gamma_0)$, as demonstrated in Figure 6.3.2 (a). To do so, we first define the orientation tensor $\underline{\underline{A}} = 3\,\underline{\underline{\sigma}}/T$, where $T(t') = \mathrm{Tr}\underline{\underline{\sigma}}$ describes the degree of chain stretch in the system (in equilibrium $T = 3$). We consider the long time relaxation behaviour of $\underline{\underline{A}}^{\infty} \equiv \underline{\underline{A}}(t' \to \infty)$ in the limit of $\tau_d \to \infty$ which, for finite t' and τ_d, effectively corresponds to values at $t' = \tau_k$, when τ_R, τ_d are well separated. Using results from Appendix I, $\underline{\underline{A}}$ obeys:

$$\partial_{t'}\underline{\underline{A}} = -\Psi[T(t')]\,(\underline{\underline{A}} - \underline{\underline{I}}), \tag{6.3.1}$$

where $\Psi[T(t')] = \beta\frac{2[1-\sqrt{3/T(t')}]}{\tau_R}\,[T(t')/3]^{\delta-1}$ and δ is a parameter in the rolie poly model that, following Ref. [92], we have set to $-\frac{1}{2}$ throughout this thesis.

From Eqn 6.3.1, when CCR is inactive ($\beta = 0$) we have that: $\underline{\underline{A}}^{\infty} = \underline{\underline{A}}^{0}$ (independently of δ) where $\underline{\underline{A}}^{0}$ is the orientation tensor immediately after the ramp. This result follows from the physics described above: without CCR the stretch and orientation relaxation processes are decoupled, and orientation, described by the orientation tensor above, relaxes only via reptation on the timescale $t' \sim \tau_d$. For a

[6]Note that it was suggested in Ref. [92] that the CCR mechanism would accelerate stress relaxation. However, the agreement of the fast and slow ramps at $t' = \tau_k$ with $\beta = 0$ was not predicted, nor was the magnitude to which CCR accelerates the stress relaxation quantified.

'fast' ramp $\dot{\gamma}_{0,s}$, it is then possible to show that[7]:

$$\begin{aligned} \sigma_{xy}^{\infty}(\gamma_0) &= \frac{3\gamma_0}{\gamma_0^2+3}, \\ \sigma_{yy}^{\infty}(\gamma_0) &= \frac{3}{\gamma_0^2+3}, \end{aligned} \tag{6.3.2}$$

where $\sigma_{xy,yy}^{\infty} = \sigma_{xy,yy}(t' \to \infty)$ in the limit $\tau_d \to \infty$, and Eqn 6.3.2 holds for $\beta = 0$ and is general in δ. These functions (Eqn 6.3.2) provide analytical solutions of the shear and normal stresses at a time $t' = \tau_k$ after a fast strain ramp of amplitude γ_0 in the RP model with inactive CCR. That is, σ_{xy}^{∞} is equivalent to the curve $\sigma(\tau_k, \dot{\gamma}_{0,s}, \gamma_0)$ shown as the lower line in Figure 6.3.2 (a). To complete the proof, both equations of 6.3.2 may be shown to be solutions of the non-stretching RP constitutive equation for shear startup (Eqn 3.2.6) with $\beta = 0$ and $\tau_d \to \infty$. This proves that (with CCR inactive) the stress once chain stretch has relaxed after a ramp applied at rate $\dot{\gamma}_{0,s}$ is exactly that resulting from a ramp applied at rate $\dot{\gamma}_{0,n}$, so that $\sigma(\tau_k, \dot{\gamma}_{0,s}, \gamma_0) = \sigma_0(\dot{\gamma}_{0,n}, \gamma_0)$, as demonstrated in Figure 6.3.2 (a) (where the analytical form of σ_{xy}^{∞} above describes the lower line/symbols).

The above demonstrates an interesting, experimentally testable result of the RP model, and will also prove useful in describing the linear stability to the growth of shear rate perturbations in Section 6.3.2.

The Lodge-Meissner relation

We note that using (see Appendix I):

$$\underline{\underline{A}}(t') = \underline{\underline{A}}^0 \exp\left[-\int_0^{t'} \Psi[T(t)]dt\right] + \underline{\underline{I}}\left\{1 - \exp\left[-\int_0^{t'} \Psi[T(t)]dt\right]\right\}, \tag{6.3.3}$$

it can be shown that the Lodge-Meissner (LM) relation [93] holds for all strain ramps performed at rates of $\dot{\gamma}_{0,s}$, independently of β or δ, that is: $N_1(t', \gamma_0) = \gamma_0\, \sigma(t', \dot{\gamma}_{0,s}, \gamma_0)$. As shown above, the residual shear stress remaining once chain

[7] Eqn 6.3.2 is obtained by combining the relation $\underline{\underline{A}}^{\infty} = \underline{\underline{A}}^0$ with the components of the stress tensor immediately after a fast ramp at rate $\dot{\gamma}_{0,s} \to \infty$, and also with T after chain stretch has relaxed in the long time limit, $T^{\infty} = 3$

stretch has relaxed after a fast ramp performed at rate $\dot{\gamma}_{0,s}$ is identical to that performed at rate $\dot{\gamma}_{0,n}$ if CCR is inactive, $\beta = 0$. Therefore, it follows that the stress relaxation of the latter ramp also follows the LM relation for all times. However, with CCR active no such guarantee exists and from our numerics we find the LM relation is violated for these slow ramps (at rates $\dot{\gamma}_{0,n}$) with active CCR, $\beta \neq 0$. Note that, within our assumption of shear homogeneity, this is the only strain ramp for which we find violation of the LM relation. This result is useful, since it provides experimentally testable results for the RP model concerning the efficacy of convective constraint release, the degree to which this occurs in experiment (and should therefore be included in the theory) is currently unknown. We will show in Section 6.3.3 that we also find failure of the LM relation during stress relaxation in which a large magnitude of shear heterogeneity arises.

6.3.2 Linear instability in the rolie-poly model

So far, we have derived a criterion for the onset of linear instability to the growth of shear rate perturbations immediately after a strain ramp, which depends only on the form of the underlying homogeneous background state. We subsequently investigated this homogeneous background state in the RP model, focusing on the stress relaxation functions resulting from strain ramps applied at two rates that are faster or slower than the stretch relaxation rate τ_R^{-1}. We showed that in the absence of convective constraint release (CCR), the stress relaxation function of a fast ramp $\dot{\gamma}_0 \gg \tau_R^{-1}$ relaxes exactly onto the stress relaxation function of a slow ramp $\dot{\gamma}_0 \ll \tau_R^{-1}$ once chain stretch has relaxed. We also showed that with CCR active, the overall stress relaxation after a fast ramp is accelerated during stretch relaxation, destroying the above agreement with the relaxation function resulting from the slower ramp.

We now turn our attention to the linear stability to shear heterogeneity during stress relaxation after strain ramps applied at the two rates $\dot{\gamma}_{0,n}, \dot{\gamma}_{0,s}$. Recall that

the criterion derived in Section 6.2:

$$\partial_t \delta\dot{\gamma}_k \mid_{t_0^+} = -\frac{1}{\eta}\frac{\partial \Sigma}{\partial \gamma} \mid_{t_0^-} \cdot \delta\dot{\gamma}_k, \tag{6.3.4}$$

predicts linear instability to the growth of shear rate perturbations immediately post-ramp, for a ramp in which the stress was a decreasing function of strain just before the ramp ended: $\partial_{\gamma_0}\Sigma < 0$. In this section we will investigate the consequences of this criterion for strain ramps in the RP model: we will show that ramps applied at a rate of $\dot{\gamma}_{0,n}$, with amplitude $\gamma_0 \gtrsim 1.7$ up to some cutoff strain amplitude, result in the growth of shear rate perturbations immediately after the ramp. However, we will also show that ramps applied at rates $\dot{\gamma}_{0,s}$ *never* result in the growth of shear rate perturbations immediately after the ramp for any strain amplitude. Despite this, for these fast ramps, we will show that *delayed* linear instability may arise once chain stretch has relaxed, depending on the efficiency of CCR. For reference throughout this subsection we recall Figures 6.3.1 and 6.3.2, and remind the reader that dotted/dashed lines and circled symbols in those figures indicate linear instability to shear heterogeneity: $\omega(t) > 0$.

Nonstretching limit: $\dot{\gamma}_0 \ll \tau_R^{-1}$

As shown in Chapter 5, shear startup at rates in the 'nonstretching' limit of the RP model (i.e., at $\dot{\gamma}_{0,n}$) results in a negative slope of the shear stress in strain $\partial_\gamma \Sigma < 0$ for strains exceeding $\gamma \sim 1.7$ (this value varies only slightly with β). Strain ramps whose strain amplitude lies in this negative slope satisfy the criterion (Eqn 6.3.4), and result in linear instability to shear heterogeneity immediately after the ramp. This is shown in Figure 6.3.2, where the shear stress immediately after the ramp $\sigma_0(\gamma_0)$, which is approximately equivalent to the shear startup function[8] $\Sigma(\gamma)$, is plotted as a function of strain amplitude. Note that stability is restored at high strain amplitudes [not shown in (a) of Figure 6.3.2]. This is because a very small, stabilising contribution to stability from reptation that was neglected in the derivation of the criterion (since $\eta \ll G\tau_d$) can stabilise the system against shear rate

[8]The latter is a (constant at fixed $\dot{\gamma}_0$) factor $\dot{\gamma}_0\eta$ larger than the former.

heterogeneity when the strain amplitude corresponds to only a very small gradient of the shear stress in strain $\partial_{\gamma_0}\sigma$. This results in a 'cut-off' strain amplitude above which linear stability to shear rate heterogeneity is restored: this is because the shear startup function eventually reaches a steady state $\partial_\gamma \Sigma \to 0$ so that the smallness of this gradient and the resulting stabilisation described above is inevitable at large strains.

After shear cessation, stress relaxation occurs via reptation in a single exponential decay, and it follows (see Appendix II for details) that the largest real part of the eigenvalues from the linear stability analysis $\omega(t')$ obeys:

$$\omega(t') = -\frac{1}{\tau_d} - \frac{1}{\eta}\left[(\sigma^0_{yy} - 1)e^{-\frac{t'}{\tau_d}} + 1 - \frac{2}{3}{\sigma^0_{xy}}^2 e^{-\frac{2t'}{\tau_d}}(1+\beta)\right], \tag{6.3.5}$$

resulting in a monotonic decay towards $\omega(t' \to \infty) = -(\frac{1}{\tau_d} + \frac{1}{\eta})$ from the value immediately after the ramp, ω_0, on a timescale $O(\tau_d)$. This means that if the system is linearly stable immediately after the ramp: $\omega_0 < 0$ it will remain stable for all $t' \to \infty$. Otherwise the system is linearly unstable initially, then finally becomes linearly stable again through reptation on the timescale τ_d.

Stretching limit: $\dot{\gamma}_0 \gg \tau_R^{-1}$

As shown in Chapter 5, shear startup at a rate $\dot{\gamma}_{0,s}$ in the RP model results in linear elastic stress growth in strain $\sigma = \gamma$. Thus, for this ramp rate, the criterion predicts linear stability to shear rate heterogeneity for *any* amplitude of strain ramp. However, the criterion only applies *immediately* after the ramp and does not dictate the long time stability properties. We show in Figure 6.3.1 (a) that although the system is linearly stable to shear rate heterogeneity immediately after the ramp performed at $\dot{\gamma}_{0,s}$, it later becomes unstable as stretch relaxation nears completion in the absence of CCR. This result can be understood as follows: in the analysis in the previous section with $\beta = 0$ we have already shown that $\underline{\underline{\sigma}}^\infty(\dot{\gamma}_{0,s}, \gamma_0) = \underline{\underline{\sigma}}^0(\dot{\gamma}_{0,n}, \gamma_0)$; i.e., after stretch relaxation has occurred, the components of the stress tensor that results from a ramp at rate $\dot{\gamma}_{0,s}$ are the same as those resulting from a ramp performed at rate $\dot{\gamma}_{0,n}$. It follows (and is simple to show) that if the latter

system is linearly unstable, so too will the former be. This gives rise to *delayed* linear instability occurring on a timescale $O(\tau_R)$ for fast ramps of rate $\dot{\gamma}_{0,s}$ with strain amplitudes $\gamma_0 > 1.7$, even though no stress overshoot arises during the ramp. This has important consequences for experiment, as we shall see later in Section 6.3.3.

In the previous subsection we showed that if CCR is active ($\beta \neq 0$) the stretch relaxation process causes accelerated relaxation of orientation (recall Eqn 6.3.1), leading to a lower stress at $t' = \tau_k$ than that of a ramp during which appreciable stretch does not arise, as shown in Figure 6.3.2 (b). Therefore, with CCR active, there is no guarantee of linear instability following chain stretch relaxation for strain amplitudes $\gamma_0 > 1.7$, as there is for the $\beta = 0$ case. In fact we find that for large enough β the accelerated orientation relaxation due to CCR at times $t' < \tau_k$ is sufficient to stabilise the system against heterogeneity, at a time when the system relaxing after the slower ramp is still linearly unstable, as shown for general strain amplitudes in (b) of Figure 6.3.2.

Comparison to literature

We now briefly consider the implications of the negative slope in the stress as a function of strain amplitude at times $t' \sim \tau_k$ for ramps applied at rate $\dot{\gamma}_{0,s}$, i.e., $\partial_{\gamma_0}\sigma(\tau_k, \dot{\gamma}_{0,s}, \gamma_0) < 0$, with regard to the experimental and theoretical literature.

Firstly, this negative slope is similar to that noted to exist in the original DE model by Marrucci and Grizzuti, who predicted steps with strain amplitudes in this negative slope to be unstable via a free energy calculation [104]. The authors also suggested that if orientation were relaxed sufficiently (either by reptation or some other mechanism) to reduce the free energy during stretch relaxation the instability might be avoided. We have confirmed that this negative slope renders the system linearly unstable to shear heterogeneity in the RP model with CCR inactive, and leads to the same delayed instability. We have also shown that this instability can be ameliorated if CCR acts during chain retraction to accelerate orientation relaxation, in agreement with Marrucci and Grizzuti's suggestion.

Secondly, the negative slope described above was considered by some experi-

mentalists to be impossible for a sample undergoing homogeneous deformation, and thought to be a direct result of strain heterogeneity [20, 135, 168, 169]. We have shown that, with homogeneity enforced, the RP model exhibits this negative slope for all β and δ indicating that shear heterogeneity is not necessary for the negative slope to exist. However, through our criterion and analytics within the RP model we have shown that for $\beta \sim 0$ the negative slope described above *is* a direct source of linear instability and would lead to shear heterogeneity. On the other hand, we have also shown that CCR may act to restabilise the system to shear heterogeneity but still give rise to the negative slope $\partial_{\gamma_0}\sigma(\tau_k, \dot{\gamma}_{0,s}, \gamma_0) < 0$, thus its existence is not a guarantee for linear instability.

So far, we have studied predictions of the RP model using calculations in which we linearised to the first order the size of heterogeneous perturbations. We now explore the full nonlinear calculations in order to allow comparison with experiments.

6.3.3 Results of shear heterogeneity

In this section we perform full nonlinear simulations, in 1D, that directly allow heterogeneity in the flow gradient direction (see Chapter 3 for details). We will show that similar 'macroscopic motions'[9] to those in experiment arise in the RP model for strain amplitudes $\gamma_0 \gtrsim 1.7$, as a result of the linear instability described in the previous subsection. Similar heterogeneity in the RP model after a step strain has also been reported elsewhere [3, 4, 6, 7]. Here, we add to these findings with comparisons of the rheological responses under different ramp rates $\dot{\gamma}_0$, and values of the CCR parameter β, and will also compare the qualitative features of the RP model with those found in experiment.

For comparison of the rheological properties with those of the homogeneously constrained system, we show the analogy of Figure 6.3.1 in Figure 6.3.3, in which we show the shear stress during and after strain ramps at rates $\dot{\gamma}_{0,s}, \dot{\gamma}_{0,n}$, both without ($\beta = 0$), and with ($\beta = 1$), convective constraint release in (a) and (b) of the figure,

[9] That is, $v(y, t') \neq 0$. In an inertialess, linearly stable system after shear cessation one expects $v(y, t') = 0$, see Chapter 2.

respectively. We also show snapshots of the velocity profile after both ramps of rates $\dot{\gamma}_{0,n}$ and $\dot{\gamma}_{0,s}$ in (c)/(d) and (e)/(f) of the figure, respectively.

As expected, we find that shear rate perturbations grow as soon as the ramp of rate $\dot{\gamma}_{0,n}$ ends, if the ramp ends as the shear stress is a decreasing function of strain. In agreement with the predictions of linear instability described above, we also find the growth of shear rate perturbations after a 'fast' ramp of rate $\dot{\gamma}_{0,s}$ when the strain amplitude exceeds $\gamma_0 > 1.7$, and the efficacy of CCR is sufficiently small $\beta \sim 0$; these shear rate perturbations only begin to grow after chain stretch has relaxed at a time $t' \sim \tau_R$ ($= 10^{-4}$ in the figure), as expected.

It is immediately clear from Figure 6.3.3 (a) that shear rate heterogeneity can vastly alter the stress relaxation functions: as the local shear rate becomes extremely large nonlinearities become important, and result in a sudden and dramatic acceleration of stress relaxation concurrent with a decay of the local shear rate. We also report that, concurrent with this sudden departure from the linearised system, failure of the Lodge-Meissner relation [93] occurs: $N(t', \gamma_0) \neq \gamma_0\, \sigma(t', \gamma_0)$. The time at which this distinctive stress 'drop' occurs is sensitive to all factors that affect the growth and magnitude of heterogeneous perturbations, i.e., τ_R, β, η, γ_0, and the magnitude q of the initial noise. As discussed in Chapter 3, noise in experiment that can seed the growth of heterogeneous perturbations can arise from various sources, such as: residual stress heterogeneity present due to the sample loading protocol, imperfect rheometer feedback (i.e., mechanical noise), or a curved geometry. In this chapter we have considered the first of these by adding an initial heterogeneous perturbation to the stress of the form $q\underline{X}\cos(\pi y/L)$, where $\underline{X}$ is an array of random numbers chosen from a uniform distribution with mean 0 and width 1, as described in Chapter 3. (Adams and Olmsted showed that a curved device results in similar 'macroscopic motions' in the RP model [4].) We find, as it was also found by Agimelen and Olmsted [6, 7], that the form of the resulting velocity profiles is extremely sensitive to the form and magnitude of the initial noise and also to any heterogeneity that arises during the ramp, though we expect the latter to be insignificant in magnitude if the duration of the ramp is small. We note that the stress relaxation function (and thus, the time at which the dramatic stress 'drop' occurs) is only

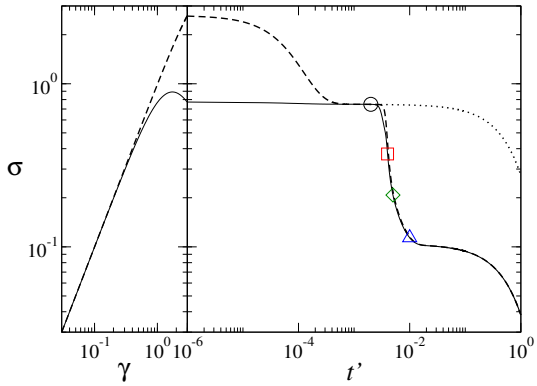

(a) $\beta = 0$

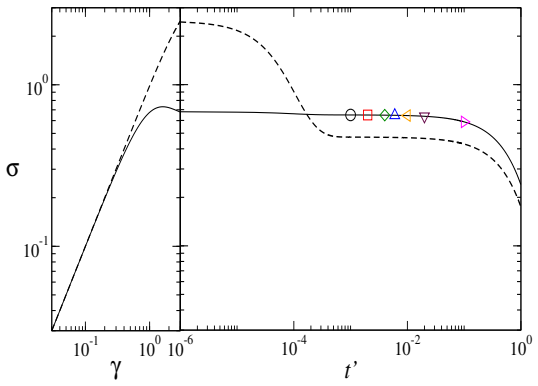

(b) $\beta = 1$

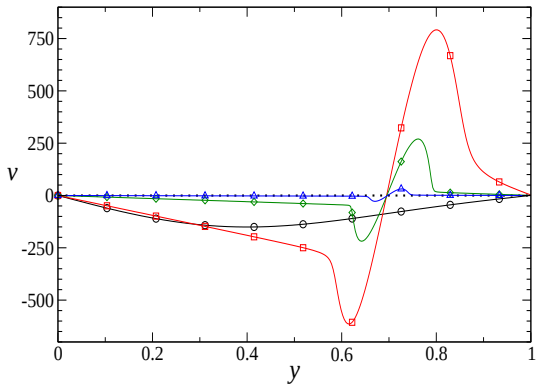

(c) $\beta = 0$, $\dot{\gamma}_0 = 500$

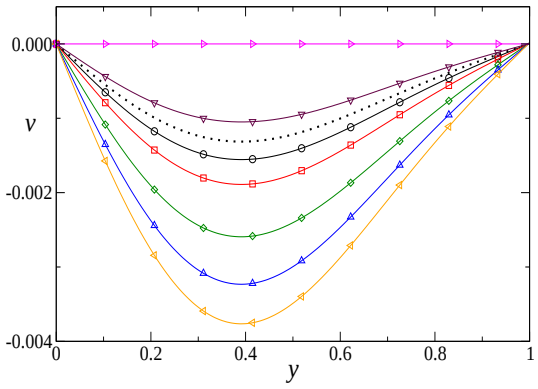

(d) $\beta = 1$, $\dot{\gamma}_0 = 500$

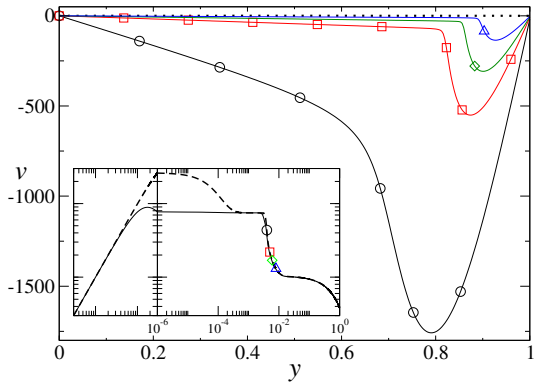

(e) $\beta = 0$, $\dot{\gamma}_0 = 10^5$

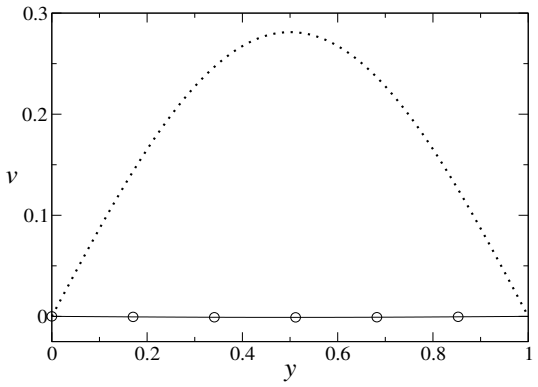

(f) $\beta = 1$, $\dot{\gamma}_0 = 10^5$

Figure 6.3.3: (a) and (b): shear stress during (*vs.* γ) and after (*vs.* t') a strain ramp of amplitude $\gamma_0 = 3$, for $\beta = 0, 1$, respectively (dotted line shows superposed result from linearised system). *Thick, dashed line:* strain ramp applied at rate $\dot{\gamma}_{0,s} = 10^5$, *thin, solid line:* strain ramp applied at $\dot{\gamma}_{0,n} = 500$. (c) and (d): velocity profiles during stress relaxation at times with corresponding symbols in (a) and (b), respectively, for the ramp at rate $\dot{\gamma}_{0,n} = 500$. (e) and (f): as (c/d) for the ramp $\dot{\gamma}_{0,s} = 10^5$, at times with symbols in the inset [inset equivalent to sub-figure (a)] for (e) or corresponding to symbols in (b) for (f). The normalised velocity profile $\hat{v}(y)$, immediately before the end of the ramp at $t = t_0^-$ is shown as a thick, dotted line, where: $\hat{v}(y) = v(y) - \dot{\gamma}_0 y$ and deviations from zero indicate slight inhomogeneity before the ramp ends. Here: $\tau_R = 10^{-4}$, $\eta = 10^{-5}$, and noise is added of the form: $\sigma(t = 0, y) = q \cos(\pi y/L)$, $q = 5 \times 10^{-4}$.

sensitive to the magnitude, rather than the form of the heterogeneity.

Despite this sensitivity, we note that the velocity profiles of systems undergoing significant 'macroscopic motions' often show a 'stationary plane'[10] with anti-symmetric like deformation on either side, as shown at $y \sim 0.7$ in Figure 6.3.3 (c). The location of this plane (and the number of stationary planes in the cell) is subject to the initial noise sensitivity described above and has been investigated in detail in [6, 7]; this may explain the non-repeatability of velocity profiles found in experiment [20, 52, 91, 137]. The local shear rate at the stationary plane can become extremely large and in extreme cases becomes spatially unresolvable [7]. This feature is also found in experiment and is often referred to as 'failure' or 'fracture' [20, 52].

The features discussed above belong to systems with small $\beta \sim 0$ and $\eta \ll G\tau_d$ that have large perturbation growth rates. For less unstable systems ($\beta \neq 0$, $\eta < G\tau_d$) 'fracture' is not seen and the stress relaxation function retains the behaviour of the linearised system so that no distinctive 'stress drop' occurs. An example of this is shown in Figure 6.3.3 (b) and (d): the local shear rate grows but is small in magnitude. In this case, this is because with larger β (here, $\beta = 1$) the slope of the shear stress in strain at the end of the ramp is negative but smaller in magnitude compared to that of $\beta = 0$. With CCR active, ramps that induce appreciable chain stretch can be stabilised to shear rate heterogeneity after chain retraction, as shown in the previous subsection. During stress relaxation after such a ramp, any residual heterogeneity at the end of the ramp decays monotonically [see (f) of Figure 6.3.3].

Relation to experimental findings

In order to clarify the origins of the 'macroscopic motions' and rheological behaviour in the RP model we have considered a possibly unrealistic separation of the timescales with regard to experiment, $\tau_d = \tau_R \times 10^4$, and a correspondingly unrealistic rate for the ramp $\dot{\gamma}_{0,s} \gg \tau_R^{-1}$. This separation of timescales corresponds to entanglement numbers $Z \sim 3300$. In experiment polymer melts that are considered to be 'well entangled' have entanglement numbers $Z > 50$, though melts with entanglement numbers larger than $Z \sim 100$ usually suffer edge fracture so that no reliable

[10] The plane is the (x, z) plane, intersecting the y axis at the point where $v(y) = 0$.

results can be obtained. Reliable results for materials with entanglement numbers up to $Z \sim 150$ have been obtained in softer materials such as DNA and wormlike micellar solutions, but an upper limit of $Z \sim 200$ still exists due to edge fracture. Therefore, a more reasonable separation of time scales in experiment has the range $\tau_d/\tau_R \sim 150 - 500$. Despite this, the qualitative features described above still hold for these more realistic values of the separation of timescales (as long as they are still reasonably separated: $\tau_d/\tau_R \gtrsim 10$), and also for an adjusted 'fast' ramp of rate $\dot{\gamma}_{0,s} > \tau_R^{-1}$ that is not as well separated from the inverse stretch relaxation time. We will not attempt to reproduce experimental data by matching the relaxation times or ramp rates, etc., to experiment as efforts have been made elsewhere [6, 7]. However, we will now use the results presented in this chapter to describe how the RP model, contrary to the claims of the Wang group [20,167,169], is indeed capable of exhibiting the qualitative features of experiment, and in doing so defend its use as a model to describe entangled polymeric systems.

Firstly, *delayed* 'macroscopic motions' associated with a sudden drop in the stress for ramps with strain amplitudes that are larger than some threshold, usually $\gamma_0 \gtrsim 1.5$, but are sufficiently small that no stress overshoot occurred during the ramp, have been reported in polymer melts [17,20] and solutions [9]. This is similar to the behaviour of the stress (and associated macroscopic motions) after the ramp of rate $\dot{\gamma}_{0,s}$ in Figure 6.3.3 (a), which results directly from the delayed linear instability described in Subsection 6.3.2. As explained, the time at which the stress 'drop' occurs in our numerics, t_{drop} (also roughly the time at which significant macroscopic motions are seen), is dependent on many factors. However, owing to the linear stability of the system, it is limited to occurring at times $t_{drop} > \tau_R$ for systems in which significant chain stretch arises during the ramp. In fact we find this time can be $O(10\tau_R)$. A similar order of magnitude was noted in experiments on melts [20], and provoked the authors to claim that the delay was not related to the stretch relaxation time, and therefore that the DE theory (or derivatives of) was not capable of describing the experiments.

Secondly, macroscopic motions and a dramatic stress drop were also found to

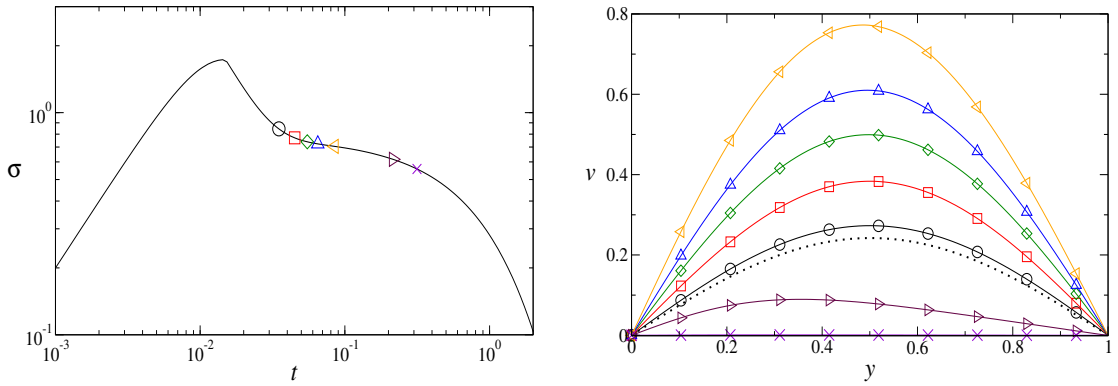

(a) (b)

Figure 6.3.4: (a) and (b) as Figure 6.3.3, for a ramp of strain amplitude $\gamma_0 = 3$ and rate $\dot{\gamma}_0 = 200$, $t_0 = 0.015$. Other parameters: $\tau_R = 10^{-2}$, $\eta = 10^{-5}$, $\beta = 0$, and noise is added of the form: $\underline{s}(t = 0, y) = \hat{\underline{s}}(t = 0) + q\underline{X}\cos(\pi y/L)$ to all components of the stress tensor, where $\underline{X}$ is an array of random numbers chosen from a flat distribution of mean 0 and width 1, and $q = 10^{-2}$.

occur (within experimental resolution) *immediately* after shear cessation [16,17] for ramps that ended as the stress was a decreasing function of strain. This is consistent with our criterion in Section 6.2, and also with our numerics in Figure 6.3.3.

Thirdly, similar macroscopic motions without a dramatic stress drop have also been reported in experiment [20, 52, 91, 135, 137, 168]. We show similar behaviour with adjusted parameters of the RP model in Figure 6.3.4, where the system shows local velocities that grow after stretch relaxation, but don't become large enough to trigger departure from the linearised system. This means that although macroscopic motions arise, no obvious change in the stress relaxation function occurs.

Finally, we consider the relation to the classification system of stress relaxation behaviour into types A, B and C, see Chapter 2. From our results with a low efficiency of CCR, $\beta \sim 0$, ramps resulting in a dramatic stress drop as seen in Figure 6.3.3 (a) would lead to a weaker damping function than that predicted by DE theory, corresponding to type C data; this is consistent with experiment [17, 135, 166]. Such results from our numerics also show failure of the LM relation, this is likewise in agreement with experiment [87]. Note that we have also shown, consistent with earlier work [67, 92, 111], that with CCR active the stress relaxation after a fast ramp ($\dot{\gamma}_0\tau_R \gg 1$) is accelerated and would also result in a weakened damping function (type C behaviour), crucially *without* any macroscopic motions.

However, all experimental results providing velocimetric data that we are aware of indicate that the accelerated stress relaxation resulting in type C behaviour is concurrent with heterogeneity in the form of macroscopic motions or 'fracture'. We therefore conclude that in order for agreement with experimental findings the efficiency of CCR must be small, $\beta \sim 0$; this was also suspected from fits to shear startup experimental data [92]. Systems that do not depart in this way from the linearised system are able to follow the DE damping function, as described by the third case above (in which we do not find failure of the LM relation). This would result in type A behaviour that may or may not show macroscopic motions; in our numerics this depends on the parameters of the model. In particular, we find that increasing the separation between the relaxation timescales τ_R, τ_d (with small $\beta \sim 0$) results in a system that is linearly unstable to heterogeneity for longer, leading to a larger magnitude of macroscopic motions and is thus more likely to produce type C data. That is, the higher the entanglement number $Z = \tau_d/3\tau_R$, the more likely type C data is to arise, in agreement with experiments that show type C data is most common to very well entangled materials [121,166]. We conclude that the RP model is capable of exhibiting both types A and C behaviour, which covers most of the experimental literature [166]. However, the RP model appears unable to show (the infrequently occurring) type B behaviour, though this data is usually found in very weakly entangled materials [121,166], for which the RP model is not an appropriate model.

While we have shown that the RP model can qualitatively describe many of the important features reported recently in experiments on polymer melts and solutions, we have not attempted to reproduce them quantitatively. To do so we should first address some of the short-comings of our approach; adjustments that could be made include: using a spectrum of relaxation times rather than a single-mode approach; finite extensibility of chains should be accounted for as outlined in [56]; other sources of noise in experiment should be considered, e.g., mechanical noise due to finite response times of the rheometer, particularly incorporating the finite time over which the shear rate is decreased at the end of the ramp; and stress gradients of the rheometer should also be included.

6.4 Conclusions

In this chapter, we have derived a criterion for the onset of linear instability to the growth of shear rate perturbations immediately after a fast strain ramp within a generalised framework that assumes a constitutive equation with separable loading and relaxation terms. The criterion predicts the growth of shear rate perturbations immediately after a ramp that ends as the shear stress is a decreasing function of strain, and is independent of fluid type.

We have investigated the shear stress relaxation functions, linear stability and resulting shear heterogeneity of entangled polymeric systems after strain ramps performed at different rates in the RP model. We showed that, for a homogeneously constrained system that forms the background state for a linear stability analysis, the stress after a 'fast' ramp of rate $\dot{\gamma}_0 \gg \tau_R^{-1}$ drops onto that of a 'slow' ramp of rate $\tau_d^{-1} \ll \dot{\gamma}_0 \ll \tau_R^{-1}$ once chain retraction in the absence of convective constraint release (CCR) has occurred. Since the stress during shear startup at a rate in the 'slow' range above is a decreasing function of strain for $\gamma \gtrsim 1.7$, independently of β, any such 'slow' ramp with a strain amplitude in this range will result in the growth of shear rate perturbations after the ramp according to the criterion above. We subsequently showed that the above results lead to a *delayed* linear instability to the growth of shear rate perturbations after a 'fast' ramp, once chain stretch has relaxed in the absence of CCR. However, we also showed that with CCR active, chain retraction causes accelerated orientation relaxation after the fast ramp and destroys the agreement with the stress of the slower ramp; this can be sufficient to stabilise the system against shear rate heterogeneity.

In full nonlinear simulations, we showed that the subsequent growth of (inhomogeneous) shear rate perturbations after such linearly unstable ramps as above can be sufficient to cause sudden departure of the stress from that of the linearised system, resulting in a dramatic drop in the shear stress and 'fracture' like velocity profiles whose form is sensitive to the initial noise. Such cases result in the failure of the LM relation and a weakened damping function, in agreement with experiment. We subsequently showed that the RP model is capable of qualitatively describing the experimental features found in polymer fluids. (Recall that examples of such

fluids include concentrated solutions or melts of high molecular weight polymers, and concentrated solutions of wormlike micelles and DNA.)

Finally, we note that the Giesekus model has linear growth of the shear stress in strain during 'fast' ramps, where 'fast' means faster than the shortest relaxation time, in this case $\dot{\gamma} \gg \lambda^{-1}$. We therefore expect the system to be linearly stable against the growth of shear rate perturbations immediately after the ramp according to the general criterion. Similar comments hold for both the scalar fluidity, soft glassy rheology and glassy polymer models.

6.5 Appendix I

This appendix contains details of the analytics concerning the long time orientation in the RP model after an ideal step strain, for which credit is given to Dr. Richard Graham.

We are interested in the stress after chain stretch has relaxed, but before orientation relaxation (reptation) has taken place significantly. To do this, we will consider the long time behaviour $\underline{\underline{\sigma}}^{\infty} = \underline{\underline{\sigma}}(t' \to \infty)$ of the RP model, where throughout we work in the limit of $\tau_d \to \infty$. In that case, and in the absence of flow, the constitutive equation of the RP model is:

$$\partial_{t'} \underline{\underline{\sigma}} = -f(T) \left[\underline{\underline{\sigma}} + \beta \left(T/3 \right)^{\delta} \left(\underline{\underline{\sigma}} - \underline{\underline{I}} \right) \right], \tag{6.5.1}$$

where $f(T) = 2 \left[1 - \sqrt{3/T(t')} \right] / \tau_R$, δ is a parameter in the RP model, and $T = \mathrm{tr}\, \underline{\underline{\sigma}}$, which describes the degree of chain stretch in the system. At equilibrium and in the long time limit $T^{\infty} = 3$, otherwise:

$$\partial_{t'} T = -f(T) \left[T + \beta \left(T/3 \right)^{\delta} \left(T - 3 \right) \right]. \tag{6.5.2}$$

We define the orientation tensor: $\underline{\underline{A}} = 3\,\underline{\underline{\sigma}}/T$, and thus:

$$\partial_{t'}\,\underline{\underline{A}} = \frac{3}{T}\left(\frac{d\underline{\underline{\sigma}}}{dt'} - \frac{\underline{\underline{\sigma}}}{T}\frac{dT}{dt'}\right). \tag{6.5.3}$$

Using this combined with Eqns 6.5.1, 6.5.2 leads to a diagonal, linear set of ODEs for $\underline{\underline{A}}$:

$$\partial_t \underline{\underline{A}} = -\Psi[T(t')](\underline{\underline{A}} - \underline{\underline{I}}), \tag{6.5.4}$$

where $\Psi[T(t')] = \beta\frac{2\left[1-\sqrt{3/T(t')}\right]}{\tau_R}\left(T(t')/3\right)^{\delta-1}$. We solve this using the integrating factor method for each component of $\underline{\underline{A}}$:[11]

$$\underline{\underline{A}}^{\infty} = \underline{\underline{A}}^{0} e^{\left[-\int_0^\infty \Psi[T(t')]dt'\right]} + \underline{\underline{I}}\left\{1 - e^{\left[-\int_0^\infty \Psi[T(t')]dt'\right]}\right\}. \tag{6.5.5}$$

The integral $I = \int_0^\infty \Psi[T(t')]\,dt' = \int_0^\infty \beta f[T(t')]\left[\frac{T(t')}{3}\right]^{\delta-1} dt'$ has analytical solutions for some values of δ; by defining $u \equiv T(t')$ we obtain:

$$I = -\beta\int_{T(0)}^{3} \frac{(u/3)^{\delta-1}}{u + \beta(u/3)^{\delta}(u-3)}du, \tag{6.5.6}$$

the simplest solution of which is for $\delta = 0$, leading to:

$$A_{xy}^{\infty} = \frac{A_{xy}^{0}}{1 + \beta - 3\beta/T_0} \quad (\text{for } \delta = 0), \tag{6.5.7}$$

and thus:

$$\sigma^{\infty}(\dot{\gamma}_{0,s}, \gamma_0) = \frac{3\gamma_0}{(\gamma^2+3)(1+\beta) - 3\beta} \quad (\text{for } \delta = 0). \tag{6.5.8}$$

6.6 Appendix II

This appendix details the derivation of the analytical solution of the largest real part of the eigenvalues from the linear stability analysis: $\omega(t')$, Eqn 6.3.5, after a strain ramp performed at a rate $\dot{\gamma}_{0,n}$ in the nonstretching limit of the RP model.

First, note that the nonstretching form of the RP model has only two dynamical

[11] The full time dependence, rather than the infinite limit $t' \to \infty$ may be found in the same way.

variables s_1, s_2, with governing equations:

$$\begin{aligned} \partial_t s_1 &= \dot{\gamma} S_1(s_1, s_2, \dot{\gamma}) \quad -s_1/\tau_d, \\ \partial_t s_2 &= \dot{\gamma} S_2(s_1, s_2, \dot{\gamma}) \quad -(s_2 - 1)/\tau_d. \end{aligned} \tag{6.6.1}$$

After the ramp the shear rate is turned off $\dot{\gamma} \to 0$, and Eqns 6.6.1 can be solved analytically:

$$\begin{aligned} s_1(t') &= s_{1,0} \exp(-t'/\tau_d) \\ s_2(t') &= (s_{2,0} - 1) \exp(-t'/\tau_d) \quad + 1, \end{aligned} \tag{6.6.2}$$

where $s_{1,0}, s_{2,0}$ are the values of s_1, s_2 immediately after the ramp. A linear stability analysis (as described in Chapter 3) performed on the system as it relaxes post-ramp provides the stability matrix $\underline{\underline{P}}(t')$:

$$\underline{\underline{P}}(t') = \begin{pmatrix} -\frac{1}{\tau_d} - \frac{S_1}{\eta} & 0 \\ -\frac{S_2}{\eta} & -\frac{1}{\tau_d} \end{pmatrix}, \tag{6.6.3}$$

resulting in the largest eigenvalue $\omega(t') = -\frac{1}{\tau_d} - \frac{S_1}{\eta}$. In the nonstretching form of the RP model $S_1 = s_2 - \frac{2}{3} s_1^2 (1 + \beta)$; substituting Eqns 6.6.2 into the solution for $\omega(t')$ results in the solution:

$$\omega(t') = -\frac{1}{\tau_d} - \frac{1}{\eta} \left[(s_{2,0} - 1) e^{-\frac{t'}{\tau_d}} + 1 - \frac{2}{3} s_{1,0}^2 \, e^{-\frac{2t'}{\tau_d}} (1 + \beta) \right], \tag{6.6.4}$$

where $s_1 = \sigma_{xy}$ and $s_2 = \sigma_{yy}$ in the model.

7

Conclusions and Outlook

7.1 Summary of the main results

In this thesis we have explored the time-dependent rheological response of three classes of complex fluids: soft glassy materials, and entangled polymeric materials above and below the glass transition, to the shear deformation protocols of step stress, shear startup and strain ramp. For each protocol we explored the use of three fluid-universal (protocol specific) criteria for the onset of linear instability to shear banding, recently derived by Dr. Suzanne Fielding.

In step stress, we showed that the rolie poly (RP) and Giesekus models for entangled polymeric materials show qualitatively similar responses of shear rate $\dot{\gamma}(t)$. (Examples of such materials include concentrated solutions and melts of polymers, and concentrated solutions of wormlike micelles and DNA.) In these models, for imposed stresses nearest those on the weakest slope of the flow curve, the shear rate

shows an initial decrease followed by a sudden, dramatic increase over several orders of magnitude in a short time, in qualitative agreement with experiments. During this increase, the shear rate undergoes a regime of simultaneous positive curvature and slope $\partial_t^2\dot{\gamma}/\partial_t\dot{\gamma} > 0$, predicted by the criterion to be linearly unstable to the growth of shear bands. We confirmed that such shear bands arise, but showed that they are only significant in the RP model: bands in the Giesekus model remain negligibly small. Next, we explored the response of the SGR model in the glass phase to a step stress. Our motive here was to obtain predictions for the times at which the system is linearly unstable to the onset of banding according to the criterion, depending on the parameters of the model and the value of the imposed stress. We showed that during 'creep' the shear rate decreases as a power law in time: $\dot{\gamma}(t) \sim t_w^{x-1}(t-t_w)^{-x}$, where t_w is the *age* of the sample, and x the 'noise temperature'. For stresses exceeding the yield stress, the creep regime ends when the shear rate passes through a minimum and undergoes a regime of positive curvature and slope during which the system is linearly unstable to the onset of banding. As the shear rate dramatically increases, it passes through an inflection point before reaching a steadily flowing state. We found that the inflection point, defined as the 'fluidisation time' τ_f, depends on the imposed stress via $\tau_\mathrm{f} \sim t_w(\Sigma - \Sigma_y)^{-\alpha}$, for stresses close to (but larger than) the yield stress, and $\tau_\mathrm{f} \sim \exp(-\Sigma)$ for larger stresses, where Σ_y is the yield stress and $\alpha \sim O(1)$. Finally, we showed that the glassy polymer model shows similar features in this step shear stress protocol as it does in the extensional loading protocol, and, using the criterion, we showed that strain hardening results in a decrease in the magnitude of transient shear banding.

In shear startup, we first described predictions of the criterion in the large shear rate limit that lead to the identification of an 'elastic' term in the criterion, and in the large strain limit leading to a 'viscous' term. The 'elastic' term in the former limit predicts that negative slopes of the shear stress in strain contribute towards linear instability to shear banding, in agreement with experimental findings. In the latter limit, the 'viscous' term recovers the well known steady state condition for shear banding. Outside these two limits the remaining 'cross' term is non-negligible. We explored all three terms and their contribution to linear instability to shear banding

in the scalar fluidity, RP and Giesekus models. In the scalar fluidity model we showed age-dependent transient shear banding arises during the negative slope of shear stress in strain. In the RP model we showed that similar time-dependent shear banding arises for imposed shear rates $\tau_d^{-1} \ll \dot{\gamma} \ll \tau_R^{-1}$, that may or may not persist to steady state depending on the ultimate shape of the constitutive curve. In the Giesekus model we found that the 'viscous' and 'cross' terms of the criterion are always large enough to stabilise the system against heterogeneity during the negative slope of shear stress in strain. As a result, the model does not show the features of appreciable time-dependent shear banding associated with the stress overshoot, in contrast to experimental findings of entangled polymeric materials. From these and the above results, we conclude that the Giesekus model is not appropriate for the description of *time-dependent* shear banding in such materials. Finally, we explored shear startup in the GP model, and demonstrated that due to the reduced magnitude of the negative slope of shear stress in strain on the addition of a polymeric component, transient shear banding is again significantly reduced in this model.

In the strain ramp protocol, we first explored the stress relaxation behaviour of a homogeneous background state in the RP model after strain ramps at rates that are 'fast' or 'slow', relative to the rate at which chain stretch relaxes τ_R^{-1}, which we later used as the basis for a linear stability analysis. We showed that, in the absence of convective constraint release (CCR), the stress relaxation function of a 'fast' ramp drops onto that of a 'slow' ramp once chain stretch has relaxed. However, we also showed that stretch relaxation with CCR active results in an additional orientation relaxation that accelerates the shear stress relaxation, destroying the agreement with the stress of the slower ramp. The criterion for the strain ramp predicts linear instability to shear heterogeneity immediately after the ramp if, immediately before the end of the ramp, the shear stress had been decreasing in strain. We used this to show that 'slow' ramps with strain amplitudes $\gamma \gtrsim 1.7$ (up to some cut-off amplitude) are linearly unstable immediately after the ramp. We also showed that although 'fast' ramps are linearly stable immediately after ramps of *any* strain amplitude, they may show (for the same strain amplitudes that the 'slow' ramp is linearly

unstable after) a *delayed* onset of linear instability once chain stretch has relaxed, as long as CCR is sufficiently inactive. Finally, we showed that the above linear instability results in 'macroscopic motions' that are qualitatively similar to those found in experiment. We showed that if these become sufficiently heterogeneous, nonlinearities become important and the stress relaxation function shows a dramatic 'drop', concurrent with failure of the Lodge-Meissner relation. Using these results, we showed that the RP model is capable of demonstrating the qualitative features found in experiment.

7.2 Outlook for future research

Limitations exist in any research project. We now outline some of the research limitations of this PhD, and some directions for future research.

Spectrum of relaxation times

Firstly, we note that throughout this thesis we have only considered a single relaxation time (or in the RP model, two relaxation times). In reality, a spectrum of relaxation times τ_i and elastic moduli G_i should be used to more accurately model complex fluids, in particular polymer melts or solutions which, even when monodisperse, have a spectrum of relaxation times [86]. It is important to note, however, that the fluid-universal criteria derived for each shear protocol in this thesis do not depend on whether a single- or multi-mode approach is used. We expect only the shape of the bulk rheological response to change when multiple modes are introduced. Therefore, the onset of banding that we have shown to depend on this bulk signal will also change. For example, for entangled polymeric materials after a fast strain ramp, we expect that a spectrum of relaxation times might smear out the otherwise clearly defined times $\tau_R \ll t' \ll \tau_d$ for which the system is linearly unstable to shear rate heterogeneity. As a result, the time for which the system is linearly unstable to shear rate heterogeneity might be much smaller, or even removed entirely. Or, in the steady state limit of shear startup in the RP model, a spectrum of relaxation times might remove the negative slope of the constitutive curve, rendering

the system linearly stable against shear banding at steady state.

Despite this limitation, we do not expect our results to change vastly under a multi-mode approach. Rather, we consider that the introduction of multiple modes is most useful for a detailed comparison with experiment.

Other shear deformation protocols, e.g., LAOS

The criteria derived by Dr. Suzanne Fielding [117] for step stress, shear startup and strain ramp deformations in the shear geometry, along with a criterion for necking in extensional deformations [56], form a set of fluid-universal criteria for the onset of linear instability to heterogeneity during time-dependent flows of complex fluids. However, what is still lacking from this understanding is a criterion for the onset of linear instability to shear banding during large amplitude oscillatory shear (LAOS). Time-dependent shear banding during this deformation protocol has recently been shown to arise in experiment [137,139,163] and also in numerics of the RP model [4]. We hope that future research in this area will explore such a criterion.

Wall slip

Throughout this thesis we have considered zero slip conditions at the walls, i.e., the velocity in the vicinity of the wall is the same as that of the wall itself: $\lim_{y\to L} v(y) = \overline{\dot{\gamma}}L$ and $\lim_{y\to 0} v(y) = 0$. However, in experiment wall slip is an extremely prevalent problem, usually combated by roughening or glueing sand paper to the rheometer plates, or, in extreme cases, super-glueing the sample to the plates [20]. In order to provide a more detailed understanding of the interplay between shear banding and wall slip, it would be necessary to incorporate conditions for wall slip into our numerics that can be tuned depending on the surface roughness.

Finally, we hope that research in this thesis will help to unify the understanding of time-dependent shear banding in complex fluids during shear deformation.

Bibliography

[1] Grace, copyright ©1991-1995 Paul J Turner, Portland.

[2] J. M. Adams, S. M. Fielding, and P. D. Olmsted. Transient shear banding in entangled polymers: A study using the rolie-poly model. *Journal of Rheology*, 55(5):1007–1032, 2011.

[3] J. M. Adams and P. D. Olmsted. Adams and Olmsted reply:. *Phys. Rev. Lett.*, 103:219802, 2009.

[4] J. M. Adams and P. D. Olmsted. Nonmonotonic models are not necessary to obtain shear banding phenomena in entangled polymer solutions. *Phys. Rev. Lett.*, 102:067801, 2009.

[5] J.M. Adams, S.M. Fielding, and P.D. Olmsted. The interplay between boundary conditions and flow geometries in shear banding: Hysteresis, band configurations, and surface transitions. *Journal of Non-Newtonian Fluid Mechanics*, 151:101 – 118, 2008.

[6] O. S. Agimelen. *The physics of fracture in an unstable polymeric liquid*. PhD thesis, University of Leeds, 2012.

[7] O. S. Agimelen and P. D. Olmsted. Apparent fracture in polymeric fluids under step shear. *arXiv:1204.4169 (preprint 2012)*.

[8] L. A. Archer. Separability criteria for entangled polymer liquids. *Journal of Rheology*, 43(6):1555–1571, 1999.

[9] L. A. Archer, Y.-L. Chen, and R. G. Larson. Delayed slip after step strains in highly entangled polystyrene solutions. *Journal of Rheology*, 39(3):519–525, 1995.

[10] J. Azaiez, R. Guénette, and A. Ait-Kadi. Entry flow calculations using multimode models. *Journal of Non-Newtonian Fluid Mechanics*, 66(2-3):271 – 281, 1996.

[11] T. Bauer, J. Oberdisse, and L. Ramos. Collective rearrangement at the onset of flow of a polycrystalline hexagonal columnar phase. *Phys. Rev. Lett.*, 97:258303, 2006.

[12] J.-F. Berret and Y. Séréro. Evidence of shear-induced fluid fracture in telechelic polymer networks. *Phys. Rev. Lett.*, 87:048303, 2001.

[13] R. B. Bird, R. C. Armstrong, and O. Hassager. *Dynamics of Polymeric Liquids. Volume 1: Fluid Mechanics*. Wiley, New York, 1987.

[14] L. Bocquet, A. Colin, and A. Ajdari. Kinetic theory of plastic flow in soft glassy materials. *Phys. Rev. Lett.*, 103:036001, 2009.

[15] A. B. Bortz, M. H. Kalos, and J. L. Lebowitz. A new algorithm for Monte Carlo simulation of ising spin systems. *Journal of Computational Physics*, 17(1):10 – 18, 1975.

[16] P. E. Boukany and S-Q. Wang. Use of particle-tracking velocimetry and flow birefringence to study nonlinear flow behavior of entangled wormlike micellar solution: From wall slip, bulk disentanglement to chain scission. *Macromolecules*, 41(4):1455–1464, 2008.

[17] P. E. Boukany and S-Q. Wang. Exploring origins of interfacial yielding and wall slip in entangled linear melts during shear or after shear cessation. *Macromolecules*, 42(6):2222–2228, 2009.

[18] P. E. Boukany and S-Q. Wang. Exploring the transition from wall slip to bulk shearing banding in well-entangled dna solutions. *Soft Matter*, 5:780–789, 2009.

[19] P. E. Boukany and S-Q. Wang. Shear banding or not in entangled DNA solutions depending on the level of entanglement. *Journal of Rheology*, 53(1):73–83, 2009.

[20] P. E. Boukany, S-Q. Wang, and X. Wang. Step shear of entangled linear polymer melts: New experimental evidence for elastic yielding. *Macromolecules*, 42(16):6261–6269, 2009.

[21] J. M. Brader, M. E. Cates, and M. Fuchs. First-principles constitutive equation for suspension rheology. *Phys. Rev. Lett.*, 101:138301, 2008.

[22] J. M. Brader, Th. Voigtmann, M. E. Cates, and M. Fuchs. Dense colloidal suspensions under time-dependent shear. *Phys. Rev. Lett.*, 98:058301, 2007.

[23] S. R. Burdette. Development of the velocisty field in transient shear flows of viscoelastic fluids. *Journal of Non-Newtonian Fluid Mechanics*, 32(3):269 – 294, 1989.

[24] J. A. Byars, R. J. Binnington, and D. V. Boger. Entry flow and constitutive modelling of fluid S1. *Journal of Non-Newtonian Fluid Mechanics*, 72(2-3):219 – 235, 1997.

[25] C. Grand, J. Arrault, and M. E. Cates. Slow transients and metastability in wormlike micelle rheology. *J. Phys. II France*, 7(8):1071–1086, 1997.

[26] J. Cao and A. E. Likhtman. Shear banding in molecular dynamics of polymer melts. *Phys. Rev. Lett.*, 108:028302, 2012.

[27] M. E. Cates. Nonlinear viscoelasticity of wormlike micelles (and other reversibly breakable polymers). *The Journal of Physical Chemistry*, 94(1):371–375, 1990.

[28] F. Caton and C. Baravian. Plastic behavior of some yield stress fluids: from creep to long-time yield. *Rheologica Acta*, 47:601–607, 2008.

[29] D. T. N. Chen, Q. Wen, P. A. Janmey, J. C. Crocker, and A. G. Yodh. Rheology of soft materials. *Annual Review of Condensed Matter Physics*, 1(1):301–322, 2010.

[30] K. Chen, E. J. Saltzman, and K. S. Schweizer. Segmental dynamics in polymers: from cold melts to ageing and stressed glasses. *Journal of Physics: Condensed Matter*, 21(50):503101, 2009.

[31] K. Chen and K. S. Schweizer. Stress-enhanced mobility and dynamic yielding in polymer glasses. *Europhysics Letters*, 79(2):26006, 2007.

[32] K. Chen and K. S. Schweizer. Suppressed segmental relaxation as the origin of strain hardening in polymer glasses. *Phys. Rev. Lett.*, 102:038301, 2009.

[33] C. Chung, T. Uneyama, Y. Masubuchi, and H. Watanabe. Numerical study of chain conformation on shear banding using diffusive rolie-poly model. *Rheologica Acta*, 50:753–766, 2011.

[34] P. Coussot, Q. D. Nguyen, H. T. Huynh, and D. Bonn. Avalanche behavior in yield stress fluids. *Phys. Rev. Lett.*, 88:175501, 2002.

[35] P. Coussot, Q. D. Nguyen, H. T. Huynh, and D. Bonn. Viscosity bifurcation in thixotropic, yielding fluids. *Journal of Rheology*, 46(3):573–589, 2002.

[36] P. Coussot and G. Ovarlez. Physical origin of shear-banding in jammed systems. *The European Physical Journal E: Soft Matter and Biological Physics*, 33:183–188, 2010.

[37] P. Coussot, J. S. Raynaud, F. Bertrand, P. Moucheront, J. P. Guilbaud, H. T. Huynh, S. Jarny, and D. Lesueur. Coexistence of liquid and solid phases in flowing soft-glassy materials. *Phys. Rev. Lett.*, 88:218301, 2002.

[38] P. Coussot, H. Tabuteau, X. Chateau, L. Tocquer, and G. Ovarlez. Aging and solid or liquid behavior in pastes. *Journal of Rheology*, 50(6):975–994, 2006.

[39] E. N. da C. Andrade. On the viscous flow in metals, and allied phenomena. *Proceedings of the Royal Society of London. Series A*, 84(567):1–12, 1910.

[40] P. G. de Gennes. Reptation of a polymer chain in the presence of fixed obstacles. *The Journal of Chemical Physics*, 55(2):572–579, 1971.

[41] C. Derec, A. Ajdari, and F. Lequeux. Rheology and aging: A simple approach. *The European Physical Journal E: Soft Matter and Biological Physics*, 4:355–361, 2001.

[42] T. Divoux, C. Barentin, and S. Manneville. From stress-induced fluidization processes to Herschel-Bulkley behaviour in simple yield stress fluids. *Soft Matter*, 7:8409–8418, 2011.

[43] T. Divoux, C. Barentin, and S. Manneville. Stress overshoot in a simple yield stress fluid: An extensive study combining rheology and velocimetry. *Soft Matter*, 7:9335–9349, 2011.

[44] T. Divoux, V. Grenard, and S. Manneville. Rheological hysteresis in soft glassy materials. *Phys. Rev. Lett.*, 110:018304, Jan 2013.

[45] T. Divoux, D. Tamarii, C. Barentin, and S. Manneville. Transient shear banding in a simple yield stress fluid. *Phys. Rev. Lett.*, 104:208301, 2010.

[46] M. Doi and S. F. Edwards. Dynamics of concentrated polymer systems. Part 2 Molecular motion under flow. *J. Chem. Soc., Faraday Trans. 2*, 74:1802–1817, 1978.

[47] M. Doi and S. F. Edwards. *The Theory of Polymer Dynamics*. Clarendon, Oxford, 1989.

[48] S. F. Edwards. The statistical mechanics of polymerized material. *Proceedings of the Physical Society*, 92(1):9, 1967.

[49] Y. Einaga, K. Osaki, M. Kurata, S. Kimura, and M. Tamura. Stress relaxation of polymer solutions under large strain. *Polymer Journal*, 2(4):550–552, 1971.

[50] M. L. Falk and J. S. Langer. Dynamics of viscoplastic deformation in amorphous solids. *Phys. Rev. E*, 57:7192–7205, 1998.

[51] A. Fall, J. Paredes, and D. Bonn. Yielding and shear banding in soft glassy materials. *Phys. Rev. Lett.*, 105:225502, 2010.

[52] Y. Fang, G. Wang, N. Tian, X. Wang, X. Zhu, P. Lin, G. Ma, and L. Li. Shear inhomogeneity in poly(ethylene oxide) melts. *Journal of Rheology*, 55(5):939–949, 2011.

[53] S. M. Fielding. Unpublished.

[54] S. M. Fielding. *Ageing, driving and effective temperatures: from 'soft rheology' to glassy dynamics*. PhD thesis, University of Edinburgh, 2000.

[55] S. M. Fielding. Complex dynamics of shear banded flows. *Soft Matter*, 3:1262–1279, 2007.

[56] S. M. Fielding. Criterion for extensional necking instability in polymeric fluids. *Phys. Rev. Lett.*, 107:258301, 2011.

[57] S. M. Fielding, M. E. Cates, and P. Sollich. Shear banding, aging and noise dynamics in soft glassy materials. *Soft Matter*, 5:2378–2382, 2009.

[58] S. M. Fielding, R. G. Larson, and M. E. Cates. Simple model for the deformation-induced relaxation of glassy polymers. *Phys. Rev. Lett.*, 108:048301, 2012.

[59] S. M. Fielding, R. L. Moorcroft, R. G. Larson, and M. E. Cates. Modeling the relaxation of polymer glasses under shear and elongational loads. *The Journal of Chemical Physics*, 138(12):12A504, 2013.

[60] S. M. Fielding and P. D. Olmsted. Flow phase diagrams for concentration-coupled shear banding. *The European Physical Journal E*, 11:65–83, 2003.

[61] S. M. Fielding and P. D. Olmsted. Kinetics of the shear banding instability in startup flows. *Phys. Rev. E*, 68:036313, 2003.

[62] S. M. Fielding, P. Sollich, and M. E. Cates. Aging and rheology in soft materials. *Journal of Rheology*, 44(2):323–369, 2000.

[63] M. Fuchs and M. E. Cates. Theory of nonlinear rheology and yielding of dense colloidal suspensions. *Phys. Rev. Lett.*, 89:248304, 2002.

[64] T. Gibaud, D. Frelat, and S. Manneville. Heterogeneous yielding dynamics in a colloidal gel. *Soft Matter*, 6:3482–3488, 2010.

[65] H. Giesekus. A simple constitutive equation for polymer fluids based on the concept of deformation-dependent tensorial mobility. *Journal of Non-Newtonian Fluid Mechanics*, 11(1-2):69 – 109, 1982.

[66] V. Gopalakrishnan and C. F. Zukoski. Delayed flow in thermo-reversible colloidal gels. *Journal of Rheology*, 51(4):623–644, 2007.

[67] R. S. Graham, A. E. Likhtman, T. C. B. McLeish, and S. T. Milner. Microscopic theory of linear, entangled polymer chains under rapid deformation including chain stretch and convective constraint release. *Journal of Rheology*, 47(5):1171–1200, 2003.

[68] K. A. Hayes, M. R. Buckley, H. Qi, I. Cohen, and L. A. Archer. Constitutive curve and velocity profile in entangled polymers during start-up of steady shear flow. *Macromolecules*, 43(9):4412–4417, 2010.

[69] D. A. Head, A. Ajdari, and M. E. Cates. Jamming, hysteresis, and oscillation in scalar models for shear thickening. *Phys. Rev. E*, 64:061509, 2001.

[70] M. E. Helgeson, M. D. Reichert, Y. T. Hu, and N. J. Wagner. Relating shear banding, structure, and phase behavior in wormlike micellar solutions. *Soft Matter*, 5:3858–3869, 2009.

[71] M. E. Helgeson, P. A. Vasquez, E. W. Kaler, and N. J. Wagner. Rheology and spatially resolved structure of cetyltrimethylammonium bromide wormlike micelles through the shear banding transition. *Journal of Rheology*, 53(3):727–756, 2009.

[72] W. Herschel and R. Bulkley. Measurement of consistency as applied to rubber-benzene solutions. *Proc. Am. Assoc. Test Mater.*, 26:621, 1926.

[73] R. S. Hoy and C. S. O'Hern. Viscoplasticity and large-scale chain relaxation in glassy-polymeric strain hardening. *Phys. Rev. E*, 82:041803, 2010.

[74] Y. T. Hu. Steady-state shear banding in entangled polymers? *Journal of Rheology*, 54(6):1307–1323, 2010.

[75] Y. T. Hu and A. Lips. Kinetics and mechanism of shear banding in an entangled micellar solution. *Journal of Rheology*, 49(5):1001–1027, 2005.

[76] Y. T. Hu, C. Palla, and A. Lips. Comparison between shear banding and shear thinning in entangled micellar solutions. *Journal of Rheology*, 52(2):379–400, 2008.

[77] Y. T. Hu, L. Wilen, A. Philips, and A. Lips. Is the constitutive relation for entangled polymers monotonic? *Journal of Rheology*, 51(2):275–295, 2007.

[78] G. Ianniruberto and G. Marrucci. A simple constitutive equation for entangled polymers with chain stretch. *Journal of Rheology*, 45(6):1305–1318, 2001.

[79] Y. W. Inn, K. F. Wissbrun, and M. M. Denn. Effect of edge fracture on constant torque rheometry of entangled polymer solutions. *Macromolecules*, 38(22):9385–9388, 2005.

[80] J. P. Bouchaud. Weak ergodicity breaking and aging in disordered systems. *J. Phys. I France*, 2(9):1705–1713, 1992.

[81] J. P. Bouchaud and D.S. Dean. Aging on parisi's tree. *J. Phys. I France*, 5(3):265–286, 1995.

[82] M. W. Johnson Jr. and D. Segalman. A model for viscoelastic fluid behavior which allows non-affine deformation. *Journal of Non-Newtonian Fluid Mechanics*, 2(3):255 – 270, 1977.

[83] S. A. Khan and R. G. Larson. Comparison of simple constitutive equations for polymer melts in shear and biaxial and uniaxial extensions. *Journal of Rheology*, 31(3):207–234, 1987.

[84] E. T. J. Klompen, T. A. P. Engels, L. E. Govaert, and H. E. H. Meijer. Modeling of the postyield response of glassy polymers: influence of thermomechanical history. *Macromolecules*, 38(16):6997–7008, 2005.

[85] R. Larson. *Constitutive Equations for Polymer Melts and Solutions*. Butterwirth Publishers, Stoneham, MA, 1988.

[86] R. G. Larson. *The Structure and Rheology of Complex Fluids*. Oxford University Press Inc., New York, 1999.

[87] R. G. Larson, S. A. Khan, and V. R. Raju. Relaxation of stress and birefringence in polymers of high molecular weight. *Journal of Rheology*, 32(2):145–161, 1988.

[88] H-N. Lee, K. Paeng, S. F. Swallen, and M. D. Ediger. Direct measurement of molecular mobility in actively deformed polymer glasses. *Science*, 323(5911):231–234, 2009.

[89] S. Lerouge and J-F. Berret. Shear-induced transitions and instabilities in surfactant wormlike micelles. In K. Dusek and J-F. Joanny, editors, *Polymer Characterization*, volume 230 of *Advances in Polymer Science*, pages 1–71. Springer Berlin Heidelberg, 2010.

[90] S. Lerouge, J-P. Decruppe, and J-F. Berret. Correlations between rheological and optical properties of a micellar solution under shear banding flow. *Langmuir*, 16(16):6464–6474, 2000.

[91] X. Li and S-Q. Wang. Elastic yielding after step shear and during laos in the absence of meniscus failure. *Rheologica Acta*, 49:985–991, 2010.

[92] A. E. Likhtman and R. S. Graham. Simple constitutive equation for linear polymer melts derived from molecular theory: Rolie-poly equation. *Journal of Non-Newtonian Fluid Mechanics*, 114(1):1 – 12, 2003.

[93] A. S. Lodge and J. Meissner. On the use of instantaneous strains, superposed on shear and elongational flows of polymeric liquids, to test the gaussian net-

work hypothesis and to estimate the segment concentration and its variation during flow. *Rheologica Acta*, 11:351–352, 1972.

[94] C.-Y. D. Lu, P. D. Olmsted, and R. C. Ball. Effects of nonlocal stress on the determination of shear banding flow. *Phys. Rev. Lett.*, 84:642, 2000.

[95] R. W. Mair and P. T. Callaghan. Observation of shear banding in worm-like micelles by NMR velocity imaging. *Europhysics Letters*, 36(9):719, 1996.

[96] R. W. Mair and P. T. Callaghan. Shear flow of wormlike micelles in pipe and cylindrical couette geometries as studied by nuclear magnetic resonance microscopy. *Journal of Rheology*, 41(4):901–924, 1997.

[97] R. Makhloufi, J. P. Decruppe, A. Aït-Ali, and R. Cressely. Rheo-optical study of worm-like micelles undergoing a shear banding flow. *Europhysics Letters*, 32(3):253, 1995.

[98] S. Manneville. Recent experimental probes of shear banding. *Rheologica Acta*, 47:301–318, 2008.

[99] S. Manneville, A. Colin, G. Waton, and F. Schosseler. Wall slip, shear banding, and instability in the flow of a triblock copolymer micellar solution. *Phys. Rev. E*, 75:061502, 2007.

[100] M. L. Manning, E. G. Daub, J. S. Langer, and J. M. Carlson. Rate-dependent shear bands in a shear-transformation-zone model of amorphous solids. *Phys. Rev. E*, 79:016110, 2009.

[101] M. L. Manning, J. S. Langer, and J. M. Carlson. Strain localization in a shear transformation zone model for amorphous solids. *Phys. Rev. E*, 76:056106, 2007.

[102] V. Mansard and A. Colin. Local and non local rheology of concentrated particles. *Soft Matter*, 8:4025–4043, 2012.

[103] V. Mansard, A. Colin, P. Chauduri, and L. Bocquet. A kinetic elasto-plastic model exhibiting viscosity bifurcation in soft glassy materials. *Soft Matter*, 7:5524–5527, 2011.

[104] G. Marrucci and N. Grizzuti. The free energy function of the Doi-Edwards theory: analysis of the instabilities in stress relaxation. *Journal of Rheology*, 27(5):433–450, 1983.

[105] G. Marrucci and N. Grizzuti. Fast flows of concentrated polymers - predictions of the tube model on chain stretching. *Gazzetta Chimica Italiana*, 118(3):179–185, 1988.

[106] K. Martens, L. Bocquet, and J-L. Barrat. Spontaneous formation of permanent shear bands in a mesoscopic model of flowing disordered matter. *Soft Matter*, 8:4197–4205, 2012.

[107] J. D. Martin and Y. T. Hu. Transient and steady-state shear banding in aging soft glassy materials. *Soft Matter*, 8:6940–6949, 2012.

[108] D. W. Mead, R. G. Larson, and M. Doi. A molecular theory for fast flows of entangled polymers. *Macromolecules*, 31(22):7895–7914, 1998.

[109] D.W. Mead and L.G. Leal. The reptation model with segmental stretch. *Rheologica Acta*, 34:339–359, 1995.

[110] E. Miller and J. P. Rothstein. Transient evolution of shear-banding wormlike micellar solutions. *Journal of Non-Newtonian Fluid Mechanics*, 143(1):22 – 37, 2007.

[111] S. T. Milner, T. C. B. McLeish, and A. E. Likhtman. Microscopic theory of convective constraint release. *Journal of Rheology*, 45(2):539–563, 2001.

[112] P. Møller, A. Fall, V. Chikkadi, D. Derks, and D. Bonn. An attempt to categorize yield stress fluid behaviour. *Philosophical Transactions of the Royal Society A: Mathematical, Physical and Engineering Sciences*, 367(1909):5139–5155, 2009.

[113] P. C. F. Møller, A. Fall, and D. Bonn. Origin of apparent viscosity in yield stress fluids below yielding. *Europhysics Letters*, 87(3):38004, 2009.

[114] P. C. F. Møller, S. Rodts, M. A. J. Michels, and Daniel Bonn. Shear banding and yield stress in soft glassy materials. *Phys. Rev. E*, 77:041507, 2008.

[115] C. Monthus and J-P. Bouchaud. Models of traps and glass phenomenology. *Journal of Physics A: Mathematical and General*, 29(14):3847, 1996.

[116] R. L. Moorcroft, M. E. Cates, and S. M. Fielding. Age-dependent transient shear banding in soft glasses. *Phys. Rev. Lett.*, 106:055502, 2011.

[117] R. L. Moorcroft and S. M. Fielding. Criteria for shear banding in time-dependent flows of complex fluids. *Phys. Rev. Lett.*, 110:086001, 2013.

[118] H. Nechad, A. Helmstetter, R. El Guerjouma, and D. Sornette. Creep ruptures in heterogeneous materials. *Phys. Rev. Lett.*, 94:045501, 2005.

[119] P. D. Olmsted. Perspectives on shear banding in complex fluids. *Rheologica Acta*, 47:283–300, 2008.

[120] P. D. Olmsted, O. Radulescu, and C.-Y. D. Lu. Johnson–Segalman model with a diffusion term in cylindrical couette flow. *Journal of Rheology*, 44(2):257–275, 2000.

[121] K. Osaki. On the damping function of shear relaxation modulus for entangled polymers. *Rheologica Acta*, 32:429–437, 1993.

[122] K. Osaki and M. Kurata. Experimental appraisal of the Doi-Edwards theory for polymer rheology based on the data for polystyrene solutions. *Macromolecules*, 13(3):671–676, 1980.

[123] K. Osaki, K. Nishizawa, and M. Kurata. Material time constant characterizing the nonlinear viscoelasticity of entangled polymeric systems. *Macromolecules*, 15(4):1068–1071, 1982.

[124] K. Osaki and J. L. Schrag. Viscoelastic properties of polymer solutions in high-viscosity solvents and limiting high-frequency behavior. I. Polystyrene and Poly-α-methylstyrene. *Polymer Journal*, 2(4):541–549, 1971.

[125] G. Ovarlez, S. Rodts, X. Chateau, and P. Coussot. Phenomenology and physical origin of shear localization and shear banding in complex fluids. *Rheologica Acta*, 48:831–844, 2009.

[126] J. Paredes, N. Shahidzadeh-Bonn, and D. Bonn. Shear banding in thixotropic and normal emulsions. *Journal of Physics: Condensed Matter*, 23(28):284116, 2011.

[127] D. Pearson, E. Herbolzheimer, N. Grizzuti, and G. Marrucci. Transient behavior of entangled polymers at high shear rates. *Journal of Polymer Science Part B: Polymer Physics*, 29(13):1589–1597, 1991.

[128] G. Picard, A. Ajdari, L. Bocquet, and F. Lequeux. Simple model for heterogeneous flows of yield stress fluids. *Phys. Rev. E*, 66:051501, 2002.

[129] C. Pozrikidis. *Introduction to Theoretical and Computational Fluid Dynamics*. Oxford University Press Inc., New York, 1997.

[130] W. H. Press, S. A. Teukolsky, W. T. Vetterling, and B. P. Flannery. *Numerical Recipes in C*. Cambridge University Press, Cambridge, 1992.

[131] L. M. Quinzani, G. H. McKinley, R. A. Brown, and R. C. Armstrong. Modeling the rheology of polyisobutylene solutions. *Journal of Rheology*, 34(5):705–748, 1990.

[132] O. Radulescu, P. D. Olmsted, and C.-Y. D. Lu. Shear banding in reaction-diffusion models. *Rheologica Acta*, 38:606–613, 1999.

[133] A. Ragouilliaux, G. Ovarlez, N. Shahidzadeh-Bonn, B. Herzhaft, T. Palermo, and P. Coussot. Transition from a simple yield-stress fluid to a thixotropic material. *Phys. Rev. E*, 76:051408, 2007.

[134] K. R. Rajagopal and A. S. Wineman. Universal relations for instantaneous deformations of viscoelastic fluids. *Rheologica Acta*, 27:555–556, 1988.

[135] S. Ravindranath and S-Q. Wang. What are the origins of stress relaxation behaviors in step shear of entangled polymer solutions? *Macromolecules*, 40(22):8031–8039, 2007.

[136] S. Ravindranath and S-Q. Wang. Steady state measurements in stress plateau region of entangled polymer solutions: Controlled-rate and controlled-stress modes. *Journal of Rheology*, 52(4):957–980, 2008.

[137] S. Ravindranath, S-Q. Wang, M. Olechnowicz, V. Chavan, and R. Quirk. How polymeric solvents control shear inhomogeneity in large deformations of entangled polymer mixtures. *Rheologica Acta*, 50:97–105, 2011.

[138] S. Ravindranath, S-Q. Wang, M. Olechnowicz, and R. P. Quirk. Banding in simple steady shear of entangled polymer solutions. *Macromolecules*, 41(7):2663–2670, 2008.

[139] Sham Ravindranath and Shi-Qing Wang. Large amplitude oscillatory shear behavior of entangled polymer solutions: Particle tracking velocimetric investigation. *Journal of Rheology*, 52(2):341–358, 2008.

[140] S. Rodts, J. C. Baudez, and P. Coussot. From 'discrete' to 'continuum' flow in foams. *Europhysics Letters*, 69(4):636, 2005.

[141] S. A. Rogers, D. Vlassopoulos, and P. T. Callaghan. Aging, yielding, and shear banding in soft colloidal glasses. *Phys. Rev. Lett.*, 100:128304, 2008.

[142] V. Rolón-Garrido and M. Wagner. The damping function in rheology. *Rheologica Acta*, 48:245–284, 2009.

[143] J. Rosti, J. Koivisto, L. Laurson, and M. J. Alava. Fluctuations and scaling in creep deformation. *Phys. Rev. Lett.*, 105:100601, 2010.

[144] J-B. Salmon, A. Colin, S. Manneville, and F. Molino. Velocity profiles in shear-banding wormlike micelles. *Phys. Rev. Lett.*, 90:228303, 2003.

[145] J-B. Salmon, S. Manneville, and A. Colin. Shear banding in a lyotropic lamellar phase. I. Time-averaged velocity profiles. *Phys. Rev. E*, 68:051503, 2003.

[146] J. Sanchez-Reyes and L. A. Archer. Step shear dynamics of entangled polymer liquids. *Macromolecules*, 35(13):5194–5202, 2002.

[147] Henningson D. S. Schmid, P. J. *Stability and Transition in Shear Flows*. Springer, New York, 2001.

[148] P. J. Schmid. Nonmodal stability theory. *Annual Review of Fluid Mechanics*, 39(1):129–162, 2007.

[149] P. J. Schmid, D. S. Henningson, M. R. Khorrami, and M. R. Malik. A study of eigenvalue sensitivity for hydrodynamic stability operators. *Theoretical and Computational Fluid Dynamics*, 4(5):227–240, 1993.

[150] M. Siebenbürger, M. Ballauff, and Th. Voigtmann. Creep in colloidal glasses. *Phys. Rev. Lett.*, 108:255701, 2012.

[151] S. Skorski and P. D. Olmsted. Loss of solutions in shear banding fluids driven by second normal stress differences. *Journal of Rheology*, 55(6):1219–1246, 2011.

[152] P. J. Skrzeszewska, J. Sprakel, F. A. de Wolf, R. Fokkink, M. A. Cohen Stuart, and J. van der Gucht. Fracture and self-healing in a well-defined self-assembled polymer network. *Macromolecules*, 43(7):3542–3548, 2010.

[153] P. Sollich. Rheological constitutive equation for a model of soft glassy materials. *Phys. Rev. E*, 58:738–759, 1998.

[154] P. Sollich, F. Lequeux, P. Hébraud, and M. E. Cates. Rheology of soft glassy materials. *Phys. Rev. Lett.*, 78:2020–2023, 1997.

[155] N. A. Spenley, M. E. Cates, and T. C. B. McLeish. Nonlinear rheology of wormlike micelles. *Phys. Rev. Lett.*, 71:939–942, 1993.

[156] J. Sprakel, S. B. Lindström, T. E. Kodger, and D. A. Weitz. Stress enhancement in the delayed yielding of colloidal gels. *Phys. Rev. Lett.*, 106:248303, 2011.

[157] S. H. Strogatz. *Nonlinear Dynamics and Chaos.* Persues Books Publishing, LLC, 1994.

[158] L. C. E. Struik. *Physical Aging in Amorphous Polymers and Other Materials.* Elsevier, New York, 1978.

[159] M. Takahashi, T. Isaki, T. Takigawa, and T. Masuda. Measurement of biaxial and uniaxial extensional flow behavior of polymer melts at constant strain rates. *Journal of Rheology*, 37(5):827–846, 1993.

[160] R. I. Tanner. *Engineering Rheology.* Clarendon Press, Oxford, 1985.

[161] P. Tapadia and S-Q. Wang. Yieldlike constitutive transition in shear flow of entangled polymeric fluids. *Phys. Rev. Lett.*, 91:198301, 2003.

[162] P. Tapadia and S-Q. Wang. Direct visualization of continuous simple shear in non-newtonian polymeric fluids. *Phys. Rev. Lett.*, 96:016001, 2006.

[163] Prashant Tapadia, Sham Ravindranath, and Shi-Qing Wang. Banding in entangled polymer fluids under oscillatory shearing. *Phys. Rev. Lett.*, 96:196001, May 2006.

[164] L.C.A. van Breemen, E.T.J. Klompen, L.E. Govaert, and H.E.H. Meijer. Extending the EGP constitutive model for polymer glasses to multiple relaxation times. *Journal of the Mechanics and Physics of Solids*, 59(10):2191 – 2207, 2011.

[165] F. Varnik, L. Bocquet, and J.-L. Barrat. A study of the static yield stress in a binary Lennard-Jones glass. *The Journal of Chemical Physics*, 120(6):2788–2801, 2004.

[166] D. C. Venerus. A critical evaluation of step strain flows of entangled linear polymer liquids. *Journal of Rheology*, 49(1):277–295, 2005.

[167] S-Q. Wang. The tip of iceberg in nonlinear polymer rheology: Entangled liquids are 'solids'. *Journal of Polymer Science Part B: Polymer Physics*, 46(24):2660–2665, 2008.

[168] S-Q. Wang, S. Ravindranath, P. Boukany, M. Olechnowicz, R. P. Quirk, A. Halasa, and J. Mays. Nonquiescent relaxation in entangled polymer liquids after step shear. *Phys. Rev. Lett.*, 97:187801, 2006.

[169] S-Q. Wang, S. Ravindranath, Y. Wang, and P. Boukany. New theoretical considerations in polymer rheology: Elastic breakdown of chain entanglement network. *The Journal of Chemical Physics*, 127(6):064903, 2007.

[170] Y. Wang and S-Q. Wang. Exploring stress overshoot phenomenon upon startup deformation of entangled linear polymeric liquids. *Journal of Rheology*, 53(6):1389–1401, 2009.

[171] E. R. Weeks, J. C. Crocker, A. C. Levitt, A. Schofield, and D. A. Weitz. Three-dimensional direct imaging of structural relaxation near the colloidal glass transition. *Science*, 287(5453):627–631, 2000.

[172] J. Yerushalmi, S. Katz, and R. Shinnar. The stability of steady shear flows of some viscoelastic fluids. *Chemical Engineering Science*, 25(12):1891 – 1902, 1970.

[173] B. Yesilata, C. Clasen, and G. H. McKinley. Nonlinear shear and extensional flow dynamics of wormlike surfactant solutions. *Journal of Non-Newtonian Fluid Mechanics*, 133(2-3):73 – 90, 2006.

[174] L. Zhou, P. A. Vasquez, L. P. Cook, and G. H. McKinley. Modeling the inhomogeneous response and formation of shear bands in steady and transient flows of entangled liquids. *Journal of Rheology*, 52(2):591–623, 2008.